Synthesis, Relaxation Dynamics and Rheology of Supramolecular Polymers

Guanghui Cui

School of Physics and Astronomy

University of Leeds

Submitted in accordance with the requirements for the degree of

Doctor of Philosophy

September 2017

The candidate confirms that the work submitted is his own, i.e. the candidate performed all the synthesis work, all the experimental work and the data analysis presented in the thesis, with the exceptions outlined below. The contribution of the candidate and the other collaborators to this work has been explicitly indicated below. The candidate confirms that appropriate credit has been given within the thesis where reference has been made to the work of others.

The synthesis work was performed in Prof. Andrew Wilson's lab in the School of Chemistry, University of Leeds. I was responsible for carrying out synthesis and characterization work, collecting and analysing the data.

The X-ray scattering measurements shown in Chapter 3 and 5 were performed in Prof. Michael Rappolt lab in the School of Food Science and Nutrition, University of Leeds. I was responsible for carrying out the experiment with the help of Dr. Sadeghpour Amin, collecting and analysing the data.

The AFM measurements shown in Chapter 3 and 5 were conducted together with Dr. Simon Connell in the School of Physics and Astronomy, University of Leeds. I was responsible for preparing the AFM samples and analysing the data.

The stochastic model in Chapter 4 (details on the model are shown in the Appendix) was inspired by the discussions of linear viscoelastic (LVE) data with Mr. Victor Boudara and Dr. Daniel Read from School of Mathematics, University of Leeds. The detailed mathematical work was conducted by Victor and Daniel. The fitting of the extensional rheological data using the upper convected Maxwell model in Chapter 4 was also conducted by Mr. Victor Boudara.

The work on self-healing coatings in Chapter 5 was conducted at the company *allnex*, Belgium, under the supervision of Dr. Patrice Roose. I was responsible for discussing the idea with Dr. Roose, performing the experiments, collecting and analysing.

To Kaiying, Keyi, Kewei.

Acknowledgements

I would like to express my sincere gratitude to my advisor Dr. Johan Mattsson for his continuous support and guidance during my PhD period. His guidance and immense knowledge helped me all the time during researching and writing of this thesis.

I would like to express my thanks to the Marie Curie Initial Training Network project (SUPOLEN) and University of Leeds for the financial support. With the generous supports, I can keep focusing on the research work. I also thank these people involved in the SUPOLEN project for their kind supports and advices. I have had really wonderful time during the whole period of the project. They are Prof. Jean-Francois Gohy, Prof. Evelyne van Ruymbeke, Prof. Dimitris Vlassopoulos, Prof. Benjamin Elias, Prof. Charles-Andr Fustin, Prof. Ole Hassager, Prof. Christian Clasen, Prof. Christian Ligour, Prof. Serge Mora, Prof. Luca Cipeletti, Prof. Giovanni Ianniruberto, Prof. W. J. Briels, Dr. Daniel Read, Dr. Johan Mattson, Dr. Mike Ries, Dr. Franck Touraud, Dr. Benot Loppinet, Dr. Carel Fitie, Dr. Benot Loppinet, Dr. Laurence Ramos, Dr. Patrice Roose, Dr. Jrmy Brassine, Dr. Guilhem Baeza, Dr. Laurence Hawke, Mr. Flanco Zhuge, Mr. Ashwinikumar Sharma, Mr. Ameur Louihichi, Mr. Salvatore Constanzo, Mr. Aamir Shabbir. Mr. Jan Hendricks, Miss Srishti Arora, Mr. Stefano Aime, Mr. Gun Woo Park, Mr. Victor Boudara and Mr. Vishal Metri.

I would like to thank my co-advisor and cooperators for their helpful discussions. Thanks especially to Dr. Mike Ries, Dr. Daniel Read, Prof. Ole Hassager, Dr. Qian Huang, Prof. Andrew Wilson, Mr. Victor Boudara, Prof. Michael Rappolt, Dr. Amin Sadeghpour, Dr. Guilhem Baeza and Dr. Simon Connell. I would like to thank Dr. Patrice Roose from *allnex*, Belgium, for hosting me in the lab for a short internship and his guidance on the development of UV curable coatings with the self-healing property.

I would like to thank Dr. Daniel Baker who really helps a lot in many aspects from the experiment setup to coding and many other things. I would also like to thank all my friends and office mates: Winke, Zhaopeng, Ben, Tingzi, Wafa, Sophie, James, Peng Bao, Steve, Sunjie, Helen, Devesh, Matt, Edgar, Nikita and Shajeth, for making the PhD life less boring.

Thanks also go to all administrative teams in the School of Physics and Astronomy and in the Soft Matter Group.

I would like to thank my parents. Although they were not patient enough to wait for this moment, they would definitely feel proud of me. Thanks to my sisters for looking after me when I was a kid and for encouraging in continuous study.

Last but certainly not least, I am deeply thankful to my wife, Kaiying. Her endless and unwavering love, devotion and sacrifices were, and remain, undeniably the cornerstone of our family. Her support, encouragement, patience and tolerance are accompanying me in going through all hardest time. Without her, my life would never have been so wonderful like this, and this thesis would never have been written. Thanks also go to my kids, Keyi and Kewei, for making my life more colourful.

Abstract

A supramolecular polymer is a complex assembly of molecules held together by noncovalent bonds, such as hydrogen bonding, host-guest interactions or coordinative bonds. The last few decades great developments have been made in the research and application of supramolecular polymers, and a wide variety of supramolecular polymers have been prepared. These supramolecular polymers have been applied within many application areas, especially for medical applications such as drug or DNA delivery into living cells, and controlled drug release. However, many fundamental aspects such as the relaxation dynamics and rheological properties over a wide temperature range as well as the detailed structure-properties relationships are still not well understood for supramolecular polymers. This thesis addresses this, and aims at a better understanding of how the supramolecular interactions affect the structure, relaxation dynamics and rheological properties of different supramolecular polymer systems over a wide timescale or temperature range ranging from the glassy to the melt states. The goal is to determine the structure-property relationships, and to provide guidelines for the design and synthesis of new supramolecular polymers.

In this thesis, the dynamics of four different supramolecular polymers are investigated. The first system is based on a comb-like polymeric backbone of poly(2-ethylhexyl acrylate) (PEHA) to which a random distribution of 2-ureido-4[1H]-pyrimidinone (UPy) supramolecular side-groups are added. A series of polymers with varying side-group UPy contents have been synthesised using the reversible addition fragmentation chain transfer (RAFT) polymerization. The second system is based on poly(propylene glycol) (PPG) for which the chain ends were functionalised using supramolecular hydrogen-bonding UPy-groups. The unfunctionalised PPG is a viscous liquid at room temperature whereas the end-functionalised UPyPPG is a rubbery material due to the formation of long extended chains formed through multiple hydrogen bonds. For this supramolecular polymer system, we have investigated two possible application areas: (i) the use of blends of PPG and UPyPPG with lithium salts in polymer electrolytes for Li-ion batteries and (ii) the use together with UV-curable components for self-healing coatings. The third system is based

on hydroxyl-capped polytetrahydrofuran (PTHF) with varying molecular weights and the fourth is a set of alkane diols of different chain-length. For both these systems, intermolecular supramolecular hydrogen bond interactions via the chain-ends will become more important for shorter chains. Generally, the relaxation dynamics, thermodynamic response and rheological response were determined using a range of experimental techniques, including broadband dielectric relaxation spectroscopy, differential scanning calorimetry (both in the standard and modulated mode), shear and extensional rheology and nuclear magnetic resonance relaxometry.

Abbreviations

T_g	Glass transition temperature
T_m	Melting point
T_b	Boiling point
UPy	2-ureido-4[1H]-pyrimidinone
PTHF	Polytetrahydrofuran
PPG	Polypropylene glycol
M_{mono}	Molecular weight of a monomer
M_n	Number average molecular weight
M_w	Weight average molecular weight
M_z	z-average molecular weight
PDI	Polydispersity of molecular weights
C_∞	Flory's characteristic ratio
D	Diffusion coefficient
ζ	Friction coefficient
τ_R	Rouse relaxation time
τ_0	Fundamental Rouse relaxation time
G'	Storage modulus
G''	Loss modulus
G_p	Plateau modulus
τ_{rep}	Reptation time
τ_s	Sticker time
VFT	Vogel-Fulcher-Tammann equation
η	Viscosity
T_k	Kauzmann temperature
H	Enthalpy
S	Entropy

V	Specific volume
τ_α	Structural relaxation time
m	Fragility
V_f	Free volume
CRR	Cooperatively rearranging region
E_a	Activation energy
k_B	Boltzmann constant
PEHA	Poly(2-ethylhexyl acrylate)
$\varepsilon*$	Complex permittivity
ε'	Real part of complex permittvity
ε''	Imaginary part of complex permittvity
$\Delta\varepsilon$	Dielectric relaxation strength
HN	Havriliak-Negami equation
CD	Cole-Davidson equation
CC	Cole-Cole equation
ω	Angular frequency
f	Frequency
λ	Shear stress
γ	Shear strain
$\dot{\gamma}$	Shear rate
G	Shear modulus
TTS	Time temperature superposition
a_T	Horizontal shift factor
b_T	Vertical shift factor
WLF	Williams-Landel-Ferry equation
T_{ref}	Reference temperature
η_E^+	Stress growth coefficient
ε_H	Hencky strain
$\dot{\varepsilon}$	Strain rate
q	Heat flow
Q	Heat rate
C_p	Heat capacity
ΔC_p	Heat capacity difference
T_{onset}	Onset temperature of a glass transition

T_{offset}	Offset temperature of a glass transition
$T_{\text{inflection}}$	Inflection temperature of a glass transition
ΔT	$\Delta T = T_{\text{offset}} - T_{\text{onset}}$
Q_m	Modulated heat rate
t_p	Modulated period
$C_{\text{p,r}}$	Reversing heat capacity
$C_{\text{p,nr}}$	Non-reversing heat capacity
T_1	Longitudinal T_1 relaxation
T_2	Transverse T_2 relaxation
τ_c	Correlation time
M_e	Entanglement molecular weight
M_c	Critical molecular weight
ϕ_{UPy}	UPy molar concentration
n_C	Number of carbon atoms
σ	Ion conductivity
kT	Thermal energy
PEG	Polyethylene glycol
PnMA	Poly(n-alkyl methacrylate)
PE	Polyethylene
PAO	Poly(alkylene oxides)
P2VP	Poly(2-vinylpyridine)

Contents

List of Figures **15**

List of Tables **33**

1 Introduction **1**

1.1 Supramolecular chemistry 1

1.1.1 Supramolecular interactions 2

1.1.2 Supramolecular polymers 6

1.2 Polymers and polymer dynamics 12

1.2.1 Basics of polymers 13

1.2.2 Structures and components of polymers 15

1.2.3 Synthesis of polymers 16

1.2.4 Single chain conformations 22

1.2.5 The Rouse model 26

1.2.6 The tube model 30

1.2.7 The sticky Rouse model 34

1.3 The glassy state and the glass transition 35

1.3.1 Supercooled liquids and glasses 35

1.3.2 The glass transition 37

1.3.3 Relaxation dynamics in supercooled liquids 38

1.4 Importance of the work 42

2 Experimental Techniques **44**

2.1 Broadband dielectric spectroscopy 44

2.1.1 Polarisation of a material in an electrical fields 45

2.1.2 Reorientation of permanent dipoles in an electrical field . . . 46
2.1.3 The relaxation of a polarized material . . . 47
2.1.4 The dielectric spectroscopy experimental set-up . . . 52
2.1.5 Sample preparation . . . 55
2.1.6 Characteristics of a typical dielectric relaxation spectrum . . . 55
2.2 Rheometry . . . 57
2.2.1 Definition of terms . . . 58
2.2.2 Oscillatory test . . . 59
2.2.3 Amplitude sweep . . . 63
2.2.4 Frequency sweep . . . 64
2.2.5 Time Temperature Superposition (TTS) . . . 66
2.2.6 Relaxation and creep experiments . . . 70
2.2.7 Rotational experiments . . . 73
2.2.8 Extensional Rheology . . . 74
2.2.9 Rheometers . . . 76
2.3 Calorimetry . . . 77
2.3.1 Differential Scanning calorimetry . . . 77
2.3.2 Temperature modulated DSC . . . 80
2.3.3 Rate dependent DSC . . . 86
2.4 Nuclear magnetic resonance (NMR) . . . 87
2.4.1 Origin of nuclear magnetic resonance . . . 87
2.4.2 The NMR spectrometer . . . 90
2.4.3 Relaxation of the magnetic moment . . . 90
2.4.4 Measurements of T_1 and T_2 relaxations . . . 92
2.4.5 Bloemberg-Purcell-Pound (BPP) Theory . . . 93
2.5 Summary . . . 94

3 Control of polymer dynamics using supramolecular side-groups 96
3.1 Introduction . . . 97
3.2 Experimental section . . . 100
3.2.1 Materials . . . 100
3.2.2 Synthesis of UPy functionalized ethylacrylate (UPyEA) . . . 100
3.2.3 Characterisations . . . 103

3.3 Results and discussions . . . 107
3.3.1 Structures . . . 107
3.3.2 Rheological responses . . . 115
3.3.3 The thermodynamic and dynamic response . . . 122
3.4 Conclusions . . . 135

4 Linear shear and extensional rheology of unentangled supramolecular side-chain polymers 136
4.1 Introduction . . . 137
4.2 Experimental section . . . 141
4.3 Results and Discussions . . . 142
4.3.1 Linear viscoelasticity and validity of TTS . . . 142
4.4 Modeling of linear shear rheology . . . 150
4.4.1 "Classic" sticky Rouse model . . . 150
4.4.2 The stochastic model . . . 151
4.4.3 Comparisons of two models with experimental data . . . 152
4.4.4 Extensional rheology and modelling . . . 156
4.5 Conclusions . . . 158

5 Supramolecular polymers based on UPy end-functionalised poly(propylene glycol): structure, dynamics, rheology and applications 160
5.1 Introduction . . . 161
5.2 Experimental section . . . 165
5.2.1 Materials . . . 165
5.2.2 Synthesis of UPy end-functionalised poly(propylene glycol) (UPyPPG) . . . 166
5.2.3 Preparation of polymeric electrolytes . . . 167
5.2.4 Preparation of self-healing coatings . . . 167
5.2.5 Characterisations . . . 168
5.3 Results and Discussions . . . 169
5.3.1 Structure . . . 169
5.3.2 Dynamics and rheological response of PPG and UPyPPG . . . 172
5.3.3 Ion transport in polymer electrolytes based on PPG and UPyPPG with added LiTFSI salts . . . 184

5.3.4 UPyPPG as an effective component for self-healing coating . 193
5.4 Conclusions 198

6 Chain-Length Dependent Relaxation Dynamics in Polytetrahydrofuran 200
6.1 Introduction 200
6.2 Experimental section 204
6.2.1 Materials 204
6.2.2 Characterizations 205
6.3 Results and Discussions 207
6.3.1 Dynamics in the melt 208
6.3.2 Dynamics near the glass transition 217
6.3.3 Dynamics of alkane diols 227
6.4 Conclusions 231

7 Conclusions and outlook 233
7.1 Overall conclusions 233
7.2 Outlook 237

A The stochastic model 239
A.1 Random placement of stickers on a chain 239
A.2 "Fast" Rouse modes – G_{fast} 240
A.2.1 Trapped and dangling chain strands 240
A.2.2 Storage and loss moduli – $G'(\omega), G''(\omega)$. 242
A.2.3 Polydispersity 243
A.3 "Sticky" modes – $G_{\text{sticky}}(t)$ 243
A.3.1 Initial spatial configuration 243
A.3.2 Sticker "hop" 244
A.3.3 Sticker detachment dynamics 245
A.3.4 Stress tensor and stress relaxation 246
A.3.5 Polydispersity 247
A.3.6 Sticker times 248

B References 250

List of Figures

1.1 Schematic illustration of chemical structures of ion-dipole interactions: (a) $Na(H_2O)_6^+$ and (b) $Ru(bpy)_3^{2+}$. The solid and dashed triangles indicate spatial positions of the bonds. 3

1.2 Schematic illustration of the hydrogen bond in (a) water and (b) triple hydrogen bonds between guanine and cytosine. The red and black balls in (a) represent the oxygen and hydrogen atoms, and oxygen atoms are partly negative charged whereas hydrogen atoms are partly positive charged. 4

1.3 Schematic illustration of transient chain model: molecules can attach and/or detach from the "core" chain through hydrogen bonds. The blue arrows indicated the end-to-end vector of the transient chain, of which the orientation corresponds to the Debye relaxation. 5

1.4 π-π stacking between benzene rings. 6

1.5 (a) Schematic illustration of supramolecular polymers assembled from end-to-end interactions,[29] (b) an example of linear supramolecular polymers based on 2-ureido-4[1H]-pyrimidinone, (UPy) functionalised polytetrahydrofuran. The red dashed lines are hydrogen bonds.[31] . 8

1.6 Schematic illustration of side chain supramolecular polymers: (a) two components system forms comb-like structure, (b) two components forms network structures and (c) one component system with self-complementary groups forms network structures.[38–40] 10

1.7 Supramolecular polymer networks from poly(butyl acrylate) bearing self-complementary UPy groups.[42] 10

1.8 (a) Schematic illustration of construction of dendrimers based on supramolecular interactions.[47] The numbers indicate the generation of the building blocks. (b) an example of self-assembly of root functionalised dendrons around a metal cation.[48] 12
1.9 Schematic illustration of structures and components of polymers: (a) linear, (b) ring, (c) comb-like, (d) star, (e) ladder-like, (f) dendritic or branched, (g) cross-linked and (h) multi-block. The color lines indicated polymer chains with different monomers. 15
1.10 Chemical structures of monomers can be polymerized using RAFT polymerisation. 18
1.11 Chemical structures of different types of initiators: (a) azo compounds, (b) organic peroxides and (c) inorganic peroxides for free radical polymerisation. (d) decomposition reaction of AIBN that produces initiator free radicals. 19
1.12 (a) General structures of common RAFT agents (b) chemical structure of a dithioester CTA and its reaction with a free radical. 20
1.13 General mechanism of a RAFT polymerisation. 22
1.14 Schematic illustration of one possible conformation for a flexible polymer with $n + 1$ atoms. 24
1.15 Schematic illustration of Rouse model for a chain with N monomers. The monomers are presented by beads which are connected by springs. 27
1.16 Schematic illustration of (a) topological constraints between long linear chains and (b) the tube model. The topological constraints from the red chains make the motion of the blue chain in the tube-like region (black lines) with the tube diameter of a. 31
1.17 Schematic illustration of stress relaxation modulus as a function of time for entangled polymer predicted by the tube model in the log-log plot. 32

1.18 Diagram showing several thermodynamic properties (enthalpy $H(T)$, entropy $S(T)$, specific volume $V(T)$ as a function of temperatures at a constant pressure. Lines in different colours and styles show properties of a material at different states which are defined in figure. Variations of H, S and V upon temperature T_m are non-continuous at melting point T_m. The red dot-dashed line is the extrapolation from supercooled liquid line. The crossover of extrapolated supercooled liquid line with crystal line is termed Kauzmann temperature, T_k, indicating that all liquids have to crystallize at this temperature, otherwise entropy of supercooled liquids at temperatures below T_k would be lower than that of corresponding crystals. This is so-called entropy crisis.[95, 96] 36

1.19 (a) The Arrhenius of plot of relaxation timescales as a function of temperatures for α, β and γ relaxations. (b) VFT behaviour of α relaxation with different values of strength parameter, D, showing different fragilities. 39

2.1 Schematic illustration of the effect of an applied electric field (E) on the polarisation of a material (P). The polarisation of (P_0) is produced when the electric field of (E_0) is applied. After the electric field is removed at $t_0 = 0$, the polarisation starts to relax to as a function of time. 48

2.2 The equation shapes for the Debye equation (solid lines with shifted $\Delta\varepsilon$ for clarity), the Cole-Cole (CC) equation (black dashed and dotted lines),the Cole-Davidson (CD) equation (red dashed and dotted lines) and the Havriliak-Negami (HN) equation (blue dashed and dotted lines). The shape parameters to create these curves are shown in legends. The curves are vertically shifted for clarity. 50

2.3 Schematic diagram showing the experimental setup of the dielectric spectroscopy measurement. 53

2.4 Schematic diagrams show the equivalent circuits for BDS measurements of ion conducting materials between two parallel plate electrodes (a) without and (b) with ions accumulate on the surfaces of electrodes. (c) Plot of $-Z''$ as a function of Z'. 54

2.5 Schematic diagrams show samples between (a) two electrodes (from top view) separated by silicon spacers and (b) in a gel cell (from cross-section view) for BDS measurements. 55
2.6 (a) Schematic diagram shows typical real ε' and imaginary ε'' parts of the complex permittivity, which contain contributions from electrode polarisation (EP), ion conductivity σ and a relaxation process (termed α relaxation as an example). (b) A typical ε'' curve for polytetrahydrofuran with molecular weight of 250 g/mol at 182 K, which contains contributions from ion conductivity σ, α and β relaxations, which are fitted using a power law, a HN equation and a Cole-Cole equation. . . 56
2.7 A typical two parallel plates model with a definition of the relevant parameters. 58
2.8 Schematic diagrams to illustrate the oscillatory shear test with a two plates model with a driving wheel linking by a stiff push rod. The top raw shows the displacements of the material at different angle positions (0°, 90°, 180°, 270° and 360°) of the driving wheel. The bottom figure shows the strain applied to the material by the rotation of the driving wheel is a sine wave as function of the time or the angle position. . . 59
2.9 Time dependent functions of $\gamma(t)$, $\lambda(t)$ and $\dot{\lambda}(t)$ for ideally elastic, ideally viscous and viscoelastic materials. 60
2.10 Vector diagram illustrating the relationship between the complex modulus G^*, the storage modulus G', the loss modulus G'' and the phase angle δ with $G^{*2} = G'^2 + G''^2$ and $\tan(\delta) = G''/G'$. 63
2.11 (a) oscillatory strain increases as function of time and (b) a typical strain sweep result as a function of strain. 64
2.12 (a) Controlled strain wave with varying frequency and a constant strain amplitude in a frequency sweep experiment, and (b) typical G' and G'' curves as a function of frequency for an ideal polymer melt or solution in a log-log plot. 65
2.13 (a) Frequency sweeps at three different temperatures (T1, T2 and T3)) for an entangled polymer in the frequency range of 0.62 to 125.6 rad/s. (b) horizontally shift T1 and T3 curves to T2 with shift factor of a_{T1} and a_{T3} to build a master curve. 67

2.14 A typical mechanical behaviour of an entangled polymer as a function of frequency. 69
2.15 Typical stress curves (a) as a function of time in a stress relaxation experiment and strain curves (b) as a function of time in a creep experiment for ideal viscous liquid (1), ideal elastic solid (2), viscoelastic solid (3) and viscoelastic liquid (4). 71
2.16 Shear stress and viscosity for materials showing ideal viscous (1), shear thinning (2) and shear thickening behaviours. 74
2.17 Schematic diagram shows the deformation of the material during an extensional rheological measurement (a) at initial state and (b) at time t 75
2.18 Schematic diagrams for strain controlled (left) and stress (right) controlled rheometers. 76
2.19 (a) A typical DSC heat flow q and (b) C_p traces for the quenched Polytetrahydrofuran with molecular weight of 2000 g/mol (PTHF2000) showing the glass transition, crystallization and melting transitions. The insets are magnifications of the dashed squares to show the step-like glass transition. 78
2.20 Definitions of onset T_{onset}, offset T_{offset}, inflection $T_{\text{inflection}}$ temperatures and ΔC_p during a glass transition process. The temperature difference ΔT between the T_{offset} and the T_{onset}, $\Delta T = T_{\text{offset}} - T_{\text{onset}}$, indicates the broadness of the glass transition. In this work, the onset temperature T_{onset} is used as the glass transition temperature T_g. 79
2.21 (a) Temperature as a function of time in a conventional DSC $f(T,t)$ and in a MDSC $f_m(T,t)$, (b) heating rate Q and modulated heating rate Q_m for silicon oil from a MDSC measurement. 81
2.22 Modulated heat flow q_m and total heat flow q_{total} as a function of temperature for the silicon oil from the MDSC measurement. 82
2.23 (a) Total heat flow q_{total}, reversing heat flow q_r and non-reversing heat flow q_{nr} and (b) total heat capacity $C_{\text{p,total}}$, reversing heat capacity $C_{\text{p,r}}$ and non-reversing heat capacity $C_{\text{p, nr}}$ as a function of temperature for the silicon oil from the MDSC measurement. 83

2.24 (a) Reversing heat capacity $C_{\mathrm{p,r}}$ and phase angle δ from the MDSC measurement of poly(2-ethylhexyl acrylate) (PEHA) as a function of temperature. The δ is corrected using the following relations: $\Delta\delta = a + b|C_{\mathrm{p,r}}|$[160] (the dashed pink line), thus the corrected phase angle: $\delta_{\mathrm{corr}} = \delta - \Delta\delta$. (b) Real C'_p and imaginary C''_p parts of the complex heat capacity C^*_p of PEHA measured by MDSC with $t_p = 60$ s, $Q = 3$ K/min and amplitude of ±1 K. C^*_p is the reversing heat capacity $C_{\mathrm{p,r}}$ from the MDSC measurement. C'_p and C''_p are calculated using the following equations: $C'_p = |C^*_p|\cos(\delta_{\mathrm{corr}})$ and $C''_p = |C^*_p|\sin(\delta_{\mathrm{corr}})$.[160] . 84

2.25 Arrhenius plot of the silicon oil measured by conventional DSC (red squares) and MDSC (pink star) with $t_p = 60$ s, $Q = 0.5$ K/min and amplitude of ±1 K. The data from conventional DSC is shifted upwards to overlap with the MDSC point by the constant a, $\log(a) = 2$. The blue dashed line is the VFT fitting curve to the data. 87

2.26 (a) Energy levels for the ^{1}H nuclei as a function of external magnetic field. The ^{1}H nuclei is a 'spin-1/2' particle, splitting into two sub-levels according to Equation 2.86 after the radiation frequency pulse perturbation. (b) The nuclear magnetic moment $\boldsymbol{\mu}$ precessing around the external magnetic field $\mathbf{B}$ with the Larmor frequency ω_0. 89

2.27 (a) Schematic diagram shows the setup of the MARAN bench-top pulse NMR analyser. (b) definition of the direction of the external magnetic field $\mathbf{B}$ (z-direction) and the RF pulse direction of the NMR analyser. 90

2.28 (a) The overall M_0 along the direction of external magnetic field in the z-direction, (b) after the RF perturbation, M_0 leaves the equilibrium state and has projections M_{xy} and M_z in the xy-plane and along the z-direction respectively. 91

2.29 Schematic diagram showing the variation of the magnetization during the T_1 measurement using inversion recovery method. 92

2.30 Schematic diagram showing the variation of the magnetization during the T_2 measurement using Hahn spin-echo pulse sequence. 93

2.31 Schematic illustration of T_1 and T_2 relaxations as a function of correlation time, τ. 94

3.1 Synthesis of UPy functionalised monomers (UPyEA) and (co)polymers containing EHA and UPyEA by RAFT polymerisation. 101
3.2 Stress σ and strain γ as a function of time for UPyPEHA14 at 263 K in a step stress relaxation measurement. 106
3.3 (a) X-ray scattering intensity measured on PEHA0 and its UPy functionalised counterparts (2, 6, 9 and 14% UPy) as a function of q. The solid lines in the SAXS region are the best fits using the combination of a powerlaw and two Gaussian equations for q_{I} and q_{II}. The solid line in the WAXS region is the best fit for UPyPEHA14 using the combination of two Gaussian equations for q_{III}. For clarity, fitted lines are other samples are not plotted. In WAXS fits, one Gaussian equation accounts for the broadening at low q side is fixed for all samples. The contributions of each fitting component are shown in Figure 3.4a and b for SAXS and WAXS respectively. 109
3.4 Examples to show the fitting contributions as discussed in Figure 3.3 for (a) SAXS of UPyPEHA9 and (b) WAXS of PEHA0. 110
3.5 AFM height (a) and phase (b) images for UPyPEHA6, see Experimental section for the preparation of the thin film. 111
3.6 Schematic diagrams show (a) nano-phase separated structures for PEHA0 and side alkyl chain arrangements, (b) transient networks through UPy dimers for UPyPEHA. For clarity, nano-phase structures are not shown. 112
3.7 (a) Master curves for samples with varying ϕ_{UPy} referring to 363 K. The black and yellow solid lines are the single SAOS measurements at 363 K. Two pictures framed black and blue illustrate the state of the matter for PEAH0 and UPyPEHA6, respectively. For samples with more then 2 mol% UPy, only part of master curves (from plateau to terminal range) are shown. Three horizontal dashed lines indicate plateau moduli calculated using equation 3.2. (b)Shift factors used to build corresponding master curves in panel (a). The solid lines in (b) are VFT fits (PEAH0 and UPyPEHA2) and Arrhenius fits (UPyPEHA6, 9 and 14), and fitting parameters are shown in Table 3.2. 116

3.8 (a) Schematic diagram shows the cooperative breaks of UPy dimers for chains to relax in the terminal region. (b) G' and G"in the frequency range between glass and rubbery plateau, obtained from the transformation of the stress relaxation experiment at 243 K for UPyPEHA6 and UPyPEHA9 and 263 K for UPyPEHA14. A free software, *iRheo*, is used to do the transformation.[145] For, PEHA0 and UPyPEHA2, the TTS results in Figure 3.7 are used. The curves are shifted vertically for clarity. 117

3.9 (a) Specific heat capacity C_p of the (co-)polymers as a function of temperatures for PEHA0 and UPyPEHA with various ϕ_{UPy}. The thermograms have been vertically shifted for clarity, allowing to illustrate broadening of glass transitions as increasing ϕ_{UPy}. (b) Temperature differences ΔT between T_{onset} and T_{offset} as well as the step amplitude ΔC_p as a function of molar UPy fraction ϕ_{UPy}. The blue and red lines are guide to eye. 123

3.10 Various definitions of the glass transition temperatures from DSC, MDSC and BDS measurements as a function of ϕ_{UPy}. 124

3.11 The real part C_p' and imaginary part C_p"of complex heat capacity C_p* for (a) PEHA0, (b) UPyPEHA2, (c) UPyPEHA6, (d) UPyPEHA92 and (e) UPyPEHA14, measured by MDSC with a period time (t_p) of 60 s and modulated amplitude of 1 K at 3 K/min heating rate, the angular frequency, $\omega = 2\pi/t_p$, thus characteristic relaxation timescale, $\tau = 1/\omega$. [268] 125

3.12 Real ε' and imaginary ε'' part of complex permittivity for (co-)polymers with varyingϕ_{UPy} at various temperatures. Solid lines are the best fitting results to the data using Equation 3.6. 127

3.13 Real ε' and imaginary ε'' part of complex permittivity as function of frequencies for a) PEHA0 with T = 236 K, b) UPyPEHA6 T = 258 K and c) UPyPEHA14 T = 272 K. The dotted and dashed lines represent the imaginary part of the different process contributions (σ, α, α^*) used to fit the data. d) Normalized ε'' at T=268 K for PEHA0 and the samples containing 2, 6, 9 and 14 % molar UPy contents. A and B in d) are the scaled factors based on the α^* relaxation peak. 128

3.14 (a) Temperature dependence of τ_α and τ_{α^*} (filled and open symbols) for (co-)polymers with varying ϕ_{UPy}, as well as MDSC results (cross filled symbols). Solid lines are fitted to τ_α data with the VFT equation excepted that for UPyPEHA14 which is fitted with the Arrhenius equation. The dashed lines are the Arrhenius fits of τ_{α^*} for PEHA0. For clarity, the Arrhenius fits for τ_{α^*} of other samples are not shown. Fitting parameters are reported in Table 3.3. (b) Plots of τ_α against T_g/T for all samples. The dash-dot lines indicate the definition of T_g when $\tau_\alpha = 100$ s. 130

3.15 (a) An example shows the fitting of ε'' spectra for γ relaxation by the combination of a Cole-Cole equation and two power laws for the low and high frequency flanks. (b-f) ε'' spectra for γ relaxations for (co-)polymers with varying ϕ_{UPy} at various temperatures. Solid lines are the best fitting results to the data. 133

3.16 (a) An example to show the fitting of ε'' spectra for the γ relaxation by the combination of a Cole-Cole function and two power laws for the low and high frequency flanks. (b-f) ε'' spectra for the γ relaxations for (co-)polymers with varying ϕ_{UPy} at various temperatures, the solid lines are the best fitting results to the data. 134

4.1 Chemical structures of PEHA and UPyPEHA with varying ϕ_{UPy}. The letter "x" in the figure indicates the $\phi_{\mathrm{UPy}} = 2, 6, 9, 14$ mol%. 142

4.2 (a) Master curves for the samples with varying ϕ_{UPy} referring to 363 K. The black and yellow solid lines are the single small amplitude oscillatory rheological measurements at 363 K. (b) the shift factors used to build the corresponding master curves in panel (a). The solid lines are the VFT fits, except for the UPyPEHA14 which is fitted by the Arrhenius equation. (c) Part of master curves where TTS works and (d) corresponding shift factors. In (d), the shift factors for PEHA0 and UPyPEHA2 are fitted with VFT equation, whereas other samples are fitted with the Arrhenius equation. Note that the master curve for PEHA0 was referred to 263 K, because the torque at 363 K is too small for the oscillation shear measurement. Thus, shift factors referring to 263 K is extrapolated to 363 K and the extrapolated shift factor at 363 K is used to shifted the master curve for PEHA0 in (a) and (c). 143

4.3 Plot of tan(δ) as a function of G^* for all samples. The blue symbols are the small amplitude oscillation shear (SAOS) measurements at all temperatures. The colour symbols on the figure for PEHA0, UPyPEHA6 and UPyPEHA14 are the SAOS measurements at the temperatures where the stress relaxation experiments are conducted. The black lines are calculated from the dynamic modulus from the stress relaxation measurements at the temperatures corresponding to the colour symbols. 145

4.4 Comparison between the dynamic shear modulus obtained from TTS (symbols) and from the conversion (lines) of stress relaxation data using *iRheo*: (a) an example of UPyPEHA14 at 263 K to estimate the accuracy of *iRheo* at low frequencies, (b) PEHA0, (c) UPyPEHA6 and (d) UPyPEHA14 at various temperatures. The data for UPyPEHA6 and UPyPEHA14 in panels (c) and (d) are vertically shifted for clarity. The blue vertical lines indicate the frequency range of a single SAOS measurement. 147

4.5 Comparison of the master curves from TTS (symbols) and from stress relaxation measurements (lines) for (a) PEHA0, (b) UPyPEHA6 and (c) UPyPEHA14. The colour lines are shifted horizontally using the TTS shift factors used to build the TTS master curves at the corresponding temperature. For example, the master curves for PEHA0 is built referring to 203 K. Thus the red lines are not shifted, but the green and pink lines are shifted using the TTS shift factors for 243 and 263 K. 149

4.6 Master curves (symbols) for UPyPEHA6 referring to 343 K, and fitting (solid lines) by (a) the stochastic model and (b) the sticky Rouse model, and the contributions from the sticky modes and the fast modes. (c) master curves (symbols) for the samples with varying UPy contents, and the fitting by the sticky Rouse model and the stochastic model. The curves in (c) are vertically shifted for clarity. The parameters used in both models are given in Table 4.1. 154

4.7 (a) Stress growth coefficient measured using the filament stretching rheometer for the UPyPEHA6 at 343 K with varying stretching rates. The dashed line represents the best fit of the multimode Maxwell model to the LVE data. (b) the stress as a function of Hencky strain corresponding to the same measurements in (a). The symbols represent the same stretching rates in both (a) and (b). 157

5.1 Synthesis of end-functionalised poly(propylene glycol) 166

5.2 AFM height (a) and phase (b) images for UPyPPG after spin casting. The inset in (b) is the cross-sectional profile inside the dotted box, with the domain spacing d being the distance between the maxima of two neighbouring peaks. 170

5.3 Schematic diagram showing the formation of nanofibres through hierarchical self-assembly involving three steps: i) chain extension through UPy dimerisation, ii) stack of UPy dimers and iii) aggregation induced phase separation of nanofibres. 170

5.4 X-ray profiles for PPG and UPyPPG. Two peaks q_1 and q_2 are detected and the peak marked by $*$ is possibly due to antioxidants in PPG.[385, 386] 171

5.5 Specific heat capacity as a function of temperatures for PPG and UPyPPG 172
5.6 Imaginary part, ε'', of complex permittivity as function of frequencies for PPG at (a) $T = 216$ K and (b) $T = 150$ K, and for UPyPPG at (c) $T = 248$ K and (d) $T = 150$ K. The light blue dashed and blue dotted lines in (a) and (c) represent imaginary parts of α', α relaxation contributions, respectively. The blue dashed lines in (b) and (d) represent γ relaxation. At some temperatures, the spectra show a high frequency contribution which is described by a power law $\varepsilon'' = A\omega^B$ (green dot-dot-dashed lines) in (a), (b) and (d). The pink dot-dashed lines in (a) an (c) are the contributions from ion conductivity. The black lines in all figures are the total fitted results. 174
5.7 Dielectric spectra for PPG and UPyPPG at different temperatures showing normal modes α', segmental or structural modes α and subglass relaxation modes γ: (a) α', α, (b) γ relaxations for PPG, (c) α', α, (d) γ relaxations for UPyPPG. The black lines in all figures are the total fitted results as described in Figure 5.6. 175
5.8 Temperature dependence of fitting parameters in equation 5.1. Shape parameters for (A) α, (B) α' and (C) γ relaxation modes for PPG and UPyPPG. Relaxation strengths $\Delta\varepsilon$ of different modes for (D) PPG and (E) UPyPPG. (F) Relative dielectric strengths $\Delta\varepsilon^{\alpha'}/\Delta\varepsilon^{\alpha}$ as a function of temperatures. 177

5.9 (a) Linear viscoelastic master curves referring to 223 K (T_{refer} = 223 K) for PPG and UPyPPG. The green and purple lines represent the SAOS data measured at 223 K. Power law exponents in terminal regions for both samples are 1 and 2 for G'' and G'. (b) The temperature dependence of the shift factors for PPG and UPyPPG. The solid lines are VFT fits whereas the dashed line is the Arrhenius fit. An obvious change from the VFT behaviour (between two vertical lines) to the Arrhenius behaviour is observed at T~283 K. (c) master curves for UPyPPG referring to 223 and 331 K. SAOS data measured below and above 283 K are referred to 223 and 331 K, respectively. The green and purple lines are the SAOS data measured at 223 and 331 K, respectively. (d) the temperature dependence of the relaxation timescales τ_{a_T} for UPyPPG from rheological measurements. τ_{a_T} is calculated: $\tau_{a_T} = \tau_{223} a_{T,223}$ (blue squares) or $\tau_{a_T} = \tau_{331} a_{T,331}$ (upper triangles). τ_{223} is the absolute timescale at 223 K obtained from the peak position by fitting glass region of G'' in (c); τ_{331} is the absolute timescale at 331 K obtained from the cross-over frequency of G' and G'' in (c); $a_{T,223}$ and $a_{T,331}$ are the shift factors used to build master curves in (c) referring to 223 and 331 K, respectively. The solid and dashed lines in (d) are the VFT and Arrhenius fits, and fitting parameters are shows in Table 5.2. 179

5.10 Shear viscosities for PPG and UPyPPG as a function of reciprocal temperature. The dashed and solid lines are the Arrhenius and VFT fits to the experimental data, and the fitting parameters are shows in Table 5.2. 180

5.11 (a) The Arrhenius plot of relaxation timescales for segmental τ_α and normal modes $\tau_{\alpha'}$ relaxations from BDS, and the timescales calculated from the rheological measurements τ_{a_T} for PPG and UPyPPG; The solid lines are the VFT fits while the dashed line is the Arrhenius fit, with fitting parameters shown in Table 5.2. (b) comparison of $\tau_{\alpha'}$ and τ_{a_T} which track chain dynamics from BDS and rheological measurements. Calculations for τ_{a_T} are described in Figure 5.9 (c) Plots of relaxation timescales against the T_g/T. 181

5.12 The Arrhenius plot of γ relaxation timescales, τ_γ, as a function of temperatures. The dashed lines are the Arrhenius fits to the data, and fitting parameters are shown in Table 5.2. 183
5.13 Plot of imaginary σ'' against real σ' part of the complex conductivity for PPG with ratio of O:Li (R) 80:1 (PPG80) at 308 K. 184
5.14 Plots of ion conductivities as a function of temperatures for PPG (a) and UPyPPG (b) with varying R. The vertical dashed lines indicate the temperature of 303 K. 185
5.15 Plots of the ion conductivities as a function R for PPG and UPyPPG at 303 K. The lines are guide to eye. 186
5.16 Heat capacity C_p as a function of temperatures for (a) PPG and (b) UPyPPG with varying ratio of O:Li, R. (c) Glass transition temperatures T_g and (d) broadness of glass transitions ΔT as a function of R for PPG and UPyPPG with varying R. Onset temperatures of glass transitions are used as T_g and $\Delta T = T_{\text{offset}} - T_{\text{onset}}$ is defined as broadness of a glass transition. The symbols in dashed frames are data points for pure PPG and UPyPPG. The error bars are smaller than symbol sizes. 187
5.17 Real ε', imaginary ε'' and derivative imaginary permittivity ε''_{der} (equation 5.2) as a function of frequencies for (a) PPG1000 at 228 K and (b) UPyPPG1000 at 248 K. The pink dot-dashed, light blue dashed and blue dotted lines represent the different relaxation contributions (σ, α' and α), respectively. Electrode polarizations (EP) are indicated in the black dashed frames. The black solid lines in both figures are the total fitted results to ε' and ε'' curves. 189
5.18 The Arrhenius plots of structural τ_α and normal modes $\tau_{\alpha'}$ relaxation timescales as a function of temperatures for (a) PPG and PPG1000, and (b) UPyPPG and UPyPPG1000. 190
5.19 Plot of ion conductivity σ as a function of segmental τ_α and normal modes $\tau_{\alpha'}$ relaxation timescales. The dotted line indicates the slope of 1, and the dashed lines are the linear fits to the data. 192
5.20 (a) Images show the self-healing property of pure UPyPPG after cutting the sample strip, (b) the force as a function of strain for the original strip and the strip after self-healing at 318 K overnight. 194

5.21 Images show the self-healing property of pure UPyPPG film (a - d) at different thermal stages heating from 303 K to 423 K at 10 K/min: (a) 303 K, (b) 333 K, (c) 373 K and (d) 413 K, and the mixture coating (e - h) of UPyPPG and TPGDA (1:1): (e) 303 K, (f) 343 K, (g) 393 K and (h) 423 K. 195
5.22 Pictures to show the self-healing property of the mixture coating (a - d) of UPyPPG and TPGDA (1:3) at different thermal stage heating from 303 K to 423 K at 10 K/min: (a) 303 K, (b) 343 K, (c) 373 K and (d) 423 K for 60 min, and the mixture coating (e - h) of UPyPPG, TPGDA and DAPPG (1:1:1): (e) 303 K, (f) 343 K, (g) 393 K and (h) 423 K for 10 min. 196
5.23 Chemical structures for (a) tripropylene glycol diacrylate (TPGDA), and (b) diacrylate poly(propylene glycol) (DAPPG). Schematic diagrams show networks with (c) high cross-linking density and (d) low cross linking density when introducing DAPPG into coatings. 197

6.1 Chemical structures and abbreviations for PTHF and alkane diols. . . 205
6.2 An example for the viscosity measurement on P650 at 313 K shows that shear stress λ increases linearly as increasing of shear rate $\dot{\gamma}$ in shear rate below 100 1/s. The red line is the linear fit to the date, and the slope of the fitted line is the viscosity. 207
6.3 a) Viscosity and (b) scaled viscosity as a function of temperature for samples with varying molecular weights. The red lines are VFT fits to the data and fitting parameters are given in Table 6.1. The viscosities in (b) are scaled to the viscosity of P2900 with scaling factors A. The scaling demonstrates that the viscosities for all samples follow a very similar temperature dependence. The inset in (b) shows the scaling factor A as a function of molecular weight. A clear change in behaviour around 1400 g/mol is observed as indicated by the pink and blue lines. 209
6.4 (a) Viscosity and (b) scaled viscosity as a function of molecular weights at varying temperatures. The viscosity in (b) are scaled to the viscosity at 303 K with scale factors B. The red line in (b) is the guide to eye. . 211

6.5 (a) T_2 as a function of temperatures for samples with varying molecular weights and (b) T_2 as a function of molecular weights at varying temperatures. The red lines in (a) are guides to eye and the lines in (b) are the fit using equation 6.6 in the range of $M_n \leq 1000$ g/mol (Rouse model region but excluding P90). Fitting parameters are shown in Table 6.2 212

6.6 Fundamental Rouse relaxation time τ_0 as a function of temperatures obtained from viscosity and NMR T_2 measurements. The lines are the Arrhenius fits, which give activation energies of 33 and 35 kJ/mol from T_2 and viscosity measurements, respectively. Fitting parameters are shown in Table 6.2. Errors are smaller than the size of symbols. . 213

6.7 (a) $1/T_1$ as a function of temperatures for samples with varying molecular weights. The red lines are guides to eye. (b) correlation timescales τ_c by solving equation 6.12. The black lines in (b) are the Arrhenius fits. Fitting parameters are shown in Table 6.2. Errors are smaller than the size of symbol. 215

6.8 Plot of τ_c from T_1 relaxations as a function of molecular weights at various temperatures, and extrapolation to the timescales τ_0 for the fundamental Rouse units from the Rouse modelling of T_2 relaxations. The lines are guides to eyes. 216

6.9 (a) A typical DSC C_p trace for the quenched P2000 shows a glass transition, a cold crystallization and a melting transition on the heating trace. The inset in (a) is the magnification of the dashed squares to show the step-like glass transition. (b) heat capacity C_p as a function of temperatures for samples with various molecular weights. The traces are shifted to the glass-side C_p of P90 by a constant A. 218

6.10 ((a) Glass transition temperatures T_g as a function of molecular weights M_n. The onset temperature during a glass transition process is used as T_g. (b) Plot of T_g as a function of the reciprocal of M_n. The blue lines are the fitted results using the Flory-Fox equation. The vertical dashed lines in (a) show the molecular weight dependence of T_g in three regions, of which transition molecular weights are M_R and M_e or M_c ($M_c \sim 2M_e$). 219

6.11 (a) Heat capacity C_p traces for P250 as a function of temperatures measured at varying heating rates from 5 to 30 K/min. The traces are shifted by a constant A to the glass-side C_p with the heating rate of 10 K/min. (b) Plots of the reciprocal of heating rates (equivalent to time) a function of T_g/T for samples with varying molecular weights. The onset temperature during a glass transition process with the heating rate of 10 K/min is used as T_g. 220

6.12 (a) dielectric loss permittivity ε'' curves for P250 at (a) 182 K and (b) 150 K. The dash-dotted, dashed and dotted lines in the figure are the contributions from conductivity σ, structural relaxation α and secondary relaxation β fitted using a power law, a HN equation and a Cole-Cole equation, respectively. 222

6.13 Dielectric loss permittivity ε'' curves for (a) P90 and (b) P250 at varying temperatures. The solid lines are the best fits to the data as discussed in Figure 6.12. 223

6.14 (a) Dielectric loss permittivity ε'' curves for samples with varying molecular weights at 188 K. (b) DSC C_p curves at 10 K/min for P250, P650 and P2000 show cold crystallization peaks around 15 to 20 K higher than T_g (indicated in the dashed frame). 224

6.15 Dielectric loss permittivity ε'' curves show β relaxation peaks for (a) P650, (b) P1000, (c)P1400 and (d) P2000 at varying temperatures. The solid lines are the best fits to the data as described in Figure 6.12b. . . 225

6.16 (a) The Arrhenius plots of timescales from various techniques as a function of temperatures: α and β relaxations from BDS, equivalent structural relaxation timescales from rate dependent DSC (RDSC), the relaxation timescales for fundamental Rouse units τ_0 calculated from viscosity and NMR T_2 measurements. The inset in (a) is the amplification of the timescales at high temperatures indicated in the dashed square. (b) and (c) are the highlights of β and α relaxations from BDS and RDSC measurements, respectively. Dashed and solid lines are the VFT and Arrhenius fits and fitting parameters are shown in Table 6.3. 226

6.17 α and β relaxations timescales as a function of temperatures from BDS for the P62, P76 and P90. The dashed and solid lines are the VFT and the Arrhenius fits to the data, and fitting parameters are shown in Table 6.4. 228
6.18 Boiling points for alkanes,[452] alcohols and diols as a function of the number of carbons n_C in linear alkyl units. The data for alcohols and diols are taken from an online chemical data base, ChemSpider.[453] 230
6.19 (a) Glass transition temperatures T_g for alkanes, alcohols and alkane diols as a function of molecular weights M. For diols, $M = 14n_C + 34$; for alcohols, $M = 14n_C + 18$; for alkanes, $M = 14n_C + 2$, where n_C is the number of carbons. Hydrogen peroxide (H_2O_2) corresponds to $n = 0$. n_C for diols are also shown on the top x-axis. (b) T_g values for alcohols and diols are scaled to the values for alkanes by a constant λ in the x-axis direction. The λ for alcohols and diols are 4 and 9, respectively. The dashed line is guide to eye. 231

A.1 Example of a set of N_c chains. On each chain k the stickers (black circles) are placed via Equation (A.1). 240
A.2 Cartoon of the system. N_s stickers are randomly placed along the backbone, separated by chains strands of molar masses M_i. M_1 and M_{N_s+1} are the molar masses of the two chain-ends. 242
A.3 Sticker i detaches (dashed circle), takes a local "hop", and reattaches to a new position: $\boldsymbol{R}_i^{\text{new}} = \bar{\boldsymbol{R}}_i + \Delta\boldsymbol{R}_i$, (circle). 244
A.4 Sticker "hop" projected on the x-axis. Upon detachment its new position (circle) is defined, on average, as $x^{\text{new}} = \bar{x}_i + \sigma_i$, which is, on average, $\sqrt{2}\sigma_i$ away from its current position (dashed circle). 248

List of Tables

3.1 Characteristics of (co-)polymers synthesised by RAFT 102

3.2 WLF and Arrhenius fitting parameters for the LVE shift factors, for PEHA0, only WLF fit in the whole temperature range was conducted; For UPyPEHA2, both WLF fit over the whole temperature range and the Arrhenius fit over the terminal range were conducted; For samples with $\phi_{\mathrm{UPy}} \geq 6$ mol%, Arrhenius fits over temperatures above 323 K were conducted. 121

3.3 VFT and Arrhenius fitting parameters for the BDS α, α^* and γ relaxations. 131

4.1 Parameters used in the stochastic and "classic" sticky Rouse models. . 153

5.1 Quantitative analysis of glass transitions for PPG and UPyPPG by DSC, BDS and rheological measurements. 173

5.2 The Arrhenius and VFT fitting parameters of α, α' and γ relaxation timescales from BDS, shift factors a_T and shear viscosity η from rheological measurements for PPG and UPyPPG. 182

6.1 VFT fitting parameters for the viscosities as a function of temperature (red lines in Figure 6.3). 210

6.2 The Arrhenius fit parameters for τ_c from T_1 analysis. 217

6.3 The VFT and Arrhenius fitting parameters for α and β relaxations with varying molecular weights. 227

6.4 The VFT and Arrhenius fit parameters for α and β relaxations for P62, P76 and P90. 229

Chapter 1

Introduction

The aim of this thesis is to investigate the relaxation dynamics of supramolecular polymers over a wide temperature range: from the glassy to the melt states. This chapter will introduce some basic concepts and examples of supramolecular interactions and supramolecular polymers. To understand the relaxation dynamics of supramolecular polymers, some fundamental aspects of polymer structures and dynamics and of glass transition related dynamics in general are necessary and these will also be introduced. Finally, the the supramolecular systems investigated in this thesis will be introduced briefly and an explanation of the importance of this work will be made.

1.1 Supramolecular chemistry

A supramolecule is a complex assembly of molecules held together by non-covalent bonds such as hydrogen bonding, host-guest interactions or coordinative bonding.[1] Supramolecules are abundant in nature. Perhaps the most well known example is the DNA double helix which is formed from two DNA single chains held together by multiple hydrogen bonds. A knowledge of the nature of supramolecular dynamics is key to understanding the function, processing and applications of supramolecular assemblies. In this section, non-covalent interactions which can be used to form supramolecular systems will be explained and some examples of supramolecular polymers based on these interactions will be introduced. This section mainly follows the books of Alberto Ciferri [2] and Jonathan Steed.[3]

1.1.1 Supramolecular interactions

Interactions between supramolecular building blocks play an important role in determining the structure and function of supramolecules. These interactions are mainly noncovalent bonds and include a wide range of attractive and repulsive forces, such as ion-ion interactions, ion-dipole interactions (metal-ligand coordination), hydrogen bonding and π-π stacking.[3] Understanding the interactions between the building blocks is key for structural design and functional control of the resulting supramolecular materials.

Ion-ion interactions

A typical example of ion-ion interactions is found in an ionic crystal such as sodium chloride (NaCl).[2, 3] The Na-ions sit in a face centered cubic (FCC) lattice and each Na^+ cation is surrounded by six Cl^- anions. The bond strength of an ionic bond is relatively strong, ranging from 100 to 350 kJ/mol, which is comparable to the strength of covalent bonds. It takes some imagination to think of NaCl as a supramolecular compound. However, this example highlights the fact that Na^+ cations can arrange six Cl^- anions around themselves through non-covalent bonds. An ionomer is another typical supramolecular material formed through ion-ion interactions. In ionomers, ionic groups are covalently bonded to a polymer backbone or side groups, and associations between ionic groups typically lead to nanometer-sized aggregates which act as physical cross-links for the supramolecular material.[4]

Ion-dipole interactions (metal-ligand coordination)

A charged ion, such as Na^+, can bond to a polar molecule such as water. This is an example of ion-dipole interactions. After dissolving sodium chloride in water, the crystal structure can be broken due to water molecules penetrating the lattice thereby destroying the ion-ion interactions and forming new interactions with the positively charged sodium ions, $Na(H_2O)_6{}^+$, see Figure 1.1a[2, 3]. These interactions are termed ion-dipole interactions, as shown in Figure 1.1. Another example is the coordination bond which forms between the vacant electron orbit and lone electron pairs. For example, Ru^{2+} ions having vacant electron orbits which can become non-covalently bonded to bi-pyridines (bpy) having lone electron pairs, see Figure 1.1b[5]. This is also termed

metal-ligand coordination. Ion-dipole interactions can be formed both in solution and in the solid state, i.e. $Na(H_2O)_6^+$ exists in water while $Ru(bpy)_3^{2+}$ can remain bound in a solid. Metal-ligand coordination has been widely used to construct supramolecular compounds[6] and this will be introduced in Section 1.1.2.

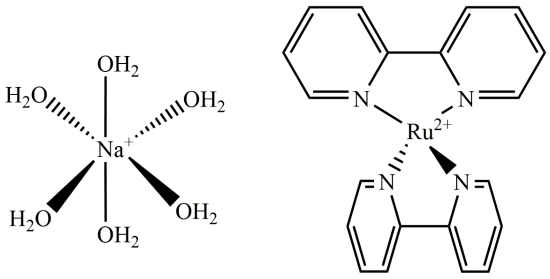

Figure 1.1: Schematic illustration of chemical structures of ion-dipole interactions: (a) $Na(H_2O)_6^+$ and (b) $Ru(bpy)_3^{2+}$. The solid and dashed triangles indicate spatial positions of the bonds.

Hydrogen bonds

Hydrogen bond interactions arise between hydrogen atoms that are attached to an electronegative atom (such as oxygen, nitrogen, or fluorine) and lone electron pairs in a neighbouring atom.[3] A simple example of a hydrogen bonding system is liquid water. The electronegative nature of oxygen atoms biases the electron cloud within an O−H bond to the oxygen atom and thus makes the hydrogen atom partly positively charged. The oxygen atom has two lone electron pairs with partial negative charge and the result is an electrostatic attraction between the opposite charges.[7] Figure 1.2a shows hydrogen bonds between water molecules, with the red spheres representing the oxygen atoms with a higher electron cloud density than the hydrogen atoms (black spheres). Hydrogen bonds can change properties of a material dramatically. Due to the hydrogen bonds between water molecules, water is liquid at room temperature while its counterpart, hydrogen sulfide (H_2S), is gaseous at room temperature. The strength of hydrogen bonds can vary from 4-120 kJ/mol, depending on the chemical structures.[3] Multiple hydrogen bonds can also be formed. For example, 1.2b shows the triple hydrogen bonds between guanine and cytosine which are basic building blocks for a DNA double helix.[8] Hydrogen bonds have been widely applied in

the formation of supramolecular polymers and this is well summarized in several review articles.[9, 10] Examples of the use of hydrogen bonds to build supramolecular materials will be shown in Sections 1.1.2.

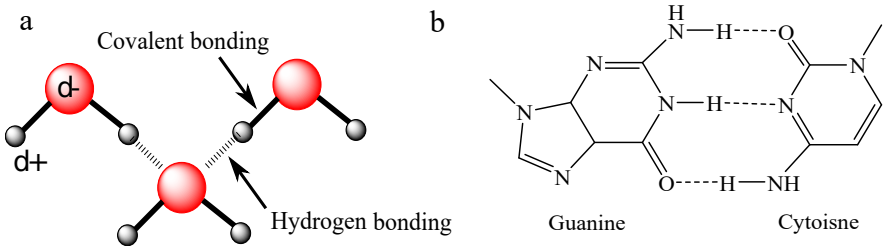

Figure 1.2: Schematic illustration of the hydrogen bond in (a) water and (b) triple hydrogen bonds between guanine and cytosine. The red and black balls in (a) represent the oxygen and hydrogen atoms, and oxygen atoms are partly negative charged whereas hydrogen atoms are partly positive charged.

Alcohols form one of the simplest molecular systems to be considered as a supramolecular material. Monohydroxy alcohols are alcohols which have only one hydroxyl group in their molecular structure. Examples include methanol, ethanol and propanol.[11] The hydroxyl groups (-OH) in these molecules can form intermolecular hydrogen bonds which have the ability to break and reform at ambient conditions. These reversible non-covalent bonds play an important role in determining the chemical and physical properties of monohydroxy alcohols. Although, many studies have been performed on these materials, their structures and dynamics are still not fully understood on a microscopic level.

One specific relaxation feature that is very clearly observed for monohydroxy alcohols is normally referred to as the Debye relaxation (see Chapter 2 for more details on the Debye relaxation).[11] This relaxation contribution has also recently been observed in some other more complex H-bonding systems including water[12, 13] and glycerol[14, 15]. The Debye relaxation was originally observed only in dielectric spectroscopy studies but it has recently been demonstrated that it can also be observed using rheology [16] and light scattering.[17] The origin of this relaxation contribution is still not well understood but several models have been proposed to explain the phenomenon. These include micellar aggregation,[18, 19] transient chain

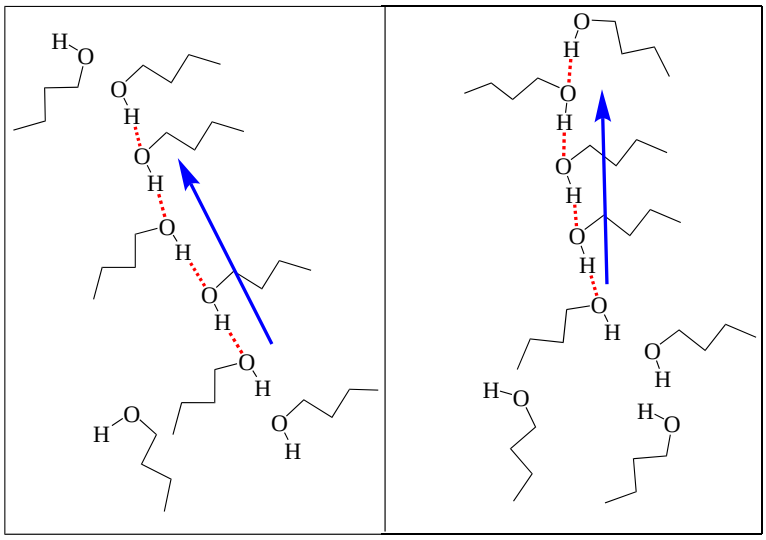

Figure 1.3: Schematic illustration of transient chain model: molecules can attach and/or detach from the "core" chain through hydrogen bonds. The blue arrows indicated the end-to-end vector of the transient chain, of which the orientation corresponds to the Debye relaxation.

mode,[16, 20] linear or branched clusters[21] and the breaking and re-forming of hydrogen bonds.[22] Recently, Gainaru and co-workers proposed a transient chain model to reveal the origin of the Debye dielectric response for n-butanol.[20] In their explanation, several butanol molecules are said to be held together temporarily by hydrogen bonding through the OH groups, forming the "core" of a chain, and other "free" molecules nearby can attach to either ends of the core or the molecules at the ends of the core can detach from the core. Since dipole reorientation is measured by dielectric spectroscopy, the composite dipole moment resulting from clustering of hydroxyl groups can be directly observed and this is believed to be linked to the the strong dielectric Debye relaxation. This underlying molecular mechanism is shown in Figure 1.3. It has also recently been shown that a polymer-type rheological response exists for monohydroxy alcohols. The strength and life time of hydrogen bonds and the speed of breaking and reforming of these bonds are all temperature dependent. At high temperatures the time required to break and reform hydrogen bonds becomes shorter. As temperature decreases, this time will become longer. At certain temperatures (a few Kelvin above T_g), the life time of the hydrogen bonds would be long enough that the

small molecules would show the rheological response of a short-chain-polymer.[16] More details on the Debye relaxation can be found in Chapter 2.

π-π stacking

The relatively weak interaction between aromatic rings is usually referred to as π-π stacking , as shown in Figure 1.4. The strength of this interaction is in the range of 5 - 50 kJ/mol. The π-π stacking interaction results in the slippery feel of graphite which can be used as a lubricant agent.[2] Graphite is composed of multiple carbon layers where each carbon is covalently bonded to three other carbons, whereas interactions between these carbon layers are due to π-π stacking.[23] The π-π interactions between stacked layers are typically not strong enough to build supramolecular materials but they can work cooperatively with other non-covalent interactions, such as hydrogen bonding, to build supramolecular materials.[24]

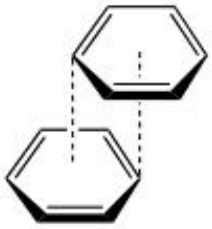

Figure 1.4: π-π stacking between benzene rings.

1.1.2 Supramolecular polymers

Unlike conventional polymers, in which monomers are linked together by covalent bonds, the interactions involved in the building of supramolecular polymers are typically secondary interactions which are reversible. Supramolecular polymers can be both natural and synthetic and are based on the various interactions described in previous sections.[25] They can also exist in a variety of different states including the liquid, solid, gel and glassy states. Unlike conventional polymers with covalently bonded main chains, the non-covalent interactions linking the building blocks of supramolecular polymers are reversible and relatively weak. This gives supramolecular polymers specific functionality which can be utilised in a wide range of important appli-

cations. Moreover, there are many supramolecular structures that can arise due to self−assembly including linear, branched, helical, micellar and mono-layered structures and three−dimensional networks. These structures are not only controllable at nanometer scales but also can be designed with advanced functionalities based on their hierarchical self−assemblies. It is therefore important to understand the structures, properties and relaxation dynamics of supramolecular systems. Supramolecular systems have potential applications in the biomedical field [26] and important applications can be found in drug delivery, gene transfection, bioimaging and diagnosis. Supramolecular polymers are more sensitive to surrounding stimuli, such as temperature, light and pH, than conventional polymers.[27] In the following, I will provide some examples of supramolecular polymers assembled from different structures, such as monohydroxy alcohols, end functionalised polymers and polymers with functionalised side groups.

Linear supramolecular polymers

Building blocks with functional groups at the chain ends can grow into much longer chains through end-to-end interactions.[28, 29] Figure 1.5a schematically illustrates supramolecular polymers formed through end-to-end interactions. These interactions can be hydrogen bonds, metal-ligand coordinations or the combination of both.[30] Figure 1.5b shows an example of a linear supramolecular polymer based on 2-ureido-4[1H]-pyrimidinone (UPy) and functionalised polytetrahydrofuran (PTHF).[31] PTHF is a linear polymer with tetramethylene repeat units linked together by ether bonds. PTHF has been used as a building block for thermoplastic elastomers, which have many advantages such as low temperature flexibility, high abrasion resistance, and excellent resiliency over a wide range of temperatures. Various products made from PTHF have been used in the fields of coatings, adhesives, sealants and the automotive industry.[32] Depending on the molecular weight, commercial PTHF based materials which are capped by hydroxyl groups can be liquid, wax or solid at room temperature. If the hydroxyl groups are exchanged with UPy groups at both ends then multiple end-to-end hydrogen bonds can form, leading to chain extension. Meijer has developed several linear supramolecular polymers using various backbones based on this strategy.[33] Chain extension can increase the tensile strength and tensile modulus

dramatically. Since the hydrogen bonds between UPy groups are temperature sensitive, supramolecular polymers are temperature sensitive as well. The supramolecular structures can be stable up to 80 ^{o}C.[31] Above this temperature, the association of the hydrogen bonds will be broken, and the viscosity decreases sharply which is ideal for industrial processing.[31]

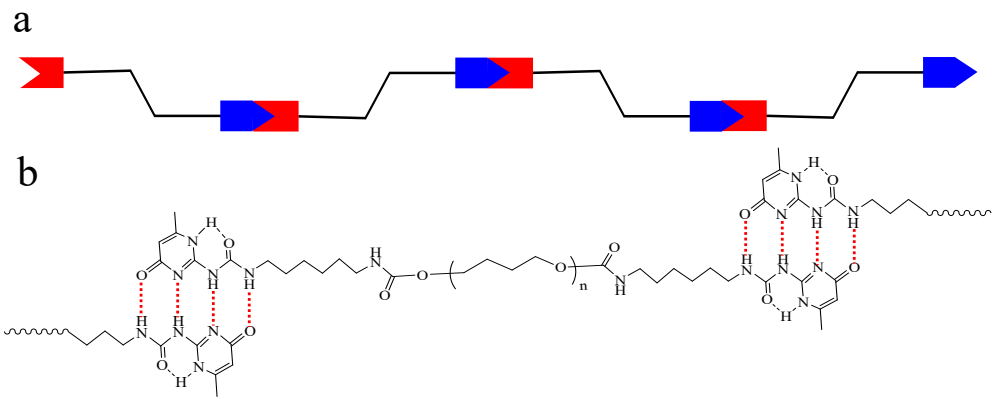

Figure 1.5: (a) Schematic illustration of supramolecular polymers assembled from end-to-end interactions,[29] (b) an example of linear supramolecular polymers based on 2-ureido-4[1H]-pyrimidinone, (UPy) functionalised polytetrahydrofuran. The red dashed lines are hydrogen bonds.[31]

End-groups also affect microscopic dynamics.[31] A study on short-chain oligopropylene glycols showed that by changing the end hydroxyl groups to methoxy groups at one or both ends, the secondary β relaxation is accelerated by one decade in timescale if the chains are short and thus the dynamics is strongly affected by the end-groups[34] For polymer systems, where chain-end interactions are not important, the β relaxation speeds up when the chains become short enough. However, it has been demonstrated that for H-bond coordinating systems such as propylene glycols, this effects is removed due to the fact that even the shortest chains form effective H-bond mediated structures that are large enough to remove any speed-up due to a shortening of the chains. Instead, for the glycols, an increasing β relaxation time is observed as the H-bonding effects become more pronounced for the shortest chains. The detailed origin of this effects is not presently clear. Also, whether it is unique to PPG or if it is a common phenomenon for all polyethers, such as polyethylene glycol (PEG) or PTHF, is unknown.

The formation of linear hydrogen bonded supramolecular polymers can be considered as a step growth process and the degree of polymerisation (DP) can be defined by the Carother equation.[35]

$$\mathrm{DP} = \frac{1}{1-p} = \frac{1}{1-(1-\chi)} = \frac{1}{\chi} \tag{1.1}$$

where p is the conversion percentage of hydrogen bonding groups, and χ is the mole fraction of unassociated hydrogen bonding groups.

$$\chi = \frac{(8K_{\mathrm{dim}}C_t + 1)^{1/2} - 1}{4K_{\mathrm{dim}}C_t} \tag{1.2}$$

where K_{dim} is the dimerisation constant, and C_t is total molar concentration of hydrogen bonding groups. For UPy groups in chloroform, $K_{\mathrm{dim}} \approx 10^7$ $(\mathrm{mol/L})^{-1}$.[36, 37] Thus, the DP can be expressed through a combination of the preceding two equations:

$$\mathrm{DP} = \frac{4K_{\mathrm{dim}}C_t}{(8K_{\mathrm{dim}}C_t + 1)^{1/2} - 1} \tag{1.3}$$

Here it is assumed that the association constant for each step is equal and the association constant for corresponding subunits is known and is the same to that of bare hydrogen bonding groups.

Side-chain supramolecular polymers

Instead of putting functional groups at the chain-ends, functional groups can also be placed onto the polymer side chains along the backbone.[9, 41] Figure 1.6 shows three strategies to build side chain supramolecular polymers.[9, 41] Kato reported the preparation of side-chain liquid crystalline supramolecular polymers by mixing polyacrylate bearing pendant and hexyloxybenzoic acidic side groups with liquid crystalline components.[38] The resulting materials formed a nematic phase covering a wide temperature range which exceeded that of the individual mesomorphic components. Moreover, when di-functional liquid crystalline components were used, supramolecular networks could be formed, as shown in the Figure 1.6(b).[39] The field of supramolecular liquid crystalline polymers has advanced significantly over the last few years and various backbones and small molecules have been developed. The last strategy involved polymers bearing self-complementary side groups.[40, 42, 43] Interactions between

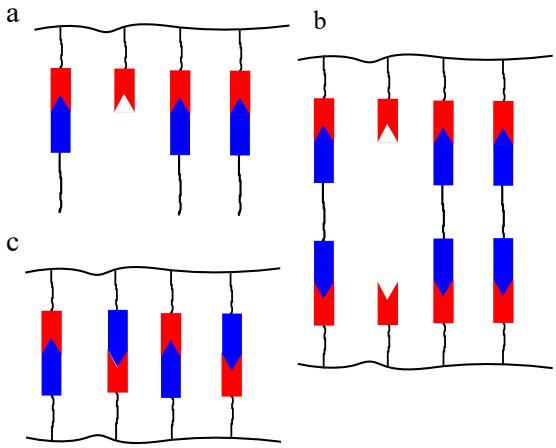

Figure 1.6: Schematic illustration of side chain supramolecular polymers: (a) two components system forms comb-like structure, (b) two components forms network structures and (c) one component system with self-complementary groups forms network structures.[38–40]

these self-complementary groups can behave as physical cross linkings and can lead to the formation of supramolecular networks, which in turn can dramatically change the mechanical properties. One example of this was presented by Meijer and Kramer,[42] who synthesised poly(butyl acrylate) with UPy side groups (Figure 1.7). Although the molecular weight of the linear polymer was below the entanglement molecular weight, the material behaved as a thermoplastic elastomer through the association of UPy groups. The bulk properties of these materials, such as glass transition temperature, moduli and relaxation timescales increased with increasing number of UPy groups per chain.[42]

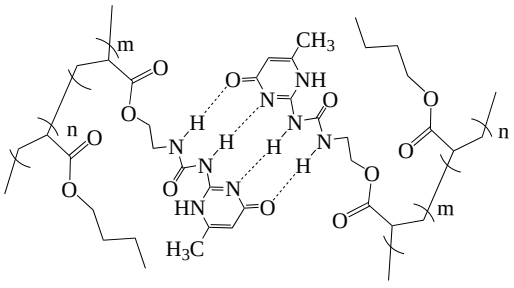

Figure 1.7: Supramolecular polymer networks from poly(butyl acrylate) bearing self-complementary UPy groups.[42]

Dendritic supramolecular polymers

Dendrimers have been widely recognized as a new class of macromolecular architecture with unique properties and applications.[44, 45] The dendritic architecture can be considered as a intermediary state, placed within the range from linear to cross-linked architectures and representing a higher level of molecular complexity.[46] Synthesis of dendrimers can be dated back to the 1980s and two main synthesis strategies have been developed since then.[2] The first one is the so-called divergent method. In this method, the growth of a dendrimer starts from a core site, which can be viewed as the root of a "molecular tree", according to certain dendritic rules and reaction principles. The second method is the so-called convergent method.[46] In this method, the dendrimer growth occurs in the opposite direction to the divergent method, i.e. from the surface of a dendrimer to its molecular root.[46] In order to form a multi-dendron architecture, an additional reaction is usually required in which several dendrons are covalently coupled. Based on the two methods, more than 100 dendrimer families have been synthesised for which both size and shape, from spheres and ellipsoids to rods, can be controlled. More details about the synthesis, structures, properties and applications of dendrimers have been reviewed elsewhere. [2, 46]

Supramolecular interactions have been used to construct dendrimers.[47] Unlike their covalent counterparts, supramolecular dendrimers show close similarity to biological systems which usually have an ability to assemble large structures from small building blocks. Self-assembly processes in biological systems are usually fast and reproducible.[47] These advantages have driven researchers to develop complex structures to mimic the biological systems. Figure 1.8a shows a strategy to construct dendrimers based on the focal point functionalised dendrons.[47] In this method, a dendron with supramolecular groups at the focal point is synthesised and aggregation through the interactions between the functional groups leads to formation of a dendritic supramolecular polymers. The most frequency used functional groups at the focal points are hydrogen bonding groups, metal-ligand coordination groups and crown ethers. Figure 1.8b shows a 3-generation supramolecular dendritic polymers through interactions between the Ln^{3+} cation and carboxylic acid groups.[48] Properties of the resulting dendrimers are highly tunable. For example, changing the groups attached to

the outer layer can make the dendrimers show varying properties, such as biocompatibility, hydrophily or hydrophobicity, which has found applications in medical field, drug and DNA delivery and controlled releasing.[49]

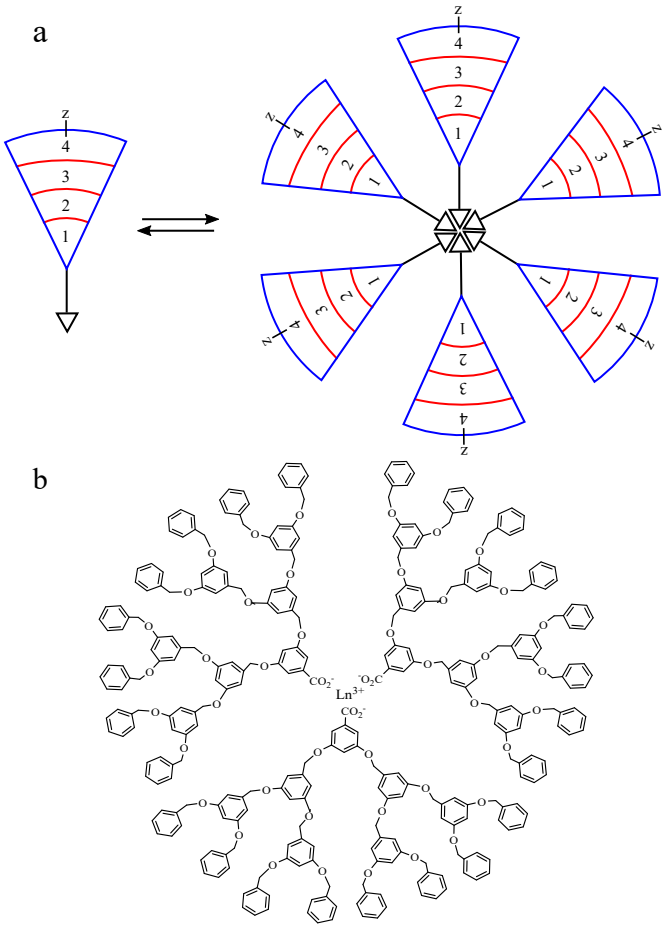

Figure 1.8: (a) Schematic illustration of construction of dendrimers based on supramolecular interactions.[47] The numbers indicate the generation of the building blocks. (b) an example of self-assembly of root functionalised dendrons around a metal cation.[48]

1.2 Polymers and polymer dynamics

A polymer is a large molecule i.e. a macromolecule, composed of many repeat units which are called monomers. Both synthetic polymers such as polystyrene and polyester,

and natural polymers such as celluloses and DNA are playing an essential and ubiquitous role in our daily life.[50] In this section, the basics of polymers and polymer dynamics will be introduced briefly, mainly following the polymer chemistry book by Ravve[51] and the polymer physics book by Rubinstein and Colby.[52]

1.2.1 Basics of polymers

A synthetic polymer can be made through polymerisation reactions which is a process of linking many monomers into a long chain or network by covalent bonds.[50, 51] The number of monomers in a macromolecule is termed the degree of polymerisation N. Thus, the molecular weight of the macromolecule is related to N and the molecular weight of the monomer M_{mono}:[51]

$$M_{\text{polym}} = NM_{\text{mono}} \tag{1.4}$$

The molecular weight is a key characteristic for polymers because it is related directly to the properties and applications of a polymeric material. In an ideal case, all polymers from a single polymerisation process contain the same number of monomers, i.e., the polymer sample is monodisperse. However, in reality, for all synthetic polymers, the molecular weight is not characterised by a single value. Polymers are instead typically polydisperse, which means that the chain-length or degree of polymerisation are distributed across a range of values.[51] Several methods have been developed to synthesise polymers in the last 6 decades, such as free radical polymerisation, step polymerisation, and cationic or anionic polymerisation.[51] The free radical polymerisation method usually gives a relatively broad molecular weight distribution.[50] Whereas cationic and anionic polymerisation need to be can give a very narrow molecular weight distribution.[53, 54]

To characterize the molecular weight distribution, several average molecular weights are defined.[52] The number average molecular weight M_n is defined as the ratio of the total weight of all polymer chains to the total number of all polymer chains:

$$M_n = \frac{\sum N_i M_i}{\sum N_i} = \sum n_i M_i \tag{1.5}$$

where N_i is the number of polymer chains with molecular weight of M_i. n_i is the number fraction of polymer chains with the molecular weight of M_i.

$$n_i = \frac{N_i}{\sum N_i} \tag{1.6}$$

M_n can be estimated using end-group analysis by NMR. The weight average molecular weight M_w is defined based on the fact that longer polymer chains contain more of the total mass of a sample than shorter chains do.

$$M_w = \frac{\sum N_i M_i^2}{\sum N_i M_i} = \sum w_i M_i \tag{1.7}$$

where w_i is the average fraction of polymer chains with molecular weight of M_i. Similarly, the z-average molecular weight M_z is defined as:

$$M_z = \frac{\sum N_i M_i^3}{\sum N_i M_i^2} \tag{1.8}$$

In general, the $(z + k)$-average molecular weight M_{z+k} can be defined as:

$$M_{z+k} = \frac{\sum N_i M_i^{k+3}}{\sum N_i M_i^{k+2}} \tag{1.9}$$

Higher order average molecular weights are more sensitive to high molecular weight components in a sample and are usually difficult to measure using experimental methods. A polydispersity index (PDI) is defined to characterize the broadness of the molecular weight distribution of a polymer:

$$\text{PDI} = \frac{M_w}{M_n} \tag{1.10}$$

The larger the polydispersity index is, the broader the molecular weight distribution is. For monodisperse polymers, the PDI in theory equals 1. For those best controlled polymerisation method such as anionic polymerisation, the PDI is usually between 1.02 and 1.2.[53] Step polymerisation usually gives a PDI around 2.[50, 51] Free radical polymerisation gives more broad PDI ranging from to 1.5 to 20.[50, 51]

1.2.2 Structures and components of polymers

A linear polymer is the simplest type of polymer and properties of linear polymers are mainly determined by the degree of polymerisation. Molecules containing a small number of monomers (typical less than 20) are usually called oligomers.[51] As the number of monomers in a polymer chain becomes larger, physical properties such as the viscosity change sharply. With the developments in synthesis techniques over the last 3 decades, a wide range of complex polymer structures have been synthesised, as shown in Figure 1.9. Polymer structures including linear, ring, comb-like, star, ladder-like, dendritic or branched, cross-linked and multiblock have been synthesised.[55, 56]

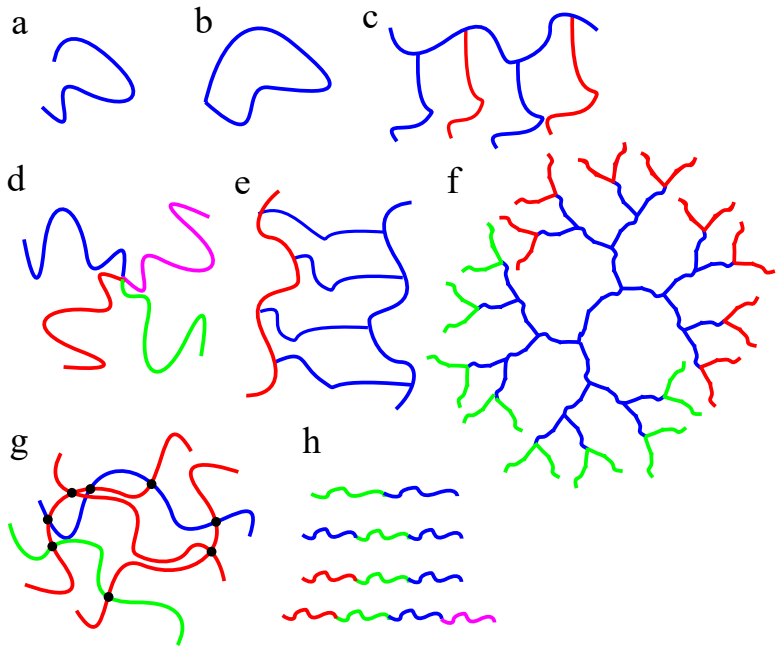

Figure 1.9: Schematic illustration of structures and components of polymers: (a) linear, (b) ring, (c) comb-like, (d) star, (e) ladder-like, (f) dendritic or branched, (g) cross-linked and (h) multi-block. The color lines indicated polymer chains with different monomers.

A polymer containing only one type of monomer is called a homo-polymer, whereas, several different types of monomers can be linked together in a single polymer chain, leading to a so-called hetero-polymer.[50, 51] The properties of hetero-polymers depend on both the structure and the fraction of each type of monomer in the polymer.

Hetero-polymers can form all the above mentioned complex structures, as shown in Figure 1.9. A polymer containing two types of monomers is called a copolymer. The arrangement of monomers along the backbone in a copolymer can include alternating or random arrangements, and grafts or blocks. In an alternating copolymer, two monomers, here termed A and B, are arranged in a alternating manner ···-A-B-A-B-A-B-A-B-···.[57] In a random polymer, two monomers are randomly distributed along the backbone ···-A-A-B-A-B-B-B-A-A-B-···.[51] Block copolymers consist of two different polymer chains covalently linked together ···-A-A-A-A-A-B-B-B-B-B-···.[58] Furthermore, linear backbones containing more than two different blocks can be synthesised which are called multiblock polymers,[59] as shown in Figure 1.9h. In recent work, a multiblock copolymer with more than 10 blocks organised in a controlled sequence was synthesized using a combination of living radical polymerisation and click chemistry.[60] These complex structures and components of polymers make it possible to tune the properties of a polymer to meet varying application requirements. For example, attaching short protein oligomers into the outer layer of a dendrimer can improve the biocompatibility and make it possible to go through the cytomembrane without causing an immunoreaction in a living cell, thus delivery of drugs into special cells such as cancer cells could be possible using this technique.[61] Moreover, block copolymers can form microphase separated structures such as spheres, cylinders, laminar or bicontinuous phases depending on the fraction and nature of the monomers used. These nanostrucutres can be used for nanofabrication and nanofilteration.[62] In summary, complex structures and multiple components of polymers broaden the applications in many fields and several reviews on these topics are available elsewhere.[63, 64]

1.2.3 Synthesis of polymers

Based on the reaction mechanism, the methods used to synthesise polymers can be classified into different classes: step growth polymerisation, free radical polymerisation, anionic polymerisation and cationic polymerisation. More details about other methods can be found in any textbook on polymer chemistry, such as *Principle of polymer chemistry* by Flory and Rawe.[50, 51] In this section, only the polymerisation method related to free radical polymerisation which is used in this work will be introduced briefly.

Reversible addition fragmentation chain transfer (RAFT) polymerisation

Free radical polymerisation is one of the most widely used methods to synthesise polymers from monomers due to its simple reaction requirements and wide monomer tolerance. Many kinds of monomers bearing various functional groups can be polymerized using free radical polymerisation.[50, 65] However, using a conventional free radical polymerisation method, it is difficult to control the molecular weight and molecular weight distribution.[50, 65] RAFT is a novel free radical polymerisation method first developed by researchers from the Commonwealth Scientific and Industrial Research Organisation (CSIRO), Australia.[66–69] RAFT polymerisation distinguishes itself from other controllable radical polymerisation methods, such as atom transfer radical polymerisation (ATRP)[56] and single-electron transfer living radical polymerisation (SET-LRP)[70] by its close relationship to conventional free-radical polymerisation. The latter two polymerisation methods are not discussed in this chapter but several review articles provide more details.[56, 71] RAFT polymerisation is essentially a free-radical polymerisation with addition of a highly active chain transfer agent (CTA). The CTA is readily fragmented during the chain transfer process to generate a new radical species through an addition fragmentation mechanism.[67] In RAFT polymerisation, the molecular weight can be tuned and the molecular weight distribution can be controlled; typically PDI<1.4.[68] Moreover, RAFT is tolerant to functional groups in both chain tranfer agents (discussed later) and monomers. Thus, polymers obtained from the RAFT technique can have various functional groups. Thus the reactivity of the polymers obtained from the RAFT technique is strengthened due to functional groups either in polymer ends or in side groups, which make it possible to synthesise complex polymeric structures through post functionalisation such as click chemistry.[72] Many complex polymer architectures have been synthesised by RAFT and post functionalisation, such as multiple block copolymers ($\geq$ 2 different polymeric blocks), multiple arms or star polymers, bottle-brush polymers, ring polymers or multiple generation dendritic polymers.[66, 69] For in-depth discussions about the RAFT technique, there are a range of good published review articles available.[66–69] In the following sections, the basics of the RAFT technique and some details for the synthesis work carried out in the thesis work are presented.

A typical RAFT synthesis system contains three basic components: monomers, initiators and chain transfer agents (CTA).[67] Due to the similarity to the conventional radical polymerisation procedure, RAFT can be conducted in bulk, solution, emulsion or dispersion conditions; thus solvent and or aqueous/organic emulsor agents can be added.

Monomers

RAFT polymerisation can be applied to many kinds of monomers and their derivatives, such as styrene derivatives, acrylamides, acrylates, acrylonitrile, vinyl acetates, vinyl formamide, vinyl chlorides as well as vinyl monomers.[67] The chemical structures of these monomers are shown in Figure 1.10. Moreover, RAFT polymerisation is tolerant to monomers with various functional groups,[68] which is a great advantage of this technique over traditional living polymerisation methods, such as anionic polymerisation. This advantage offers polymers with post-functionality and makes it possible to tune properties of polymers further and to broaden applications. During the polymerisation process, the carbon-carbon double bonds are activated by initiators and form free radicals.[65] The detailed mechanism will be discussed in section 1.2.3.[67]

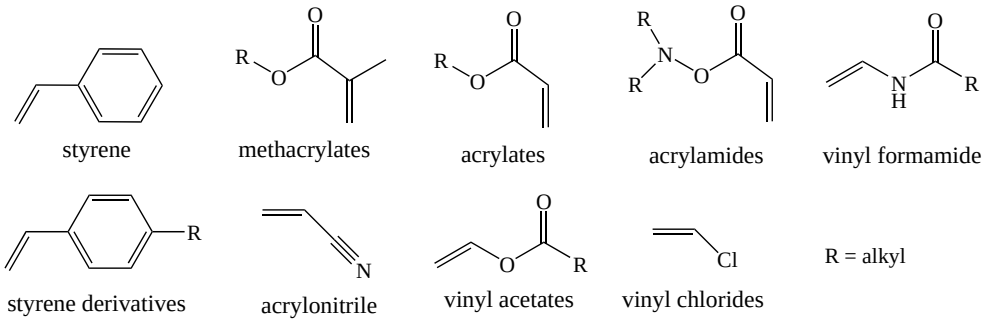

Figure 1.10: Chemical structures of monomers can be polymerized using RAFT polymerisation.

Initiators

The quantity of initiators used in a RAFT polymerisation is normally very small, but initiators are essential to start the polymerisation.[65] Initiators can produce free radicals that are activated either by a high temperature or by light.[65] A radical is an atom,

molecule, or ion that has an unpaired valence electron. Thus, most radicals are highly reactive to other compounds or itself. There are three general classes of initiators, i.e. azo compounds, organic peroxides and inorganic peroxides. Some examples as shown in Figure 1.11a. There are two important factors to consider when choosing initiators: (i) their half-life time ($t_{1/2}$, the time that half the amount of initators is consumed) at a certain temperature, which determines the speed of the initiation stage and (ii) the polymerisation temperature.[65] Figure 1.11d shows the decomposition reaction used to produce the free radicals upon heating.[65] Free radicals from initiators can activate monomers and form monomer radicals which act as reactive center for chain growth. AIBN is one of the most widely used initiators in radical polymerisations due to the fact that it has good solubility in monomer-based solutions and a $t_{1/2}$ of about 1 hour at 90 °C; consequently, it can continuously supply sufficient radicals at a moderate temperature. Moreover, the decomposition rate of AIBN is almost solvent independent and the initiator can thus be used in different types of solutions. Another initiator, 1,1'-azobis-(cyclohexanecarbonitrile) (ABCN), is also used because it has a $t_{1/2}$ of about 2 hours at 110 °C, which is important when a relatively high temperature is required for the dissolution of some monomers with poor solubility.

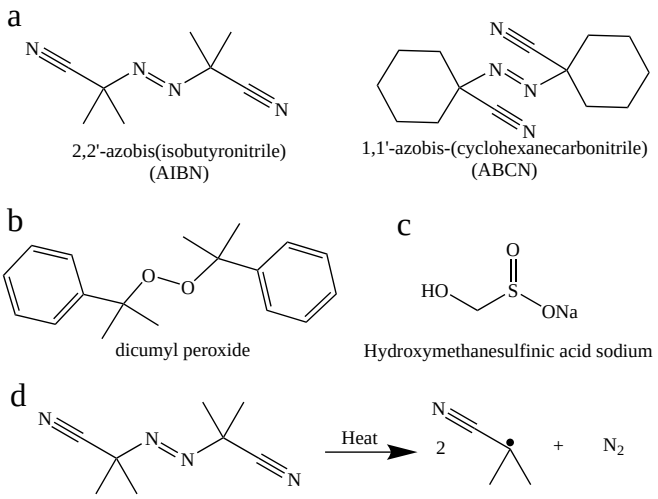

Figure 1.11: Chemical structures of different types of initiators: (a) azo compounds, (b) organic peroxides and (c) inorganic peroxides for free radical polymerisation. (d) decomposition reaction of AIBN that produces initiator free radicals.

Chain transfer agents

CTA is of key importance for a RAFT polymerisation. CTA is readily fragmented during the chain-transfer process to generate a new radical species through an addition fragmentation mechanism.[73] It provides control of the molecular weight distribution through forming a reaction equilibrium between the propagation center and the CTA (see section 1.2.3).[73] Hundreds of differnt CTAs have been synthesised and tested for RAFT polymerisation and most of them are found within four classes: dithioester, trithiocarbonate, xanthate and dithiocarbamate.[74], see Figure 1.12a. Figure 1.12b shows the chemical structure of dithioester CTA, and the reaction equilibrium with one free radical. The effectiveness of a CTA depends on the monomer structures and the properties of leaving groups -R and -Z which can activate and deactivate the carbon-sulphur (-C=S-) double bonds.[73] A guideline for selection of proper CTAs suitable for different monomers can be found in the references[67, 73].

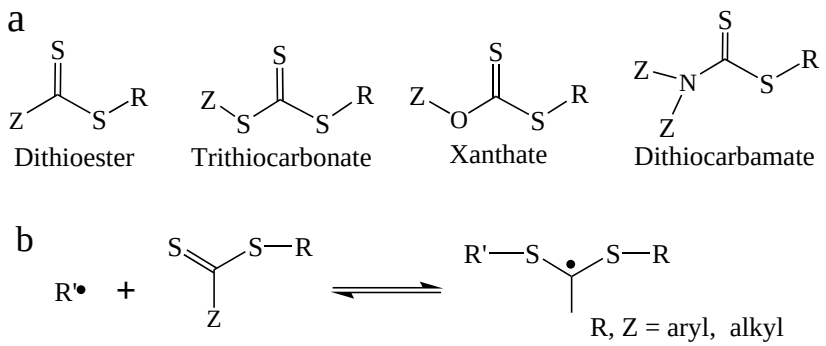

Figure 1.12: (a) General structures of common RAFT agents (b) chemical structure of a dithioester CTA and its reaction with a free radical.

Solvents

In RAFT, the solvents are not strictly required if a monomer is liquid and the polymer is soluble in the monomer.[73] However, under some circumstances, for example when the monomer is solid and the polymer cannot be dissolved in its monomers, then a solvent is essential to conduct the polymerisation. One of the advantages of RAFT is its tolerance to functional groups, which means that a wide variety of solvents can be used. Examples include alcohols, ethers (THF, anisole and dioxane), toluene, DMF,

MDSO and water. In this work, DMF was used to dissolve the functionalised solid monomer.

The RAFT mechanism

The generally accepted mechanism behind the synthesis of homo-polymers via the RAFT process is described in Figure 1.13. The mechanism involves five main steps: (a) initiation, (b) pre-equilibration, (c) re-initiation, (d) chain equilibration, and (e) termination.[67, 73]

(a) Initiation: Generation of radicals from the homolysis of initiators and reactions with monomers to form chain radicals.

(b) Pre-equilibration: Chain radicals can propagate further until they are captured by addition to the reactive -C=S- bond of the CTA and form intermediate radicals which can form fragments reversibly to produce CTA-capped polymeric species (macro-CTA) and a re-initiating a radical R·. [this sentence is not totally clear. Look it over and try to make it clearer.]

(c) Re-initiation: The released R· radical can react with monomers again to start a new propagation process. After the initial CTA are completely consumed, the polymerisation system is controlled by the presence of one macro-CTA.

(d) Chain equilibration: This step involves the rapid exchange of dithioester groups between the macro-CTA and the active propagating radicals. Each generated macro-radical has an equal probability of undergoing chain growth, promoting homogenous chain growth, leading to a low molecular weight distribution.

(e) Termination: The polymerisation is terminated via bi-radical termination and/or disproportionation.

RAFT has many advantages, including: (i) the controllable molecular weight and low molecular weight distribution, (ii) a high tolerance to functional groups, (iii) the wide range of polymerisable monomers in varying solvents and temperatures, (iv) no need of metal catalysts which is not good for medical applications and (v) many commercially available CTAs[66, 68, 69] Moreover, funtional end or side groups make it

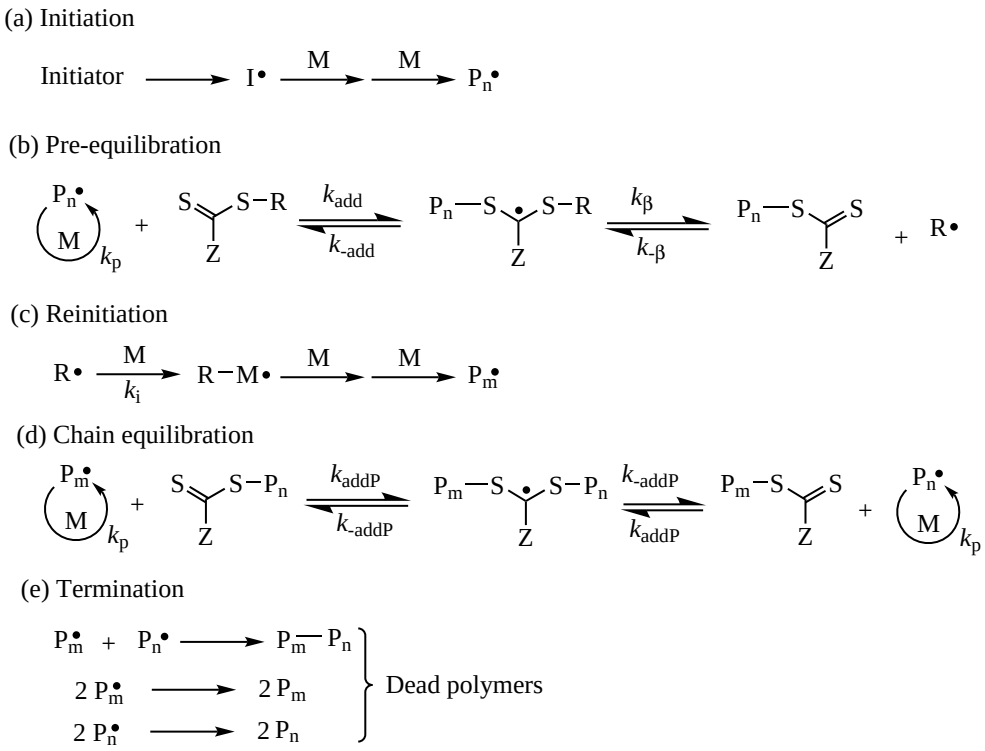

Figure 1.13: General mechanism of a RAFT polymerisation.

possible to synthesise complex polymeric architectures.[68] However, it does also have some drawbacks.[67] Examples of drawbacks include the fact that (i) a particular CTA is only suitable for a limited set of monomers; (ii) the multi-step synthetic process is usually required to synthesise a CTA for polymerisation of a particular monomer; (iii) the CTA is usually unstable over long time periods; (iv) the gradual decomposition of thiocarbonylthio moiety can release a pungent odour; (v) the presence of a CTA moiety in polymers, especially for low molecular weight polymers, makes polymers coloured, and further chemical reactions are required to remove the colour; (vi) the free radical concentration in RAFT needs to be kept low to avoid terminations, hence the reaction rate for RAFT is actually lower than for conventional free radical polymerisation.

1.2.4 Single chain conformations

Understanding the chain conformations of polymers is important for understanding the structure-property relationships of polymeric materials. In this section we will

discuss so called ideal chains, which are characterised by the assumption that there are no interactions between monomers if they are separated far apart from each other along the polymer chain.[52] In reality, this is an approximation, but for polymer melts where excluded volume interactions are screened or in polymer solutions at a temperature where the attractive and repulsive interactions are balanced, the ideal chain approximation gives a good picture of the real system[52]. Attractive and repulsive interactions are typically temperature dependent.[52] At high temperatures, repulsive forces typically dominate and chains swell in solution, whereas at low temperatures, the attractive forces dominate and chains are in a collapsed state. At a certain temperature, attractive and repulsive forces cancel each other and the chains are nearly in an ideal conformation. This temperature is called the θ-temperature.[52] The ideal chain approximation is an essential starting point for many of the key models in polymer physics.

To illustrate the conformations for a polymer chain, let us start with the simplest polymer, polyethylene -$(CH_2)_n$-. The distance between two neighbouring carbon atoms is almost a constant and equals the -C-C- bond length, $l = 0.154$ nm. And the angle between two neighbouring bonds is also almost a constant, $\theta = 68°$.[75] For four consecutive CH_2 groups, there are two ways to arrange them and these two arrangements are termed *cis* or *trans* isomers.[76] It has been shown that the *trans* state is the lowest energy state. If all CH_2 groups are arranged in the *trans* state, the polymer would be in a rod-like zig-zag conformation, and the chain has the largest end-to-end distance $R_{\max}$ which is determined by the number n and the length l of -C-C- bond and the angle θ between two neighbouring bonds.

$$R_{\max} = nl\cos(\theta/2) \tag{1.11}$$

For flexible polymer with $n + 1$ atoms along the backbone, the bond vector $\vec{r_i}$ goes from atom A_{i-1} to atom A_i, as shown in Figure 1.14. The end-to-end vector is the summation of all n bond vectors along the backbone:

$$\vec{R_n} = \sum_{i+1}^{n} \vec{r_i} \tag{1.12}$$

Different chains have different conformations resulting in different bond vectors and different end-to-end vectors. However, the average end-to-end vector for an isotropic

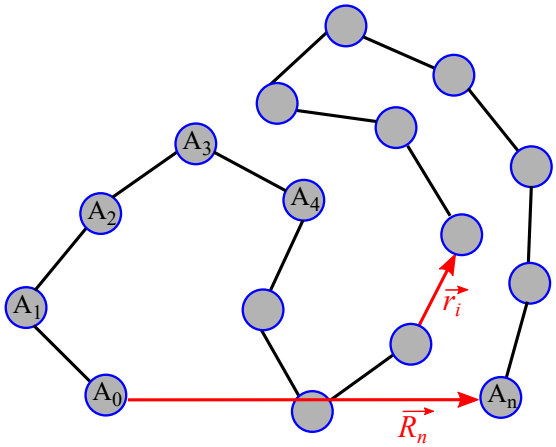

Figure 1.14: Schematic illustration of one possible conformation for a flexible polymer with $n + 1$ atoms.

polymer chain collection should be zero:[52]

$$\langle \vec{R}_n \rangle = 0 \tag{1.13}$$

For a set of chains which show no preferred orientation, the ensemble average of the end-to-end vector should be zero. The simplest non-zero average is the mean-square end-to-end distance $\langle R^2 \rangle$ which is defined as:

$$\langle R^2 \rangle = \langle \vec{R}_n^2 \rangle = \langle \vec{R}_i \cdot \vec{R}_j \rangle = \left\langle \left(\sum_{i+1}^{n} \vec{r}_i \right) \cdot \left(\sum_{i+1}^{n} \vec{r}_j \right) \right\rangle = \sum_{i=1}^{n} \sum_{j=1}^{n} \left\langle \vec{r}_i \cdot \vec{r}_j \right\rangle \tag{1.14}$$

For the backbones only containing one bond length $l = |\vec{r}_i|$, the scalar product can be expressed in terms of the angle θ between $\vec{r}_i$ and $\vec{r}_j$:

$$\vec{r}_i \cdot \vec{r}_j = l^2 \cos\theta_{ij} \tag{1.15}$$

Thus the mean-square end-to-end distance can be expressed as:

$$\langle R^2 \rangle = l^2 \sum_{i=1}^{n} \sum_{j=1}^{n} \left\langle \cos\theta_{ij} \right\rangle \tag{1.16}$$

The freely jointed chain model is one of the simplest models for ideal polymer chains.[52] In the freely jointed chain model, the bond length is a constant $l = |\vec{r}_i|$, and there are no correlations between $\vec{r}_i$ and $\vec{r}_j$, thus $\langle cos\theta_{ij} \rangle = 0$ for $i \neq j$, under the condition

that atoms A_i and A_j are far separated from each other ($|i - j| \gg 1$). There are only n non-zero terms in equation 1.16 when $i = j$, $\langle \cos\theta_{ij} \rangle = 1$. Thus the mean-square end-to-end distance can be expressed as:

$$\langle R^2 \rangle = nl^2 \tag{1.17}$$

For any ideal chain, there is no correlation between bond vectors of two monomers which are separated far enough from each other, thus for an arbitrary bond vector $\vec{r_i}$, the summation over all other bond vectors $\vec{r_{ij}}$ converges to a finite number which can be defined as:

$$C_i^{'} = \sum_{j=1}^{n} \langle cos\theta_{ij} \rangle \tag{1.18}$$

Substituting equation 1.18 into equation 1.16 gives:

$$\langle R^2 \rangle = l^2 \sum_{i=1}^{n} C_i^{'} = l^2 n \frac{1}{n} \sum_{i=1}^{n} C_i^{'} \tag{1.19}$$

Flory's characteristic ratio C_∞ is defined as the average of the constant $C_i^{'}$ over all bonds along backbone of a polymer:

$$C_\infty = \frac{1}{n} \sum_{i=1}^{n} C_i^{'} \tag{1.20}$$

Substituting equation 1.20 into equation 1.19 gives

$$\langle R^2 \rangle = C_\infty n l^2 \tag{1.21}$$

The above equation shows that for an ideal chain $\langle R^2 \rangle$ is proportional to the number of bonds n along the backbone multiplied by the square of the bond length l^2 and with a coefficient C_∞. The Flory's characteristic ratio shows dependence on the local stiffness of a polymer chain.[77] Many flexible polymers have C_∞ value ranging from 7 to 9, such as poly(ethylene oxide) (PEO, $C_\infty = 6.7$) and polypropylene (PP, $C_\infty = 5.9$). C_∞ tends to increase as side groups become larger because of sterically hindering effect, for example, C_∞ for polystyrene (PS) is 9.5.[78]

Some properties of many flexible polymer are independent of their local chemical structures, which can be interpreted by an equivalent freely jointed chain model.[52] In this model, the definition for $\langle R^2 \rangle$ and $R_{\max}$ is the same to that in the freely jointed

chain model. Instead of considering a single monomer as the unit, several freely jointed effective bonds with a length of b compose the equivalent chain. The effective bond length b is defined as the Kuhn length,[79] and the following equation holds:

$$Nb = R_{\max} \tag{1.22}$$

and the mean-square end-to-end distance is:

$$\langle R^2 \rangle = Nb^2 = bR_{\max} = C_\infty nl^2 \tag{1.23}$$

Thus the number and length of the effective bonds unit can be calculated as

$$N = \frac{R_{\max}^2}{C_\infty nl^2} \tag{1.24}$$

$$b = \frac{\langle R^2 \rangle}{R_{\max}} = \frac{C_\infty nl^2}{R_{\max}} \tag{1.25}$$

The Kuhn length is usually equivalent to the length of several monomers, and is an important parameters used in models to describe polymer dynamics.[52, 79]

1.2.5 The Rouse model

The Rouse model is a successful model to effectively describe polymer dynamics for unentangled polymer liquids.[80–82] In the Rouse model, the monomers are represented by N beads which are connected by springs.[82] The springs have a root-mean-square size of b, as shown in Figure 1.15. In this model, the beads only interact with each other through the springs, and each bead has its own friction with a friction coefficient of ζ. Thus the total friction coefficient for a whole chain is the summation over all beads:

$$\zeta_R = N\zeta \tag{1.26}$$

where ζ_R is the total friction coefficient for a Rouse chain. The Einstein equation relates the diffusion coefficient D to the friction coefficient ($D = kT/\zeta$). Thus, the diffusion coefficient for a whole Rouse chain can be obtained through the Einstein equation:

$$D_R = \frac{kT}{\zeta_R} = \frac{kT}{N\zeta} \tag{1.27}$$

where D_R is the diffusion coefficient for a Rouse chain. The Rouse time τ_R is the characteristic time during which a polymer chain diffuses a distance of its own size:

$$\tau_R \approx \frac{R^2}{D_R} \approx \frac{R^2}{kT/(N\zeta)} = \frac{\zeta}{kT} N R^2 \tag{1.28}$$

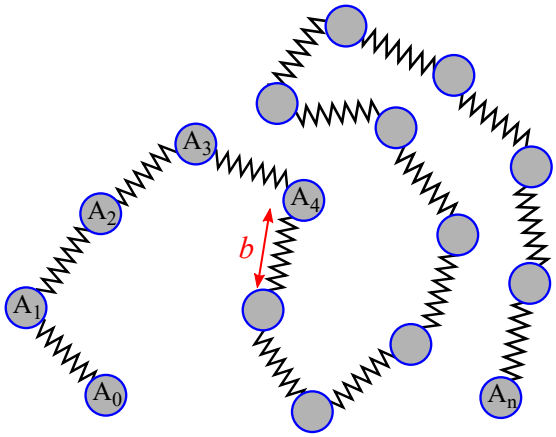

Figure 1.15: Schematic illustration of Rouse model for a chain with N monomers. The monomers are presented by beads which are connected by springs.

The Rouse time is an important parameter for understanding time-dependent properties of polymers.[80, 81] For time-scales shorter than the Rouse time $\tau < \tau_R$, the whole chain does not have enough time to relax, thus the chain shows viscoelastic properties. However, for time-scales longer than the Rouse time $\tau > \tau_R$, the whole chain can diffuse, and the chain thus shows only viscous properties.

The size of a polymer R is related the number of monomers along the backbone:

$$R \approx bN^{\nu} \tag{1.29}$$

Here ν is the reciprocal of the fractal dimension of a polymer, and $\nu = 1/2$ for an ideal chain.[52] A chain with N beads has $N - 1$ springs to connect them. For a chain long enough, the number of springs can be approximated by N. For the individual beads in a Rouse chain, the timescale for motion can be expressed as:

$$\tau_0 = \frac{\zeta b^2}{kT} \tag{1.30}$$

where τ_0 is also called the Kuhn monomer relaxation time. Substituting equations 1.29 and 1.30 into the equation 1.28, the Rouse time can be expressed as:

$$\tau_R \approx \frac{\zeta}{kT} N R^2 = \frac{\zeta b^2}{kT} N^{1+2\nu} \approx \tau_0 N^{1+2\nu} \tag{1.31}$$

For ideal chains, $\nu = 1/2$, and the Rouse time can thus be expressed as:

$$\tau_R = \tau_0 N^2 \tag{1.32}$$

Rouse in 1953 published the full calculation of the relaxation time for ideal chains with a coefficient:[82]

$$\tau_R = \frac{\zeta b^2}{6\pi^2 kT} N^2 \tag{1.33}$$

The above equations demonstrate that the Rouse relaxation time is proportional to the square of the number of monomers in a chain. The monomer relaxation time τ_0 and the Rouse relaxation time τ_R are two important characteristic time-scales in predicting the time-dependent chain relaxation behaviour. For $\tau < \tau_0$, even monomers do not have enough time to relax, thus a chain shows elastic response. For $\tau_0 < \tau < \tau_R$, a chain shows viscoelastic response. For $\tau > \tau_R$, a chain shows viscous response.

The longest relaxation in the Rouse model is the relaxation time for a whole chain which is expressed in equation 1.32. Thus the relaxation time for a chain section involving N/p monomers can be expressed as:

$$\tau_p \approx \tau_0 \left(\frac{N}{p}\right)^2 \quad \text{for} \quad p = 1, 2, 3, ..., N \tag{1.34}$$

When the mode index $p = N$, $\tau_p = \tau_0$, which means that the relaxation time for a monomer is the shortest time in the Rouse model. When $p = 1$, $\tau_p = \tau_R$, which means that the relaxation time for a whole chain is the longest relaxation time in the Rouse model. The mode index p breaks a chain into p sections, and each section has N/p monomers which relax independently on a timescale of τ_p. The larger the p value means the fewer the monomers involved to relax, thus the shorter the relaxation time is. Therefore, at a time of τ_p after a step strain is applied, the modes with mode index larger than p can relax, but the modes with mode index smaller than p can not relax.

The number of unrelaxed modes per chain after τ_p equals the mode index p, and each mode can contribute an energy on the order of kT to the stress relaxation modulus.

Thus the stress relaxation modulus after τ_p is proportional to the product of the thermal energy kT and the number density of sections with N/p monomers ($\phi/(b^3N/p)$):

$$G(\tau_p) \approx \frac{kT}{b^3}\frac{\phi p}{N} \tag{1.35}$$

where ϕ is the volume fraction for the chain sections with N/p monomers. By combining equations 1.34 and 1.35, the stress relaxation modulus in the Rouse model for intermediate time-scales can be expressed as:

$$G(t) \approx \frac{kT}{b^3}\phi\left(\frac{t}{\tau_0}\right)^{-1/2} \quad \text{for } \tau_0 < t < \tau_R \tag{1.36}$$

It is also known that the stress relaxation modulus shows an exponential decay when $t > \tau_R$. Thus the stress relaxation modulus in the Rouse model in the terminal region can be expressed as:

$$G(t) \approx \frac{kT}{b^3}\phi\left(\frac{t}{\tau_0}\right)^{-1/2}\exp(-t/\tau_R) \quad \text{for } t > \tau_R \tag{1.37}$$

In the frequency domain, the storage and loss moduli for the Rouse model can be expressed as:

$$G'(\omega) \approx \frac{\phi kT}{b^3N}\frac{(\omega\tau_R)^2}{\sqrt{[1+(\omega\tau_R)^2]\left[\sqrt{1+(\omega\tau_R)^2}+1\right]}} \quad \text{for } \omega < 1/\tau_0 \tag{1.38}$$

$$G''(\omega) \approx \frac{\phi kT}{b^3N}\omega\tau_R\sqrt{\frac{\sqrt{1+(\omega\tau_R)^2}+1}{1+(\omega\tau_R)^2}} \quad \text{for } \omega < 1/\tau_0 \tag{1.39}$$

In the frequency range $1/\tau_R \ll \omega \ll 1/\tau_0$, G' and G'' of the Rouse model are equal to each other and scales as the square root of frequency:

$$G'(\omega) \approx G''(\omega) \sim \omega^{1/2} \quad \text{for } 1/\tau_R \ll \omega \ll 1/\tau_0 \tag{1.40}$$

At high frequencies $\omega > 1/\tau_0$, no modes can relax in the Rouse model and the chains are in the glassy state. At low frequencies $\omega < 1/\tau_R$, the storage modulus is proportional to the square of the frequency, $G'(\omega) \sim \omega^2$, and the loss modulus is proportional to the frequency, $G'(\omega) \sim \omega$, which is the universal case for the terminal response for viscoelastic liquids.

1.2.6 The tube model

When polymer chains become long enough, a chain can impose topological constraints on other chains; thus they cannot cross each other, as shown in Figure 1.16a. These topological constraints are called entanglements. The reptation model, also called tube model, is a molecular model used to describe polymer dynamics for entangled polymer fluids.[83, 84] In the tube model, the topological constraints from all surrounding chains make a given chain not relax as freely as in the Rouse model. Instead, the given chain can only diffuse through these surrounding chains, and motion of the given chain is restricted in a tube-like region, as shown in Figure 1.16b. The motion of the blue chain can only diffuse within the tube region (indicated by black lines) because of the topological constraints imposed by the red chains. A chain can only diffuse in the tube-like region indicated by black lines in Figure 1.16b because of the constraints imposed by the chain from other nearby chains, and the diffuse path of a chain can undergo, as indicated by the green dotted line in Figure 1.16b is called the primitive path.

Monomers along the backbone are constrained to stay close to the primitive path with a certain degree of fluctuations, which defines the width of the constraint tube, called the tube diameter a. In the network of long linear chains, there are many entanglement points and the strand between two entanglement points are called the entanglement strand with a molecular weight of M_e composed of N_e monomers. Thus the entanglement molecular weight $M_e = N_e M_0$, where M_0 is the molecular weight for monomers. The tube diameter is related to the end-to-end distance of the entanglement strand:

$$a \approx bN_e^{1/2} \tag{1.41}$$

The entanglement strands determine the plateau modulus G_p:

$$G_p = \frac{\rho RT}{M_e} \tag{1.42}$$

The importance of entanglements on the elasticity of polymers has been proven by computer simulations and experimental observations.[52]

One can view the tube as composed of N/N_e sections, and each section contains N_e monomers. Thus, the motion of the whole chain can be considered as the random

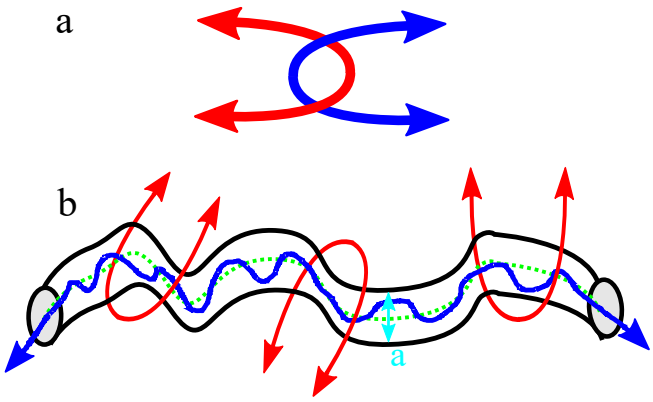

Figure 1.16: Schematic illustration of (a) topological constraints between long linear chains and (b) the tube model. The topological constraints from the red chains make the motion of the blue chain in the tube-like region (black lines) with the tube diameter of a.

walk of entanglement strands (N/N_e strands of size a) or random walk of monomers (N monomers of size b).

$$R \approx a\left(\frac{N}{N_e}\right)^{1/2} \approx bN^{1/2} \tag{1.43}$$

The average length $\langle L \rangle$ of the primitive path is the product of a and the number of entanglement strands:

$$\langle L \rangle \approx a\frac{N}{N_e} \approx \frac{Nb^2}{a} \approx \frac{bN}{N_e^{1/2}} \tag{1.44}$$

For a polymer with $N \gg N_e$, stress relaxation remains almost constant in a wide time or frequency range because of entanglements. The volume occupied by an entanglement strand V_e can be expressed as:

$$V_e = \frac{M_e}{\rho N_{Av}} \tag{1.45}$$

Where ρ is the density for a polymer and N_{Av} is the Avogadro's constant. The V_e is also related to the number N_e and the volume of monomers V_0:

$$V_e = \frac{M_e}{\rho N_{Av}} = V_0 N_e \approx V_0\frac{a^2}{b^2} \tag{1.46}$$

Thus, the plateau modulus is related to M_e for an entanglement polymer can be expressed as:

$$G_p \approx \frac{\rho RT}{M_e} \approx \frac{kT}{V_0 N_e} \approx \frac{b^2 kT}{a^2 V_0} \tag{1.47}$$

The above equation means that the plateau modulus is related to the thermal energy of unrelaxed chain strands carry.

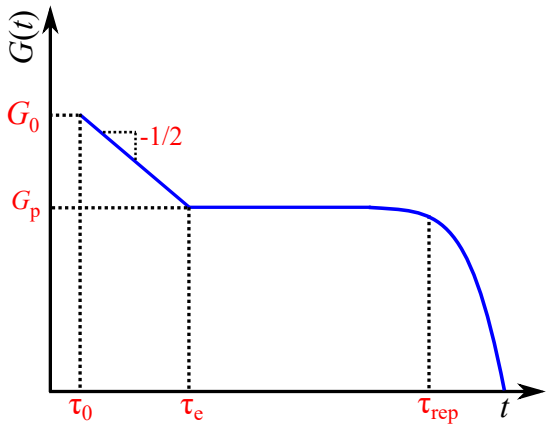

Figure 1.17: Schematic illustration of stress relaxation modulus as a function of time for entangled polymer predicted by the tube model in the log-log plot.

The motion of chains in the tube region is in the manner of curvilinear diffusion, which is characterized by the number of monomers N and the friction coefficient ζ between monomers. Thus, based on the Einstein equation, the curvilinear diffusion coefficient D_c can be expressed as:

$$D_c = \frac{kT}{N\zeta} \tag{1.48}$$

The reptation time τ_{rep} is defined as the time a chain takes to diffuse out the original tube with a average length $\langle L \rangle$:

$$\tau_{rep} \approx \frac{\langle L \rangle^2}{D_c} \approx \frac{\zeta b^2 N^3}{N_e kT} \tag{1.49}$$

The above equation predicts that the reptation time is proportional to the cube of molecular weigh $\tau_{rep} \sim N^3 \sim M^3$. However, in experiments, the power law exponent is measured to be 3.4, $\tau_{rep} \sim M^{3.4}$ which shows a slight disagreement with the tube model.

The reptation model can be used to predict the stress relaxation modulus $G(t)$ for entangled polymers. On the length scale larger than the tube diameter a, topological constraints are not important and entanglement strands show similar dynamics of unentangled polymer melts which can be described by the Rouse model. The longest Rouse

relaxation time τ_e for the entanglement strand with N_e monomers can be expressed as:

$$\tau_e = \tau_0 N_e^2 \tag{1.50}$$

The time dependent stress relaxation modulus for entangled polymers was calculated by Doi and Edwards in 1978:

$$G(t) = \frac{8}{\pi^2} G_p \sum_{\text{odd}p} \frac{1}{p^2} \exp\left(- \frac{p^2 t}{\tau_{rep}} \right)^2 \tag{1.51}$$

The stress relaxation modulus is shown schematically in Figure 1.17. The repatation time in this model can be calculated as:

$$\tau_{rep} = 6\tau_0 \frac{N^3}{N_e} = 6\tau_e \left(\frac{N}{N_e} \right)^3 \tag{1.52}$$

Equation 1.51 is the so-called Doi-Edwards equation which is the first molecular model for viscoelastic properties of entangled polymers.

The relationship between molecular weights and the viscosity can usually be described by $\eta \propto M^\alpha$, where α equals 1 for unentangled polymers and about 3.4 for entangled polymers from experimental data. Based on the Maxwell theory, $\eta = G(\tau)\tau$.[85] In the Rouse model, the modulus corresponding to the timescale of the longest Rouse mode is related to the product the number density of chains and thermal energy kT, $G(\tau) = kT\phi/(Nb^3)$. The relaxation time of the longest Rouse mode is $\sim \tau_0 N^2$, thus, $\eta = G(\tau)\tau \propto N$, which means that for unentangled polymers, the viscosity is proportional to the molecular weight. For entangled polymers, the tube model predicts that the viscosity is proportional to M^3, see Equation 1.52. In reality, one typically observes a larger exponent: $\eta \propto M^{3.4}$.[52, 83] The tube model ignores tube length fluctuations which might relax on shorter timescales. It also does not include the constraints release, which means that entanglements also fluctuates due to the fact that chains that provide the constraints can diffuse and release their entanglement effects. Both the contour length fluctuations and the constraint release lead to the power of 3.4, instead of the value of 3 predicted by the model. Thus, further modifications to the tube model are under investigation to improve the predication.

1.2.7 The sticky Rouse model

To be able to predict and hence design and control viscoelastic properties of supramolecular polymers (see Section 1.1.2), it is important to understand how to model the rheological response. The most commonly used model to describe rheology of unentangled associating polymers is the sticky Rouse model, which is based on the idea that stress can be relaxed through breaking and reformation of reversible cross linking groups, i.e. stickers.[4, 86–90] Stickers are non-covalent and reversible bonds between polymer chains which act as physical cross-links. For the normal Rouse modes with lengths shorter than the distance between two sticky groups, M_s, stress relaxation of these Rouse modes is essentially Rouse-like. However, for the chain segments longer than M_s, the stress relaxation is controlled by the association and dissociation of sticky groups.[88, 89] Based on these ideas, the Rouse relaxation modulus with considering molecular weight distribution can be expressed as:

$$G_R(t) = \sum_i \frac{\rho w_i RT}{M_i} \sum_{p=1}^{N_i} \exp\left(\frac{-tp^2}{\tau_0 N_i^2}\right) \tag{1.53}$$

where ρ is the density of a polymer, w_i and M_i are weight fraction and molecular weight of the ith chain. $N_i = M_i/M_0$ is the number of elementary Rouse segments per chain, M_0 and τ_0 are molecular weight and characteristic time of the elementary Rouse unit, respectively. For supramolecular polymers, the Rouse segments longer than M_s can feel the constraints from the association of sticky groups.[4] For the time scales shorter than the association time τ_s, the stress relaxation is controlled by τ_s. The relaxations of lower Rouse modes ($p = 1$ to $p = N_{s,i}$) are delayed, where $N_{s,i}$ is the average number of sticky groups on the ith chain fraction. Thus, the sticky Rouse relaxation modulus can be expressed as:

$$G_s(t) = \sum_i \frac{\rho w_i RT}{M_i} \left[\sum_{p=1}^{N_{s,i}} \exp\left(\frac{-tp^2}{\tau_s N_{s,i}^2}\right) + \sum_{p=N_{s,i}+1}^{N_i} \exp\left(\frac{-tp^2}{\tau_0 N_{s,i}^2}\right) \right] \tag{1.54}$$

The above equation includes two contributions. The first contribution sums over the Rouse modes contribution longer than M_s (low order Rouse mode), whereas the second contribution sums over Rouse modes contribution shorter than M_s (high order Rouse modes).

1.3 The glassy state and the glass transition

If you ask someone in the street what a glass is, you will most likely not get an exact definition but most people can surely give many examples, including windows, bottles etc. However, although glass is an ancient material that has been used by human beings for over thousands of years, the nature of glass and particularly the nature of the glass transition has never been fully understood. [91, 92] In the words of the Nobel prize winner Philip Anderson:
"*The deepest and most interesting unsolved problem in solid state theory is probably the theory of the nature of glass and the glass transition.*"[93]

1.3.1 Supercooled liquids and glasses

There are three well defined thermodynamic equilibrium states for a substance: gas, liquid and crystalline solid. As temperature decreases, the motion of molecules becomes slower[91] and the specific volume generally decreases. For most liquids, undergoing different cooling rates can result in different structures: an ordered crystal, a supercooled liquid, or a disordered solid glass[91, 92]. Some materials including some polymers can never form a crystal. If the cooling rate is slow enough, the molecules have enough time to find their equilibrium positions within an ordered crystal structure, which minimises the free energy. Crystals have long range periodicity, and the temperature when this transition becomes thermodynamically preferred is termed the melting point, T_m.

The second route occurs if the cooling rate is fast enough and a liquid is clean enough so that nucleation and thus crystallization can be avoided. The liquid will then not crystallize at the melting point, but will reach lower temperatures and exist in a thermodynamically metastable state termed the supercooled liquid. As temperature decreases in the supercooled state, the motion of the molecules become ever slower. When the characteristic time-scale of molecular motions becomes longer than the time-scale characterising cooling, there is not enough time to form a crystal and a disordered solid with a liquid-like structure can be formed; this solid is called a glass [91, 92]. The temperature at which the characteristic motions of molecules reaches a typical experimental time-scale of 100 seconds is called the glass transition temperature, T_g.

A supercooled liquid is in a metastable state [91, 92] with regards to the equilibrium crystal state. The viscosity, η, increases rapidly with decreasing temperature in the supercooled state and the temperature dependence can usually be described by the Vogel-Fulcher-Tammann (VFT) equation:[94]

$$\eta = \eta_0 \exp\left(\frac{DT_0}{T - T_0}\right) \tag{1.55}$$

A material behaves like a solid when η reaches around 10^{12} Pa·s, which is termed the glass. A glass does not long range ordered structures as crystals show, instead, the glass has random structures on the molecular scale as liquids show. The temperature when η reaches around 10^{12} Pa·s is termed the glass transition temperature T_g.

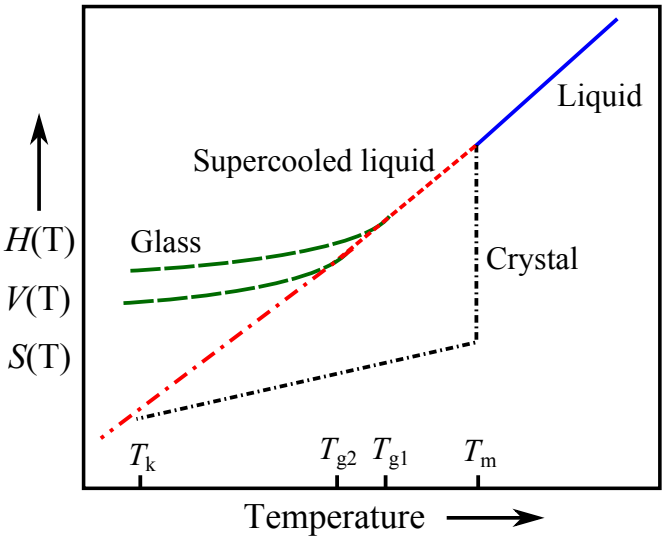

Figure 1.18: Diagram showing several thermodynamic properties (enthalpy $H(T)$, entropy $S(T)$, specific volume $V(T)$ as a function of temperatures at a constant pressure. Lines in different colours and styles show properties of a material at different states which are defined in figure. Variations of H, S and V upon temperature T_m are non-continuous at melting point T_m. The red dot-dashed line is the extrapolation from supercooled liquid line. The crossover of extrapolated supercooled liquid line with crystal line is termed Kauzmann temperature, T_k, indicating that all liquids have to crystallize at this temperature, otherwise entropy of supercooled liquids at temperatures below T_k would be lower than that of corresponding crystals. This is so-called entropy crisis.[95, 96]

1.3.2 The glass transition

The transition from liquid to glass is called the glass transition and involves two states, the supercooled liquid and the glassy state [91, 92]. The former state is a metastable state and the latter is a non-equilibrium state. Taking the most common SiO_2 glass as an example, at high temperature above T_m, the SiO_2 glass melt is a viscous liquid. As temperature decreases, the viscosity of the melt increases sharply, especially when the temperature is approaching T_g. After the temperature goes below T_g, the melt becomes a long-range disordered, non-equilibrium solid. Figure 1.18 describes a variation of the enthalpy $H(T)$, entropy $S(T)$ and specific volume $V(T)$ as the temperature decreases from above T_m to below T_g.[97] There are two routes for an equilibrium liquid to become solid when the temperature approaches T_m. One is to crystallize and form a stable, equilibrium crystal for materials that can crystallize. In this case, a discontinuous decrease in first order thermodynamic properties, such as the volume, can be observed, see Figure 1.18. The other one is to go to the so-called supercooled liquid state if the cooling rate is fast enough so that crystallization can be avoided.

As the temperature decreases further, the supercooled liquids turns into a glass. During the glass transition, no discontinuous changes in volume, enthalpy and entropy are observed. Instead, a change of the slope of the thermodynamic properties as function of temperature is observed in the glass region, as shown in Figure 1.18. Moreover, the T_g depends on the cooling rate. The higher cooling rate results in a higher T_g, $T_{g1} > T_{g2}$, as shown in Figure 1.18. Thus, the T_g is not a fixed value for a certain material. Within the glass transition range, as shown in Figure 1.18, the entropy of the liquids is higher than the corresponding crystals. If the supercooled liquid does not go into the glassy state when the temperature decreases, then in theory, there would be crossover temperature at which the liquid and the corresponding crystalline states have the same entropy. This hypothesized temperature is called the Kauzmann temperature (T_k).[95] In the crystal state main contribution to entropy is vibrations and in supercooled state both vibrational and configurational degrees of freedom contribute. Thus, at T_k the configurational part of entropy would effectively approach zero. If temperature is reduced further the configurational entropy would become negative, which is unphysical. This paradox is so−called entropy crisis.[95, 96]

1.3.3 Relaxation dynamics in supercooled liquids

A range of characteristic relaxation mechanisms are generally observed for glass-forming materials. These are often named using Greek letters, as α, β and γ, and the relaxations are normally termed in order of decreasing relaxation time for a fixed temperature.[98] Examples are shown in Figure 1.19a. In this section, these relaxation processes will be introduced.

The structural α relaxation

The α relaxation is the primary structural relaxation which is related to the glass transition.[98] On time-scales longer than the α relaxation time-scale, τ_{alpha}, the material behaves like a liquid, whereas on timescales shorter than τ_{alpha}, the material behaves like a solid. Based on the Maxwell theory of viscosity, the relation between viscosity and the structural relaxation time-scale is:

$$\eta = G_{\infty}\tau_{\alpha} \tag{1.56}$$

where η is the viscosity, and G_{∞} is the instantaneous shear modulus, respectively. The temperature for which the viscosity reaches or above 10^{13} Pa·s,[99] which corresponds to a timescale around 100 s, is normally defined as glass transition temperature T_g. The temperature dependence of the α relaxation time-scale can be described using the VFT equation:[94]

$$\tau = \tau_0 \exp\left(\frac{DT_0}{T - T_0}\right) \tag{1.57}$$

where T_0 is the temperature at which τ_{α} tends to infinity, and D is the so-called strength parameter and is a measure of the temperature dependence of τ_{α}. The dynamics of different liquids approach their glass transition temperatures differently. A so called fragility parameter, m, has been proposed to describe the difference in temperature dependence of the viscosity or structural relaxation time between different liquids when forming a glass. m is defined as the slope of $\log_{10}\tau_{\alpha}$ at T_g in the Arrhenius plot:[100]

$$m = \left.\frac{d(\log_{10}\tau_{\alpha})}{d(\frac{T_g}{T})}\right|_{T=T_g} \tag{1.58}$$

Angell classified glass-formers according to their fragilities. The dynamic behaviour of strong liquids when the temperature approaches T_g can be described by the Arrhenius

equation, which is a near straight line in the Angell plot with a m value around 16.[92] The dynamics of fragile liquids when the temperature approaches T_g deviates from the Arrhenius equation, and can be described by the VFT equation. The more it deviates from the Arrhenius behaviour, the larger the m value is (Figure 1.19b).[101] It is also clear that τ_α for glass-formers with a smaller value of D shows a stronger temperature dependence (larger m value, Figure 1.19b).

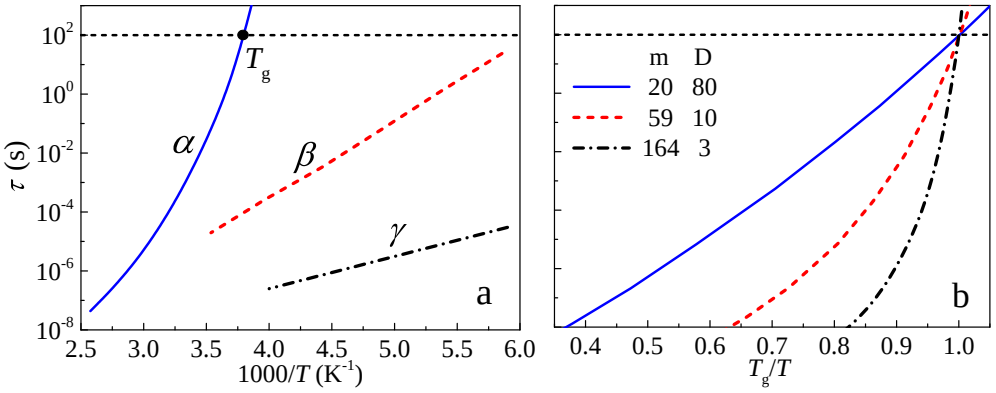

Figure 1.19: (a) The Arrhenius of plot of relaxation timescales as a function of temperatures for α, β and γ relaxations. (b) VFT behaviour of α relaxation with different values of strength parameter, D, showing different fragilities.

Theoretical models used to explain the glass transition

Debates on the origin of the glass transition phenomenon (the slowing down of the α relaxation within the supercooled state) have led to many attempts to understand the phenomenon in theory, and many theoretical models have been proposed. [91, 92, 96, 100, 102–105] Since there are so many approaches, it is out of the scope of this thesis to introduce all models in detail. However, two of mostly discussed models will be introduced briefly and these are also mentioned in the latter chapters of this thesis.

One of these models is called the free volume model and is based on the assumption that the volume of a material can be divided into two parts: one part is the volume occupied by molecules and the other is the volume not occupied by molecules, which can thus be shared by molecules once displacements of molecules occur.[106] The latter part was termed free volume, V_f. The core idea is that V_f of a material has to be large enough for structural relaxation to occur. As the temperature decreases, V_f

decreases. At a certain temperature, there is not enough V_f for structural relaxation to occur, meaning the motions of the molecules are arrested. Thus, within this type of model, the structural relaxation is related to the temperature dependence of V_f:[92]

$$\tau = \tau_0 \exp(\frac{A}{V_f}) \tag{1.59}$$

The above equation yields a VFT-like behaviour of the temperature dependent α relaxation time-scales based on simple modeling of the temperature dependence of V_f[92] An extension to the free volume model was also proposed. In the extended model, a material can be considered as a mixture of two regions: one is liquid-like and the other is solid-like.[107] Relaxations in the liquid-like region is due to exchange of free volume between molecules. As the temperatures decreases, the liquid-like regions became smaller, while on the contrary, the solid-like regions became lager. The glass transition occurs at the temperature where the solid-like regions occupy the whole material. Although the free volume models show some success when applied to some polymers, they have significant drawbacks. First of all, the free volume can not be defined precisely. Secondly, a material measured at constant volume can also show a glass transition.[108] These drawbacks indicate that only consideration of redistribution of free volume is not enough to explain the origin of a glass transition.

Other models were proposed that were based instead on the temperature dependence of the entropy. In such entropy based models, an increase of the α relaxation time-scale with decreasing temperature is related to a decreasing number of molecular configurations and thus a decreasing configurational entropy, S_c. Thus, the glass transition occurs at a temperatures where $S_c = 0$. One of the most discussed entropy models was proposed by Adam and Gibbs.[109] The concept of cooperatively rearranging regions (CRR) was introduced which was defined as subregions of a material. Relaxations of the subregions were not dependent on the surrounding subregions, and the size of the CRR increases upon a decrease of temperature (more molecules are included in a CRR).[105] Based on the assumption that the activation energy of the α relaxation is proportional to the size of the CRR, the α relaxation time-scale can be expressed as[92]

$$\tau = \tau_0 \exp \frac{A}{TS_c(T)} \tag{1.60}$$

The above equation implies that an increasing of the α relaxation time is related to an increase of the size of CRRs with decreasing temperatures. Although many aspects of the entropy model has been demonstrated to be consistent with data for many systems,[92] the determination of configurational entropy by experimental methods is difficult, but it can be estimated as the difference between the total entropy and the vibrational entropy. The total entropy is measurable by DSC and the vibrational entropy can be estimated as the extrapolation of crystal entropy into the supercooled or glassy region. However, even if the configurational entropy can be approximately estimated, the CRR size determined from the estimated entropy only contains a very small number of molecules.[110] and the relaxation of such a small CRR size is less likely independent on the surroundings.[92]

Secondary relaxations

In addition to the structural α relaxation, secondary relaxations which occur at lower temperatures or at higher frequencies have been observed in polymers[111] and small molecular glass formers,[112] which are usually termed β and γ. Compared with the α relaxation, these secondary relaxations show some different features: i) they occur at higher frequencies for a fixed temperature or at lower temperatures, even below T_g, for a fixed probe time-scale or frequency; ii) the relaxation strength as determined for instance from dielectric or mechanical spectroscopy are usually symmetric on log-log plots; iii) the temperature dependence of the secondary relaxation timescales usually follows the Arrhenius behaviour within the glassy state (Figure 1.19a):

$$\tau = \tau_0 \exp(\frac{E_a}{k_B T}) \tag{1.61}$$

where E_a is activation energy, and k_B is the Boltzmann constant.

The β relaxations are general amongst glass-forming materials, however, there is no general agreement on the origin of secondary β relaxations. In polymers, it was proposed that β relaxation is related to both intermolecular and intramolecular motions.[111] It has been demonstrated that for many polymers e.g. with side-groups that the β relaxation has a side-group component but also requires backbone motions, and for polymers without side groups, β relaxations can also be observed.[113] In small molecular glass formers, β relaxations can also be observed and are of largely

intermolecular nature.[112] Understanding the role played by secondary relaxations is important for glassy dynamics, and it was suggested that β relaxations are also linked to the α relaxations,[114] and investigations on secondary β relaxations are still a hot topic currently.[115]

1.4 Importance of the work

In this thesis, the relaxation dynamics of four supramolecular systems will be investigated. The first system is based on a comb-like polymeric backbone of poly(2-ethylhexyl acrylate) (PEHA) to which a random distribution of 2-ureido-4[1H]-pyrimidinone (UPy) side groups are added. A series of polymers with a systematic variation of the concentration of UPy-based side-groups has been synthesised using reversible addition fragmentation chain transfer (RAFT) polymerisation. The second system is based on poly(propylene glycol) (PPG) for which its chain ends are functionalised using UPy hydrogen-bonding groups forming a polymer with supramolecular end-groups (UPyPPG). The unfunctionalised PPG is a viscous liquid at room temperature whereas UPyPPG is a rubbery material due to the formation of long extended chains through multiple end-to-end hydrogen bonds. The third system is based on polytetrahydrofuran (PTHF) which contains hydroxyl end-groups. We investigate a range of PTHFs with different molecular weights. Finally, the fourth system consists of alkane diols which contain varying number of backbone carbons between two hydroxyl chain-ends.

The last few decades have witnessed great developments in research and application fields related to supramolecular materials. Many supramolecular systems have been prepared by chemists, and applications of these supramolecular systems have been tested for use in a wide range of areas; examples include materials for medical applications such as drug or DNA delivery into living cells and controlled drug release. However, many fundamental aspects such as the rheological response, the relaxation dynamics over a wide temperature range, and structure-property relationships are not well understood. This thesis is aimed at reaching a better understanding of how supramolecular interactions affect the structure, rheology and relaxation dynamics over a wide temperature range ranging from the glassy to the melt state for a range of different supramolecular oligomer and polymer systems. The aim is to build

up a better understanding of this material which can provide guidelines for the design and tuning of new supramolecular materials in the future. We have also investigate a few potential applications of our synthesized chain-end functionalised supramolecular polymer within the application area of Li-ion batteries and self-healing coating areas, respectively.

Chapter 2

Experimental Techniques

A range of experimental techniques were used to probe the dynamics of the supramolecular materials in the melt and glassy states, covering timescales from $\sim 10^{-10}$ to 10^{3} s. These techniques include broadband dielectric spectroscopy (BDS), rheometry , differential scanning calorimetry (DSC), temperature modulated DSC (MDSC), rate dependent DSC (RDSC) and Nuclear magnetic resonance (NMR). This chapter will detail the theoretical and experimental aspects of these techniques.

A number of complementary techniques were also used to characterise the molecular weight and structure of the supramolecular materials, such as size exclusion chromatography (SEC), small angle X-ray scattering (SAXS) and wide angle X-ray scattering (WAXS). Since these techniques do not directly probe the relaxation dynamics of the systems, the details of these will not be discussed here but will instead be discussed in the relevant results chapters.

2.1 Broadband dielectric spectroscopy

The structural relaxation dynamics of an amorphous material near the glass transition occur on timescales spanning many orders of magnitude. Broadband dielectric spectroscopy (BDS) is a widely used technique to study the dynamics near the glass transition temperature, T_g, because its operational frequency range can cover many orders of magnitude, from from $\sim 10^{-6}$ to 10^{11} Hz. The spectrometer used in this work has a frequency range of 10^{-2} to 10^{6} Hz, corresponding to timescales ranging from $\sim$16 and 10^{-7} s.[116] In the following sections, the theoretical aspects of

the BDS will be introduced, following the books of Schönhals,[117] Böttcher and Rip,[118] Runt and Fitzgerald[119] and the PhD theses of Baker,[115] Gainaru[120] and Blochowicz.[121] Subsequently, several empirical functions used to fit and analyse the dielectric spectra will be explained and finally some general experimental details will be given.

2.1.1 Polarisation of a material in an electrical fields

External electric fields can result in a macroscopic polarisation, **P**, of a material.[118, 122] This polarisation can be attributed to several mechanisms: (i) the reorientation of the permanent dipoles of the molecule, μ; (ii) a displacement of the electron clouds relative to their nuclei; and (iii) a displacement of nuclei relative to other nuclei.[118, 123] The first mechanism is of particular interest, because it occurs in the detectable frequency range of the spectrometer used in this work. When studying the slow dynamics near T_g, the reorientation of permanent dipoles can give information about the molecular dynamics within a material.[124] The latter two cases, leading to a so-called induced polarisation, $\mathbf{P}_\infty$, occuring on timescales faster than 10^{-13}s, and this is thus not directly detectable using our spectrometer.

Besides the above three mechanism, materials can also show other macroscopic polarisations if they contain charged species.[117] An external electric field can lead to the diffusion of these charged species. At long timescales or low frequencies, these species can accumulate at the surface of the electrodes, resulting in an extra macroscopic polarisation. This is the so called DC-conductivity,[117] which can result in a sharp increase in the imaginary part of permittivity so that it can even surpress the signal due to molecular fluctuations.[115] In some inhomogenous materials, such as partly crystallized or phase separated materials, the charged species can also accumulate at the interfaces of different phases, and this leads to a so-called Maxwell-Wagner-Sillars (MWS) polarisation.[117] When analysing the dielectric spectra, careful attention must be paid if the spectra contain a DC-conductivity relaxation.

2.1.2 Reorientation of permanent dipoles in an electrical field

According to Maxwell's equations, the interaction of an applied electric field **E** to a material can be expressed as:[117, 118]

$$\mathbf{D} = \varepsilon_s \varepsilon_0 \mathbf{E} \tag{2.1}$$

where **D** is the dielectric displacement field due to the applied field and ε_0 and ε_s are the permittivity of free space and static permittivity, respectively. The applied electric field must be small enough to avoid nonlinear effects. The polarisation, **P**, describes the dielectric displacement due to the response of the material to **E**, and is defined as:

$$\mathbf{P} = \varepsilon_0(\varepsilon_s - 1)\mathbf{E} \tag{2.2}$$

The term $\varepsilon_s - 1$ is a measure of how easily the material can be polarized by the applied electrical field. As discussed in Section 2.1.1, the permanent dipoles of molecules are randomly oriented in the material due to thermal fluctuations.[122, 124] However, when an electric field is applied the permanent dipoles will start to align with the field. After a certain amount of time the polarisation will reach a maximum value oriented in the direction of the applied electrical field, generating a macroscopic dipole. This is termed as orientational polarisation, $\mathbf{P}_0$.[117, 118] The total macroscopic polarisation should be the sum of the orientation polarisation and the induced polarisation, $\mathbf{P} = \mathbf{P}_\infty + \mathbf{P}_0$. Here we assume that there are no charged species in the material for simplicity.

The orientational polarisation of a material is the sum over all microscopic permanent dipoles of molecules within a volume V. For simplicity, we consider the external electric field is along the z direction. Thus the orientational polarisation along the z direction can be expressed as:

$$\mathbf{P}_0 = \frac{1}{V}\sum_{i=1}^{N} \mu_i \cdot \mathbf{z} = \frac{N}{V} < \mu >_z \tag{2.3}$$

where $< \mu >_z$ and N are the average of all dipole moments in the z direction and the number of dipoles. In reality, the molecular dipoles are not aligned exactly with the external electric field due to the thermal fluctuations.[122, 124] Thus, the angle of a dipole with the z direction, θ, needs to be taken into the consideration. According to

the Boltzmann statistics one obtains:[120]

$$< \mu >_z = \frac{\int_0^{\pi} \mu_z \exp(\frac{\mu_z \mathbf{E}}{\mathrm{k_B T}}) \mathrm{d}\Omega}{\int_0^{\pi} \exp(\frac{\mu_z \mathbf{E}}{\mathrm{k_B T}}) \mathrm{d}\Omega} \tag{2.4}$$

where T is the temperature, k_B is the Boltzmann constant, and $d\Omega$ is the differential space angle. The factor $\exp(\mu\mathbf{E}/\mathrm{k_B}T)\mathrm{d}\Omega$ is the probability for the dipole moment to change angles, and $d\Omega = 2\pi \sin\theta \mathrm{d}\theta$.[120, 121] μ_z is the projection of a dipole on the z direction, $\mu_z = \mu cos\theta$. Here it is assumed that the dipoles are non-interacting and so one can define the potential energy of a dipole as $U = -\mu E \cos\theta$.[117, 118, 121] Thus, equation 2.4 can be simplified to:

$$< \mu_z >= \frac{\mu^2 \mathbf{E}}{3 k_B T} \tag{2.5}$$

Inserting equation 2.5 into equation 2.3, a relationship between the orientational polarisation and applied external field can be derived:[117]

$$\mathbf{P}_0 = \frac{\mu^2}{3 k_B T} \frac{N}{V} \mathbf{E} \tag{2.6}$$

One can further define an equation for the relationship between the dipole moment and the dielectric relaxation strength, $\Delta\varepsilon$, as follows:

$$\Delta\varepsilon = \varepsilon_s - \varepsilon_\infty = \frac{1}{3\varepsilon_0} \frac{\mu^2}{k_B T} \frac{N}{V} \tag{2.7}$$

Where ε_0 and ε_∞ are the permittivity at static state and as the frequency tends to infinity respectively. With the aid of equation 2.7, the so-called Curie law,[117, 118] one can estimate the average molecular dipole moments from the dielectric spectra.

2.1.3 The relaxation of a polarized material

When an electric field is applied, the permanent dipoles of the molecules will start to align with the field and it will take a certain amount of time for the orientation polarisation to reach its maximum value. If the electric field is subsequently removed,

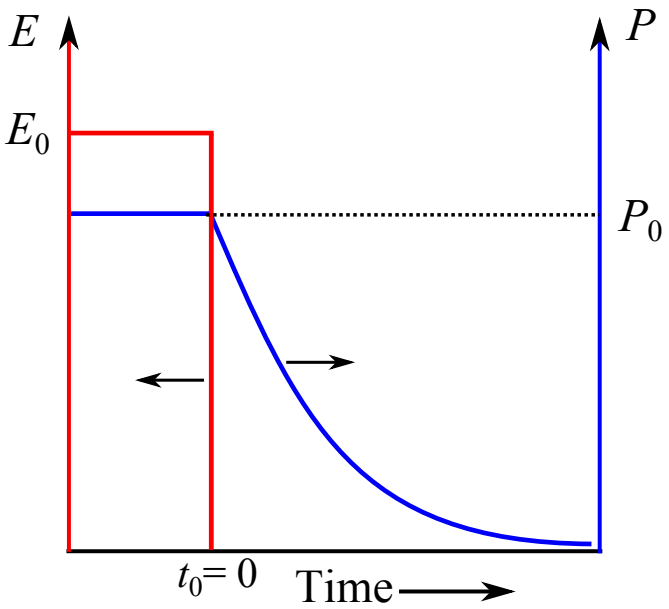

Figure 2.1: Schematic illustration of the effect of an applied electric field (E) on the polarisation of a material (P). The polarisation of (P_0) is produced when the electric field of (E_0) is applied. After the electric field is removed at $t_0 = 0$, the polarisation starts to relax to as a function of time.

the polarisation will start to relax to its equilibrium value,[120] as shown in Figure 2.1. The relaxation of the polarisation can be described by a relaxation function, $\Phi(t)$:

$$\Phi(t) = \frac{\mathbf{P}_0(t)}{\mathbf{P}_0(t=0)} \tag{2.8}$$

When the applied electric fields is in the linear regime, it only introduces a small perturbation to the molecules.[120] Thus the response of the material to this small perturbation follows the fluctuation dissipation theorem,[117] which means that the response of the material to the perturbation is similar to the equilibrium thermal fluctuation without an external field. In other words, applying a small electric field to a material can cause the molecules to deviate from their equilibrium orientation but the deviation degree is equivalent to thermal fluctuations without any electric field. Therefore, to a good approximation, one can probe molecular dynamics by indirect measurement of the dipolar reorientation of molecules using dielectric spectroscopy.[117, 123] However, the applied external electric field has to be small enough so that the fundamental properties of the materials are not changed by the applied field. If a harmonic electric

field, $E^*(\omega)$ is applied, the polarisation will become frequency dependent as well:

$$\mathbf{P}^*(\omega) = \varepsilon_0(\varepsilon_s - 1)\mathbf{E}^*(\omega) \tag{2.9}$$

The complex field, $\mathbf{E}^*(\omega)$, is related to the complex permittivity, ε^*, which is composed of real and imaginary parts:[115, 117]

$$\varepsilon^* = \varepsilon' - i\varepsilon'' \tag{2.10}$$

The real part, ε', is a measure of the energy stored in the material, whereas the imaginary part, ε'', is a measure of the energy loss in the material as a function of frequency.[123] The complex permittivity is related to the relaxation function, in equation 2.8. The relation between the relaxation function, $\Phi(t)$, and the complex permittivity, ε^*, can be described in the following equation:[117, 118]

$$\frac{\varepsilon^* - \varepsilon_\infty}{\Delta\varepsilon} = 1 - i\omega \int_0^\infty \Phi(t)e^{-i\omega t}d(t) \tag{2.11}$$

The application of frequency dependent electric fields, $\mathbf{E}^*$, to a material results in a frequency dependent polarisation, $\mathbf{P}$, which is the result of the orientation and relaxation of the permanent dipoles in a material. The relaxation of the polarisation is related to the complex permittivity, ε^*, based on equation 2.11, and dielectric spectroscopy can measure ε^* over a wide range of frequencies. Thus, microscopic dynamics can be probed in a dielectric measurement through the probing of the relaxation of the permanent dipoles.[117, 123]

The changing rate of the macroscopic polarisation is proportional to its value at a given time, t, which can be expressed in a differential form:[117, 125]

$$\frac{d\mathbf{P}}{dt} = \frac{-1}{\tau_D}\mathbf{P}(t) \tag{2.12}$$

where τ_D is the Debye characteristic timescale.[117] In the simplest case, the relaxation function, $\Phi(t)$, follows a single exponential law:

$$\Phi(t) = e^{-t/\tau_D} \tag{2.13}$$

Substituting equation 2.13 into equation 2.11 produces the complex permittivity, ε^*:

$$\varepsilon^* = \varepsilon_\infty + \frac{\Delta\varepsilon}{1 + i\omega\tau_D} \tag{2.14}$$

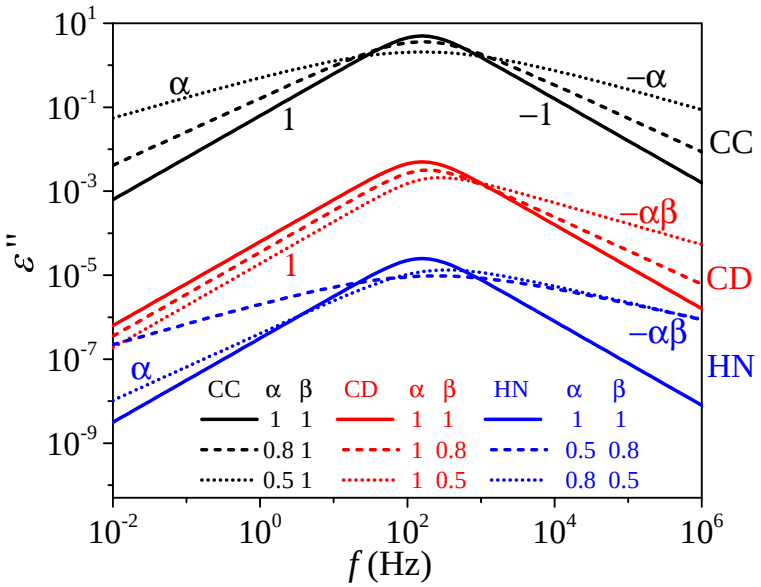

Figure 2.2: The equation shapes for the Debye equation (solid lines with shifted $\Delta\varepsilon$ for clarity), the Cole-Cole (CC) equation (black dashed and dotted lines),the Cole-Davidson (CD) equation (red dashed and dotted lines) and the Havriliak-Negami (HN) equation (blue dashed and dotted lines). The shape parameters to create these curves are shown in legends. The curves are vertically shifted for clarity.

where ε_∞ is the permittivity at high frequency, $\Delta\varepsilon$ is the difference between static and high frequency permittivity, $\Delta\varepsilon = \varepsilon_\infty - \varepsilon_s$, and τ_D is the characteristic relaxation timescale. This is the so−called Debye function. The imaginary component, ε'', of a Debye relaxation is manifested as a peak as a function of frequency, with symmetric gradients at low and high frequencies in a log-log plot, equal to 1 and -1 respectively. In Figure 2.2, three solid lines show the shape of a Debye relaxation peak, shifted vertically for clarity. The real part of the permittivity, ε' is step-like in frequency. The dielectric relaxation strength, $\Delta\varepsilon$ is defined as the difference between the real part of the permittivity, ε', as the frequency tends to 0 and infinity, $\Delta\varepsilon = \varepsilon_s - \varepsilon_\infty$, which is the same as the integral area under the peak of the imaginary part:

$$\Delta\varepsilon = \frac{2}{\pi}\int_0^\infty \frac{\varepsilon''(\omega)}{\omega} d\omega \tag{2.15}$$

In reality the dielectric relaxation peaks are often observed to be broader than a Debye relaxation peak. To describe these relaxation peaks, several empirical mod-

ifications of the Debye equation have been proposed. One such modification is the Cole-Cole (CC) equation:[126]

$$\varepsilon^*_{CC}(\omega) = \varepsilon_\infty + \frac{\Delta\varepsilon}{1 + (i\omega\tau_{CC})^\alpha} \tag{2.16}$$

where α is a stretching parameter, which is in the range of 0 to 1. The value of α changes the broadness of the peak in ε'' symmetrically on a logarithmic frequency axis. The smaller the value of α is, the broader the peak is, as shown by the black dashed and dotted lines in the Figure 2.2. The Debye equation is obtained by setting α to 1. The β relaxation in ε'' is usually manifested as a symmetric peak.

If the dielectric loss peak is not symmetric, the Cole-Davidson equation is required to describe the relaxation peak:[127]

$$\varepsilon^*_{CD}(\omega) = \varepsilon_\infty + \frac{\Delta\varepsilon}{(1 + i\omega\tau_{CD})^\beta} \tag{2.17}$$

where β describes the asymmetric stretching of the high frequency flank of the loss peak as shown by the red dashed and dotted lines in the Figure 2.2. In the Debye and CC equations, the characteristic relaxation timescale is proportional to the reciprocal of the frequency at which ε'' reaches a maximum: $\tau = 1/2\pi\omega_p$. However, as is obvious from Figure 2.2 the peak position in the CD equation changes with the shape parameter β in the following way:

$$\omega_p = \frac{1}{\tau_{CD}}\tan(\frac{\pi}{2\beta + 2}) \tag{2.18}$$

To give more freedom to fit a peak with varying gradients of both the low and high frequency flanks, the Havriliak-Negami (HN) equation was proposed, which combines both stretching effects of the CC and CD equations:[128]

$$\varepsilon^*_{HN}(\omega) = \varepsilon_\infty + \frac{\Delta\varepsilon}{(1 + (i\omega\tau_{HN})^\alpha)^\beta} \tag{2.19}$$

Using the HN equation to fit a loss peak gives the gradients of α and $\alpha\beta$ at low and high frequency flanks in a log-log plot, respectively, as shown by the blue dashed and dotted lines in the Figure 2.2. In most cases, the HN equation can describe the loss peak well. In a similar manner to the CD equation, the peak position of the HN equation is related to both shape parameters, α and β , in the following way:[128, 129]

$$\omega_p = \frac{1}{\tau_{NH}}[\sin(\frac{\alpha\pi}{2\beta + 2})]^{1/\alpha}[\sin(\frac{\alpha\beta\pi}{2\beta + 2})]^{-1/\alpha} \tag{2.20}$$

2.1.4 The dielectric spectroscopy experimental set-up

The broadband dielectric spectrometer (BDS) used in this work consists of a frequency analyser (Novocontrol Alpha-N) connected separately to a standard sample cell (Novocontrol BDS 1200) was used to conduct all dielectric measurements in this study. To conduct a dielectric measurement, a sample is placed between two electrically conductive electrodes (see the schematic diagrams in Figure 2.3). A sinusoidally varying voltage, V, is applied these two electrodes. The material has a complex capacitance, C^*, which is a function of the area, A, the distance between the electrodes, d, and the complex dielectric permittivity of the material, ε^*:[117]

$$C^* = \frac{\varepsilon_0 \varepsilon^* A}{d}. \tag{2.21}$$

By applying a sinusoidal voltage:

$$V^* = V_0 e^{i\omega t}, \tag{2.22}$$

the spectrometer can measure the complex current, $I(\omega)$, which has a phase difference, $\phi(\omega)$, to the applied voltage:[117]

$$I^* = I_0 e^{i(\omega t + \phi(\omega))} \tag{2.23}$$

Based on Ohm's law, the complex impedance of the material is defined as $Z^* = V(\omega)/I(\omega)$, which also be expressed in terms of real and imaginary parts: $Z^* = Z' + jZ''$. Based on the complex impedance, the permittivities can be calculated:[115, 117, 130]

$$\varepsilon^* = \frac{1}{i\omega Z^*(\omega) C_0} \tag{2.24}$$

$$\varepsilon' = \frac{-Z''}{\omega C_0 (Z'^2 + Z''^2)} \tag{2.25}$$

$$\varepsilon'' = \frac{Z'}{\omega C_0 (Z'^2 + Z''^2)} \tag{2.26}$$

Thus, accurate measurements of ε requires high accuracy measurements of the complex impedance. By measuring ε^* at a series of frequencies, one can get a relationship between the frequency and the real, ε' , and imaginary, ε'', parts of ε^*. A plot of imaginary part against the frequency is most often used in analysis of dielectric results.

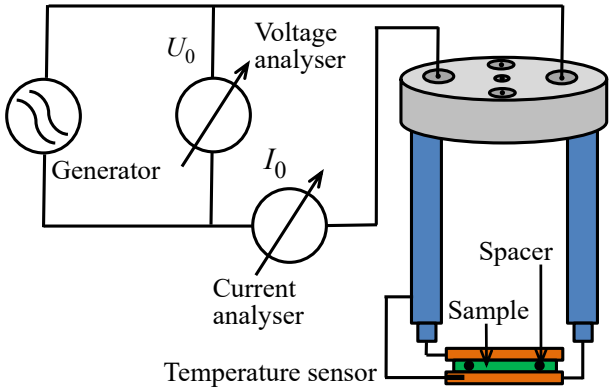

Figure 2.3: Schematic diagram showing the experimental setup of the dielectric spectroscopy measurement.

BDS is a useful to tool to measure ion conductivities for lithium ion batteries. The real part Z' of the complex impedance is called the resistance and is only attributed to a pure resistance R. The imaginary part Z'' is called the reactance and is only attributed to a pure capacitance C through $1/(j\omega C)$. An ion conducting material between two plate electrodes in a BDS measurement can be represented using the parallel circuit in Figure 2.4a. In the parallel circuit,[131]

$$\frac{1}{Z^*} = \frac{1}{Z_R} + \frac{1}{Z_C} = \frac{1}{R} + \omega C j = \frac{R}{1 + R\omega C j} \tag{2.27}$$

Thus, the real and imaginary parts of the complex impedance can be expressed as:

$$Z' = \frac{R}{1 + \omega^2 R^2 C^2} \tag{2.28}$$

$$Z'' = \frac{-\omega R^2 C}{1 + \omega^2 R^2 C^2} \tag{2.29}$$

The plot of $-Z''$ as a function of Z' gives a semi-circle (red line in Figure 2.4c), and Z^* can be represented by a vector which points to the edge of the semi-circle. At high frequency limit, $Z' = R$ which is the diameter of the semi-circle, and $Z'' = 0$. At high frequency limit, $Z^* = Z' = Z'' = 0$.

If the frequency of the signal applied to a material is low or the material contains charged species, ions with opposite charges can accumulate at the surface of each electrode, forming layers of ions which cause a capacitive effect, C_e. An equivalent

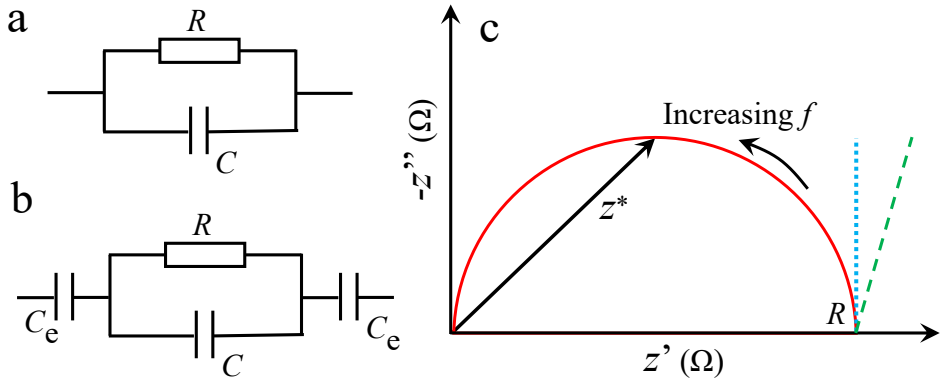

Figure 2.4: Schematic diagrams show the equivalent circuits for BDS measurements of ion conducting materials between two parallel plate electrodes (a) without and (b) with ions accumulate on the surfaces of electrodes. (c) Plot of $-Z''$ as a function of Z'.

circuit shown in Figure 2.4b can be used to describe this phenomenon.[132] In this circuit, the Z' and Z'' can be expressed as:

$$Z' = \frac{R}{1 + \omega^2 R^2 C^2} \tag{2.30}$$

$$Z'' = \frac{-\omega R^2 C}{1 + \omega^2 R^2 C^2} - \frac{2}{\omega C_e} \tag{2.31}$$

The capacitive effect from ion layers leads to a vertical line (dotted line in Figure 2.4c) in the plot of $-Z''$ against Z'. In reality, there are many other factors can affect the response from the ion layers. For example, if the surfaces of electrodes are not smooth, irregularly capacitive effects can change the slope of the vertical line,[131] as the dashed line in Figure 2.4c shows.

Complex impedance is also related to the ion conductivity σ^* of a material:

$$\sigma^* = \frac{d}{A}\frac{1}{Z^*} \tag{2.32}$$

where d and A are the distance between two electrodes and the area of the electrodes. Thus, the real σ' and imaginary σ'' parts of the complex ion conductivity σ^* can be expressed as:

$$\sigma' = \frac{d}{A}\frac{Z'}{Z'^2 + Z''^2} \tag{2.33}$$

$$\sigma'' = \frac{d}{A}\frac{-Z''}{Z'^2 + Z''^2} \tag{2.34}$$

2.1.5 Sample preparation

BDS can be used to measure samples both in liquid and solid states. In this work, the BDS measurements for all samples are performed using the two electrodes setup in Figure 2.5a. To prepare the solid samples, the bottom electrode was placed on a a hot stage at a temperature at least 80 K higher than the T_g of the particular sample. Thus depending on the sample, the temperature of the hot stage is different. Then, the sample was placed onto the bottom electrode. After the sample is melted, three silicon spacers each with a diameter of 100 μm were placed into the sample melt, and the top electrode was placed on the spacers. The diameters for the bottom and top electrodes are 30 and 20 mm, respectively. For liquid samples, a similar procedure was applied at the room temperature (without the hot stage). For polymeric electrolytes (see Chapter 5) which are viscous liquids, the gel cell in Figure 2.5b was used. First of all, the sample was placed into the cylindrical groove with 18 mm in diameter and 6.8 mm in thickness generated by the bottom electrode unit and the Teflon insulators, then the top electrode was placed onto the sample.

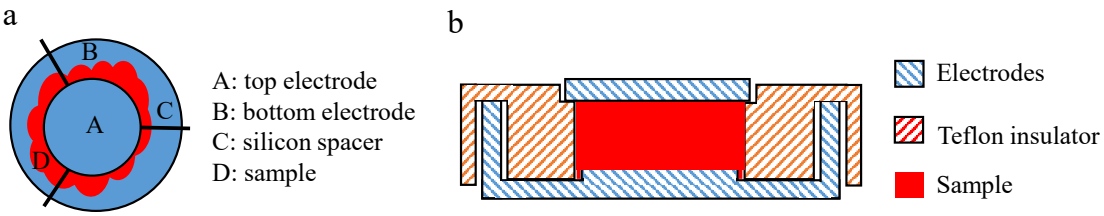

Figure 2.5: Schematic diagrams show samples between (a) two electrodes (from top view) separated by silicon spacers and (b) in a gel cell (from cross-section view) for BDS measurements.

2.1.6 Characteristics of a typical dielectric relaxation spectrum

A dielectric loss spectrum can contain several contributions in the frequency range of our spectrometer at a certain temperature.[117] Figure 2.6a shows the schematic diagram of a dielectric curve which contains several responses. With increasing frequency, an electrode polarisation (EP), ion conductivity σ and α relaxation are shown. As discussed above, a relaxation process usually shows a peak in the ε'' curve and a step feature in the ε' curve. In an ideal situation there should not be charged species

in a material, meaning that no ion conductivity signal should be detected. Unfortunately, in most cases a contribution from the ionic conductivity can be detected. The conductivity, σ_0, has the following contribution to ε^*:[117, 123]

$$\varepsilon^*_{\text{cond}}(\omega) = -i\frac{\sigma_0}{\varepsilon_0\omega} \tag{2.35}$$

The contribution from ion conductivity is only observed in dielectric loss curves ε'' and can be described by a power-law flank at low frequency. Thus in a plot on double logarithmic axes, it is manifested as a straight line and the slope of the line is the exponent of the power law. Sometimes, the sample contains charged mobile carriers, such as metal ions. Furthermore, the contribution to ε'' from the orientation of dipoles of the target molecules can be suppressed by the conductivity signal. Thus, samples with high ionic conductivity should be pre-cleaned before a dielectric measurement in order to remove these charged species.[130] As decreasing frequency, charged species in the material have enough time to move, and form ion layers on the surfaces of each electrode. This is the so-called electrode polarisation (EP). EP can result in very high values of ε' and ε'', which can mask other dielectric responses.

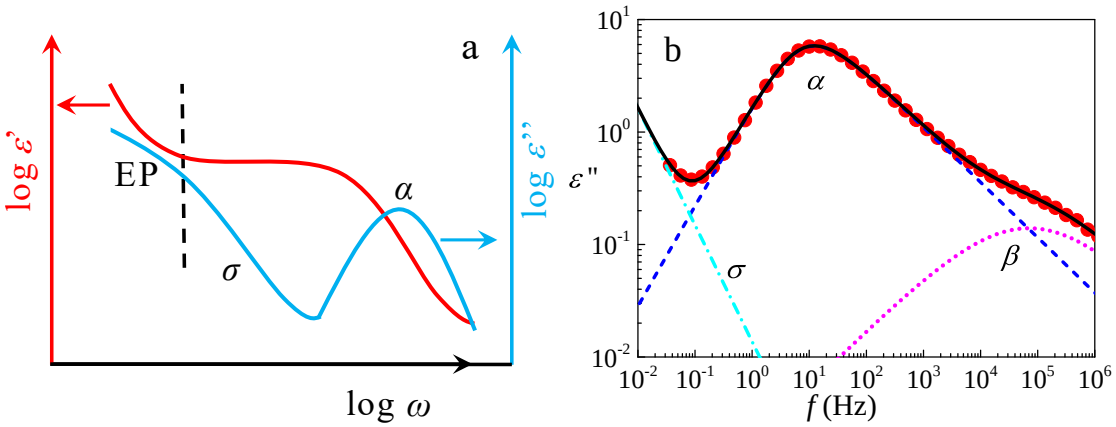

Figure 2.6: (a) Schematic diagram shows typical real ε' and imaginary ε'' parts of the complex permittivity, which contain contributions from electrode polarisation (EP), ion conductivity σ and a relaxation process (termed α relaxation as an example). (b) A typical ε'' curve for polytetrahydrofuran with molecular weight of 250 g/mol at 182 K, which contains contributions from ion conductivity σ, α and β relaxations, which are fitted using a power law, a HN equation and a Cole-Cole equation.

A summation over several expressions is used to describe the dielectric response containing several contributions. The fitting procedure was conducted using the Novocontrol WinFit software which uses non-linear curve fitting algorithms to minimize mean squared deviation (MSD) between the fits and the experimental results. Figure 2.6b shows a typical ε'' curve for polytetrahydrofuran with molecular weight of 250 g/mol at 182 K. As increasing frequency, several contributions from ion conductivity σ, α and β relaxations are observed, which are fitted using a power law (dot-dashed line), a HN equation (dashed line) and a Cole-Cole (dotted line) equation, respectively. The black solid line is the total fitted results (summation over each contribution) to the experimental data, and the solid line goes through all symbols which shows that the experimental data can be described well using this fitting procedure. Based on the number of contributions that are detected, the number of contributions used to fit the experimental data was adjusted. The specific fitting procedures used for different data sets are discussed in each chapter.

2.2 Rheometry

The term "rheology" comes from the Greek word "Rhei", meaning "to flow".[133] The effects of the rheological properties of matter are abundant in nature. A simple substance, water, for example, is a low viscosity liquid that flows easily, showing ideal viscous behaviour. On the other hand, steel is a solid at room temperature and can only be deformed upon the action of a large force, thus showing an ideal elastic behaviour for small deformations. In between these two limits, there are materials which show a mixture of viscous and elastic behaviour, termed viscoelastic.[134] Rheology is used to describe the deformation and flow properties of a material and rheometry is the technique used to measure its rheological properties. The macroscopic rheological properties of a material are the external representation of the internal nature of the material. Thus, the rheological properties of a material can give information on its microscopic structure and dynamics. In this chapter, rheological definitions, theory and experimental methods related to my work will be introduced, mainly following the books of Meger,[135] Ferry,[134] Larson[133] and Graessley.[136]

2.2.1 Definition of terms

Let us imagine, for simplicity, putting a soft material with a thickness, h, between two parallel plates. After applying a force, F on the top plate, as shown in Figure 2.7, the material will be deformed in the horizontal direction with a displacement, L. This is the two-plate model that is widely used to define rheological parameters.[135] The two plates are parallel to each other, and the lower plate is fixed to a hard support whereas the top plate can move parallel to the lower plate. Based on this geometry, one can define the shear stress λ, shear strain γ, shear rate $\dot{\gamma}$ and shear modulus G.[135]

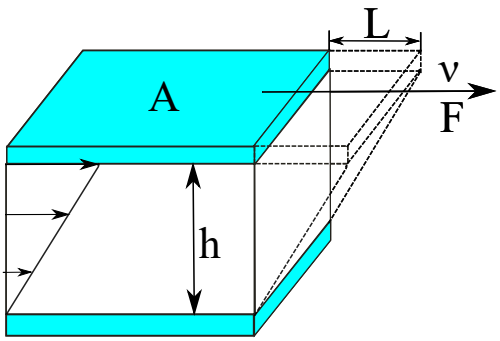

Figure 2.7: A typical two parallel plates model with a definition of the relevant parameters.

- Shear stress, $\lambda = F/A$, where F is the applied force to deform the material and A is the area of the top surface of the material. The shear stress has a unit of N/m^2 or Pascal (Pa).

- Shear strain, $\gamma = L/h$, where L is the displacement of the material under the applied force, and the h is the thickness of the material or the gap between two plates. The shear strain has a unit of 1 which means the deformation is dimensionless. In practice, it is usually expressed in percentage.

- Shear rate, $\dot{\gamma} = v/h$, where v is the velocity of the deformation, The shear rate has a unit of 1/s.

- Shear modulus, $G = \lambda/\gamma$, the shear modulus has a unit of Pa. This equation is also called 'Hooke's Law' for ideal elastic materials which shows that the force

is proportional to the deformation. The higher the value of G, the stiffer the material is.

2.2.2 Oscillatory test

In section 2.2.1, we have only considered the case in which a simple shear is applied to the material. However, in reality, an oscillatory shear is often used to study the rheological properties of a material. An illustrative diagram of this is shown in Figure 2.8. In this case, the bottom plate remains stationary. There is a stiff push rod connecting the top plate with a driving wheel. The driving wheel can rotate at certain speed and, simultaneously, the push rod can move the top plate back and forth, applying an oscillatory strain to the material. The force is measured at the bottom plate. The rotation of the driving wheel generates the time dependent functions $\lambda(t)$, $\gamma(t)$ and $\dot{\gamma}(t)$ within a complete oscillation cycle. During the rotation, when the driving wheel passes 0° and 180° the displacement of the top plate is zero. Therefore $\gamma = 0$ and $\lambda = 0$ and $\dot{\gamma}$ is at a maximum. When the driving wheel passes 90° and 270° the top plate has maximum displacement with the opposite direction. At these two positions, the strain is at a maximum and $\dot{\gamma} = 0$. The oscillatory strain is a sine wave as a function of time or angle. The response to the applied oscillatory strain, the stress λ , is dependent on the nature of the material.

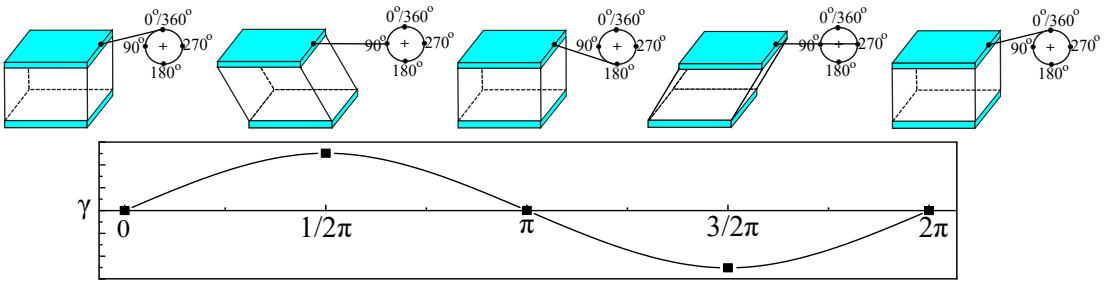

Figure 2.8: Schematic diagrams to illustrate the oscillatory shear test with a two plates model with a driving wheel linking by a stiff push rod. The top raw shows the displacements of the material at different angle positions (0°, 90°, 180°, 270° and 360°) of the driving wheel. The bottom figure shows the strain applied to the material by the rotation of the driving wheel is a sine wave as function of the time or the angle position.

For ideally elastic materials Hooke's law applies. There is no time lag between the applied strain wave and the resulting stress wave. In other words, there is no phase shift and thus the shift angle δ is zero $\delta = 0$. However, the shear rate function is shifted by 90° compared to the $\gamma(t)$ function and therefore the $\dot{\lambda}(t)$ function is a cosine wave. Moreover, the shear rate $\dot{\gamma}(t)$ is the time derivative of γ, $\dot{\gamma}(t) = d\gamma/dt$, which appears as a cosine wave. All waves are shown as the light green curves in the Figure 2.9. The rheological functions for ideally elastic materials can be expressed as following:

$$\gamma(t) = \gamma_A \sin(\omega t) \tag{2.36}$$

$$\lambda(t) = \lambda_A \sin(\omega t) \tag{2.37}$$

$$\dot{\gamma}(t) = \mathrm{d}\gamma/\mathrm{d}t = \gamma_A \omega \cos(\omega t) \tag{2.38}$$

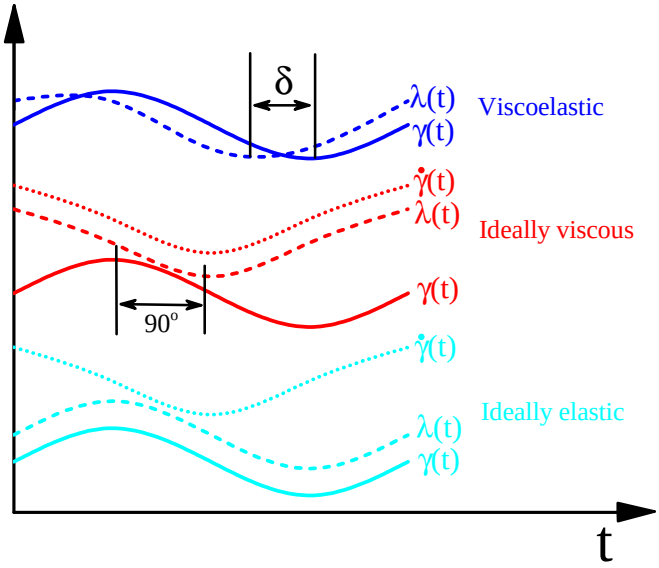

Figure 2.9: Time dependent functions of $\gamma(t)$, $\lambda(t)$ and $\dot{\lambda}(t)$ for ideally elastic, ideally viscous and viscoelastic materials.

For ideally viscous materials, Newton's law applies:[136]

$$\lambda = \eta \dot{\gamma}(t) \tag{2.39}$$

where η is the viscosity which characterises the resistance of the sample to flow. The viscosity is a constant within a certain shear rate range and is an inherent property of

the material under these conditions.[133] Thus the $\lambda(t)$ wave and $\dot{\gamma}(t)$ are in phase with each other, in other words, both are cosine waves.[135] However, there is a phase shift, $\delta = 90°$, between the $\lambda(t)$ wave and the $\gamma(t)$ wave, as the red curves show in the Figure 2.9.

Materials showing a rheological response between the ideal elastic and ideal viscous behaviour are termed viscoelastic. In this case, the response of the material to the applied sine strain wave is neither a sine wave or a cosine wave. There is a phase shift δ ($0° < \delta < 90°$) between the applied strain $\gamma(t)$ and the response $\lambda(t)$:[134]

$$\lambda(t) = \lambda_A \sin(\omega t + \delta), 0° < \delta < 90° \tag{2.40}$$

For fluid materials which show viscoelastic properties, such as liquid shampoo and body cleaner, the phase shift is between 45° and 90°. These materials are fluid at rest and have no dimensional stability. In viscoelastic solid materials, such as tire rubber and hand cream, the phase shift is between 0° and 45°. These materials are solid at rest and can maintain their shapes. [135]

The parameters above can also be expressed using complex numbers:

$$\gamma^* = \gamma_0 e^{i\omega t} \tag{2.41}$$

$$\lambda^* = \lambda_0 e^{i(\omega t+\delta)} \tag{2.42}$$

Thus, the complex modulus, G^*, can be expressed as:

$$G^* = \frac{\lambda^*}{\gamma^*} = \frac{\lambda_0}{\gamma_0} e^{i\delta} = G' + iG'' \tag{2.43}$$

Where G' and G'' are the storage modulus and loss modulus. Based on the Euler's formula, $e^{i\delta} = \cos(\delta) + i\sin(\delta)$, one thus obtains:

$$G^* = \frac{\lambda_0}{\gamma_0} e^{i\delta} = \frac{\lambda_0}{\gamma_0}(\cos(\delta) + i\sin(\delta)) = G' + iG'' \tag{2.44}$$

Thus, G' and G'' can be expressed as:

$$G' = \frac{\lambda_0 \cos\delta}{\gamma_0} \tag{2.45}$$

$$G'' = \frac{\lambda_0 \sin\delta}{\gamma_0} \tag{2.46}$$

The complex modulus describes the viscoelastic properties of a material, containing both elastic and viscous components. Mathematically, the complex modulus is a vector which can be projected onto the x and y axes with an angle δ.[134] The projection onto the x axis is called the storage modulus, G', which represents the elastic portion of the viscoelastic properties, whereas the projection onto the y axis is called the loss modulus, G'', which represents the viscous portion of the viscoelastic properties, as shown in the Figure 2.10. G' is a measure of the energy stored in the sample by extending or stretching the internal structures during deformation. Once the load is removed, the stored energy acts as the driving force to reform the material to its original shape. A material which can store deformation energy completely shows reversible deformation behaviour.[134] G'' is a measure of the deformation energy which is lost by the material during deformation. Viscous flow always involves the relative motion of internal components such as molecules, clusters or particles. The friction between these components produces frictional heat which may either heat up the sample or be exchanged with the environment. As a consequence, the energy is dissipated.[134] A material which loses its deformation energy completely during the deformation process shows irreversible deformation behaviour. Based on Pythagoras' theorem, the relationship between the complex modulus, storage modulus and loss modulus can be expressed as the following:[134]

$$G^{*2} = G'^2 + G''^2 \tag{2.47}$$

and the loss factor or damping factor is defined as:

$$\tan(\delta) = G''/G' \tag{2.48}$$

The loss factor indicates the ratio between the viscous and elastic components of a viscoelastic material.

Similar to the geometry in Figure 2.10, one can also define the complex viscosity η^* based on Newton's laws, and its real, η', and imaginary, η'', parts as follows:[134]

$$\eta^* = \lambda^*/\dot{\gamma}^* \tag{2.49}$$

The complex viscosity has an unit of Pa·s. The relationship between the components can be expressed as:

$$\eta^{*2} = \eta'^2 + \eta''^2 \tag{2.50}$$

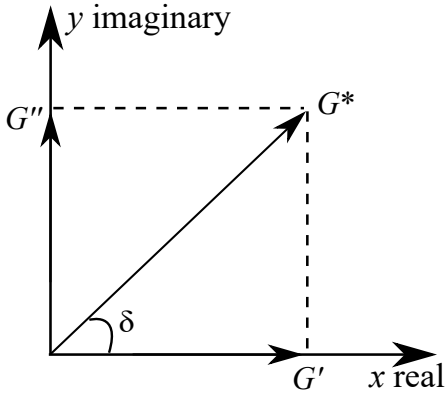

Figure 2.10: Vector diagram illustrating the relationship between the complex modulus G^*, the storage modulus G', the loss modulus G'' and the phase angle δ with $G^{*2} = G'^2 + G''^2$ and $\tan(\delta) = G''/G'$.

$$\tan(\delta) = \eta'/\eta'' \tag{2.51}$$

η' represents the viscous portion and η'' represents the elastic portion of the complex viscosity. The relationship between complex modulus G^* and complex viscosity η^* can be expressed as:

$$|G^*| = \omega|\eta^*| \tag{2.52}$$

$$\eta' = G''/\omega \tag{2.53}$$

$$\eta'' = G'/\omega \tag{2.54}$$

2.2.3 Amplitude sweep

Amplitude sweep measurements are performed to determine the deformation range of a material i.e. the range over which a material can be linearly deformed without being destroyed. This is important in practice, because most of our measurements are required to be performed in the linear region (non-destructive range). Thus it is better to do amplitude sweeps to determine the range of the linear region before doing any other measurements.[135] There are two ways to do the amplitude sweep measurements: a strain sweep or a stress sweep. In my work, a strain sweep has been used. In a strain sweep, a gradually increasing strain is applied to a material during an oscillatory measurement (Figure 2.11a), and the loss and storage moduli are measured and plotted as a function of strain (Figure 2.11b). The linear viscoelastic (LVE) region region indicates

the strain range within which a strain is applied without a change of the rheological response as characterised e.g. by the moduli. This behaviour typically means that the applied deformation does not lead to any destruction of the internal structures of the material. This region is indicated by the plateau in Figure 2.11b. As the strain increases further, exceeding the LVE region, the moduli start to decrease, which is often related to the internal material structures changing, and the material starts to flow, or the material breaks in a brittle way. In general, one should perform amplitude sweep measurements to determine the LVE region when examining an unknown material.

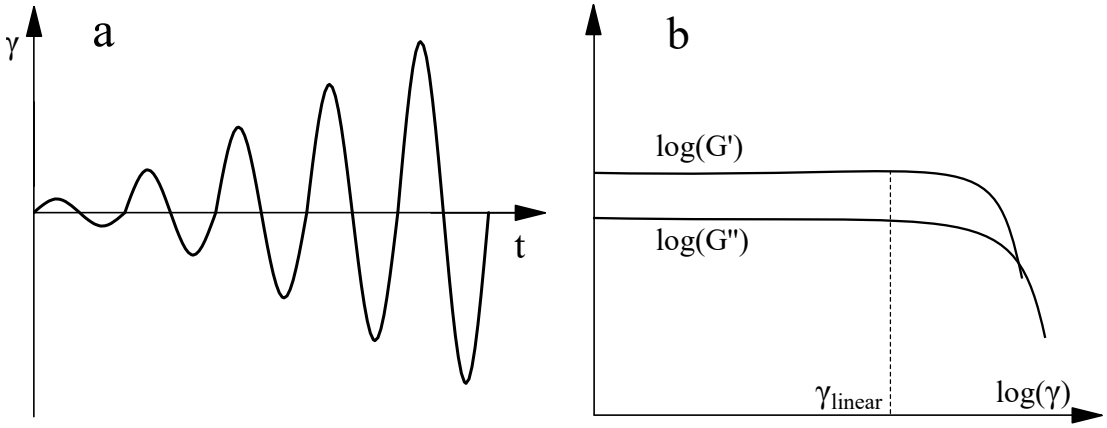

Figure 2.11: (a) oscillatory strain increases as function of time and (b) a typical strain sweep result as a function of strain.

2.2.4 Frequency sweep

Frequency sweep measurements can be used to test the time dependent properties of a material in the non-destructive range, i.e. LVE region, because time is the reciprocal of frequency. Low frequencies correspond to slow motions or long timescale behaviour, whereas high frequencies correspond to fast motions or short timescale behaviour.[136] The frequency sweep experiment provides information on the internal structure and the long term stability of a material.

In a frequency sweep with controlled strain, the amplitude of the applied strain is a constant but the frequency varies with time: $\gamma(t) = \gamma_A \sin(\omega t)$, with γ_A = constant and $\omega = \omega(t)$, as shown in Figure 2.12a. Here one has to bear in mind that the applied strain has to be in the LVE range and therefore pre-measurement amplitude sweeps

have to be conducted to determine the LVE range. The shear rate can be calculated, $\dot{\gamma} = \gamma_A \omega$.

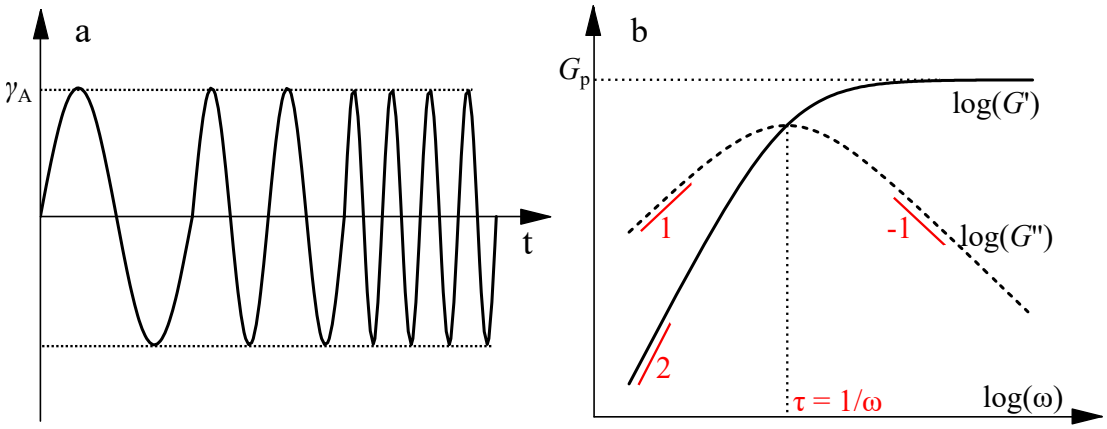

Figure 2.12: (a) Controlled strain wave with varying frequency and a constant strain amplitude in a frequency sweep experiment, and (b) typical G' and G'' curves as a function of frequency for an ideal polymer melt or solution in a log-log plot.

Figure 2.12b shows typical G' and G'' curves as a function of frequency for an ideal polymer melt or solution. As frequency increases, G' first increases with a power law exponent of 2 and then reaches a plateau, G_p. Simultaneously, G'' first increases with a power law exponent of 1. After reaching a maximum value, usually half of the plateau value in the G' curve, G'' starts to decrease as the frequency increases with a power law exponent of -1. One can explain the frequency (time) dependent behaviour by considering energy conservation.[134] Increasing frequency is equivalent to probing faster motion. The polymer chains or temporary networks due to entanglement become increasing inflexible and rigid. In this case, more energy can be stored in the polymer to extend or stretch the chain structure. Moreover, the relative motion between chains becomes less and less, which means less energy is lost due to frictional heat between chains. As a consequence, G' increases and G'' decreases as a function of increasing frequency.[136] When $G' > G''$, elastic behaviour is dominant over viscous behaviour. On the other hand, decreasing frequency is equivalent to probing slower motions. The polymer chains or the temporary networks become increasingly flexible and soft. Thus the flipping between polymer chains or unentanglement becomes more likely to happen, meaning more energy is lost through friction. Thus, viscous behaviour becomes

dominant over elastic behaviour, with $G'' > G'$.[136]

This idealized and simplified case for polymer melt or solution can be predicted by a single Maxwell model,[134, 136] which is combination of an elastic spring and a viscous dashpot connected in series. The spring and the dashpot simulate elastic behaviour and viscous behaviour,respectively. In the Maxwell model, the frequency or time dependence of G' and G'' can be expressed as follows:

$$G'(\omega) = G_p \frac{\omega^2\tau^2}{1+\omega^2\tau^2} \tag{2.55}$$

$$G''(\omega) = G_p \frac{\omega\tau}{1+\omega^2\tau^2} \tag{2.56}$$

where G_p is the plate modulus and the τ is the relaxation time. From these two equations, one observes that, at low frequency, $\omega \to 0$ and the development of G' can be described by a power law with an exponent of 2 because G' is proportional to the ω^2. G'' can be described by a power law with an exponent of 1 because G'' is proportional to ω. At high frequency, $\omega \to \infty$, the behaviour of G'' is well described by a power law with an exponent of -1 because G'' is proportional to ω^{-1}, and G' reaches a plateau, G_p.[134, 136] Since $\lim_{\omega\to 0} = 0$ and $\lim_{\omega\to\infty} = G_p$, Maxwell fluids act as flexible liquids at low frequency (long timescale) but as rigid solids at high frequency (short timescale). The parameter, G_p reflect the rigidity of the material.[135] At the point where $G' = G''$, requiring $\omega\tau = 1$, G'' reaches its maximum value, $G''_{max} = G_p/2$. Moreover, at the crossover point, the elastic and viscous behaviours are balanced, and the frequency at this point is related to the characteristic relaxation time of the material, $\tau = 1/\omega$.[136]

2.2.5 Time Temperature Superposition (TTS)

In the previous section, the time dependent behaviour of a material was discussed. This is of particular importance in practice, as knowledge of the long term performance of a material is valuable and the frequency sweep provides a method to evaluate it. However, in reality, a rheometer can only probe a limited frequency range, from $\sim 10^{-3}$ rad/s to a few hundreds of rad/s.[135] Time temperature superposition (TTS) is a method used to determine the temperature dependent behaviour of a viscoelastic material over a wide frequency range by shifting measured data at varying temperatures

to a reference temperature.[52] The assumption behind TTS is that frequency, time or temperature have a comparable effect on the rheological behaviour of a material. For example, for a typical polymer melt, both heating the sample and shearing at a slow rate can decrease the value of G'.

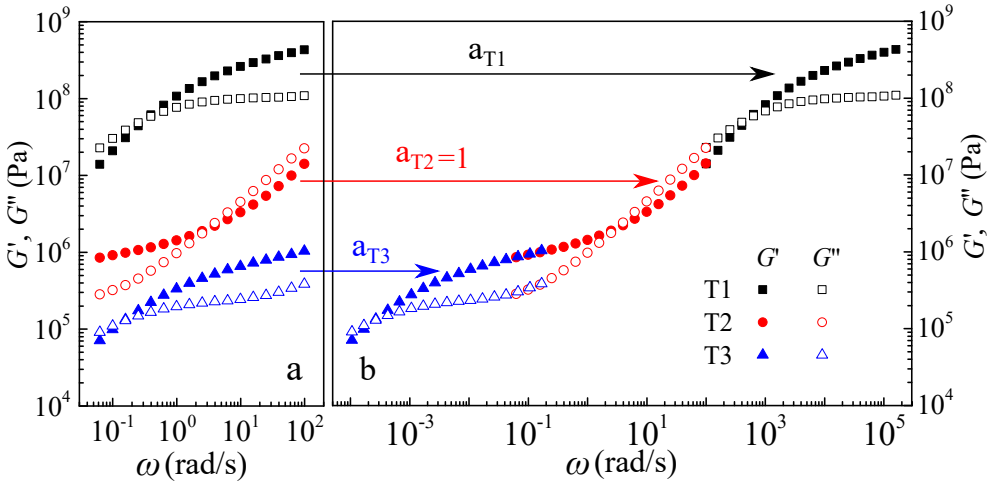

Figure 2.13: (a) Frequency sweeps at three different temperatures (T1, T2 and T3)) for an entangled polymer in the frequency range of 0.62 to 125.6 rad/s. (b) horizontally shift T1 and T3 curves to T2 with shift factor of a_{T1} and a_{T3} to build a master curve.

To construct a so-called master curve, several frequency sweep measurements at different temperatures are conducted. Each spectra contains G', G'', G^* or η^* data as a function of frequency. The resulting curves are shifted in frequency to a selected reference temperature measurement through multiplication by a shift factor, a_T. This process results in a single curve showing frequency dependent behaviour over a wide frequency range.[52] Figure 2.13 shows an example for an entangled polymer at three different temperatures (T1, T2 and T3). G' and G'' measured at T1 and T3 are shifted to the curve measured at T2 with shift factors of a_{T1}, $a_{T1} > 1$, and a_{T3}, $a_{T3} < 1$, and a new curve, covering around 10 decades in frequency, is obtained. Such a master curve allows for the prediction of the deformation behaviour of a material over much longer or shorter timescales than would be possible over the timescale of an experiment. As discussed previously, increasing temperature results in a shorter relaxation timescale τ. Thus, the shift factor between two temperatures can be expressed as:

$$a_T = \tau(T)/\tau(T_{\text{ref}}) \tag{2.57}$$

This equation also involves the viscosity of ideal viscous liquid: $a_T = \eta(T)/\eta(T_{ref})$. a_T parameters as a function of temperature can be described by the empirical Williams-Landel-Ferry (WLF) equation:[134]

$$a_T = \exp\left(\frac{-C_1(T - T_{\text{ref}})}{C_2 + (T - T_{\text{ref}})}\right) \tag{2.58}$$

where C_1 and C_2 are coefficients related to specific materials. In some circumstances, the Arrhenius equation can also be used depending on the nature of the material:

$$a_T = A\exp\left(\frac{-E_a}{RT}\right) \tag{2.59}$$

where A is a pre-factor and E_a and R are the activation energy and universal gas constant respectively. Occasionally it is also necessary to correct the curves in the y-direction using vertical shift factors, b_T:

$$b_T = \frac{\rho_{\text{ref}} T_{\text{ref}}}{\rho T} \tag{2.60}$$

where ρ is the density of the material at different temperatures. However, in some cases the temperature dependent densities for many polymers are not available, thus one can choose to use only horizontal shift factors. The Van-Gurp-Palmen (VGP) plot[137, 138], i.e.loss tangent $\tan(\delta)$ vs the complex modulus G^*, can be used to investigate the accuracy of this approach, which removes all explicit time-dependence from the data, and indicates whether an accurate frequency-shift TTS is possible or not.

The application of TTS is conditional on the fact that the material should be "thermorheologically simple", meaning all relaxation processes of a polymer including segmental relaxations and chain modes follow the same temperature dependence.[139] In general, many polymers without cross-links or filled nanoparticles in both melts or solutions meet this criteria. Contrary to thermal-rheological simple materials, thermal-rheological complex materials show structural modifications as a function of temperature. These modifications include assembly or disassembly of superstructures, temperature responsive interactions, gelation and cross-linking reactions. TTS usually is not applicable to these materials.[140–144]

Figure 2.14 shows a typical master curve of G^* as a function of frequency, ω, for an entangled amorphous polymer. At high frequency, $\omega > \omega_3$ (short timescale or low temperature), the complex modulus reaches a maximum value and becomes independent

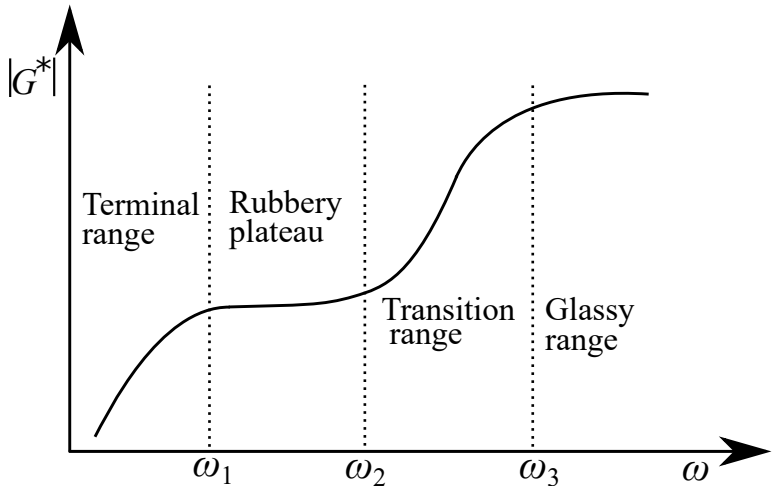

Figure 2.14: A typical mechanical behaviour of an entangled polymer as a function of frequency.

to further increases of frequency. Motion between polymer chains is limited because at such high frequencies almost all parts of the polymer are immobilized.[117] In this "frozen state"', the chain motion is far slower than the applied oscillatory strain, thus only a small amount of the energy is consumed by the chain friction and most of the energy is stored. The sample behaves like a stiff solid and is said to have entered the glassy state.[135] In the transition range $\omega_2 < \omega < \omega_3$, the chain segments have enough time to relax, thus G^* starts to decrease rapidly with decreasing frequency. After this transition region, there is a rubber plateau where G^* is more or less constant but with a much smaller value of G^* than in the glassy state. In this frequency range $\omega_1 < \omega < \omega_2$, the relative chain-glide between polymer chains is no longer possible and thus entanglements act as physical cross-linking points and form a temporary network.[134] The polymer still shows the behaviour of a viscoelastic solid. As the frequency decreases further to the so-called terminal range, $\omega < \omega_1$, the whole chain can relax and flow over the probed timescale. In this frequency range, the frequency dependent behaviour can be described by the Maxwell model and the polymer shows the behaviour of a viscoelastic liquid.[134]

2.2.6 Relaxation and creep experiments

Relaxation and creep experiments can be used to test the viscoelastic behaviour of a material. In a stress relaxation experiment, a step strain is applied to the material and the strain remains constant. The response of the corresponding stress as a function of time, $\lambda(t)$, is recorded. In practice, before the real test, a small pre-strain is usually applied to the material in order to eliminate the effect of pre-stress in the material and to improve the reproducibility of the experimental data. The relaxation time for the pre-strain, γ_1 , should be long enough so that the stress from the pre-strain, λ_1, is negligible before the experiment is started.[135] Figure 2.15 (left) shows typical stress curves as a function of time for an ideal viscous liquid (1), ideal elastic solid (2), viscoelastic solid (3) and viscoelastic liquid (4).[135] After the pre-strain step, t_1, a relatively large step strain, γ_2, produces a stress, λ_2 , to the test material. γ_2 remains constant for the remaining experiment time ($t > t_1$). Here one should note that γ_2 should be in the linear viscoelastic range. After this, the developing stress as a function of time is recorded. For an ideal viscous liquid, e.g. water, there is no resisting force once the applied strain stops and so the stress relaxes quickly to zero, as shown by the red line in the Figure 2.15 (left). On the contrary, the stress for an ideal elastic material remains constant once the step strain is constant. The rigid internal structure of an elastic material is unable to lose any stress thus the no stress relaxation happens, as shown by the green line in the figure. The response for viscoelastic materials lies in between these two extreme cases. The response stress starts to relax after the applied step strain stops but the relaxation speed is much slower than that for an ideal viscous liquid. For viscoelastic solids (dashed blue line), the stress can only relax to a certain extent even after a relatively long timescale. $\lambda(t)$ reaches the equilibrium stress λ_e. This means that the molecules are not free to move and this is usually attributed to the chemical or physical cross-links inside the material.[133] The material behaves like a gel and a cross-linked rubber. For viscoelastic liquids (solid blue line), the response can eventually relax to zero. This behaviour is typical for a polymer melt or a concentrated polymer solution.

After applying the step strain, the polymer chains have initially not had enough time to rearrange themselves to adapt to the strain. Thus an internal stress is induced in the polymer. After the applied step strain stops, the polymer chains tend to return

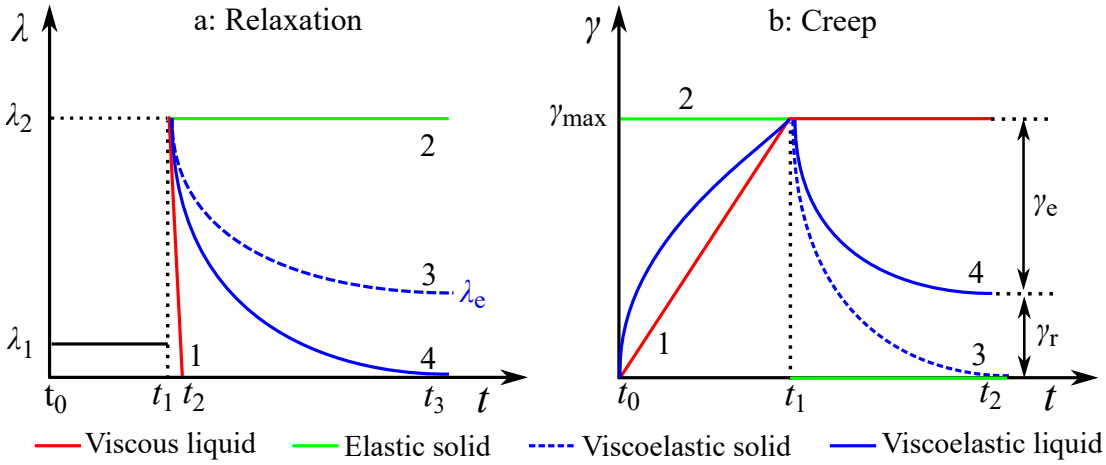

Figure 2.15: Typical stress curves (a) as a function of time in a stress relaxation experiment and strain curves (b) as a function of time in a creep experiment for ideal viscous liquid (1), ideal elastic solid (2), viscoelastic solid (3) and viscoelastic liquid (4).

to their original state (a stress free state) through slow motion of the chains. As a consequence, the internal stress is relaxed gradually and the relaxation occurs with delayed timescales.[134] For non-cross-linked polymers, the internal stress can be relaxed completely if the time is sufficiently long because disentanglement can happen due to slow chain diffusion. For partly chemical or physical cross-linked networks, the extent of the relaxation depends on the viscous component of the material. For fully cross-linked networks, no relaxation can occur and the material behaves like a ideal elastic material.[135]

Since the relaxation time is related to the molecular size, stress relaxation curves $\lambda(t)$ can be used to obtain information about the internal structure. For example, a faster relaxation will have steeper damping at relatively short relaxation times in the $\lambda(t)$ curve, indicating a greater fraction of small molecules in the material.[135] A $\lambda(t)$ curve with a wider relaxation distribution indicates a wider molecular weight distribution. The stress value at relative long times indicates the overall molecular weight. The larger the value, the longer the relaxation timescale and thus the higher the overall molecular weight.[135]

In a creep experiment, a stress, λ_1 , is applied to a material in the time interval t_0 to t_1. The developing strain as a function of time $\gamma(t)$ due to the step stress is recorded.[134, 135] Here one has to note that the linear viscoelastic range should not

be be exceeded. For an ideal viscous liquid, after applying the step stress, a gradual continuous deformation occurs, reaching a maximum value, γ_{max}, at time t_1. After t_1, the applied stress is removed. The material cannot return to its original shape because the deformation is non-reversible.[135] There is no energy stored in the viscous liquid during the deformation process and as a result the material does not demonstrate elastic behaviour. Thus, $\gamma(t)$ becomes constant with respect to t as shown by the red line in the Figure 2.15 (right). For an ideal elastic solid (green lines), a step stress results in a step strain, and after removing the stress, the strain immediately goes to zero. The whole deformation energy is stored during the deformation process for an elastic material, allowing the material return to its original shape once the loading is removed.[134] A viscoelastic material shows both elastic and viscous deformation. The elastic deformation occurs immediately after the stress is applied but the viscous deformation is delayed. After removing the stress load, the deformation can be recovered partially or completely depending on the internal structure of the material. Both the development and recovery $\gamma(t)$ curves show an exponential functional shape.[134] For viscoelastic solids (dashed blue line), the deformation can be fully recovered if the test time is sufficiently long. Cross-linked materials such as gels and rubbers display this behaviour.[134] For a viscoelastic liquid (solid blue lines), it is possible for the deformation to be recovered but it is also possible that the stress can reach an equilibrium value even after very long timescales. This is termed γ_e. The stress caused by partial deformations will remain permanently and is termed γ_r. The stresses γ_e and γ_r indicate the elastic and viscous portion of the viscoelastic behaviour, respectively. During deformation recovery, part of the energy is stored in the material whereas the other is consumed by chain friction. Therefore, the deformation for a viscoelastic liquid is not completely reversible.[134]

Both the $\lambda(t)$ and $\gamma(t)$ data can be converted to storage, G', and loss, G'' , moduli through the integration of the $G(t)$ and $J(t)$ curves. In this work, stress relaxation experiments have been conducted and the data were converted to G' and G'' using the following equation:

$$G^* = i\omega \int_0^\infty e^{i\omega t} G(t) dt \tag{2.61}$$

The real and imaginary parts of G^* represent the storage and loss moduli of the test material. There are several rheology analysis softwares which enable this conversion to

be done. We chose the open access software, *iRheo*, developed by Manlio Tassieri from the University of Glasgow UK.[145] The choice to use *iRheo* was made because this software uses an over sampling technique in order to make the conversion. Usually, the data at the beginning of a test are discarded due the limitation of the data acquisition rates of the rheometer. However, in the *iRheo* software, data points are numerically interpolated between the original data points using a standard non-overshooting cubic spline, generating a new data set which can then be used to calculate the G' and G'' curves. Thus, *iRheo* can extend the frequency range of G' and G'' curves from a single stress relaxation experiment, taking the data recorded at very short timescales into account.

2.2.7 Rotational experiments

Rotational experiments are usually used to test the flow properties of various fluids. Rotational tests can be performed by control of either the shear stress or the shear rate. In the former case, the shear stress or torque is controlled by the rheometer whereas in the later case the rotation speed, the shear rate, $\dot{\gamma}$, is controlled by the rheometer. In both cases, the flow behaviour of the material in response to the applied shear stress or the shear rate is recorded.[135] Figure 2.16 shows three typical flow curves as a function of shear rate $\dot{\gamma}$, which show ideal viscous, shear thinning and shear thickening characteristics.

For an ideal viscous liquid, the stress increases linearly with the applied shear rate and the viscosity, defined as $\eta = \lambda/\dot{\gamma}$, is a constant with varying shear rate. This behaviour is shown by the blue line in the figure. Examples of materials showing ideal viscous behaviour include water and cooking oil. Contrary to this, many materials have shear rate dependent viscosities and the flow curves of these materials either decrease or increase with the increasing shear rate.

For shear thinning materials, the increase of the shear stress is slower than the increase of the shear rate. Thus the viscosity, i.e. the ratio of the shear stress to the shear rate, decreases as the shear rate increases, as shown by the red dashed lines in the Figure 2.16. Most polymer melts or polymer solutions show ideal viscous behaviour at low shear rates but demonstrate shear thinning behaviour at high shear rates.[135] When shear is applied to a polymer material, the polymer coils can deform in the

direction of the applied force. Thus the polymers show signs of orientation and can disentangle to a certain extent, resulting in the reduction of the flow resistance, i.e. the viscosity. If the shear rate is sufficiently high, all chains become disentangled and the viscosity is therefore independent of the shear rate. The viscosity at low shear rate is a constant and is called the zero-shear viscosity, η_0. In the shear thinning region, the viscosity is a function of the shear rate $\eta = f(\dot{\gamma})$. The viscosity in the second plateau region is called the infinite-shear viscosity η_∞.

Finally, some materials show shear thickening behaviour. In this case, both the shear stress and viscosity increase sharply as the the shear rate increases. Examples of materials which demonstrate shear thickening behaviour are starch dispersions, ceramic suspensions and filled elastomers.[135]

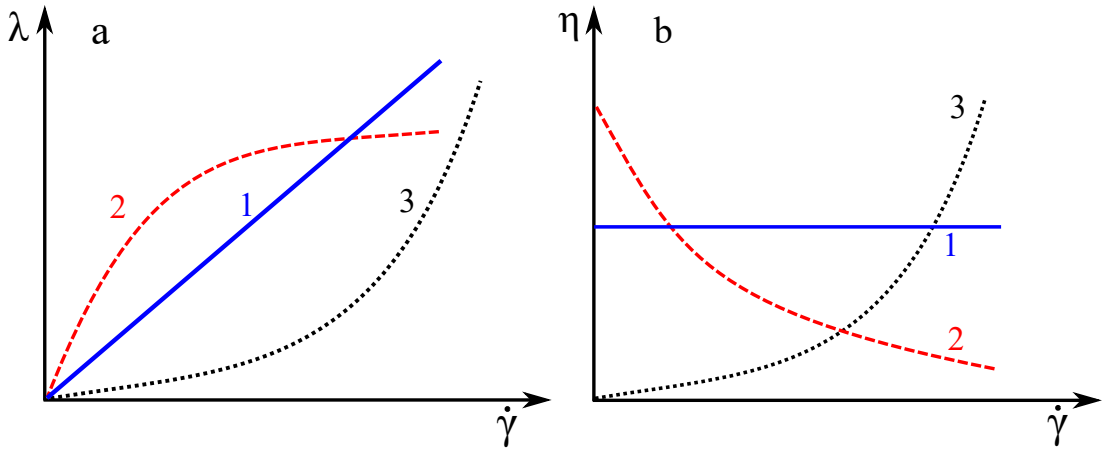

Figure 2.16: Shear stress and viscosity for materials showing ideal viscous (1), shear thinning (2) and shear thickening behaviours.

2.2.8 Extensional Rheology

Extensional rheology involves measurement of the response of a material under uniaxial extension.[135] Figure 2.17 shows the deformation of a material during an extensional rheological measurement. The sample is placed between two circular plates. The bottom plate is stationary during the measurement whereas the top plate moves upwards at certain speed so that the material between two plates undergoes uniaxial

extension. The mid-plate diameter of the sample at the initial state is D_0. After time t, it decreases exponentially to $D(t)$.[146, 147] Thus, the strain rate, $\dot{\varepsilon}$, can be defined:

$$\dot{\varepsilon} = -\frac{2}{R}\frac{dR}{dt} \tag{2.62}$$

where R is the mid-plate radius i.e. $R = D/2$. The Hencky strain, ε_H, is defined as:

$$\varepsilon_H(t) = -2\ln\frac{R(t)}{R_0} \tag{2.63}$$

where R_0 and $R(t)$ are the radii of the sample at $t = 0$ and at time t. The transient stress growth coefficient, η_E^+ , is a function of time at a fixed Hencky strain rate, which can be expressed:

$$\eta_E^+ = \frac{F(t)/(\pi R(t)^2)}{\dot{\varepsilon}} \tag{2.64}$$

where $F(t)$ and $R(t)$ are the transient force and transient radius of the sample at time t. At low strain rates, the extensional viscosity is three times that of the transient shear viscosity (the Trouton ratio)[136] and the corresponding curve is termed the stress growth curve. However, at high extensional rates, the increase of the viscosity can follow the stress growth curve, due to the orientation and stretching of polymer chains. This phenomenon is known as strain hardening.[135] An example of this is shown in Chapter 5.

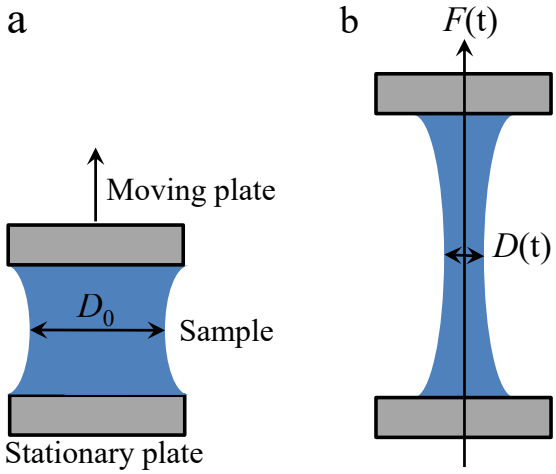

Figure 2.17: Schematic diagram shows the deformation of the material during an extensional rheological measurement (a) at initial state and (b) at time t

Extensional rheological measurements were conducted using a filament stretch rheometer (FSR) at Denmark Technical University.[148] The FSR is equipped with a sensor at bottom to measure the force and a laser at side to measure the diameter of the sample. The FSR is also equipped with an oven capable of controlling temperature from 15 °C to 350 °C with accuracy of ±0.2 °C.

2.2.9 Rheometers

Two types of rheometers are used in this work: a stress controlled rheometer (MCR 302, Anton Paar) and a strain controlled rheometer, (ARES G1, TA instrument). In a strain controlled rheometer (left hand side of Figure 2.18), the displacement or the strain is controlled by a motor connected to the bottom plate. The transducer connected to the top plate measures the torque or stress applied to the material by the motor.[135] In a stress controlled rheometer (right hand side of Figure 2.18), the bottom plate is fixed and the displacement sensor and the motor are combined together. The displacement and the torque are measured.[135] Knowledge of the measurement geometry, such as the diameter of the plates and the gap between two plates, allows for several rheological parameters to be calculated according to the definitions in the section 2.2.1.

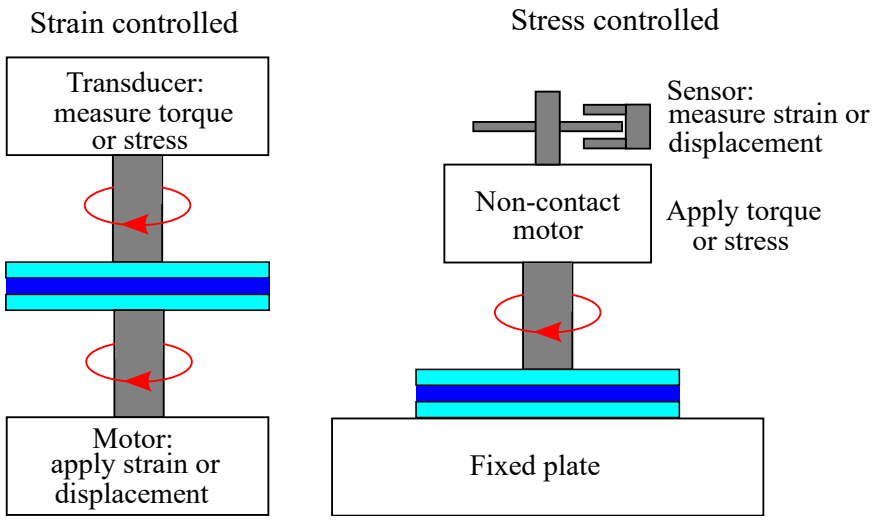

Figure 2.18: Schematic diagrams for strain controlled (left) and stress (right) controlled rheometers.

2.3 Calorimetry

In this section, the theoretical and experimental aspects of the calorimetric methods used to characterize the dynamics of the glass transition will be explained. These calorimetric methods include differential Scanning calorimetry (DSC), temperature modulated DSC (MDSC) and rate dependent DSC (RDSC). This section mainly follows books and review articles by Hohne,[149] Freire,[150] Gill,[151] Wunderlich[152] and Simon.[153]

2.3.1 Differential Scanning calorimetry

Differential scanning calorimetry (DSC) is a technique used to measure the difference in heat flow between a sample and a reference as a function of temperature.[149, 150] There are two types of DSC instruments which use different methods in order to determine the heat flow. Power compensation DSC[149, 150] involves placing a sample and a reference into two separate furnaces and then monitoring the temperature difference, ΔT, between the sample and the reference. To satisfy the condition that $\Delta T = 0$ during a thermodynamic transition, different electrical powers are supplied to the heaters of the sample and reference furnaces. The heat flow of the sample is then calculated from the difference in the supplied electrical power. Heat-flux DSC involves placing a sample and a reference into the same furnace with ΔT being measured directly and then used to calculate the heat flow through the sample. All DSC measurements in this work were performed on a TA Instruments Q2000, which is an example of a heat-flux DSC.

In a classical DSC measurement, the temperature is set to increase or decrease linearly with time, and the heat flow, q, as a function of temperature is recorded. The heat flow is the rate of change of the enthalpy, H:[150]

$$q = \frac{dH}{dt} \tag{2.65}$$

The heat capacity, C_p , is related to the change of enthalpy as a function of temperature:[149]

$$C_p = \frac{dH}{dT} \tag{2.66}$$

Thus, experimentally, C_p can be obtained by dividing the heat flow by the heating or cooling rate, $Q = dT/dt$:[149]

$$C_p = \frac{q}{Q} \tag{2.67}$$

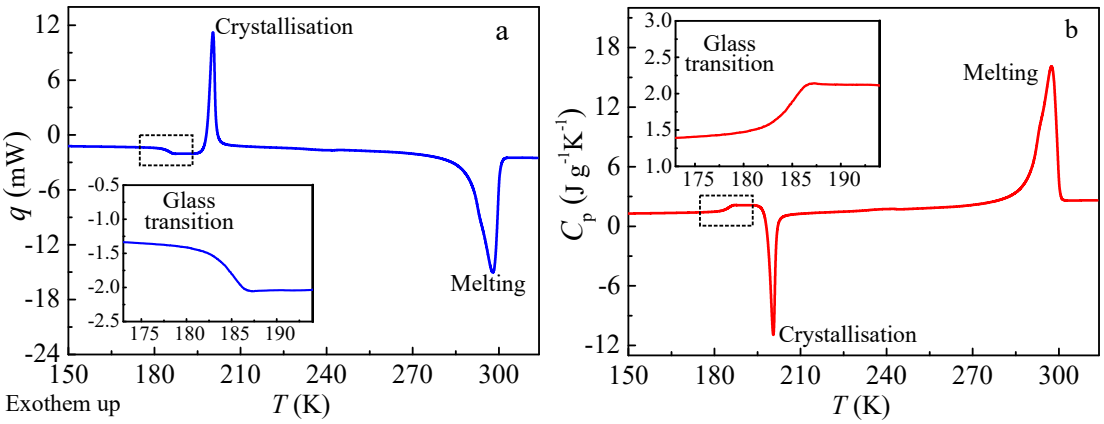

Figure 2.19: (a) A typical DSC heat flow q and (b) C_p traces for the quenched Polytetrahydrofuran with molecular weight of 2000 g/mol (PTHF2000) showing the glass transition, crystallization and melting transitions. The insets are magnifications of the dashed squares to show the step-like glass transition.

An accurate measurement of the heat flow is very important to the success of a DSC measurement. Figure 2.19 shows typical DSC traces of the heat flow and C_p for a quenched PTHF sample. In this representation (exothem up) positive heat flow indicates the flow of heat out of the sample and negative heat flow indicates the flow of heat into the sample.[149] In the traces, three transitions can be observed. At a temperature of around 190 K, a step-like decrease in the heat flow is observed and this is a characteristic of the glass transition. At temperatures higher than the glass transition temperature, the molecules are able to move more freely. In a quenched PTHF sample, the polymer chains tend to form a crystal structure when they have enough mobility. Thus cold crystallization occurs upon further heating, represented by an exothermic peak in the heat flow trace.[149] Finally, an endothermic peak indicative of the melting of the crystalline structure in the sample is observed in the heat flow trace. Figure 2.19b shows the equivalent specific heat capacity trace to that in Figure 2.19a. The same transitions can be observed from the C_p trace, but with an inverse peak direction.[149]

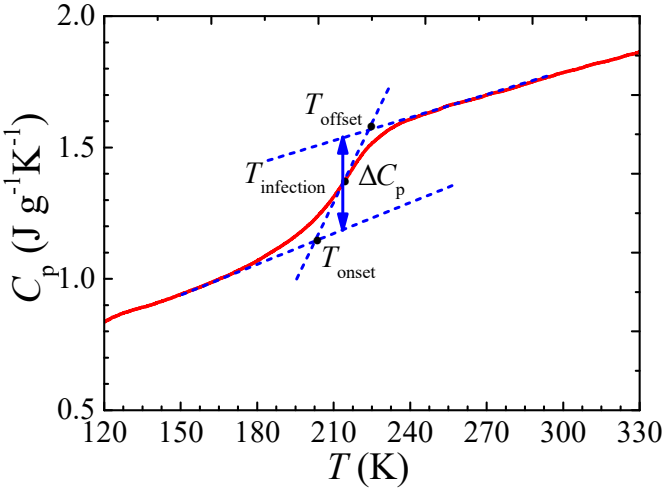

Figure 2.20: Definitions of onset T_{onset}, offset T_{offset}, inflection $T_{inflection}$ temperatures and ΔC_p during a glass transition process. The temperature difference ΔT between the T_{offset} and the T_{onset}, $\Delta T = T_{offset} - T_{onset}$, indicates the broadness of the glass transition. In this work, the onset temperature T_{onset} is used as the glass transition temperature T_g.

Analysis of all features observed in the DSC traces obtained during this study was performed using the TA Universal Analysis software package. Figure 2.20 shows the analysis of the step-like glass transition in C_p. The glass transition step is analysed by first placing two points on the baseline on either side of the step.[154] The analysis software then calculates the first derivatives at these two points, which are the slopes of the tangent lines at these two points. Thus, two lines tangential to these chosen points are drawn. Moreover, a third line tangential to the inflection point of the step. The crossover temperature between the tangent line through the inflection point and the tangent line from the low temperature side is termed the onset temperature T_{onset}, and the crossover point on the other side is termed the offset temperature T_{offset}. The temperature difference $\Delta T = T_{offset} - T_{onset}$ between the offset and onset temperature indicates the breadth of the glass transition. And the C_p difference between two tangent lines from the low and high temperature points is defined as the ΔC_p which can be related to the entropy difference during the glass transition [155, 156]:

$$\Delta C_p = T_g \left(\frac{\partial S^{\,\text{liquid}}}{\partial T} - \frac{\partial S^{\,\text{solid}}}{\partial T} \right) \Bigg|_{T=T_g} \tag{2.68}$$

where $S^{\,\text{liquid}}$ and $S^{\,\text{solid}}$ are the entropy of the material in the liquid and solid states.

Often, T_{onset} is used to define T_g or alternatively $T_{\text{inflection}}$ is chosen instead.[157] Moreover, in a plot of dC_p/dT against T, there will be a peak corresponding to the inflection point and the peak position can be used to define T_g. It seems that this is a better way to determine the T_g, because it is less affected by the arbitrary placement of the starting tangent points. However, the inflection point is more affected by the thermal history of the material and calculation of the derivative of C_p can induce errors into the results.[150] Therefore, in this work, T_{onset} is used as the glass transition temperature.

It is widely accepted that the heating or cooling rates used in a DSC measurement can affect the glass transition temperature. This is because the glass transition is a time-related process.[116] The reciprocal of the heating or cooling rates, $1/Q$, is related to the characteristic timescale for the glass transition dynamics.[158, 159] However, $1/Q$ is not directly the structural (α) relaxation, but it corresponds to a constant multiplied by this timescale. To characterize the absolute timescale, temperature modulated DSC is used in this work and will be introduced in the nest section.

2.3.2 Temperature modulated DSC

In a conventional DSC measurement, the relationship between temperature and time, $f(T,t)$, is set to be linear. This single heating rate produces a single heat flow rate which is the summation of all heat flows that occur at a temperature or time point.[150] In a temperature modulated DSC (MDSC) measurement, two simultaneous heating rates are applied to the sample. One is a linear heating rate, Q, which is the same as the rate applied in a conventional DSC measurement, and the other is a sinusoidal heating rate, Q_m, which is overlaid onto the normal linear heating rate.[151–153] The relationship between temperature and time in an MDSC experiment, $f_m(T,t)$, is therefore sinusoidal. Figure 2.21a shows temperature as function of time for conventional DSC (blue line) and for MDSC (red line). The temperature increases linearly with the time in a conventional DSC experiment whereas for MDSC, the temperature increases in an oscillatory manner. The linear heating rate, Q, oscillatory period, t_p, and the amplitude are three key parameters for a successful MDSC measurement.[153] These will be discussed later. Figure 2.21b shows the linear heating rate Q and modulated heating rate, Q_m , for a MDSC measurement. Two heating rates are applied to the sample and produce separate heat flows which are recorded by the calorimeter.

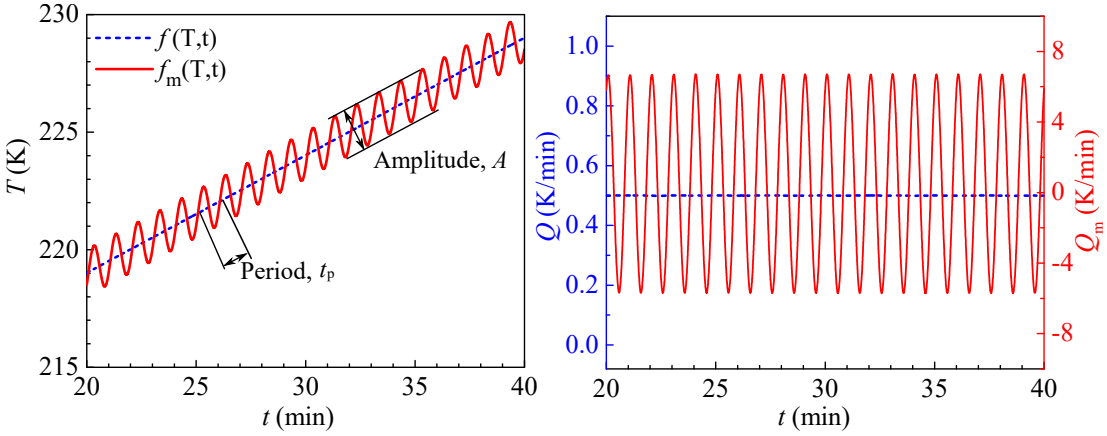

Figure 2.21: (a) Temperature as a function of time in a conventional DSC $f(T,t)$ and in a MDSC $f_m(T,t)$, (b) heating rate Q and modulated heating rate Q_m for silicon oil from a MDSC measurement.

Figure 2.22 shows the modulated heat flow, q_m , and the total heat flow, q_{total} , as a function of temperature in a MDSC measurement. q_m is due to the modulated heating rate, Q_m, and q_{total} is the summation of all heat flows through the sample. The step in the q_{total} is indicative of the glass transition of the silicon oil. The total heat flow in a MDSC measurement can be expressed as:[153]

$$q_{\text{total}} = \frac{dH}{dT} = C_p \frac{dT}{dt} + g(T,t) \tag{2.69}$$

q_{total} is equivalent to conventional DSC at the same heating rate. dT/dt is the heating rate and contains both linear and modulated components. C_p is the heat capacity, calculated from the measured heat flow in response to the modulated heat flow.[153] $C_p dT/dt$ is called the reversing heat flow component, q_r , of the total heat flow.[153] $g(T,t)$ is the kinetic component of the total heat flow and this is the difference between the total heat flow and the reversing heat flow.[153] $g(T,t)$ is also called the non-reversing heat flow component, q_{nr}, with $q_{\text{nr}} = q_{\text{total}} - q_r$.[153]

MDSC has several advantages over conventional DSC. Conventional DSC only provides a single heat flow signal which is the summation of all thermal events happening in the sample. This sometimes makes it difficult to detect particularly small transitions and to explain the data. MDSC can record the total heat flow and the heat capacity component of the total heat flow, thus making it possible to detect the kinetic

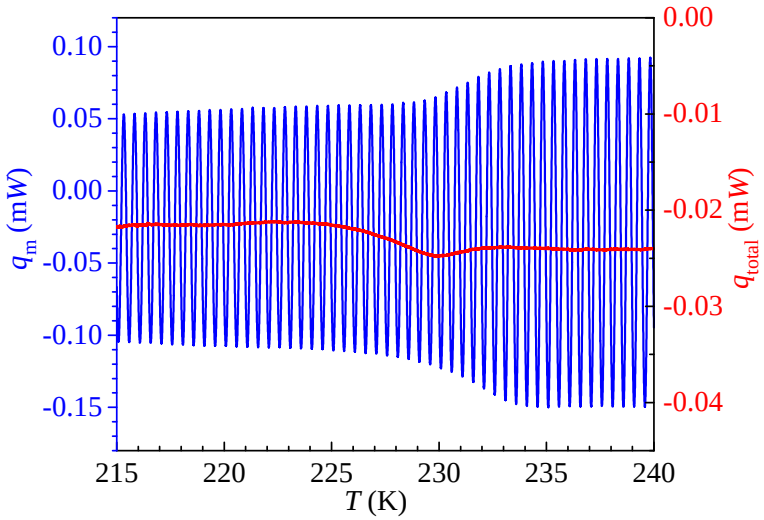

Figure 2.22: Modulated heat flow q_m and total heat flow q_{total} as a function of temperature for the silicon oil from the MDSC measurement.

component, resulting from events such as cold crystallization or enthalpic relaxation. Therefore, MDSC can resolve complex transitions or separate transitions happening within the same temperature range.[153]

From the heat flow traces, the heat capacities can also be calculated:[153]

$$C_{\text{p,total}} = \frac{q_{\text{total}}}{Q} K_{\text{total}} \tag{2.70}$$

$$C_{\text{p,r}} = \frac{A_{qm}}{A_{Qm}} K_r \tag{2.71}$$

$$C_{\text{p,nr}} = C_{\text{p,total}} - C_{\text{p,r}} \tag{2.72}$$

where $C_{\text{p,total}}$, $C_{\text{p,r}}$ and $C_{\text{p,nr}}$ are the total heat capacity, reversing heat capacity and non-reversing heat capacity respectively. A_{qm} and A_{Qm} are the modulated heat flow amplitude (see Figure 2.22) and modulated heating rate amplitude (see Figure 2.21b), respectively. K_{total} and K_r are the calibration constants for the total and reversing heat capacity respectively. Equation 2.72 holds on the assumption that the heat capacity responses are the same for both the linear and modulated components. Figure 2.23 shows q_{total}, q_r, q_{nr} and $C_{\text{p,total}}$, $C_{\text{p,r}}$ and $C_{\text{p, nr}}$ as a function of temperature for silicon oil from a MDSC measurement. From the total heat flow and heat capacity traces, a step-like transition accompanied by an enthalpy relaxation peak can be observed, indicating

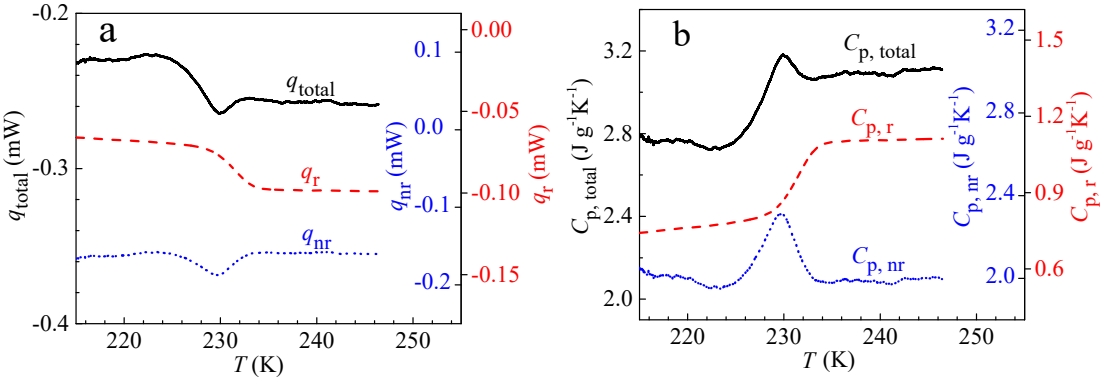

Figure 2.23: (a) Total heat flow q_{total}, reversing heat flow q_r and non-reversing heat flow q_{nr} and (b) total heat capacity $C_{\text{p,total}}$, reversing heat capacity $C_{\text{p,r}}$ and non-reversing heat capacity $C_{\text{p, nr}}$ as a function of temperature for the silicon oil from the MDSC measurement.

that the two thermal events occur simultaneously during the glass transition process. Since MDSC can distinguish the signal from the reversing heat flow or reversing heat capacity component to the kinetic component, the q_r and $C_{\text{p,r}}$ traces show a pure step characteristic, whereas, the q_{nr} and $C_{\text{p,nr}}$ traces show peaks due to the enthalpy relaxation.

Before doing a MDSC experiment, it is good practice to optimise the measurement parameters: average heating rate Q, modulation period (t_p in seconds) and modulation amplitude (A_m). The average heating rate should be slow enough to allow a sufficient number of modulation cycles over the targeted transitions. Generally, at least 4 to 6 cycles over the transition are required for good data quality.[152–154] The modulation period should be long enough to allow sufficient heat flow between the sample and the sensor. The modulation amplitude should be large enough for good sensitivity but not so large that the resolution of the data is reduced due to the insufficient cooling or heating power of the instrument. In practice, an amplitude set between ±0.2 and ±2 K is recommended for the Q2000 instrument.[154] The linear heating rate cannot be too slow as this can significantly increase the experiment time and reduce the amplitude of the total heat flow. It cannot be too fast as this can reduce the effective modulated cycles during a transition. There is an equation which can be used to estimate the ideal

linear heating rate:[154]

$$Q = 60 \times \frac{T_{1/2}}{nt_p} \tag{2.73}$$

where Q is the linear heating rate in K/min and $T_{1/2}$ is the full width at half height for the transition of interest. n is the number of modulation cycles over the transition of interest which has a minimum value of 4-6 cycles. Ideally a conventional DSC measurement should be performed initially to determine $T_{1/2}$ before a MDSC experiment. Glass transitions normally occur over a relatively wide temperature range and therefore a relatively fast average heating rate can be used. However, for samples which have an enthalpy relaxation in combination with glass transition, a slow average heating rate is required in order to separate these two features.[153] In the case of silicon oil, shown in Figure 2.22, an average heating rate of 0.5 K/min was used which allowed around 20 modulation cycles over the glass transition but only 5 modulation cycles for the enthalpy relaxation peak.

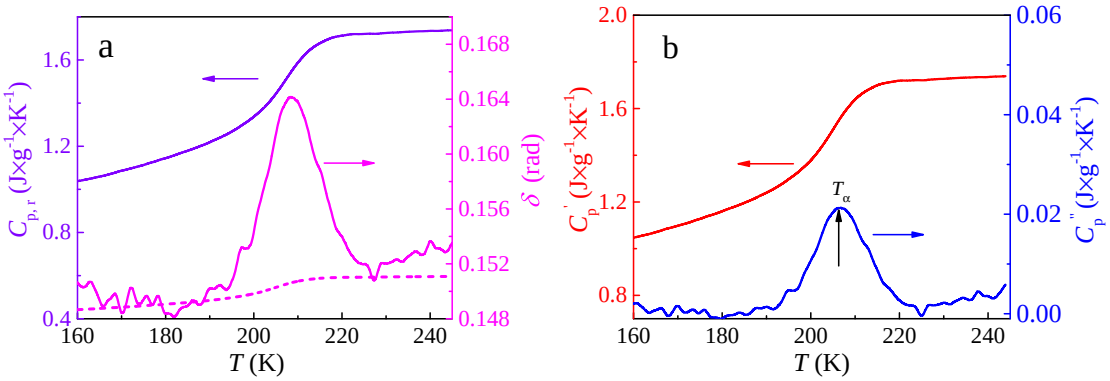

Figure 2.24: (a) Reversing heat capacity $C_{\mathrm{p,r}}$ and phase angle δ from the MDSC measurement of poly(2-ethylhexyl acrylate) (PEHA) as a function of temperature. The δ is corrected using the following relations: $\Delta\delta = a + b|C_{\mathrm{p,r}}|$[160] (the dashed pink line), thus the corrected phase angle: $\delta_{\mathrm{corr}} = \delta - \Delta\delta$. (b) Real C_p' and imaginary C_p'' parts of the complex heat capacity C_p^* of PEHA measured by MDSC with $t_p = 60$ s, $Q = 3$ K/min and amplitude of ±1 K. C_p^* is the reversing heat capacity $C_{\mathrm{p,r}}$ from the MDSC measurement. C_p' and C_p'' are calculated using the following equations: $C_p' = |C_p^*|\cos(\delta_{\mathrm{corr}})$ and $C_p'' = |C_p^*|\sin(\delta_{\mathrm{corr}})$.[160]

In a MDSC measurement there is a phase angle δ between the heating rate and the measured heat flow rate which is related to the intrinsic properties of the material.[153]

A MDSC experiment allows the determination of the frequency dependent heat capacity of a material, and the real C'_p and imaginary C''_p parts of the complex heat capacity C^*_p can be calculated using the following equations:[153, 158–160]

$$C^*_p = C'_p - iC''_p \tag{2.74}$$

$$C'_p = |C^*_p|\cos(\delta) \tag{2.75}$$

$$C''_p = |C^*_p|\sin(\delta) \tag{2.76}$$

Both δ and $|C^*_p|$, i.e. the reversing heat capacity $|C_{\mathrm{p,r}}|$ can be measured directly from the MDSC measurement. Howver, since it takes a non-negligible amount of time for heat to flow from the heater to the sample in any DSC measurement, this leads to an additional phase angle which is added to that of the intrinsic material behaviour. This additional phase angle thus has be to been considered when calculating the real C'_p and imaginary C''_p parts from the complex heat capacity using equation 2.75 and 2.76. The correction to the phase angle was reported by Weyer etc. using the relation:[160]

$$\delta_{\mathrm{corr}} = \delta - \Delta\delta = \delta - (a + b|C^*_{\mathrm{p}}|) \tag{2.77}$$

The measured δ from the MDSC measurement is the superposition of two phase angles due to the intrinsic properties of the material and the heat transfer ability of the instrument. Equation 2.77 can separate these two components and allow investigation of the thermal response only due to the intrinsic properties of the material. An example of the correction is shown in Figure 2.24a, where the reversing heat capacity or the complex heat capacity and the phase angle are plotted as a function of temperature. The measurement was performed on poly(2-ethylhexyl acrylate) (PEHA) with t_p = 60 s, Q = 3 K/min and amplitude of ±1 K. The phase angle due to the heat transfer lag can usually lead to the uneven baseline, which can be corrected by subtracting the contribution from $\Delta\delta$, where $\Delta\delta = a + b|C_{\mathrm{p,r}}|$[160] (the dashed pink line Figure 2.24a). Thus, the real C'_p and imaginary C''_p heat capacity should be calculated using the correct phase angle:

$$C'_p = |C^*_p|\cos(\delta_{\mathrm{corr}}) \tag{2.78}$$

$$C''_p = |C^*_p|\sin(\delta_{\mathrm{corr}}) \tag{2.79}$$

Figure 2.24b shows the real and imaginary parts of the complex heat capacity of PEHA calculated using the measured reversing heat capacity and the corrected phase

angle in Figure 2.24. The dynamic glass transition temperature, T_α, is related to the structural relaxation process and can be determined from the peak position in the imaginary heat capacity trace. In MDSC, measurement of T_α is similar to other techniques which probe dynamics, such as dielectric spectroscopy and rheometry. In all these cases, the glass transition temperature is dependent on the frequency of the external perturbation. In MDSC, the perturbation is the modulated heat flow. The frequency is related to the modulated period t_p:[153, 160]

$$\omega = \frac{2\pi}{t_p} \tag{2.80}$$

Thus the characteristic timescale can be determined:

$$\tau = \frac{1}{\omega} = \frac{t_p}{2\pi} \tag{2.81}$$

For the Q2000 DSC, the modulated period cannot be varied over a wide range but one can still determine the timescale of the glass transition over a certain temperature range. The combination of MDSC with other techniques allows for the mapping of a wide range of relaxation timescales.

2.3.3 Rate dependent DSC

It is widely accepted that the glass transition temperature, T_g, depends on the heating or cooling rate.[116] Thus, it is interesting to probe T_g at systematically varying heating rates. The timescale is proportional to the heating rate Q:[159]

$$\tau \sim \frac{a}{Q} \tag{2.82}$$

where a is a constant. Figure 2.25 shows an Arrhenius plot of $1/q$ measured by conventional DSC and the timescale measured using MDSC as a function of temperature. The data from conventional DSC (red squares) are shifted to overlap with the data point (pink star) measured with MDSC by the constant, a.[159] Thus, a combination of conventional DSC data obtained with varying heat rates and MDSC data, one can probe an extended frequency range in order to study the dynamics of the glass transition. Combination of this data with dielectric or rheological data allows this frequency range to be extended further. This method has been verified on various glass formers.

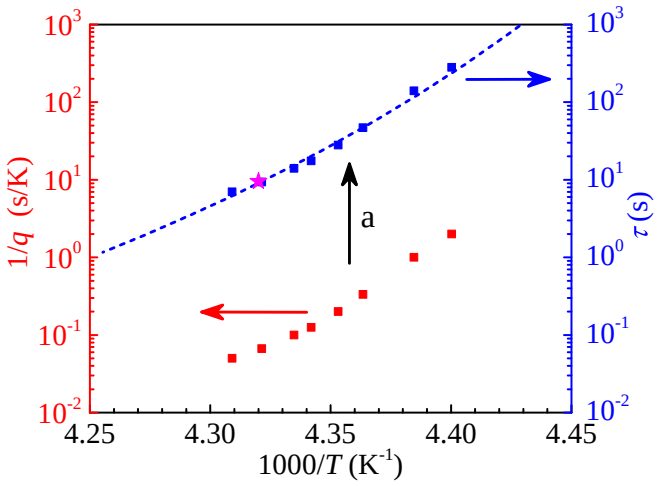

Figure 2.25: Arrhenius plot of the silicon oil measured by conventional DSC (red squares) and MDSC (pink star) with t_p = 60 s, Q = 0.5 K/min and amplitude of ±1 K. The data from conventional DSC is shifted upwards to overlap with the MDSC point by the constant a, log(a) = 2. The blue dashed line is the VFT fitting curve to the data.

2.4 Nuclear magnetic resonance (NMR)

In this section, the theoretical and experimental aspects of nuclear magnetic resonance (NMR), used to investigate polymer dynamics in the melt, will be introduced. This section mainly follows the books of Hore,[161] Levitt[162] and the PhD thesis of Radhi.[163]

2.4.1 Origin of nuclear magnetic resonance

All subatomic particles, such as protons, electrons and neutrons, have an intrinsic property called spin in the form of the angular momentum **L**.[162] The vector **L** is an intrinsic property of particles and is not introduced by the rotation of the particles. The magnitude of L can be expressed as:

$$L = [I(I+1)]^{1/2}\hbar \tag{2.83}$$

where $\hbar$ is the reduced Planck's constant and I is the spin quantum number which can equal one of following values, $I = 0, 1/2, 1, 3/2, 2, \cdots$, depending on the nuclei themselves. A general rule can be used to predict I: i) if the number of protons and

neutrons of a nucleus are both even, then $I = 0$; ii) if the number of protons and neutrons of a nucleus are both odd, then $I = 1, 2, 3, \cdots$; iii) if either of the number protons or neutrons is even and the other is odd, then $I = 1/2, 3/2, 5/2, \cdots$. For example, I for ^{1}H and ^{13}C is equal to 1/2, and I for ^{2}H and ^{14}N is equal to 1. Subatomic particles with a spin quantum number of I are usually termed 'spin-I' particles. For example, both ^{1}H and ^{13}C are 'spin-1/2' particles. The spin angular momentum is a vector and so both the direction and the magnitude can be quantified. The angular momentum $\mathbf{L}$ for a spin-I particle can have $2I + 1$ projections on a chosen axis. For example the projection on the z-axis can be quantified as:

$$L_z = m\hbar \tag{2.84}$$

where m is the magnetic quantum number which has $2I + 1$ values between I and $-I$, $m = I, I - 1, I - 2, \cdots, -I + 1, -I$. For example, for ^{1}H and ^{13}C, $L_z = \pm 1/2\hbar$.

The spin angular momentum of nuclei can produce magnetic moments, $\boldsymbol{\mu}$, [162] which are proportional to $\mathbf{L}$:

$$\boldsymbol{\mu} = \gamma \mathbf{L} \tag{2.85}$$

where γ is the gyromagnetic ratio. In the absence of an external magnetic field, magnetic moments, $\boldsymbol{\mu}$ for 'spin-I' nuclei have $2I + 1$ possible orientations. There are no energy differences between these states, thus they are randomly oriented. However, in an external magnetic field this is no longer the case and different orientations will have different energy levels. The energy of magnetic moments in an external magnetic field $\mathbf{B}$ can be expressed as:

$$E = -\boldsymbol{\mu}\mathbf{B} \tag{2.86}$$

Substituting equations 2.84 and 2.85 into equation 2.86 gives:

$$E = -m\hbar\gamma B \tag{2.87}$$

Here, E is the energy for orientations in the z-axis direction. Equation 2.86 shows that the energy is proportional to the magnetic quantum number and the strength of the external filed which is defined as the z-axis direction (γ and $\hbar$ are constants). Thus the energy gap for 'spin-I' nuclei is $\gamma\hbar B$. For example, ^{1}H is a 'spin-1/2' particle which has two magnetic quantum numbers, $m = +1/2$ and $m = -1/2$. In an external magnetic field, some of the magnetic moments will align parallel with the external magnetic field

and will therefore populate the lower energy level and some will align anti-parallel with the external magnetic field and will populate the higher energy level[162] (see Figure 2.26a). The NMR signal comes from the net energy absorption ΔE after the disturbance of a radio frequency (RF) pulse. The nuclear magnetic resonance condition is:

$$\Delta E = \hbar\omega = \hbar\gamma B \tag{2.88}$$

$$\omega = \gamma B \tag{2.89}$$

where ω is the angular frequency of the RF pulse, also called the Larmor frequency.

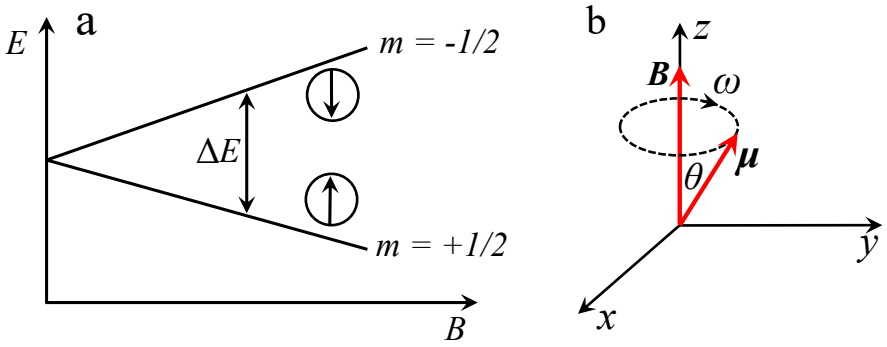

Figure 2.26: (a) Energy levels for the ^{1}H nuclei as a function of external magnetic field. The ^{1}H nuclei is a 'spin-1/2' particle, splitting into two sub-levels according to Equation 2.86 after the radiation frequency pulse perturbation. (b) The nuclear magnetic moment $\boldsymbol{\mu}$ precessing around the external magnetic field **B** with the Larmor frequency ω_0.

The motion of a magnetic moment can be described in terms of the precession of the magnetization vector $\boldsymbol{\mu}$ around the external magnetic field, B, with a frequency, ω, (the Larmor frequency) at an angle θ as shown in Figure 2.26b. The Larmor frequency is given by the equation 2.89. The potential energy for the precession can be expressed as:

$$E = -\mu B = -\mu B\cos\theta \tag{2.90}$$

where θ is the precession angle. Nuclear spins can be excited by the RF pulse through absorption of energy.[161] After the pulse is switched off, a spin in the excited state can return to the equilibrium state, emitting the energy it has absorbed over some time. This is the so-called magnetization relaxation process, during which the magnetization

relaxation in the z-direction M_z returns to its original value, M_0. The signal decay in the xy-plane is detected, and is typically characterised by a single exponential decay.[161, 162]

2.4.2 The NMR spectrometer

In this work, a MARAN bench-top pulse NMR analyser, manufactured by Resonance Instruments Ltd, U.K. and operating at 20 MHz for protons, was used to acquire data. Figure 2.27(a) shows the schematic diagram of the setup of this NMR analyser. The sample in the tube is placed in the magnetic field **B** created by the permanent magnets in the z-direction (Figure 2.27b). The RF pulse is generated by the coil in which the sample tube is placed. The energy of the RF pulse corresponds to the energy difference between two different spin states. Thus the frequency of the RF pulse is given by the equation 2.88 and 2.89.

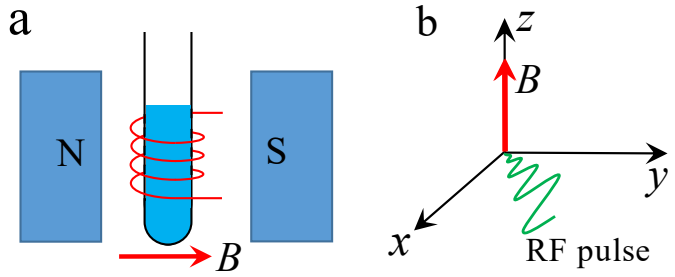

Figure 2.27: (a) Schematic diagram shows the setup of the MARAN bench-top pulse NMR analyser. (b) definition of the direction of the external magnetic field **B** (z-direction) and the RF pulse direction of the NMR analyser.

2.4.3 Relaxation of the magnetic moment

As discussed above, without an external magnetic field B_0, the nuclear magnetic moments μ are randomly oriented, thus the vector sum of these nuclear magnetic moments equals zero. After the application of an external magnetic field, the total magnetic moment vector M_0 is the sum of μ along the direction of the external magnetic field as shown in Figure 2.28a. After a perturbation in the form of an RF pulse, M will leave the equilibrium state and precess about the pulse. The projections of M on the xy-plane and

z-direction are defined as the M_{xy} and M_z components, respectively, see Figure 2.28b. After removal of the RF pulse, M will recover back to the equilibrium state gradually. This process is the so-called magnetization relaxation.[161, 162] The relaxation in the z-direction is the longitudinal T_1 relaxation and the relaxation in the xy-plane is the transverse T_2 relaxation.[161] The T_1 relaxation process can be described by the equation:

$$\frac{dM_Z}{dt} = -\frac{M_z - M_0}{T_1} \tag{2.91}$$

If M_0 is tilted onto the xy-plane, i.e. $M_z = 0$, the recovery of the magnetization can be described in the integrated form:

$$M_z(t) = M_0(1 - e^{-t/T_1}) \tag{2.92}$$

The above equation means that after a time constant T_1, 63% of magnetization can be recovered in the z-direction. T_1 relaxation is related to the energy exchange between the spin system and the surrounding environment (lattice), thus T_1 relaxation is also known as spin lattice relaxation.[161]

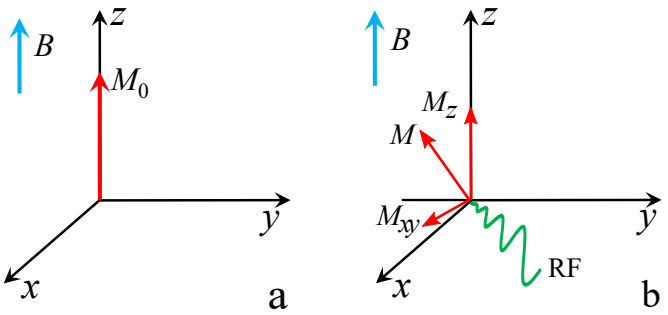

Figure 2.28: (a) The overall M_0 along the direction of external magnetic field in the z-direction, (b) after the RF perturbation, M_0 leaves the equilibrium state and has projections M_{xy} and M_z in the xy-plane and along the z-direction respectively.

The transverse relaxation time T_2 can be described using the following equation:[161]

$$\frac{dM_{xy}}{dt} = -\frac{M_{xy}}{T_2} \tag{2.93}$$

$$M(t) = M_{xy}e^{-t/T_2} \tag{2.94}$$

The T_2 relaxation describes the process by which the nuclear spin magnetization loses its phase coherence. Unlike the T_1 relaxation, the T_2 relaxation does not require the energy exchange but is instead related to the local variation of the magnetic field strength which leads to the phase decoherence of the precessing spins. The greater the magnetic field strength variation, the faster the phase decoherence of the precessing spins.[161]

2.4.4 Measurements of T_1 and T_2 relaxations

Inversion recovery is the commonly used method to conduct a T_1 measurement.[161, 162] In this method, a 180° RF pulse in the $+z$ direction is first applied to the sample which inverts the magnetization from the $+z$ direction to the $-z$ direction as shown in Figures 2.29a and b. After a certain time t, the magnetization inverts back to the $+z$ direction as shown in Figure 2.29c. After the delay time t, a 90° RF pulse is applied, tilting the magnetization onto the xy-plane as shown in Figure 2.29d. The magnetization and signal intensity are then recorded in z-direction as shown in Figure 2.29e. The RF pulse sequences are shown in 2.29f. The magnetization from the inversion recovery method can be described by the following equation:

$$M(t) = M_0(1 - 2e^{-t/T_1}) \tag{2.95}$$

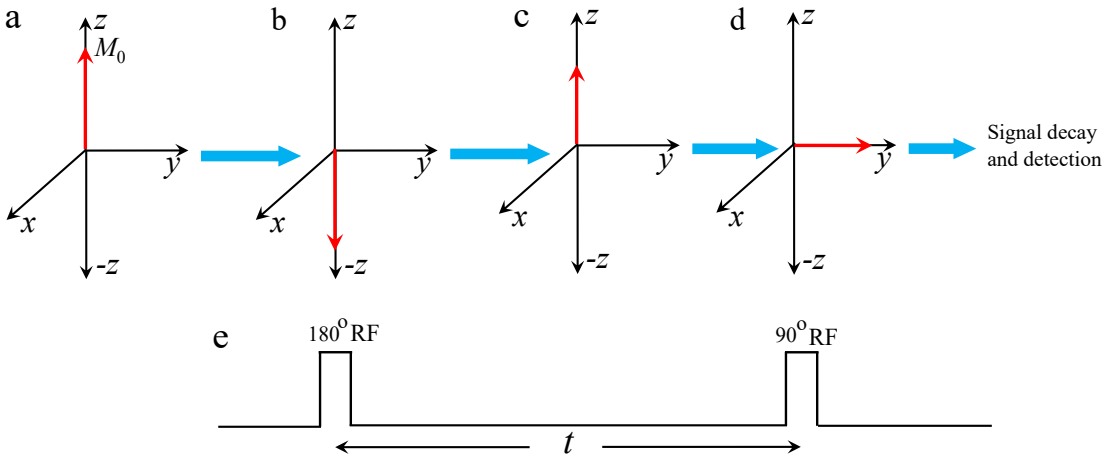

Figure 2.29: Schematic diagram showing the variation of the magnetization during the T_1 measurement using inversion recovery method.

A Hahn Spin-Echo pulse sequence is used to conduct a T_2 measurement.[161, 162] In this method, a 90° RF pulse is applied, tilting the magnetization onto the xy-plane

as shown in Figures 2.30a and b. After certain time t_1, the magnetization can spread in the xy-plane as shown in Figure 2.30c. Following this, a 180° RF pulse is applied which flips the magnetization horizontally as shown in Figure 2.30d. After certain time t_2, the echo is recorded, which reveals the decoherence (Figure 2.30e). The RF pulse sequences are shown in 2.30f. In a simple case, the T_2 relaxation can be described by an exponential decay:

$$M(t) = M_{xy}e^{-t/T_2} \tag{2.96}$$

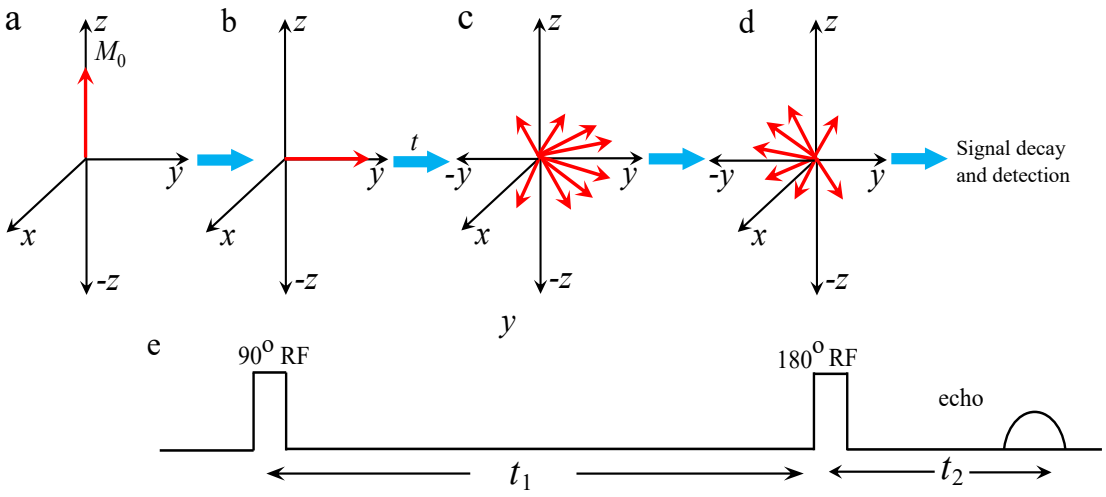

Figure 2.30: Schematic diagram showing the variation of the magnetization during the T_2 measurement using Hahn spin-echo pulse sequence.

2.4.5 Bloemberg-Purcell-Pound (BPP) Theory

For systems containing protons, the most important relaxation mechanism is the dipole-dipole interaction. The BBP theory was proposed to describe the relaxation times of some simple systems such as bulk water in terms of the correlation time, τ.[164] This theory is based on the assumption that a single reorientational correlation time τ of a molecule is responsible for the relaxation. Based on this, the relaxation times can be expressed as:[164]

$$\frac{1}{T_1} = 2A\left(\frac{\tau}{1+\omega^2\tau^2} + \frac{4\tau}{1+\omega^2 4\tau^2}\right) \tag{2.97}$$

$$\frac{1}{T_2} = A\left(3\tau + \frac{5\tau}{1+\omega^2\tau^2} + \frac{2\tau}{1+4\omega^2\tau^2}\right) \tag{2.98}$$

where τ is the correlation time and ω is the Larmor frequency which is specific to the equipment used. A is a constant:

$$A = \frac{3}{20}\gamma^4\hbar^2\left(\frac{\mu_0}{4\pi}\right)^2 r^6 \tag{2.99}$$

where γ is the gyromagnetic ratio for protons, $\hbar$ is the reduced Planck constant, μ_0 is the permeability of free space and r is the distance between two interacting protons.

Figure 2.31 compares the T_1 and T_2 data as a function of τ. The values of T_1 and T_2 are equal at very short correlation times. T_1 has a minimum and then increases as the correlation time increases. On the other hand, T_2 continues to decrease, which means in practice that the NMR peaks get broader as the molecular size or viscosity increases. Therefore, the T_1 and T_2 relaxations and the spectral resolution depend on the molecular size and the viscosity of the solution.[161, 163]

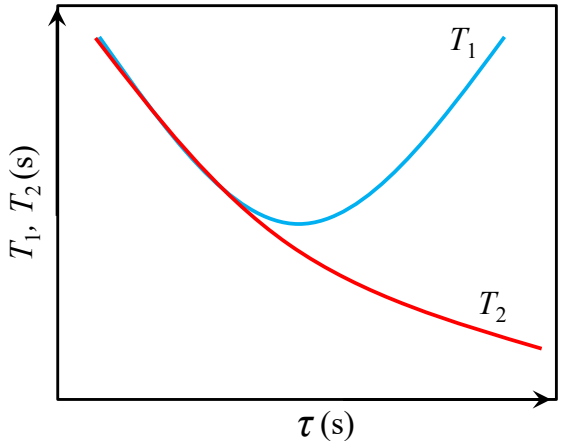

Figure 2.31: Schematic illustration of T_1 and T_2 relaxations as a function of correlation time, τ.

2.5 Summary

The four main techniques used in this work to probe the dynamics of materials over a wide timescale range have been introduced. Broadband dielectric spectroscopy is useful to study the glassy dynamics and sub-glass transitions. Its large operational

frequency and temperature range means that the dynamics of such materials can be analysed over a wide range of timescales. Various different types of rheometry were introduced showing that the microscopic structures of materials could be studied through analysis of their macroscopic properties. Differential scanning calorimetry is a powerful method to study thermally driven events, including the glass transition, melting, crystallization and degradation. In this work, conventional DSC, modulated DSC and rate dependent DSC measurements are combined together to study the dynamics of the glass transition. NMR is a versatile technique and was used to investigate several aspects of chemical compounds such as their molecular structure, motion and conformation. T_1 and T_2 relaxometry measurements were used in this work to probe the dynamics of polymer melts.

Chapter 3

Control of polymer dynamics using supramolecular side-groups

In this chapter, comb-like polymers based on 2-ethylhexyl acrylate (EHA) and 2-ureido-4[1H]-pyrimidinone (UPy) units are synthesised via RAFT polymerisations. The former monomers give the polymers a comb-like structure, whereas the latter monomers generate side-group supramolecular interactions (hydrogen bonds) acting by the formation UPy dimers, where the dimers are linked by quadruple hydrogen bonds. We investigate the structure, dynamics and rheology of these supramolecular side-chain polymers where the UPy side-chain molar concentration was systematically varied and encompassed 0, 2, 6, 9 and 14% of UPy units. We demonstrate that these polymers which contain a significant fraction of alkyl side-chains demonstrate nano-phase segregated structures due to the incompatibility between the polymer backbone and the alkyl side-chains. This is reflected in the dynamics, which show two separate relaxation processes near the glass transition temperatures T_g, as observed using broad-band dielectric spectroscopy. For the pure non supramolecular polymer, the slowest relaxation is assigned as the α relaxation which is related to structural relaxation and thus the glass transition. The faster observed relaxation is due to relaxations of alkyl chains within the nano-phase segregated alkyl-rich regions. We term this relaxation α^*, and demonstrate that it shows similarities to relaxations observed in polyethylene α_{PE}. The random addition of supramolecular UPy-groups along the polymer backbones significantly slows down the α relaxations, leading to higher T_gs.

As the concentration of UPy groups along the backbone is increased, the glass transitions become weaker and broader due to the physical cross-linking of UPy dimers between chains. For the polymer with 14 mol% UPy, the α relaxation changes from the usual Vogel-Fulcher-Tammann VFT behaviour to an Arrhenius behaviour, which implies that the α relaxation is mainly controlled by dynamics of supramolecular groups. On the other hand, addition of UPy groups has a much smaller effect on the α^* and γ relaxations. The α^* relaxation is controlled by the size of alkyl regions which in our case are more or less fixed, as demonstrated by x-ray measurements. The γ relaxation in the sub-glassy state is mainly due to local motions of the side groups and is not significantly affected by the inter-chain supramolecular interactions. On the macroscopic scale, the addition of UPy groups along the backbone changes the mechanical properties dramatically. For polymers with 0 and 2 mol% UPy groups, the materials are viscous liquids at room temperature. However, polymers with 6, 9 and 14 mol% UPy groups are rubbery solids and demonstrate clear rubber plateaus in the elastic storage modulus, covering almost 4 decades in frequency. The supramolecular interactions also delay the terminal relaxations, decrease the power law exponents corresponding to the terminal regime and increase the activation energies for polymers to flow. These phenomena are rationalized in terms of the addition of supramolecular physical cross-links, the UPy dimers. In the intermediate frequency range between the glassy response and the rubber plateau, the addition of UPy groups also decreases the effective power law exponents, characterising the response, from ~0.5 to ~0.2, as the UPy concentration increases from 0 to 14 mol%, showing a change of the dynamics from Rouse-like to gel-like behaviour.

3.1 Introduction

Supramolecular materials made of covalently bonded chains, intermolecularly connected through secondary reversible interactions, such as hydrogen bonding,[165–172] metal-ligand coordinations,[173–178] hydrophobic interactions,[179, 180] or ionic aggregations,[181–184] have been of great interest for many years. As a matter of fact, the intrinsic reversibility of such secondary bonds leads to the formation of transient networks,[140, 170, 185–190] with stimuli-responsive properties that can be controlled e.g. through a variation of the temperature,[191–193] moisture or pH,[194–196], In

particular, supramolecular polymer can provide new and unique opportunities in terms of materials processing and this is highly relevant to industrial applications.

Nano-phase segregated structures in the range of 1-3 nm have been reported for polymers with comb-like architecture containing long alkyl side chains because of incompatibility between polymer backbones and side alkyl chains.[197–204] Materials with such nano-scale structures are of a great interest in many fields, for example, as organic semi-conductors in thin-film transistors,[205] surfactants component for biomedical applications,[206] organic photovoltaic cells[207] and light emitting diodes.[208] Understanding the relaxation dynamics across a wide range of length- and time-scales of such nano-phase segregated materials is important in order to be able to fully utilise the potential of these materials in applications. It has been shown that nano-phase segregation phenomena widely exists in many polymers, and depends on the chemistry, flexibility and glass transition temperature of the polymer backbones.[197, 198, 200–204] For polymer systems with alkyl side-chains, it has been demonstrated that the size of the alkyl side chain region is the key parameter that controls the dynamics inside the alkyl region.[203]

In this chapter, poly(2-ethylhexyl acrylate-co-UPyEA) (UPyPEHA) with varying UPy concentrations ϕ_{UPy} are synthesised using RAFT polymerisation.[67, 168, 209–211] Two monomers are chosen. One is 2-ethylhexyl acrylate and the other is modified by 2-ureido-4[1H]-pyrimidinone (UPy) groups. The former one leads to nano-phase segregated structures[203] and the latter one provides supramolecular interactions, forming transient networks due to quadruple hydrogen bonds between UPy groups.[212, 213] The UPy hydrogen bonding group is chosen because of its easy chemical synthesis, strong association constant ($k_{\mathrm{asso}} > 10^6$ M^{-1} in chloroform), temperature sensitivity and self-complementarity.[33, 166, 214, 215] The physical and chemical aspects of UPy-based supramolecular materials have been widely studied, both with a focus of increasing the fundamental understanding and additionally to develop new applications, such as stimuli-responsive,[170, 174, 191, 216–218] temperature sensitive[192, 193, 210, 216, 219, 219] or self-healing properties.[167, 220–224] Attaching UPy groups to the ends of linear polymers or oligomers, (forming so-called 'telechelic' building-blocks, one example is given in Chapter 5), enables chain-extension and thus a qualitative change of the mechanical behaviour from liquid-like to rubber-like at room temperature.[33, 166, 170, 225–228] On the contrary, at

high temperature, hydrogen bonds are more likely to be dissociated, which drastically decreases the melt viscosities. This behaviour is potentially of high interest for industrial processing.[33, 166] Alternatively, UPy groups can be attached to the polymer backbone as side groups by random co-polymerisation of conventional and UPy-functionalized monomers.[168, 186, 210, 213, 229, 230] By tuning the molecular weight of the polymer backbone, as well as the concentration of UPy groups along the backbone, ϕ_{UPy}, a broad range of properties such as glass transition temperatures and melt viscosities can be controlled.

In this chapter, we study a series of polymers both without and with varying concentrations of supramolecular UPy groups along the chains. All polymers are below their entanglement molecular weight ($M_e \sim 30$ kg/mol, as estimated by comparison to the similar polymer poly(hexyl acrylate) (PHA)),[231]) Thus, a series of samples with varying ϕ_{UPy} (0, 2, 6, 9 and 14mol%) were synthesised. The nano-phase segregated structures were characterized by small angle x-ray scattering (SAXS) and atomic force microscopy (AFM). The dynamics were investigated by differential scanning calorimetry (DSC), broadband dielectric spectroscopy (BDS) and rheological measurements. As ϕ_{UPy} increases, the glass transitions become much weaker and broader, and the temperature dependences change from a Vogel-Fulcher-Tammann (VFT)[232] behaviour to an Arrhenius behaviour. These results indicate that as chain segments between two UPy groups becomes shorter, relaxations occur over a broader range of timescales, corresponding to more constrained states. Similar behaviours have been observed in other systems such as nanocomposites showing gel-like behaviour over a wide frequency range ($\sim$ 6 decades) for high nanoparticle loading.[233] In the melt state, the characteristic relaxation timecales and power law exponents in the terminal regime decrease as ϕ_{UPy} increases because inter-chain hydrogen bonds act as an extra friction and slow down chain relaxations.[186] Inside the nano-phase segregated regions, the relaxation dynamics of the alkyl chains are independent on the surrounding matrix and is only slightly affected by increasing ϕ_{UPy}. In the sub-glassy state, a γ relaxation is observed that is related to local motions of side groups,[234] and is not affected by inter-chain supramolecular interactions. Our work, supported by structural evidences, investigate effects of supramolecular interactions and nano-phase separations on the dynamics and rheology of polymer networks ranging from the glassy state to the melt state.

3.2 Experimental section

3.2.1 Materials

All chemicals were purchased from Sigma Aldrich. 2-ethylhexyl acrylate (EHA) was passed through a basic aluminium oxide column to remove monomethyl ether hydroquinone which act as stabilizers before polymerisation. 2,2-azobis(isobutyronitrile) (AIBN) and 1,1'-azobis(cyclohexanecarbonitrile) (ABCN) were re-crystalized from ethanol twice before use. 2-isocyanatoethyl acrylate (ICEA), 2-amino-4-hydroxy-6-methylpyrimidone (AHEP) and molecular sieve adsorbent were used as received. 4-cyano-4-[(dodecylsulfanylthiocarbonyl) sulfanyl] pentanoic acid was used as chain transfer agent (CTA) for the RAFT polymerisations. Solvents, i.e. tetrahydrofuran (THF), dimethyl sulfoxide (DMSO), chloroform, dichloromethane (DCM) were dried using molecular sieves for two days before use.

3.2.2 Synthesis of UPy functionalized ethylacrylate (UPyEA)

Synthesis of UPy side-chain functionalized polymers involves two steps: synthesis of 2-(3-(6-methyl-4-oxo-1,4-dihydropyrimidin-2-yl)ureido)ethyl acrylate (UPyEA) and co-polymerisation of UPyEA with EHA monomers.[210, 211, 235] Synthesis procedure for UPyEA is shown in Figure 3.1. AHEP (4.03 g, 32.2 mmol) was dissolved in 60 ml of DMSO at 150 °C. The solution was then cooled to room temperature and ICEA (5.0 g, 35.5 mmol) was added. After 3 hours under stirring, the reaction solution generated white solids. Most DMSO was removed under a high vacuum using a rotary evaporator, and washed with a large amount of acetone, yielding UPyEA as white powders. Yield: 8.4 g, 98%. ^{1}H (500 MHz, d_6-DMSO) δ: 2.11 (3H, s, -C$\underline{H}_3$), 3.47 (2H, q, J = 5 Hz, -C$\underline{H}_2$-CH$_2$-O-), 4.20 (2H, t, J = 5 Hz, -CH$_2$-C$\underline{H}_2$-O-), 5.8 (1H, s, -C$\underline{H}$-C(=O)-), 5.98 (1H, dd, J_1 = 5 Hz, J_2 = 10 Hz, -CH=C$\underline{H}_2$(*trans*)), 6.20 (1H, dd, J_1 = 5 Hz, J_2 = 15 Hz,-C$\underline{H}$=CH$_2$), 6.37 (1H, dd, J_1 = 5 Hz, J_2 = 15 Hz, -CH=C$\underline{H}_2$(*cis*)). ^{13}H (500 MHz, d_6-DMSO) δ: 168.2, 166.1, 154.4, 152.2, 131.1, 128.0, 104.8, 61.0, 45.4, 18.9. υ_{max}(neat, cm^{-1}): 2956, 2169, 1733, 1703, 1659, 1578, 1522, 1455, 981, 967; ESI-HRMS calculated for [$C_{11}H_{14}N_4O_4$+H]$^+$: 267.1260 g/mol, found 267.1090 g/mol.

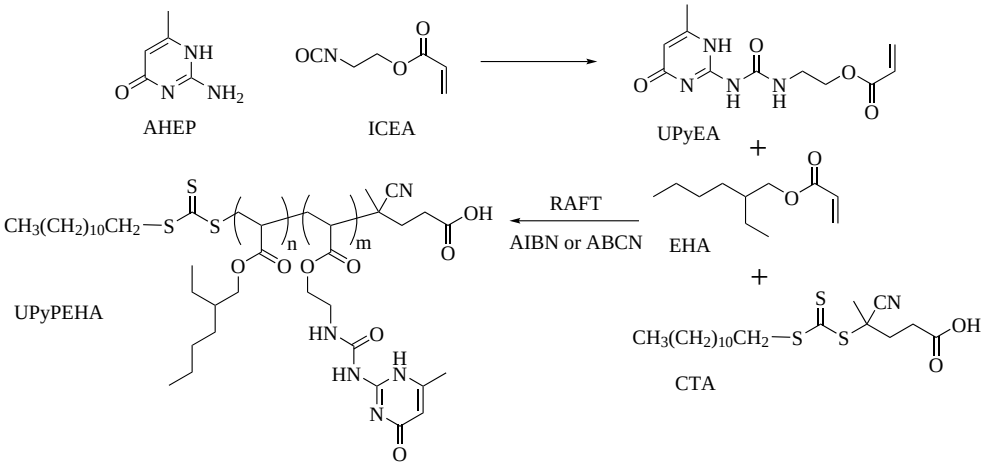

Figure 3.1: Synthesis of UPy functionalised monomers (UPyEA) and (co)polymers containing EHA and UPyEA by RAFT polymerisation.

A general procedure for RAFT polymerisation of co-polymers is as follows: a calculated amount of monomers (EHA and UPyEA), CTAs, initiators (ACBN), and DMF were added into a round-bottom flask. The flask was then connected to a vacuum line, and subsequently the flask was immersed into liquid nitrogen to make sure all chemicals inside were frozen. In the frozen state, the air in the flask was pumped out through the vacuum line over a period of 15 mins. After this, the valve between the pump and the flask was closed. The flask was immersed into methanol which can help warm up the mixture in the flask quickly. The freeze-pump-thaw cycle was repeated at least three times to remove the oxygen in the solution; this is important since the oxygen can otherwise react with radicals and terminate the polymerisation. After three freeze-pump-thaw cycles, the flask was immersed into a pre-heated oil bath to start the polymerisation. After a prescribed time, to stop the polymerisation, the flask was removed from the oil bath, immersed into a mixture of ice and water and the flask was opened to air.

To purify the polymer, a small amount of chloroform was added to the viscous solution and the diluted solution was precipitated drop by drop into large amount of methanol (at least 10 times excess in volume). This was performed twice to remove any residual monomers, followed by filtration and drying under vacuum at 60 °C for one day. The synthesis procedure is shown in Figure 3.1. Five (co-)polymers were

Table 3.1: Characteristics of (co-)polymers synthesised by RAFT

sample code	M_n [1] (g/mol)	PDI [1]	φ [2] (%)	$M_{\text{n,theory}}$ [3] (g/mol)	Feeding ϕ_{UPy} (%)	ϕ_{UPy} [4] (%)	[UPy] [5]	[EHA] [6]
PEHA	17200	1.05	65	19400	–	–	–	–
UPyPEHA2	16600	1.24	70	21400	4	2	2	–
UPyPEHA6	22000	1.38	76	24800	8	6	7	16
UPyPEHA9	23700	1.71	79	25300	10	9	13	10
UPyPEHA14	24600	2.26	84	29200	15	14	17	6

[1] Measured by SEC, Polydispersity Distribution Index (PDI), PDI = M_w/M_n;

[2] $\varphi = m_{\text{polymers}}/m_{\text{monomers}} \times 100\%$, where m_{polymers} and m_{monomers} are the mass for polymer after purification and the mass for fed monomers;

[3] $M_{\text{n,theory}} = M_{\text{CTA}} + (\frac{[\text{EHA}]}{[\text{CTA}]} \times M_{\text{EHA}} + \frac{[\text{UPyEA}]}{[\text{CTA}]} \times M_{\text{UPyEA}}) \times \varphi$, where M_{CTA}, M_{EHA} and M_{UPyEA} are molecular weights of CTA, EHA and UPyPEHA, respectively; [CTA], [EHA] and [UPyEA] are the feeding concentrations of CTA, EHA and UPyEA, respectively.

[4] ϕ_{UPy} = [UPyEA]/([UPyEA]+[EHA]) in the synthesised polymers;

[5] the number of UPy groups per chain;

[6] the number of EHA monomers between two neighbouring UPy groups;

synthesised using RAFT method,[210, 229] and detailed characteristic information is show in Table 3.1. Note that: i) changing the ratio between the total amount of two monomers and the amount of CTA can tune the molecular weights of co-polymers; ii) changing the ratio between EHA and UPyEA can tune the ratio of UPyEA (ϕ_{UPy}) in the co-polymers. iii) to increase solubility of UPyEA in DMF, high temperature is required, e.g. ~130°C and polymerisation time for the polymer with high UPy ratio was also slightly longer. iv) for synthesis of homo-polymer poly(2-ethylhexyl acrylate) (PEHA), the polymerisation was conducted in toluene at 80 °C and used AIBN as the radical initiators. Here we note that the reaction activities of HEA is larger than that of UPyEA,[50] which may lead to the gradient distribution of UPyEA along a polymer chain. However, in the discussion below and modelling in Chapter 4, we assume that the UPyEA monomers are randomly distributed along a chain. Molecular weights and distribution were measured using SEC, as shown in Table 3.1. Typical NMR result UPyPEHA is as follows: ^{1}H (500 MHz, d_6-DMSO) δ: 0.7-2 (-C$\underline{H}_2-C\underline{H}-$ in polymer backbone), 3.2 (2H, -C$\underline{H}_2$-S-), 3.8-4.2 (4H, -O-C$\underline{H}_2 - CH_2 - CH-$ and -

O-C$\underline{H}_2$ − CH_2 − NH−), 5.8 (1H, pyrimidyl-H); ^{12}C (500 MHz, d_6-DMSO) δ: 14.0, 18.9, 22.6, 24.1, 28.8, 29.4, 30.6, 32.4, 35.4, 38.9, 41.9, 45.4, 60.9, 67.5, 104.8, 125.2, 152.1, 154.4, 168.2. ii) PEHA: ^{1}H (500 MHz, d_6-DMSO) δ: 0.7-2 (-C$\underline{H}_2$ − $C\underline{H}$− in polymer backbone), 3.9 (2H, -O-C$\underline{H}_2$ − CH_2 − CH−); ^{12}C (500 MHz, d_6-DMSO) δ: 11.1, 14.0, 22.9, 23.9, 24.1, 28.2, 28.9, 29.1, 29.4, 31.0, 35.4, 38.9, 41.9, 43.4, 46.8, 67.5, 125.2, 172.0, 175.2.

3.2.3 Characterisations

General introductions to the characterisation methods used in the work are provided in Chapter 2. However, we provide some specific details below for each technique used.

Nuclear magnetic resonance (NMR)

NMR (^{1}H and ^{13}C) characterisations were performed using a Bruker 500M Hz NMR instrument with tetramethylsilane (TMS) as the internal standard and deuterated chloroform ($CDCl_3$) and d_6-DMSO were used as solvents for PEHA and UPyPEHA, respectively. Polymer solutions with concentration about 50 mg/ml were used and 512 scans were performed to obtain spectra with good signal-to-noise ratio. UPyEA solution in d_6-DMSO with concentration about 4 mg/ml and 512 scans were performed.

Size exclusion chromatography (SEC)

The average molecular weight and polydispersity (PDI) were measured using SEC, a Waters Breeze instrument equipped with multiple water columns covering molecular weight range from 2000 to 80000 g/mol with tetrahydrofuran as the eluant (1 mL/min) and a Waters 2410 refractive index detector was used. A polystyrene standard was used for calibration. Polymer solution with concentrations of about 1 mg/ml were used for the measurements.

Small and Wide Angle X-ray scattering

Small and wide angle X-ray scattering (SAXS/WAXS) experiments were performed using a SAXSpace system (Anton Paar, Graz, Austria) with an x-ray incident wavelength of λ =0.154 nm. For this experimental set-up, described in detail elsewhere,[236]

the minimum and maximum accessible scattering vectors are q_{min} =0.06 nm^{-1} and q_{max} = 18.5 nm^{-1}, respectively, where $q = 4\pi sin\theta/\lambda$, and 2θ is the scattering angle.q_{min} and q_{max} correspond to a maximum/minimum spatial resolution of 0.34/104 nm. A Mythen X-ray detector (Dectris Ltd., Baden, Switzerland) was used to record the 1D scattering patterns at sample-to-detector distances of 317 mm (SAXS) and 130 mm (SAXS and WAXS), respectively. Each polymer sample was filled into a paste cell (Anton Paar, Graz, Austria) of 1 mm thickness and sealed with a thin Kapton polyimide film window. All experiments were performed at a temperature of 25°C ± 0.1°C, using a typical exposure time of 1 hour. Background scattering from the empty cell as well as from the solvent was subtracted following standard procedures.[236] The reduced SAXS data were analysed using a simple empirical fit combining a powerlaw with either one or two Gaussian contributions to follow the overall structural trends.

(Modulated) Differential Scanning Calorimetry ((M)DSC)

The calorimetric response of the synthesised polymers were determined using a TA Q2000 heat flux Differential Scanning Calorimeter (DSC) using both standard and modulated DSC (MDSC). For both DSC and MDSC, the samples were first heated to T =403 K using a heating rate of 20 K/min, and the samples were kept for 5 min to ensure a good thermal contact with the sample pans, after which they were cooled to T =103 K at a rate of 20 K/min. The subsequent measurements were performed on heating from T =103 to 403 K using a heating rate of 10 K/min for the standard DSC measurements. The MDSC measurements were also conducted on heating, in which a 1 K amplitude sinusoidal temperature oscillation with a 60 s modulation period was added to a linear heating ramp characterized by either 2 or 3 K/min heating rate.

Broadband Dielectric Spectroscopy (BDS)

Broadband Dielectric Spectroscopy (BDS) was performed using a Novocontrol Alpha-N analyser (10^{-2} to 10^{6} Hz) connected to a sample cell through a high impedance active test interface (Novocontrol 2-Wire Test Interface ZG2). Data were collected over a broad temperature range of -160 to 130 °C on heating with a temperature accuracy of ±0.1°C using a Novocontrol Quatro cryo-system. The polymer samples were sandwiched between 20 mm diameter metal electrodes and the inter-electrode spacing was

set using 0.1 mm silica spacers. More details about the sample preparation are shown in Section 2.1.5, Chapter 2.

Oscillatory and stress relaxation shear rheology

Small amplitude oscillation shear measurements (SAOS) and step strain stress relaxation experiments were performed using a Rheometrics Advanced Expansion System (ARES) strain-controlled rheometer equipped with two complementary Force Rebalance Transducers. The experiments were conducted within a temperature range from T_g ($\approx$ 203 to 215 K) to T=403 K using a convection oven operating under nitrogen flow with a temperature control better than ±0.5 K. A plate-plate geometry was used in the experiments and either 3 or 10 mm diameter parallel plates were used depending on the composition of the samples and on the testing temperature. Polymer films with a thickness of about 1.5 mm were obtained by placing the polymers in a round mold at T=403 K under vacuum for 3 days. The films were placed between the rheometer plates and their edges were trimmed to match the geometry. For the range of determined material moduli, we confirmed that our results are not influenced by a variation of plate diameters (3, 5 and 10 mm plates) and thus recorded torques, demonstrating that we are not influenced by instrument compliance effects.[184]

For the oscillatory shear experiments, the complex shear modulus ($G^* = G' - iG''$) was determined over an angular frequency range of 0.628 to 62.8 rad/s. To obtain the rheological response over a wider frequency range, time-temperature superposition (TTS) using horizontal shift factors was used. We note that vertical shifts are also often used to account for the temperature variation of the density. However, with the amount of the polymers available in this work, we could not reliably determine the temperature dependent densities and thus choose to use only horizontal shift factors. To investigate the accuracy of this approach we plot the loss tangent $\tan(\delta)$ vs the complex modulus G^* in a so-called Van-Gurp-Palmen (VGP) plot [137, 138] (Chapter 4, Figure 4.3). This representation removes all explicit time-dependence from the data, and so indicates whether an accurate frequency-shift TTS is possible or not. Based on this plot, we find that for the data where TTS works well, as described in more detail further on, master curves are formed without the need for vertical shifts, thus supporting our approach of only using horizontal shift factors. TTS was initially conducted using the

software, *Orchestrator* from TA instrument, which takes both G' and G'' into account in the fitting procedure. For the samples with 0, 2 and 6 mol% UPy groups, TTS was solely performed using this fitting procedure. For the samples with 9 and 14% UPy groups, the initial fitting was performed in the same manner, subsequently followed by small manual horizontal adjustments (¡ ±10 %) aimed to result in a continuous G' curve. Also, as further described below, we demonstrate that when TTS works well, the results are fully consistent with those resulting from stress relaxation measurements, which cover a wider frequency range without need for TTS, further supporting the fact that the introduction of a vertical shift factor is not necessary within the accuracy of the experiments for our polymers (details about TTS are given in Chapter 4).

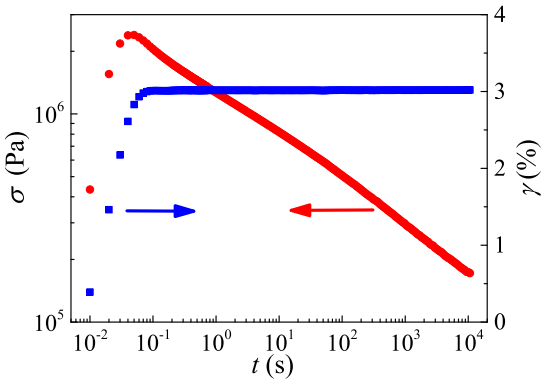

Figure 3.2: Stress σ and strain γ as a function of time for UPyPEHA14 at 263 K in a step stress relaxation measurement.

In stress relaxation experiments, a step strain with a rise time from 0.01 to 0.1 s within the linear regime was applied to the material and this strain subsequently remained constant over time. The stress responding to the applied strain was recorded as a function of time.In practice, before the real test, a small pre-strain was applied to the material which aims to eliminate the effect of pre-stress in the material and improve the experiment reproducibility. The waiting time for the pre-strain to relax should be long enough so that the pre-stress from the pre-strain is negligible. A free software, *iRheo*, was used to do the transformation from stress relaxation data to dynamic moduli.[145] The advantage using *iRheo* for the transformation is that it takes account of the response also from the initial strain ramp period and extends the frequency range of the transformed moduli. Figure 3.2 shows the stress and strain as a function of time for

UPyPEHA14 at 263 K, as an example to illustrate the input data for *iRheo* to conduct the transformation. The interpretation of the output from *iRheo* and the assessment of its accuracy are discussed later.

Atomic Force Microscopy (AFM)

Atomic Force Microscopy (AFM) was performed on the polymer films using an Icon FastScan-Bio AFM (Bruker), in standard Tapping Mode (repulsive regime) in air with a TESPA-V2 (Bruker) probe at 284 kHz. Whilst the amplitude setpoint is normally set to the minimum to achieve stable imaging, to enhance phase contrast a slightly lower amplitude, approximately 85% of the free amplitude (approximately 10 nm) was used. Low magnification surveys were performed both optically and with AFM, revealing an extremely flat spin coated polymer film with occasional widely spaced (10-30 μm) pores cause by solvent venting. Between the pores the surface roughness (Ra) was 0.14 nm at a scan size of 500 nm. Images presented here are the phase images only with a contrast range of about 1 degree, acquired at 1024 pixel resolution. The relevant image features were only visible at a scan-range of less than 1 μm. The AFM sample was prepared by dissolving UPyPEHA6 in CH_3Cl (3 mg/ml) and spin-coated onto silicon wafer at 3000 rpm for 30 s. The sample was left at room temperature for a week to dry solvents.

3.3 Results and discussions

3.3.1 Structures

The structures of the five polymers were investigated using SAXS/WAXS, as described in the experimental section and the results are showed in Figure 3.3, where scattering intensities $I(q)$ are plotted versus the scattering vector, q. For all polymers, either two or three maxima are observed in $I(q)$, and the two higher q contributions, here termed q_{II} and q_{III}, are observed for all polymers; However, only the UPy-containing polymers show the low-q scattering maximum, termed q_{I}. To investigate how the three scattering contributions vary with ϕ_{UPy}, we perform a simple empirical analysis by describing $I(q)$ as a sum of two Gaussian functions, representing the observed maxima and a powerlaw

that empirically describe the rise in intensity at low q, (Figure 3.4a and b), using the following equation:

$$I(q) = mq^{-n} + \sum_{i=1,\,2} a_i \exp\left(\frac{-(q-b_i)^2}{2c_i^2}\right) \tag{3.1}$$

where b_i gives peak positions. In the case of fitting the SAXS data, the peak positions for q_{I} do not change significantly with increasing ϕ_{UPy}. Thus in the fits, b_1 is fixed to 1.50, i.e. $q_{\mathrm{I}} = 1.5$ nm^{-1}. b_2 decreases slightly with increasing ϕ_{UPy}. q_{II} equals 4.3, 4.3, 4.2, 4.2 and 4.1 nm^{-1} for PEHA0, UPyPEHA2, UPyPEHA6, UPyPEHA9 and UPyPEHA14, respectively. For the fitting of the WAXS data we use a sum of two Gaussians (the powerlaw contribution in equation 3.1 is not included in these fits), where the first Gaussian accounts for the broadening at the low q side and this Gaussian is fixed in position for all samples. All fitting parameters corresponding to the second Gaussian are kept free. Since the peak at q_{III} is described using a sum of two Gaussians, the peak positions for q_{III} are defined as the q values corresponding to the maxima of the sums of the two Gaussians. We find that q_{III} equals 12.9, 12.9, 13,0, 13.0 and 13.1 nm^{-1} for PEHA0, UPyPEHA2, UPyPEHA6, UPyPEHA9 and UPyPEHA14, respectively. The high-q diffraction peak, here observed at q_{III} ~13.0 nm^{-1} and thus corresponding to distances of $d_{\mathrm{III}} \sim 2\pi/q_{\mathrm{III}} \sim 0.48$ nm, is a general characteristic of amorphous polymers and typically originates from correlations between atoms situated in different chains.[203, 204] Since chains are typically interacting through van der Waals interactions this scattering contribution is often termed the van der Waals peak.[237] For amorphous polymer without side-chains this contribution is normally observed around 15 nm^{-1} and shifts to lower q for increasing temperature, due to thermal expansion.[237] Importantly, a range of scattering studies using x-ray and/or neutron scattering, have investigated comb-like polymers, similar to our PEHA0, with alkyl-based side-chains including poly(n-alkyl methacrylates),[197, 199, 230] poly(n-alkyl acrylates),[202]poly(di-n-alkyl itaconates)[198] and poly(alkylene oxides).[201] X-ray and/or neutron scattering studies on these systems also demonstrate a scattering peak in the same wave-vector range as our q_{III} peak.

To study the corresponding correlations in more detail, isotope labelling was used in neutron scattering studies on poly(n-alkyl) methacrylates (PnMAs).[200, 201, 238] Fully deuterated PnMAs show a clear peak at q_{III}, whereas it was demonstrated that

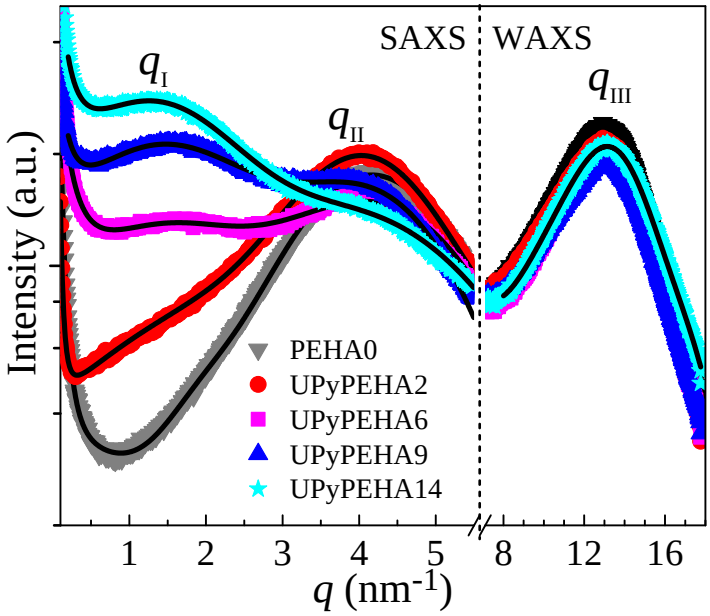

Figure 3.3: (a) X-ray scattering intensity measured on PEHA0 and its UPy functionalised counterparts (2, 6, 9 and 14% UPy) as a function of q. The solid lines in the SAXS region are the best fits using the combination of a powerlaw and two Gaussian equations for q_{I} and q_{II}. The solid line in the WAXS region is the best fit for UPyPEHA14 using the combination of two Gaussian equations for q_{III}. For clarity, fitted lines are other samples are not plotted. In WAXS fits, one Gaussian equation accounts for the broadening at low q side is fixed for all samples. The contributions of each fitting component are shown in Figure 3.4a and b for SAXS and WAXS respectively.

when the side chain was made nearly invisible to neutrons by using partial deuteration, the scattering peak at q_{III} disappears demonstrating that for polymers with significant alkyl side-chains this contribution is due to correlations between atoms situated within the alkyl side-groups.[200, 238] Moreover, it was demonstrated that the structure factor peak obtained on pure deuterated polyethylene (PE) is very similar both in terms of peak position and temperature dependence further supporting the conclusion that the peak at q_{III} reflects correlations between atoms situated in the side-group of different monomers and the presence of alkyl-rich side-chain PE-like nanometer sized domains in these types of polymers.[200, 238] These results were further confirmed by neutron scattering work on poly(alkylene oxides) (PAOs)[201] where isotope labelling together with neutron polarisation analysis was used to separate incoherent and coher-

ent scattering contributions and the neutron scattering investigation was combined with atomistic MD computer simulations.[238] These studies also confirmed the existence of alkyl nano-domains and that the q_{III} peak was due to correlations between atoms situated in different side-chains (SC) and also in this system the peak is consistent with that corresponding to the amorphous fraction of PE at the relevant temperatures .[239] Referring to Figure 3.3, we see that for our five polymers, the q_{III} peak position is relatively insensitive to a variation in the UPy concentration and the peak position is at most shifting very weakly towards higher q as ϕ_{UPy} increases.

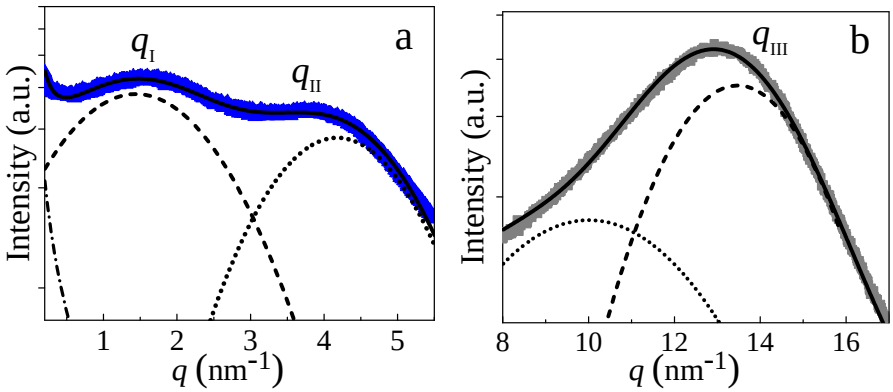

Figure 3.4: Examples to show the fitting contributions as discussed in Figure 3.3 for (a) SAXS of UPyPEHA9 and (b) WAXS of PEHA0.

For comb-like polymers with alkyl-type side-chains discussed above, the scattering maximum corresponding to our scattering peak at q_{II}, here observed at q_{II} ~4.2 nm^{-1} and thus corresponding to distances of $d_{II} \sim 2\pi/q_{II}$ ~1.5 nm,(Figure 3.6a), was also consistently observed.[202–204] It has been clearly demonstrated that the location of the q_{II} maximum is directly related to the length of the side-chains, where the peak is observed at lower q for longer side-chains supporting an interpretation where the peak is related to the average size of the alkyl nano-domains and d_{II} ~1.5 nm is consistent with our side-chains containing 8 carbon atoms.[203] In the neutron scattering investigations both on PnMAs and POAs,[200, 201, 238] the origin of this peak was investigated in detail and it was demonstrated that this peak remains as the alkyl side-chains were made nearly invisible to neutrons. Thus, the peak at q_{II} is interpreted as due to correlations between main-chain (MC) structural units and thus to correspond to

an average inter-chain distance. Given this interpretation, q_{II} thus directly provides information about the size of the alkyl nano-domains. For POAs, the combined neutron and MD simulation study revealed that the correlations underlying the peak at q_{II}, include partial structure factor contributions not only from positive correlations between main chains (MC-MC), as discussed above, but also from positive SC-SC correlations and negative MC-SC correlations.[201] This is expected due to the fact that there is a depletion of side-chains at the position of the main chains. However, the fact that several different correlations contribute means that the variation e.g. with temperature of the peak at q_{II} can be quite complex to interpret. Typically, in the previous studies this peak has been observed to be relatively insensitive to temperature, but as discussed in reference,[238] given its complex origin, this does not necessarily mean that there is no effect of temperature on the separate underlying structural correlations.

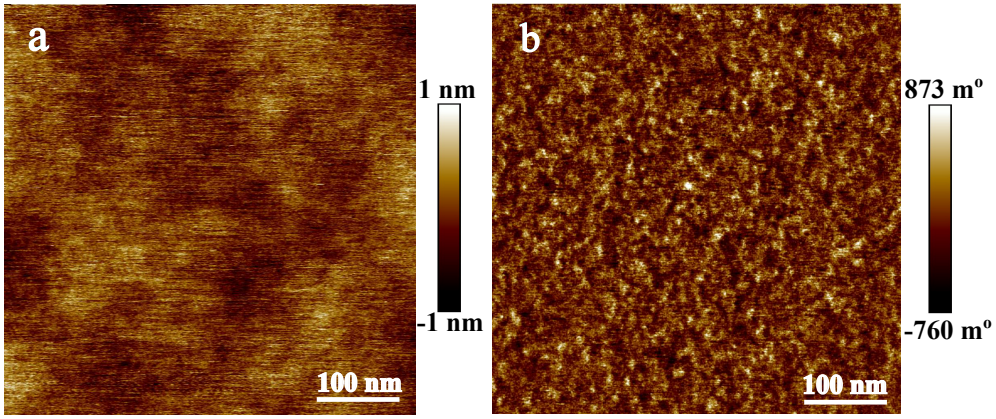

Figure 3.5: AFM height (a) and phase (b) images for UPyPEHA6, see Experimental section for the preparation of the thin film.

The generality of the results, as discussed above, for the peaks at q_{II} and q_{III} have recently been investigated using MD computer simulation also in a more generic bead-spring model for comb-type co-polymers.[238] These simulations confirmed the interpretations of both the scattering peak at q_{II} and q_{III}, and thus the existence of nano-segregation also in such simple model polymers. Importantly, the simulations also demonstrated that nano-segregation can occur even in systems where the main-chain and side-chain energetic interactions are identical, where the segregation will thus be of entropic origin.[238] The existence of PE-like nm-sized domains in the comb-like

polymers is further demonstrated by the effects on dynamics, as demonstrated in experiments using broadband dielectric spectroscopy,[203] calorimetry[202] or neutron spin echo investigations,[238] as discussed in more detail below where we compare these results with our experimental results. As shown in Figure 3.3, the q_{II} peak position is not very sensitive to a variation in UPy concentration and within the accuracy of our empirical analysis we can only deduce a possible shift towards lower q of about 0.3 nm^{-1} between the PEHA0 and the UPyPEHA14 samples, thus demonstrating that the size of the alkyl-rich regions remain at 1.5 nm are not sensitive to the addition of the cross-linkers. However, we do observe a decrease in the intensity of the peak at q_{II} which is reasonable given that the higher the UPy side-chain concentration is, the lower the density of alkyl side-chains becomes.

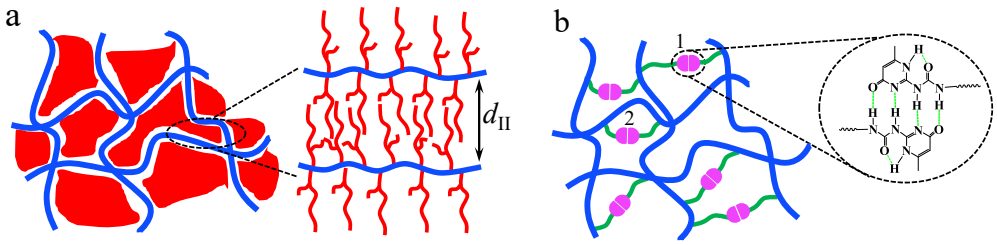

Figure 3.6: Schematic diagrams show (a) nano-phase separated structures for PEHA0 and side alkyl chain arrangements, (b) transient networks through UPy dimers for UPyPEHA. For clarity, nano-phase structures are not shown.

Finally, as shown in Figure 3.3, for the UPy-containing polymers a third scattering maximum is observed at lower q, marked as q_I. The maximum is observed at $q_I \sim 1.5$ nm^{-1} for all UPy concentrations and within the accuracy of our analysis we do not find evidence for any significant variation in its peak position. In a simple interpretation, q_I would thus correspond to a characteristic length-scale of $d_I \sim 2\pi/q_I \sim 4.19$ nm. Moreover, it is clear that the strength of the maximum increases systematically with increasing UPy concentration. This demonstrates that the q_I peak is directly linked to the presence of UPy groups. The strong hydrogen bond affinity between UPy groups with typical bond energies of ~70 kJ/mol (~28 kT at T =298 K)[214, 215] means that we do not expect any UPy monomers to exist freely in polymers, and instead the observed scattering contribution should arise due to the presence of UPy dimers

(Figure 3.6b). However, the remaining question is what arrangement of the dimers that the scattering maximum represents; there are several potential options.

The fact that the q_I peak position is relatively insensitive to UPy concentration, and that the peak strength increases roughly proportionately with UPy concentration, is indicative that the peak may be due to the typical "form factor" for electron density surrounding a single UPy dimer (rather than from structure factor correlations between dimers). The possible origin of the observed q_I peak may be discussed as a type of "correlation hole" effect.[240, 241] A correlation hole arises e.g. in systems such as diblock or triblock copolymers where the scattering properties varies between the blocks so that certain block(s) scatter more than others. Since any chosen block is connected to a block of the opposite type, it is thus surrounded by a "depletion region" where the probability of finding a block of its own kind is lowered which modulates the total q-dependence of the scattered intensity. Combined with the q-dependent scattering from a certain block itself, its form factor, this can give rise to a peak in the q-dependent scattered intensity.[240] Such behaviour is not only typically observed in block copolymers and has been observed also in supramolecular systems with a block-like nature where one of the block-types includes UPy groups. Our UPyPEHA system is a random copolymer and as such one would not expect to observe any correlation hole effects. However, the formation of supramolecular links through UPy dimers means that each high electron density dimer is connected on each side via an alkyl chain to the backbone to which in turn more alkyl chains are connected. Thus, surrounding each UPy dimer there will be an effective "depletion zone" where it is less probable to find another dimer. The combination of the scattering form factor of the dimer together with the lowered probability of other dimers to be situated nearby could be expected to lead to a peak in the scattered intensity at q-vectors consistent with our observations. The fact that we find a systematic increase in the scattering contribution at q_I with increasing UPy concentration and the lack of any significant variation of the peak position with UPy concentration both support this interpretation.

We may note that, at higher UPy concentrations, the "depletion zone" surrounding a dimer may in turn give rise to correlations between dimers, as the structures become packed together. As discussed above, we know that in all these systems free alkyl chains tend to segregate into alkyl-rich regions with a characteristic size on nanometer scale. Thus, it is possible that at least for high UPy concentrations the distance between

two dimers can be correlated through the backbone-backbone correlations across the alkyl-rich regions. We can not exclude that this mechanism could come into play at least for the higher UPy concentrations, but the systematic nature of the variation of the amplitude of the q_I peak with UPy concentration suggests that this mechanism is likely of less importance.

Although it is well known that UPy functionalised polymers can in some situations form self-assembled or aggregated structures,[172, 225] we do not find evidence for UPy aggregates in our samples. In previous work that show self-assembled structures, the fibre structure is observed as a structure factor peak at $q \sim 1$ nm^{-1} in SAXS which is related the inter-fibre distance.[225] As discussed above, we also observe a feature at $q_I \sim 1.5$ nm^{-1}, however, as outlined above, we do not think that this is due to a structure factor contribution from such structures, but instead believe that our low-q SAXS contribution is due to a correlation-hole effect. Moreover, UPy associated aggregates based on crystallisation will melt at around 120 °C[242] and are typically clearly observed in calorimetric studies. As shown below, however, we do not observe any sign of a structural change or melting in our DSC data, see Figure 3.9. Another way to observe structures in supramolecular systems is to image the samples using AFM techniques.[225] To test this, we performed AFM experiments on the UPyPEHA6 sample. The resulting height and phase images are shown in Figure 3.5. The film with a thickness of about ~30 nm thickness spin-coated onto a silicon wafer reveal an extremely flat film with a surface roughness of 0.14 nm and a phase contrast variation of about a degree, both at a scan size of 500 nm; the relevant image features were only visible at a scan range of less than 1 μm. We thus do not find any evidence to support the formation of UPy-based aggregates or crystalline regions, supporting our interpretation. We also note that the linkage groups situated between the polymer chains and the UPy groups, can play an important role in the formation of fibre-like structures. Holger et al. reported that the use of urea or urethane groups as the linkage groups between a poly(ethylene butylene) (PEB) backbone and the UPy groups can promote the formation of the fibre structure. The reason for this is the formation of hydrogen bonds between these groups and nearby chains.[226] On the contrary, polymers without any linkage hydrogen bonding groups, did not form the fibre structure. In our case, we do not have urea or urethane groups between the UPy groups and the polymer backbone, again supporting the lack of aggregated structures. In summary, We can

not totally exclude the formation of UPy-based aggregated or crystalline structures, but we do not find any evidence for the existence of these in our samples. Instead, to summarise our main conclusions are:

a) We find direct support for nano-segregated alkyl side-chain rich regions in all samples on length-scales of ~1.5 nm, which is fully consistent with results for other comb-like polymers with alkyl-rich side chains that typically contain alkyl-rich regions in the size range of 0.5-2 nm. The sizes of the alkyl-rich regions are not significantly affected by the addition of UPy groups, even though some evidence for a small size increase is found.

b) We do not find evidence for any organisation of the UPy dimers into aggregates or other organised structures. We interprete the scattering maximum observed for the UPy containing polymers at low q to be due to a "correlation hole" type effect and thus support an overall random arrangement of UPy dimers through the system.

3.3.2 Rheological responses

The significant effects that the addition of UPy-containing associating side-groups have on the rheological properties, together with the fact that the associations are reversible and temperature dependent, give these types of supramolecular materials unique processing properties[166] as well as self-healing aspects,[223] which have found applications un many fields, including printings,[243, 244] cosmetics,[245, 246] adhesives and coatings.[247–249] The strong effect on the rheology is illustrated by the insets of Figure 3.7a, where the upper left photo (blue frame) depicts the UPyPEHA6 polymer and the lower right (black frame) the UPyPEHA2 polymer. As shown, the room temperature properties of the UPyPEHA2 and the UPyPEHA6 polymers, differ quite dramatically. PEHA0 is a viscous liquid at room temperature whereas UPyPEHA6 is a solid rubbery material.

The linear viscoelastic (LVE) shear response for the five polymers were determined, as outlined in the experimental section. Master curves were constructed for each sample using time-temperature superposition (TTS) at a reference temperature of 363 K, as shown in Figure 3.7. We find that TTS works well over full temperature ranges for PEHA0 and UPyPEHA2, but for UPyPEAH6, UPyPEAH9 and UPyPEAH14, it only works sufficiently well at temperatures higher than 323 K. TTS is

based on the concept of thermo-rheological simplicity[139] meaning that all underlying relaxation mechanisms such as segmental (α) relaxations and chain relaxations (Rouse and/or reptation dynamics) follow the same temperature dependence.[143, 144] Thus, TTS is generally an approximation and for supramolecular systems, dynamics of supramolecular cross-links add to the complexity and it is by no means obvious that TTS should work.[144, 230, 250] For a very detailed investigation of the temperature range for which TTS is valid in our polymers, and a detailed model analysis of the rheological response are shown in Chapter 4. Our objective in this chapter is to demonstrate main effects that an increasing cross-link density has on rheological responses and to relate these effects to variations in structures, dynamics and thermodynamics.

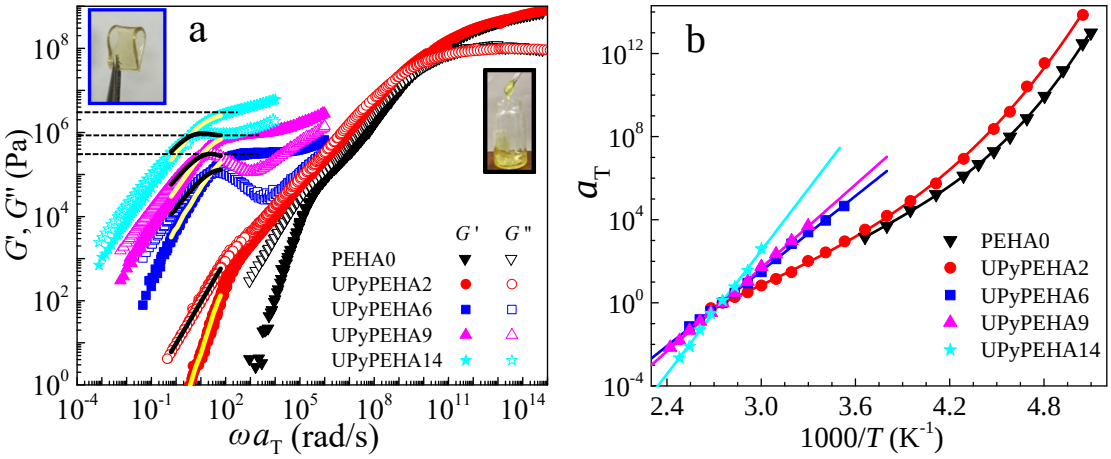

Figure 3.7: (a) Master curves for samples with varying ϕ_{UPy} referring to 363 K. The black and yellow solid lines are the single SAOS measurements at 363 K. Two pictures framed black and blue illustrate the state of the matter for PEAH0 and UPyPEHA6, respectively. For samples with more then 2 mol% UPy, only part of master curves (from plateau to terminal range) are shown. Three horizontal dashed lines indicate plateau moduli calculated using equation 3.2. (b)Shift factors used to build corresponding master curves in panel (a). The solid lines in (b) are VFT fits (PEAH0 and UPyPEHA2) and Arrhenius fits (UPyPEHA6, 9 and 14), and fitting parameters are shown in Table 3.2.

As shown in Figure 3.7a, for PEHA0 and UPyPEHA2, the data can be roughly divided into three regimes: a high-frequency regime ($> 10^{11}$ Hz) characteristic of the glassy state, an intermediate frequency regime ($10^5 \sim 10^{11}$ Hz) where chain-modes

active in melts (including temporary cross-links from UPy groups) are determining the behaviours, and a terminal regime at low frequencies ($< 10^5$ Hz), where chain modes are relaxed and samples flow. The same overall behaviour is also observed for polymers with higher ϕ_{UPy}; however, since the effects of supramolecular cross-linking groups on the dynamics here become significant, these samples are not thermorheologically simple over full temperature ranges and we have thus only included data over a frequency range for which TTS can be used to construct a master curve. We see that within this dynamic range, the tail of the intermediate frequency range described above is observed, followed by a plateau-like regime caused by the supramolecular cross-links and eventually the terminal regime at the lowest frequencies.

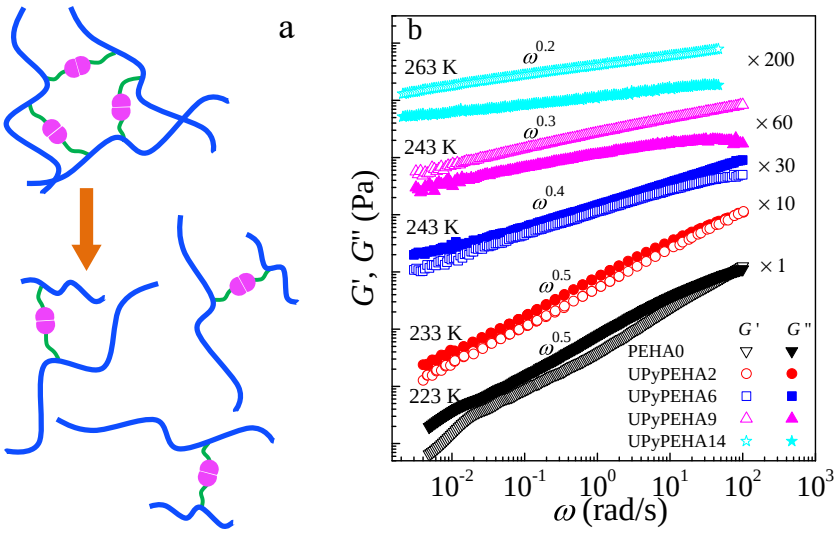

Figure 3.8: (a) Schematic diagram shows the cooperative breaks of UPy dimers for chains to relax in the terminal region. (b) *G*' and *G*"in the frequency range between glass and rubbery plateau, obtained from the transformation of the stress relaxation experiment at 243 K for UPyPEHA6 and UPyPEHA9 and 263 K for UPyPEHA14. A free software, *iRheo*, is used to do the transformation.[145] For, PEHA0 and UPyPEHA2, the TTS results in Figure 3.7 are used. The curves are shifted vertically for clarity.

Since all our polymers are characterised by molecular weights below the entanglement molecular weight for PEHA0, the development of a plateau and a rubber-like response for higher ϕ_{UPy} is solely due to temporary cross-links formed by UPy dimers.

Note that we have not explicitly determined the entanglement molecular weight for PEHA0, but our conclusion is supported both by a comparison to a similar polymer poly(hexyl acrylate)[231] which has an M_e ~30 kg/mol whereas the molecular weights of our samples are smaller than 30 kg/mol, and the fact that we do not observe a plateau modulus in the rheological response for PEHA0, as shown in Figure 3.7a. The elastic plateau modulus (G_N) can be estimated using the following equation:

$$G_N = \upsilon_x RT = \frac{\rho RT}{M_{\mathrm{UPy}}} \tag{3.2}$$

where M_{UPy} is the molecular weight of a strand between UPy groups, which can be estimated from SEC and NMR measurements (shown in Table 3.1). υ_x is the strand density in the network and ρ is the mass density of a polymer. The estimated G_N for UPyPEHA6, UPyPEHA9 and UPyPEHA14 are 3×10^5, 3×10^9 and $3\times10\times^6$ Pa, as horizontal dashed lines indicated in Figure 3.7a. We find that this simple approximation captures the plateau behaviour for all three systems quite well, again demonstrating that the origin of the elastic behaviour in these polymers is the UPy-based associations.

For UPyPEHA2 (two UPy groups per chain on average, see Table 3.1), the main effect of the UPy dimers is the slowing down of the terminal relaxation time, from $\sim 10^{-5}$ s to 10^{-2} s at reference temperature $T = 363$ K. As ϕ_{UPy} is further increased to 6 mol% and above, the terminal relaxation time is further slowed down, and the growth of a plateau modulus becomes clear. We also find that the addition of UPy groups along polymer backbones changes the powerlaw slopes in the terminal regimes.[186, 251] For conventional polymers, the slopes are usually 1 and 2 for G'' and G in terminal regimes, respectively.[134] This is also the case for case for PEHA0 and UPyPEHA2. For UPyPEHA6 and UPyPEHA14, the slopes are 1.2 (G') and 0.9 (G''), and 0.8 (G') and 0.7 (G''), respectively. These results demonstrate that the true terminal relaxation regime is not yet reached within the time window of the experiment.

The breaking of UPy-based associations followed by chain relaxations gives rise to the end of the "plateau" region of the relaxation spectrum, but there are apparently relaxation modes at lower frequencies than this, indicating that full relaxation of the chains requires multiple rearrangements of the dimers. Thus, the inter-chain hydrogen bonding associations delay the relative motion of chains, acting like extra inter-chain

friction for supramolecular polymers. This behaviour is predicted for example from the "sticky Rouse" model often used to model chains with multiple sticky groups along backbones.[184, 252, 253]

Temperature-dependent horizontal shift factors a_T(T) used to build master curves are presented in Figure 3.7b; no vertical shift factor was needed to build the master curves, which demonstrates that for each sample the polymer density is at most very weakly temperature dependent. For polymers with $\phi_{\mathrm{UPy}} \geq 6$ mol%, for $T > 323$ K where TTS is successful, the shift factors a_T(T) are well fitted using the Arrhenius equation with fit parameters provided in Table 3.2. An Arrhenius equation can also describe UPyPEHA2 data well above $T = 323$ K, whereas in the low temperature range find, a_T(T) are best described using the WLF equation. For PEHA0, the data in the whole temperature range is only fitted using the WLF equation. The WLF and Arrhenius fit parameters are provided in Table 3.2.

A change in the temperature dependence of the dynamics from a low temperature WLF to a high temperature Arrhenius behaviour has previously been reported for a range of different supramolecular systems.[185, 186, 189, 210, 230] It was demonstrated that for poly(arcylate)s carrying hydrogen bonding supramolecular associating groups of either single, double or quadruple type, the change to a high temperature Arrhenius behaviour, controlled by supramolecular associations, was observed only for the relatively strong quadruple hydrogen bonding groups.[185] Many small molecular glass-forming liquids follow an Arrhenius temperature behaviour of their characteristic structural relaxation time at temperatures ~100 K above their glass-transition temperature.[254] However, within the dynamic range of interest here, the onset of Arrhenius behaviour observed for polymers containing supramolecular groups characterised by high associating energies, is due to fact that at the corresponding relatively high temperatures the dynamics are totally dominated by the supramolecular associations. At temperatures ~100 K higher than T_g, the segmental relaxations is fast and the chain dynamics leading to the terminal decay, are controlled by the supramolecular associations. Thus, one expects the activation barrier controlling the chain rearrangements to be related to a relevant average supramolecular association energy. An important question, however, is how this activation barrier energy varies with ϕ_{UPy}?

Activation energies E_a and pre-factors τ_0 for four UPy-containing polymers were determined from fitting of the data to an Arrhenius equation ($\tau = \tau_0 \exp(E_a/(kT))$)

and the results are shown in Table 3.2. We find that E_a increases systematically with increasing ϕ_{UPy}, ranging from 78 kJ/mol for UPyPEHA2, to 191 kJ/mol for UPyPEHA14. The bonding energy between UPy dimers in chloroform is typically ~70 kJ/mol.[214, 215] For unentangled chains with one UPy group (or none), full relaxation of their internal configurations and their contribution to stress relaxation is possible without breaking any UPy dimers. Hence, the long-time stress relaxation must be due only to those chains with two or more UPy groups. Typically, the UPy groups are spaced far apart along the chain and so the chain between UPy groups is flexible. Hence, the critical events permitting stress relaxation is likely to involve the breaking of a UPy dimer, followed by internal rearrangement of chains and re-association of UPy groups. As discussed above, UPyPEHA2 contains on average two two UPy groups per chain. Hence, it is reasonable that the E_a for UPyPEHA2 appears to close to the UPy dimer bond energy.

However, for samples with more than 2 mol% UPy groups, terminal stress relaxation cannot be achieved through the cumulative effect of a succession of "single dimer breaking" events. For UPyPEHA9 and UPyPEHA14, the number of EHA monomers between two UPy groups are ~13 and ~6, respectively, which in turn is close to the Kuhn length for the polymer poly(hexyl acrylate) that has a structure similar to PEHA0,[231] indicating that the chain segment between two consecutive UPy groups is not flexible. Thus, when a single dimer is broken, it is likely that the inter-UPy-group chain segment does not have enough flexibility to effectively "search" for a new UPy-group to pair with. Instead, of exchanging association partner, it will then return its original UPy partner and no stress is lost.[184] Only when several dimers are broken cooperatively can the chain achieve enough flexibility to relax stress. We thus arrive at the simple picture showed in the sketch of Figure 3.8a, where the terminal relaxation is controlled by cooperative breaking of several UPy dimers. As a simple approximation, we can use the ratio of the determined activation energy and the single dimer association energy to estimate the number of dimers needed for flow. We find that this number is set by ϕ_{UPy}, and ranges from ~1 to 3 for our polymers.

Interestingly, we find that the Arrhenius pre-factor τ_0, determined in the fits, decreases from values consistent with a typical vibrational time-scale of $\tau_0 \sim 10^{-14}$ s to significantly lower values for increasing ϕ_{UPy},[255] as shown in Table 3.2. A variation

Table 3.2: WLF and Arrhenius fitting parameters for the LVE shift factors, for PEHA0, only WLF fit in the whole temperature range was conducted; For UPyPEHA2, both WLF fit over the whole temperature range and the Arrhenius fit over the terminal range were conducted; For samples with $\phi_{UPy} \geq 6$ mol%, Arrhenius fits over temperatures above 323 K were conducted.

Sample codes	WLF fits		Arrhenius fits	
	C_1	C_2	-$\log_{10}(\tau_0)$ (s)	E_a (kJ/mol)
PEHA0	9.9±0.3	109.9±1	–	–
UPyPEHA2	11.3±0.4	89.9±0.9	15±0.1	78±0.7
UPyPEHA6	–	–	22±0.2	108±1.1
UPyPEHA9	–	–	24±0.1	116±1.2
UPyPEHA12	–	–	38±0.1	191±0.6

of the pre-factor is commonly found for the temperature dependent structural α relaxation of liquids and polymers. To account for this variation, a relevant activation free energy is often considered and an activation entropy ΔS is thus introduced, according to:

$$\tau = \tau_0 \exp\left(\frac{E_a - T\Delta S}{kT}\right) = \tau_0 \exp\left(\frac{-\Delta S}{k}\right)\exp\left(\frac{\Delta H_a}{kT}\right) \tag{3.3}$$

and a variation in the pre-factor tau0 is thus associated with a variation in the activation entropy ΔS. Many liquids, particularly within the highly viscous regime, show significant non-zero values of $\Delta S/k$.[256, 257] Moreover, for a wide range of different systems including polymers, proteins, and small molecular formers, $\Delta S \approx \Delta H$ (or $\Delta S \approx E_a$ at constant pressure), a behaviour often termed an entropy-enthalpy compensation rule or a Meyer-Nelder rule.[257, 258] As shown in equation 3.3, this is equivalent to stating that the Arrhenius attempt time-scale τ_0 varies exponentially with the activation energy. For our supramolecular system the pre-factor variation, described above, translates to a finite activation entropy which varies with ϕ_{UPy} (given that we assume that τ_0 remains constant and the pre-factor variation is due to an increasing activation entropy with an increasing ϕ_{UPy}). We find that the activation entropy determined in this manner increases systematically with increasing activation energy (or enthalpy) and the observed behaviour is thus similar to that often find in literature.[256–258]

Finally, to investigate the behaviour in the intermediate frequency range between the glassy and plateau regimes for all our polymer samples without any need to use TTS, we conducted stress relaxation upon step strain experiments at chosen temperatures, as described in the Experimental section. We converted the stress relaxation modulus to frequency dependent storage and loss shear moduli using the software *iRheo* and obtained data over ~4 decades in frequency. The results are shown in Figure 3.8b for our polymers, and as shown we observe a clear variation of the frequency-dependent powerlaw-like response where a higher ϕ_{UPy} corresponds to a smaller effective powerlaw exponent. For PEHA0, the storage modulus can approximately be described as $G' \propto \omega^{0.5}$, as expected for a dynamic regime dominated by Rouse behaviour.[134] However, as ϕ_{UPy} is increased, the powerlaw exponent systematically decreases from 0.5 and a value of ~0.2 is found for UPyPEHA14. The presence of associating UPy groups along the backbone clearly affects the relaxation mode distributions. Interestingly, similar results have been observed for nano-composites prepared from silica nanoparticles (SNP) dispersed in poly(2-vinylpyridine) (P2VP).[233] For this system, a powerlaw exponent of 0.5 is observed for pure P2VP, but the powerlaw is decreasing for increasing SNP loading and reaches ~0.2 for material with 31% (in volume) SNP loading.

3.3.3 The thermodynamic and dynamic response

DSC measurements for our five polymers were performed on heating with a heating rate of 10 K/min, as described in detail in the Experimental section. The measured temperature-dependent specific heat capacity C_p data are shown in Figure 3.9a, clearly demonstrating the C_p step characteristic of a glass transition for each polymer. Even though it is clear that the glass transition becomes broader with increasing ϕ_{UPy}, as discussed in more detail below, we do not find evidence for multiple glass transitions even though the data for the highest ϕ_{UPy} is somewhat more noisy. As discussed above, for PnMAs with similar structure to our PEHA0, segregation on the nanometer scale was demonstrated for polymers containing linear alkyl side-chains with more than $n_C > 3$ carbons.[203] The nano-segregation was also observed in dynamic and viscoelastic properties as characterized by broadband dielectric spectroscopy[203], neutron scattering[200] and rheology.[199, 203] With regards to calorimetry, a broadening

of the complex heat capacity C_P^* response was observed for alkyl chains with $n_C > 3$ and for alkyl chains of $n_C > 10$, two separate peaks in the imaginary part of the complex heat capacity C_p'' were observed indicating the presence of two separate glass transitions, where the higher temperature transition is the conventional glass-transition and the lower temperature transition was assigned to the nano-segregated polyethylene-like regions. For our PEHA0 sample with $n_C = 8$ (a 6 carbon alkyl chain with a 2-carbon branch), we observe only one step in C_p and correspondingly one step in C_p' and one peak in C_p'' in the calorimetric response determined using MDSC (see Figure 3.11). Thus, our calorimetry results are consistent with the calorimetry results for PnMAs.

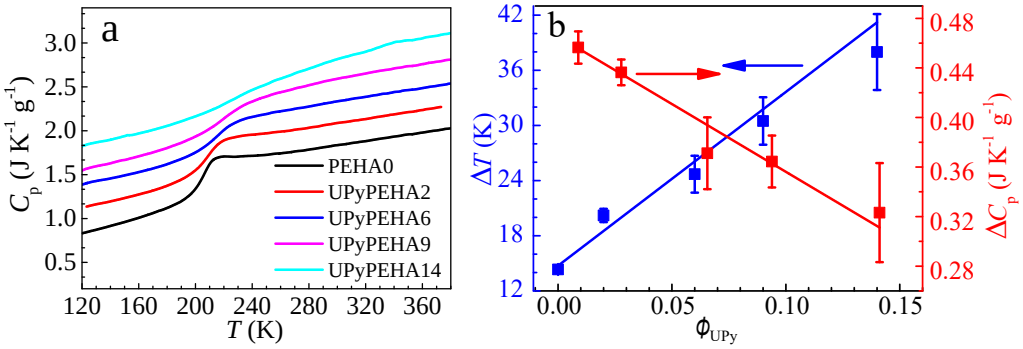

Figure 3.9: (a) Specific heat capacity C_p of the (co-)polymers as a function of temperatures for PEHA0 and UPyPEHA with various ϕ_{UPy}. The thermograms have been vertically shifted for clarity, allowing to illustrate broadening of glass transitions as increasing ϕ_{UPy}. (b) Temperature differences ΔT between T_{onset} and T_{offset} as well as the step amplitude ΔC_p as a function of molar UPy fraction ϕ_{UPy}. The blue and red lines are guide to eye.

As shown in Figure 3.10, glass transition temperatures based on different definitions, increases systematically with ϕ_{UPy}. A similar phenomenon of T_g on ϕ_{UPy} has been previously observed for other supramolecular systems.[213] We note that both for our system and for these reported supramolecular systems, the crosslink concentration is <15 mol%. The typical bonding energy between UPy dimers is 70 kJ/mol which for temperatures near T_g corresponding to 42 kT. Thus, near T_g most crosslinks (UPy dimers) are "active" and we can view UPy-containing polymers as effectively chemically cross-linked polymers. It is thus interesting to compare the T_g behaviour in our system with the behaviours observed for chemically cross-liked polymer

systems.[259–261] The observed cross-linking dependence of T_g can typically, at least up to moderate cross-linking densities of ~25%, be well described using a linear behaviour, as shown in a range of publications[259–261] and the observed behaviour has been modelled based on both free volume and entropy arguments.[262, 263]

The breadth of the glass transitions is clearly increasing with ϕ_{UPy}, as seen directly in Figure 3.9a and quantified as $\Delta T = T_{\mathrm{offset}} - T_{\mathrm{onset}}$ in Figure 3.9b. This result demonstrates that as ϕ_{UPy} increases, the distribution of time-scales characterising motions underlying the structural α relaxations becomes wider. This is expected since the addition of cross-links will induce a variety of environments for the polymer segments where the effects on their dynamics are determined by the distance and connection to one or several cross-links. Similar effects are also observed in other cross-linked rubbers[262] and other supramolecular materials.[233] Finally, the strength of the transition ΔC_p, characterised by the step height on a C_p curve is shown in Figure 3.9b and it is clear that ΔC_p decreases nearly linearly with increasing ϕ_{UPy}. Considering that $\Delta C_p = T_g(\partial S^{\mathrm{melt}}/\partial T - \partial S^{\mathrm{glass}}/\partial T)|_{T_g}$ (see Chapter 2),[155] and the fact that T_g increases with ϕ_{UPy}, thus T_g-renormalised ΔC_p ($\Delta C_p/T_g$) decreases as increasing ϕ_{UPy}, indicating that less entropy is released during glass transitions for samples with higher ϕ_{UPy}.

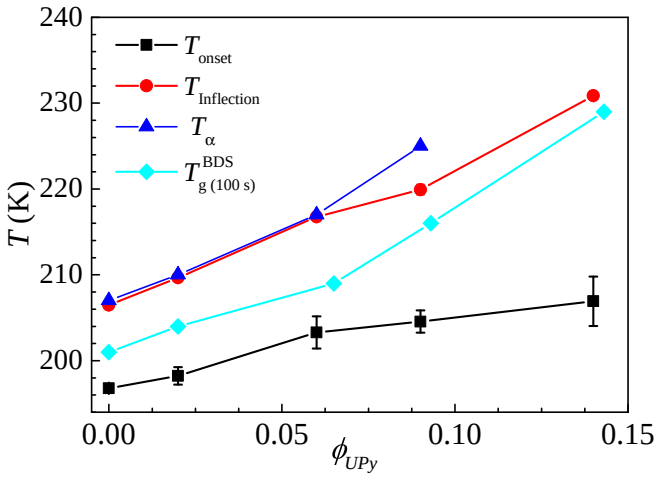

Figure 3.10: Various definitions of the glass transition temperatures from DSC, MDSC and BDS measurements as a function of ϕ_{UPy}.

That an increasing cross-link density reduces the magnitude of released degrees

of freedom at the glass-transition is expected and similar results are typically also observed for other cross-linked polymer systems.[260, 261] Moreover, the change in heat capacity ΔC_p at T_g has sometimes been used to define a thermodynamic fragility and attempts have been made to correlate this with the dynamic fragility m, defined as the temperature dependence of structural relaxation time ($m = d(\log\tau_\alpha)/d(T_g/T)|_{T=T_g}$) when temperature approaches T_g[264]). We will show below that the dynamic fragility m for our polymer system decreases with increasing ϕ_{UPy}, which is consistent with such a correlation. It has been demonstrated, however, that the relevance of such correlations depends very much on the particular system.[265, 266] Small molecular glass-formers show only a weak, if any, correlation between ΔC_p and m;[266] polymers show a decreasing ΔC_p which decreases with increasing m, whereas inorganic glass-formers show an increasing ΔC_p with increasing m.[266] The behaviour for our supramolecular polymers with a controlled degree of cross-linking is thus closest to that observed for inorganic glasses, where the coordination number between the fundamental units can be accurately determined.[267]

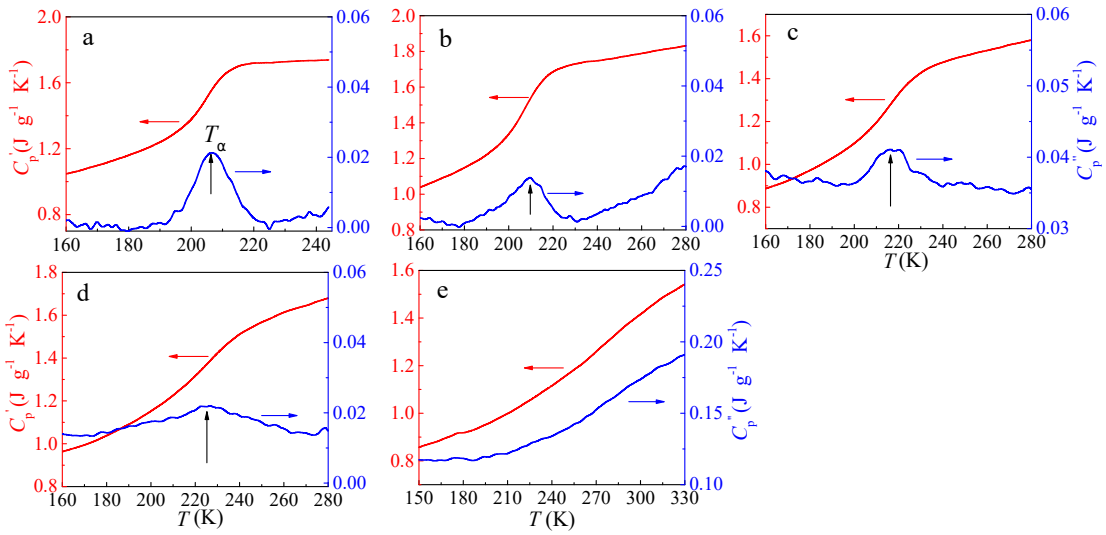

Figure 3.11: The real part C_p' and imaginary part C_p"of complex heat capacity C_p* for (a) PEHA0, (b) UPyPEHA2, (c) UPyPEHA6, (d) UPyPEHA92 and (e) UPyPEHA14, measured by MDSC with a period time (t_p) of 60 s and modulated amplitude of 1 K at 3 K/min heating rate, the angular frequency, $\omega = 2\pi/t_p$, thus characteristic relaxation timescale, $\tau = 1/\omega$. [268]

The real part C_p', imaginary part C_p"of complex heat capacity C_p* and heat flow phase angle (δ) can be determined from MDSC measurements (see Chapter 2 for details):[268]

$$C_p^* = C_p' - iC_p'' \tag{3.4}$$

$$\tan(\delta) = C_p''/C_p' \tag{3.5}$$

C_p' and C_p" are plotted as a function of temperatures in Figure 3.11. During the glass transition, a step-like increase in the C_p' curve and a peak feature in the corresponding C_p" curve are observed for PEHA0 (Figure 3.11a). The temperature corresponding to the peak position in C_p" curve is defined as the glass transition temperature (T_α).[268, 269] As ϕ_{UPy} increases, the step characteristic becomes less and less obvious and the peak becomes broader, which is consistent with the ΔT and ΔC_p data shown in Figure 3.9b. For UPyPEHA14, the peak characteristic disappeared completely, thus T_α cannot be measured for UPyPEHA14. The modulated heat rate ω in a MDSC measurement is related to the period time t_p: $\omega = 2\pi/t_p$, thus the characteristic relaxation time τ which is related to the structural relaxation can be determined: $\tau = 1/\omega$.[269–271] Plot of τ against $1000/T_\alpha$ is shown in Figure 3.14a, which is consistent timescales for α relaxations from BDS (discussed below).

To further characterise the molecular relaxation behaviour of the synthesised polymers, BDS is performed over a frequency range from 10^{-2} to 10^6 Hz, as described in Experimental section. Figure 3.12 shows full dielectric spectra (ε' and ε'') for all samples at various temperatures. Starting with PEHA0, we find that, in addition to a contribution from ionic dc-conductivity (σ_{dc}) at the lowest frequencies, two relaxation processes are observed and they are situated relatively close together (Figure 3.13a). As discussed in detail below, we assign the slowest relaxation, termed α, to the structural or segmental relaxation, which is directly related to the glass transition of polymers. The higher frequency relaxation, here termed α^*, is assigned to relaxations within the alkyl-rich nano-segregated regions. Both α and α^* relaxations are observed for all polymers as shown in Figure 3.12; We find that increasing ϕ_{UPy} leads to a decrease of peak amplitude for both relaxations, and particularly a significant change of their relative amplitude. This is clearly demonstrated in Figure 3.13d where α^* data have been rescaled so that the peak amplitude is the same for all samples, and the horizontal and vertical rescale factors A and B are listed in the legend. In relation to the

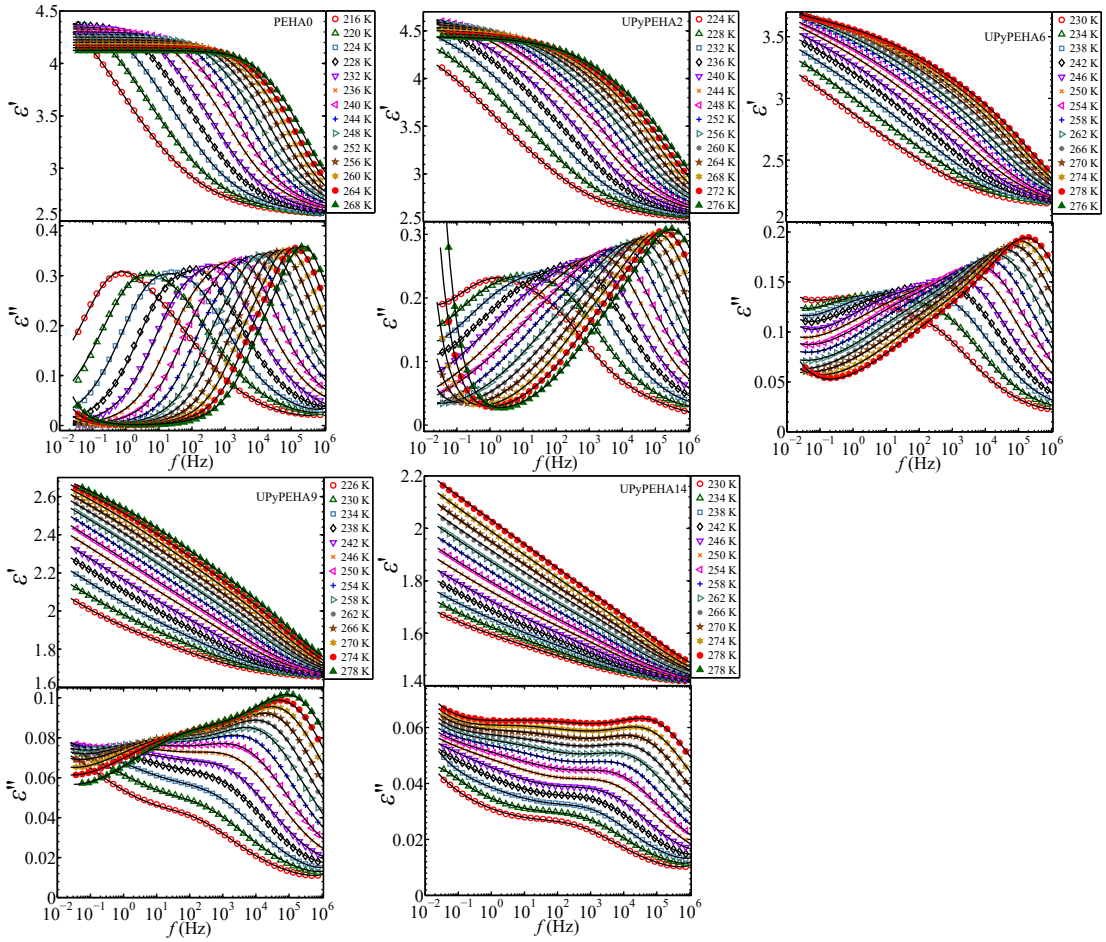

Figure 3.12: Real ε' and imaginary ε'' part of complex permittivity for (co-)polymers with varyingϕ_{UPy} at various temperatures. Solid lines are the best fitting results to the data using Equation 3.6.

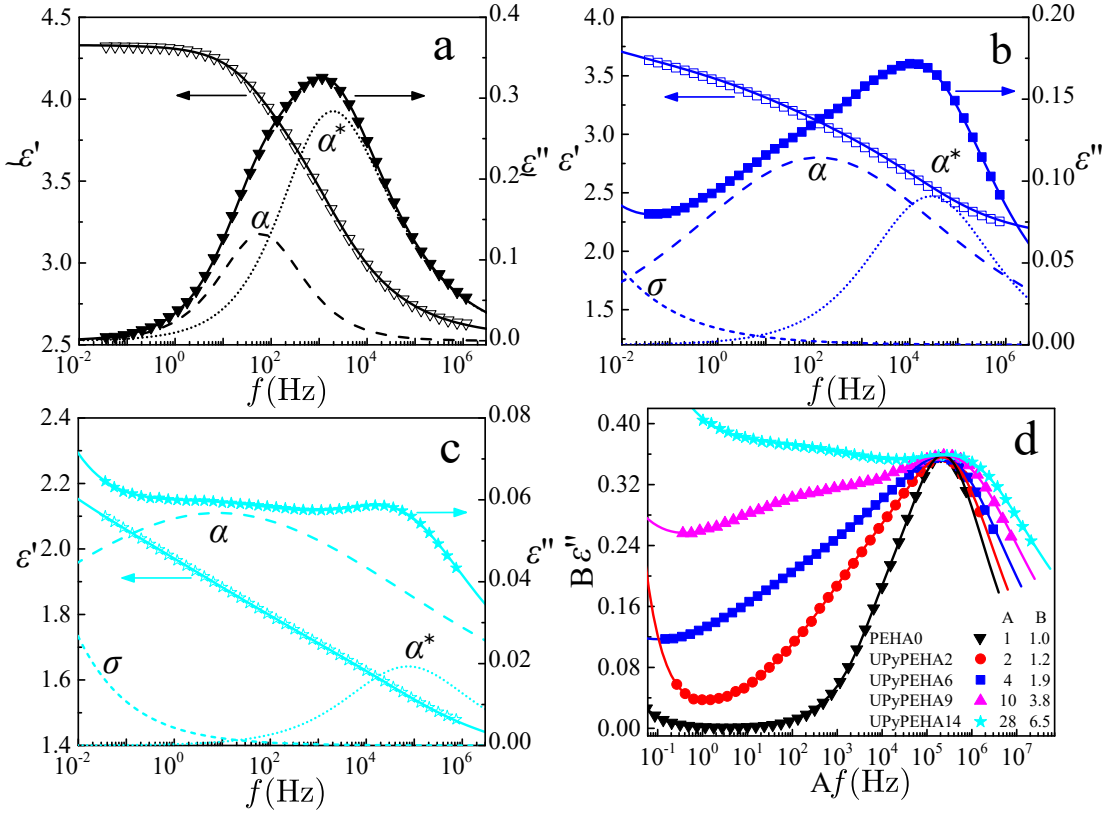

Figure 3.13: Real ε' and imaginary ε'' part of complex permittivity as function of frequencies for a) PEHA0 with $T = 236$ K, b) UPyPEHA6 $T = 258$ K and c) UPyPEHA14 $T = 272$ K. The dotted and dashed lines represent the imaginary part of the different process contributions (σ, α, α^*) used to fit the data. d) Normalized ε'' at T=268 K for PEHA0 and the samples containing 2, 6, 9 and 14 % molar UPy contents. A and B in d) are the scaled factors based on the α^* relaxation peak.

α^* relaxation, the α relaxation becomes stronger for increasing ϕ_{UPy}. The α-relaxation itself becomes weaker for increasing ϕ_{UPy} but the variation is relatively small, so the main observed effect in Figure 3.13d is due to a weakening of the α^* relaxation for increasing ϕ_{UPy}. The other effect is a broadening upon increasing ϕ_{UPy} observed for both the α and α^* relaxations. Both the decreasing strength and the broadening of the α relaxation with increasing ϕ_{UPy} are consistent with our DSC results, as described above. The Havriliak-Negami[272] (HN) equation was used to fit the relaxation contributions to the real $\varepsilon'(\omega, T)$ and imaginary $\varepsilon''(\omega, T)$ parts of complex dielectric permittivity

$\varepsilon^*(\omega,\ T)$ and an additional powerlaw exprssion was added to account for the ionic DC-conductivity at low frequencies. The total fitting equations can be expressed as following:

$$\varepsilon^* = -i\frac{\sigma}{\varepsilon_0\omega} + \varepsilon_\infty + \sum_{j=\alpha,\alpha^*} \frac{\Delta\varepsilon_j}{(1+(i\omega\tau_j)^{a_j})^{b_j}} \tag{3.6}$$

Where ε_∞ is the high-frequency limiting dielectric permittivity, $\Delta\varepsilon_j$ is the relaxation strength for the jth relaxation process (α, α^* and γ), a_j and b_j are respectively the asymmetric and symmetric shape parameters, and σ is the direct current conductivity. All relaxations except the α^* relaxation for PEHA0, could be well described using a value of $b = 1$ in Equation 3.6, corresponding to a Cole-Cole expression (symmetrical on a logarithmic frequency axis);[273] The fact that the α and α^* relaxations are situated quite close together and the fact that the simpler Cole-Cole fits work well, makes the use of a more general asymmetric HN-expression unreliable and we choose to simplify the fitting by restricting the fits to one shape parameter only characterizing the full response. For the PEHA0 sample, however, an asymmetric shape had to be introduced to account for the α^* relaxation shape. The shape parameter a for the α relaxation of PEHA0 varies between 0.6 and 0.8, and between 0.15 and 0.3 for UPyPEHA at different temperatures. The shape parameter a for the α^* relaxation of all sample varies between 0.45 and 0.7. The shape parameter b for the α^* relaxation of PEHA0 varies between 0.6 and 0.7 at different temperatures. In the Cole-Cole equation, fitted timescales are the reverse of peak frequencies, $\tau_{CC} = 1/\omega_p$. Whereas in the HN equation, peak timescales τ_{HN} need to be corrected using the equation below: (see Chapter 2)

$$\omega_p = \frac{1}{\tau_{HN}}[\sin(\frac{\alpha\pi}{2\beta+2})]^{1/\alpha}[\sin(\frac{\alpha\beta\pi}{2\beta+2})]^{-1/\alpha} \tag{3.7}$$

Fitting examples are shown in Figure 3.13a-c, where the fits to α, α^* relaxations and the DC-conductivity are shown by dashed, dotted lines and short dashed lines. The temperatures of curves in Figure 3.13a-c are chosen so that characteristic timescales for both relaxations are observable in the probed frequency window (T=236, 258 and 272 K for PEHA0, UPyPEHA2 and UPyPEHA14, respectively). The total fits of full responses at various temperatures are shown in solid lines in Figure 3.12. From the fitting results we can determine the temperature-dependent characteristic timescales for both α and α^* relaxations (τ_α and τ_{α^*}), which are shown in Figure 3.14a. Temperature

dependences of τ_α are well described using the VFT equation except that for UPyPEHA14 which is better described using the Arrhenius equation, as shown in Figure 3.14a; all fitting parameters are shown in Table 3.3. Data points obtained from MDSC are also included in the plot, as cross-filled symbols shown, and these data points are consistent with the VFT fits of τ_α, which confirms that the slower relaxation is the structural α relaxation, relating to glass transitions; for UPyPEHA14, the response in C_p'' is too broad to determine a peak and we could thus not assign a data point to this polymer based on MDSC, see Figure 3.11.

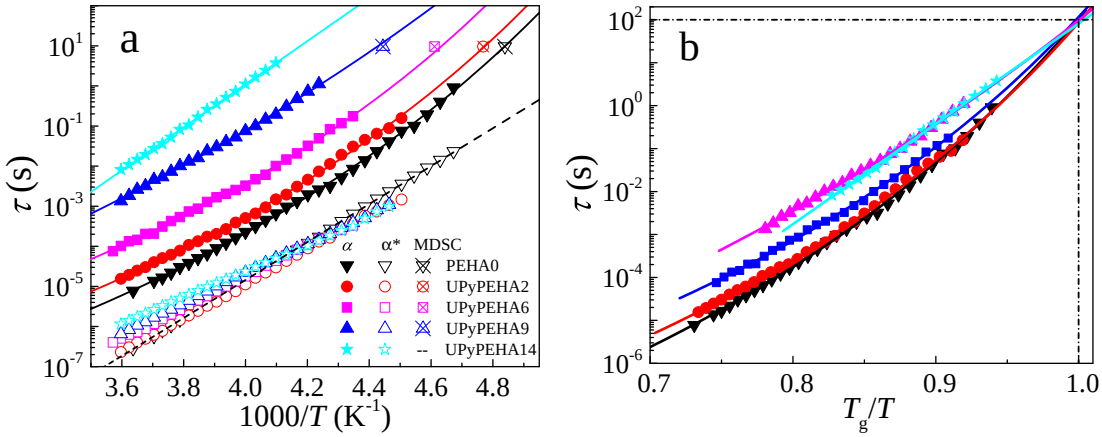

Figure 3.14: (a) Temperature dependence of τ_α and τ_{α^*} (filled and open symbols) for (co-)polymers with varying ϕ_{UPy}, as well as MDSC results (cross filled symbols). Solid lines are fitted to τ_α data with the VFT equation excepted that for UPyPEHA14 which is fitted with the Arrhenius equation. The dashed lines are the Arrhenius fits of τ_{α^*} for PEHA0. For clarity, the Arrhenius fits for τ_{α^*} of other samples are not shown. Fitting parameters are reported in Table 3.3. (b) Plots of τ_α against T_g/T for all samples. The dash-dot lines indicate the definition of T_g when τ_α = 100 s.

We find that α relaxations significantly slow down upon addition of UPy groups, which is reflected in increasing glass transition temperatures (Figure 3.10). T_g is defined as the temperature when τ_α = 100 s. Thus, glass transition temperatures from BDS measurement $T_{\mathrm{g,\,100\,s}}^{\mathrm{BDS}}$ can be obtained, which show similar variations as function of ϕ_{UPy}, to the results from DSC measurements in Figure 3.10. It is also clear from Figure 3.14a that the significant slowing down observed for the α relaxation is not observed for the α^* relaxation which is much less affected by UPy addition. Thus, α and

α^* relaxations separate from each other with increasing ϕ_{UPy}.

The dynamic fragility for each polymer is defined as $m = d(\log\tau_\alpha)/d(T_g/T)|_{T=T_g}$[264] and is a measure of temperature sensitivity of dynamics at T_g. A material which shows a large m value (> 120) is termed fragile and which shows a small value (~ 16) is termed strong. Network glass-formers characterized by covalent bonds are typically strong, whereas small molecular liquids or polymers are typical fragile. Hydrogen bonding systems usually have intermediate fragility.[264] The development towards a more Arrhenius-like behaviour as the UPy concentration is increased can be directly seen if the α relaxation data are plotted in an Arrhenius plot with a T_g-scaled abscissa, as shown in Figure 3.14b. We find that PEHA0 polymer has an intermediate fragility of $m \sim 40$ and that fragilities decrease with increasing ϕ_{UPy}, as shown in Table 3.2, and UPyPEHA14 has a fragility of $m \sim 16$ and is thus strong. For chemically cross-linked polymers an increase in fragility has been reported with increasing cross-linking density and the behaviour has been conceptualized as due to an enhanced cross-link mediated coupling between relaxing molecular segments[274–276] However, in our case, m decreases with increasing ϕ_{UPy}, which is opposite to the chemically cross-linked polymers.

Table 3.3: VFT and Arrhenius fitting parameters for the BDS α, α^* and γ relaxations.

		PEHA0	UPyPEHA2	UPyPEHA6	UPyPEHA9	UPyPEHA14
α	-$\log_{10}(\tau_0)$ (s)	12±0.4	11±0.4	10±0.5	12±0.9	21±0.4
	D	18±2	16±2	15±3	33±0.4	–
	T_0 (K)	130±4	133±6	138±7	106±16	–
	E_a (kJ/mol)	–	–	–	–	12±0.4
	m	40±3	38±1	35±3	26±2	16±3
	T_g (K)	196±4	198±3	203±4	204±2	207±3
α^*	-$\log_{10}(\tau_0)$ (s)	24±0.1	22±0.1	20±0.1	19±0.1	18±0.1
	E_a (kJ/mol)	91±0.3	82±0.3	74±0.4	71±0.1	63±0.4
γ	-$\log_{10}(\tau_0)$ (s)	14±0.3	13±0.4	14±0.1	13±0.3	14±0.3
	E_a (kJ/mol)	24±0.2	22±0.4	25±0.5	23±0.4	24±0.3

Figure 3.14a also shows that temperature dependences of τ_{α^*} can be well described using the Arrhenius equation for all polymers, see fitting parameters in Table 3.3. We

do not observe any dramatic changes of α^* relaxation with ϕ_{UPy}. As described above, we find that our SAXS data for PEHA0 are consistent with those of other polymers that show nano-segregated alkyl regions and in particular, our system is closely related to the PnMAs.[203] In previous work on PnMAs, it was observed that in addition to α relaxation a faster relaxation mode, corresponding to our α^*, was also observed and its characteristic relaxation time was directly related to the number of alkyl side-chain carbons n_C. For $n_C > 3$ in PnMAs, it was observed that α^* relaxation slows down and becomes stronger as n_C increases. It was argued that this relaxation for long enough side chains was due to PE-like dynamics α_{PE} dynamics in the confinement of surrounding backbone chains. In our case, the side group is composed of 8 carbons (a 6-carbon chain with 2-carbon short branch), thus, τ_{α^*} we observed is close to what was reported.[203] Given that the α^* and α relaxations are situated close together in frequency, as discussed above, small variations in the Arrhenius fit parameters between our polymers have to be interpreted with caution. However, within the estimated accuracy of our analysis, we find evidence for a slight decrease of the the activation energies from ~91 to 63 kJ/mol when the ϕ_{UPy} increases from 0 to 14 mol%, as shown in Table 3.3.

In addition to α and α^* relaxations, all five polymers show a third relaxation which enters the experimental frequency window at low temperatures (< 150 K). Following the terminology often adapted for other acrylate polymers, we denote this γ relaxation.[234] ε'' spectra of γ relaxations for all samples at various temperatures are shown in Figure 3.15b-f. As increasing temperature, peak positions for γ relaxations move towards higher frequencies and peak heights increase slightly. To obtain γ relaxation timescales, ε'' spectra are fitted using a combination of a Cole-Cole equation and two power laws to account for the low and high frequency contributions, see Equation 3.6. The contritions from each relaxation process is shown in Figure 3.15a, taking PEHA0 at 130 K as an example. The same fitting procedure is applied to all other samples at various temperatures. We found that the shape of γ relaxations remains similar for all polymers, with the shape parameter a around 0.25.

Similarly, Figure 3.16 shows the Arrhenius plot of the temperature dependent γ relaxation timescales τ_γ whthin the glassy state for all polymers. Within the accuracy of the abalysis, we find very small, if any, effects on the γ relaxation dynamics resulting from the supramolecular interactions. Fried et al. reported that, in the case of

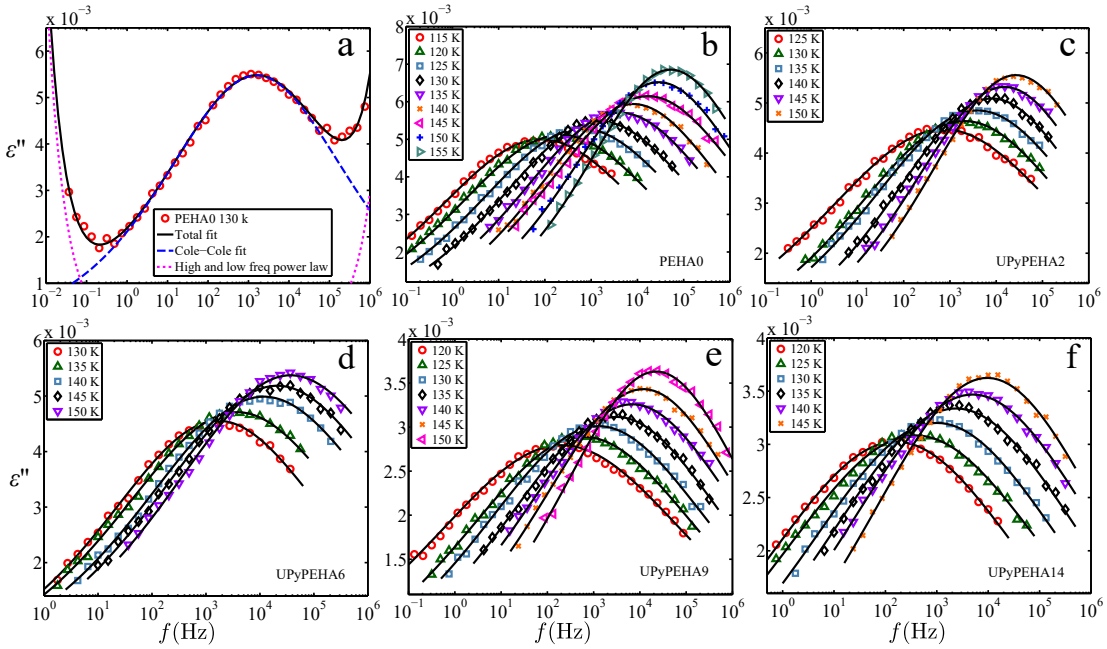

Figure 3.15: (a) An example shows the fitting of ε'' spectra for γ relaxation by the combination of a Cole-Cole equation and two power laws for the low and high frequency flanks. (b-f) ε'' spectra for γ relaxations for (co-)polymers with varying ϕ_{UPy} at various temperatures. Solid lines are the best fitting results to the data.

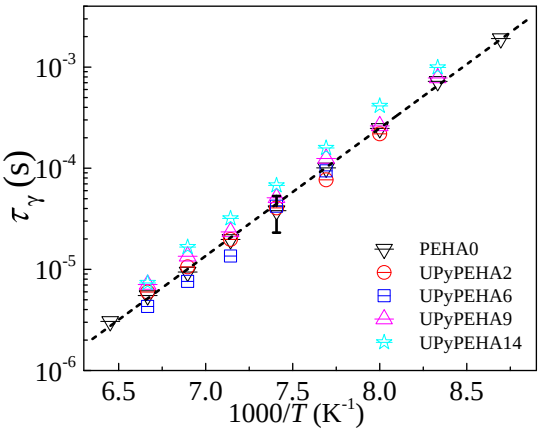

Figure 3.16: (a) An example to show the fitting of ε'' spectra for the γ relaxation by the combination of a Cole-Cole function and two power laws for the low and high frequency flanks. (b-f) ε'' spectra for the γ relaxations for (co-)polymers with varying ϕ_{UPy} at various temperatures, the solid lines are the best fitting results to the data.

poly(n-alkyl acrylates) (PnAA) and poly(n-alkyl methacrylates) with $n_C > 3$, a low temperature relaxation ($\sim$ 125-160 K) with a typical activation energy $\sim$ 25 kJ/mol can be observed and it was suggested that this relaxation involves the motion of side groups of four atoms sequence -O-C-C-C or O-C-C-C-C-.[234] The Arrhenius fits of τ_γ give activation energies around 22-25 kJ/mol, thus consistent with the behaviour observed in other similar polymers.[234] The observations of the γ relaxation that is largely independent of the addition of supramolecular interactions are also consistent with the fact that no significant structural change is observed at short length-scales in the WAXS data, as shown in Figure 3.3. Finally, we note that for short alkyl side-chain polymers including PnMA and PnAA with $n_C < 3$, a secondary beta relaxation with an activation energy typically ~80 kJ/mol, which is slower than the γ relaxation can be observed within the glassy state.[277, 278] We do not find evidence for this in our system, but note that the existence of the α^* relaxation due to the nano-segregated alkyl regions is situated in the dynamic range where such a relaxation would be expected and β relaxation of for poly(acrylate) polymers may be suppressed by the strong α^* relaxations.[277–279]

3.4 Conclusions

A series of PEHA-based supramolecular (co)polymers with the "stickers" being UPy side groups have been synthesised via RAFT polymerisation. Both the structure, dynamics and rheology of these polymers have been studied. We find that the addition of supramolecular UPy groups strongly hampered the segmental motions, leading to increasing glass transition temperatures and a significant broadening of the glass transition. The addition of UPy groups also leads to the temperature dependent structural relaxation changing from VFT to Arrhenius-like. For the highest investigated UPy concentration of 14% mol, the number of monomer units between two UPy groups was found to be close to the number of units corresponding to the estimated Kuhn length of the pure polymer. This provides an explanation for the significant change of the dynamics and rheology as the supramolecular groups will significantly inhibit the relaxations and the full behaviour will thus be dominated by the supramolecular interactions. Even though we find that the UPy groups play an important role near T_g, we find that they only weakly impact the more local relaxations α^* and γ, where the former is related to relaxations within nano-segregated alkyl-rich regimes and the latter is related to side-group dominated relaxations. On the macroscopic scale, a reversible network is formed due to the supramolecular interactions as evidenced by the appearance of a finite plateau modulus which increases with an increasing concentration of UPy side-chains. In summary, in this work, we have investigated the effects of supramolecular interactions on the polymer structure, dynamics and rheology. We demonstrate that the rheology, as well as the relaxation dynamics are tunable via the adjustment of the side-chain sticker density.

Chapter 4

Linear shear and extensional rheology of unentangled supramolecular side-chain polymers

Due to the possibility of detailed control of material properties that supramolecular associations allow, supramolecular polymers are important within a wide range of applications including printing, adhesives, coatings, cosmetics, surgery and nanofabrication. Moreover, to control and tune the behaviour of supramolecular materials and to develop new application it is of key importance to understand their rheological response. Here, we present a systematic investigation of the linear shear rheology for a series of unentangled polymers for which the concentration of randomly distributed supramolecular side-groups are systematically varied. Due to the limited frequency range of any rheometer, time-temperature superposition (TTS) is typically used to probe the rheological properties over a wide frequency range. However, TTS is an approximation based on the assumption that all relaxation processes of a polymer including segmental relaxations and chain modes follow the same temperature dependence. Given this, TTS has to be used with caution and is normally at best a reasonable approximation over a limited temperature or time (frequency) range for many polymers. For supramolecular polymers, the additional associations typically introduce an additional temperature dependence, which makes the interpretations of their rheological response particularly challenging. Addressing this, we perform a detailed investigation of the validity of TTS for our polymers. This is necessary for the inter-

pretation of the rheological response and the work might also provide a guidance as to when TTS can be used to investigate the rheology of supramolecular polymers. Moreover, we find that the "sticky Rouse" model normally used to interpret the rheological response of supramolecular polymers fits our experimental data well in the terminal regime, but is less successful in the rubbery plateau regime. We propose some modifications to the "sticky Rouse" model, which includes more realistic assumptions with regards to (i) the random placement of the stickers along the backbone, (ii) the contributions from dangling chain ends and (iii) the chain motion upon dissociation of a sticker and re-association with a new coordination involves a finite sized "hop" of the chain. Our model provides an improved description of the plateau region. Finally, we investigate the extensional rheological response of one of our supramolecular systems and the strong strain hardening is observed which can be modelled using the upper convected Maxwell model.

4.1 Introduction

Supramolecular polymers are made of covalent chains connected through reversible interactions, such as hydrogen bonding, [165, 166, 170–172, 190, 191, 214, 221, 225, 226, 229, 280–286] metal-ligand coordination,[30, 174, 175, 178, 287, 288, 288–295] and ionic aggregation.[181, 183, 184, 187, 251, 296, 297] The ability to vary and control the interactions in supramolecular systems provides an efficient tool to tune the structure, dynamics and rheology.[174, 227, 287] Among the possible supramolecular interactions, quadruple hydrogen bonding groups, 2-ureido-4[1H]-pyrimidinone (UPy), were chosen in this study since their properties and behaviour with regards to chemical synthesis are well understood. [33, 286] The UPy groups are characterised by a strong association constant ($k_{\text{asso}} > 10^6$ in chloroform), [214, 298] leading to significant effects on material properties, and the hydrogen (H-) bonding nature of UPy interactions leads to interesting and useful temperature sensitivity of the interactions. [170, 228]

Supramolecular polymers based on UPy groups have been widely investigated and materials with important properties such as stimuli-responsive,[170], self-healing [220–224] and temperature responsive [193, 219] properties have found applications

within printing, [243, 244, 248, 249] cosmetics, [245, 246] adhesives [299] and coatings. [247] As an example of how supramolecular associations can play an important role, for inkjet printing applications a UPy-modified polyether mixed with stabilizers, antioxidants and colourants was used in work by Jaeger et al.[244]. The ink needs a low viscosity during droplet ejection, but should be highly viscous or even solid once it is deposited on the print surface. The supramolecular associations here ensure the solid-like nature of the printed ink at ambient temperatures, but the elevated temperatures during deposition dissociates the network leading to the low deposition viscosity. It is important to understand the rheological response in applications such as those mentioned above to optimise the material efficiency and facilitate a proper control of the material behaviour. The effect of UPy addition on the linear viscoelasticity of supramolecular polymers have previously been investigated[186, 213, 229, 300, 301]. However, few studies exist where the rheological response is characterised for a systematic variation of supramolecular side-group density[213].

Time temperature superposition (TTS) is a commonly used and often powerful method to evaluate the linear rheological properties of a material over a wide time or frequency window. [134] TTS is based on the assumption that the underlying friction coefficient for all relevant relaxation processes (segmental as well as chain relaxation including Rouse and/or reptation mechanisms) is the same, that is to say, these relaxation processes all arise as the summation of increments of the same "local" motions and therefore are accelerated or retarded by the same factor as temperature is varied. [134] A material for which TTS is applicable is termed "thermorheologically simple". [139] Although TTS is commonly used, it is well known that TTS breaks down for many polymers because of the different temperature dependence of segmental and chain relaxation processes. [140, 140–144]. Commonly, polymers start to show different temperature dependences of segmental relaxation and chain relaxation processes when the segmental relaxation time (τ_α) becomes longer than $\sim 10^{-7}$ - 10^{-5} s.[144] It has also been observed that highly "fragile" polymers, including polymers such as polystyrene, for which the segmental relaxation time is strongly temperature dependent near the glass-transition temperature, exhibit more significant deviations from TTS behaviour.[144, 302, 303] A supramolecular polymer is characterised by at least two types of interactions: the usual chain-chain interaction (friction effect) and additional supramolecular interactions. The chain motions associated with these two

interactions, respectively, can be expected to behave differently as temperature is varied leading to a breakdown of TTS. To what degree TTS still approximately holds for a particular supramolecular system will depend on the specific material and interaction details, but it is not uncommon for TTS to be applied to supramolecular systems [140, 186, 212, 213, 229, 300, 301]

Several theoretical models have been proposed to describe the rheological response of telechelic polymers [304, 305] and unentangled [184, 252, 253, 306, 307] or entangled [308–312] supramolecular polymers. For unentangled polymers with supramolecular side-groups, the polymer type relevant to our work, the so-called sticky Rouse model has been proposed. [184, 252, 253, 306, 307] Here, the standard Rouse model for single chain dynamics is modified to take into account the effects of the sticker interactions on the viscoelastic properties of the supramolecular material. The associations and dissociations of the sticky groups are assumed to act as an extra friction between polymer chains and thus to delay the terminal relaxation. The sticky Rouse model can be generalized to account both for polydispersity in the overall molecular weight and for variation in the total number of stickers per chain. [186] This model has been used to describe data on supramolecular polymers and it typically fits the experimental data quite well in the terminal regime. [184, 186, 313] However, a relatively large mismatch between data and theory can often be observed in the rubber plateau region, [184, 186] and we find the same to be true for the polymers in the present investigation.

One possible reason for the mismatch is that, in sticky Rouse model, supramolecular groups are assumed to be evenly distributed along the chain. More precisely, the slowest modes of the Rouse spectrum are assumed to be uniformly retarded by the sticky group timescale, without changing their essential mode distribution, whilst the faster modes are left as is; this is closely equivalent to assuming an even distribution of stickers along the chain. For our polymers we need to relax this hypothesis because (i) our four supramolecular polymers have a relatively low sticker concentration (2, 6 9 and 14 mol%) and, (ii) random co-polymerization implies a random placement of the stickers along the backbone. Moreover, (iii) the contribution to the response from dangling chain ends, which differs from the relaxation modes of segments of chain "trapped" between stickers, is not considered in the common formulation of the sticky Rouse model and finally (iv) the chain motion upon dissociation of a sticker

and re-association with a new coordination involves a finite sized "hop" of the chain, rather than a continuous motion with increased friction, as assumed in the standard sticky Rouse model. We find that our model can fit data precisely in the terminal region and improves the fit the in the rubber plateau region. However, whilst we have included some extra and essential details in our model, we still find that the fit is not perfect, especially for samples with higher sticker concentration. We provide a discussion regarding what elements might still be missing from the model, to provide a full description of the rheology.

The relevant deformation and flow conditions during polymer processing is often of extensional character. However, for supramolecular polymers with side-chain functional groups, relatively few studies have been reported.[182, 314, 315] As an example, Shabbir and coworkers[315] have reported the extensional rheology of poly(butyl acrylate-co-acrylic acid) with varying acrylic acid content. H-bonds can form between acrylic acid groups and introduce chain-chain interactions. They observed strain hardening for strain rates significantly smaller than the inverse of the reptation time, indicating that the strain hardening for their studied polymer system is attributed to stretching of chain segments which are restricted by hydrogen bonding groups. Similar observations were also made for ionomers.[182, 314] In ionomers, the supramolecular interactions originate from association of ionic groups covalently attached to either the polymer backbone or the side groups. Associations between these ionic groups typically lead to nanometer-sized aggregates which act as physical cross-links. The magnitude of the strain hardening in ionomers was related to the strength of these ionic cluster and a stronger cohesive strength of the ionic clusters leads to a more pronounced strain hardening. The ionic aggregates of ionomers thus correspond to chain-chain interactions via H-bonds for our UPy-based supramolecular polymers.

In the present paper, we present a detailed investigation of the rheological responses of a series of linear, unentangled polymers in which the concentration of randomly distributed supramolecular side- groups is systematically varied. The molecular weights for all samples (Table 3.1) are below the entanglement molecular weight ($M_e \sim 30$ kg/mol for a similar polymer, i.e. poly(hexyl acrylate) (PHA)), [231] meaning that the cross-linking effects of reversible supramolecular side group interactions can be readily identified. A homo-polymer, poly(ethylhexyl acrylate) (PEHA) and four copolymers (UPyPEHAx) composed of ethylhexyl acrylate and 2-(3-(6-methyl-4-oxo-1,4-

dihydropyrimidin-2-yl)ureido)-ethyl acrylate (UPyEA) with varying concentrations of UPyEA (ϕ_{UPy}) of 2, 6, 9 and 14 mol%, respectively, are synthesized using RAFT polymerization, [67, 69] see Figure 4.1. The letter "x" in the abbreviation indicates different concentrations of ϕ_{UPy} expressed in mol%. We focus on four particular aspects of the rheology of our samples: (i) the effects of adding UPy-based side-groups on the linear viscoelasticity, (ii) a detailed investigation of the extent to which TTS can be applied to our series of polymers. We complement our small amplitude oscillatory shear experiments with measurements of stress relaxation resulting from a step shear strain, where the time-dependent response is converted to the frequency domain to extend the frequency range accessed at a single temperature (iii) detailed modelling of the linear rheological response using both a standard and a modified version of the sticky Rouse model, and (iv) extensional rheology measurements on one of our supramolecular polymers, UPyPEHA6, together with upper convected Maxwell modelling.

4.2 Experimental section

Five polymers were synthesised by RAFT polymerization, see Table 3.1. The first homo-polymer (PEHA0) was synthesized from ethylhexyl acrylate (EHA). Other four copolymers were synthesised from EHA and 2-(3-(6-methyl-4-oxo-1,4-dihydropyrimidin-2-yl)ureido)-ethyl acrylate (UPyEA) with systematically increasing concentrations of UPyEA. The chemical structures of the polymers are shown in Figure 4.1. The details of the synthesis and the characterisation of these polymers were reported in Chapter 3. Some key characteristics of the samples, including their number average molecular weight Mn, their polydispersity indices (PDI), the number of UPyEA side-groups per chain, and the average number of EHA monomers between UPyEA side-groups are listed in Table 3.1. Two UPy groups are interacting through the formation of quadruple hydrogen bonds, as shown in the sketch in Figure 4.1 and thus dimers of interacting UPy groups, lead to reversible supramolecular associations and hence a transient network of polymer chains.

Small amplitude oscillation shear measurements (SAOS) and step strain stress relaxation experiments were the same to the descriptions in the Experimental Section of Chapter 3, thus they are not repeated again here. In the extensional rheology experiments, the time-dependent extensional stress growth coefficient (i.e. stress divided by

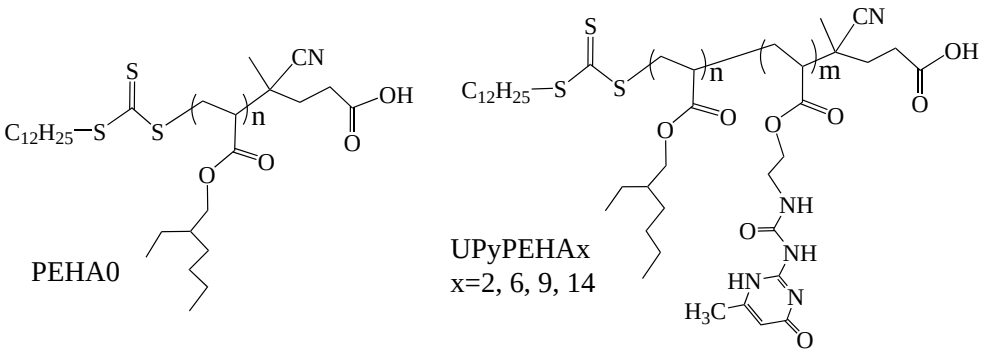

Figure 4.1: Chemical structures of PEHA and UPyPEHA with varying ϕ_{UPy}. The letter "x" in the figure indicates the $\phi_{\mathrm{UPy}} = 2, 6, 9, 14$ mol%.

strain rate, $\sigma/\dot{\varepsilon}$) was measured using a filament stretching rheometer (DTU-FSR).[316] Cylindrical stainless steel sample plates with a diameter of 5.4 mm were used for the measurements. Measurements were performed at a constant Hencky strain rate ($\dot{\varepsilon}$) imposed at the mid-filament diameter using a real-time control software. The time-dependent Hencky strain (ε) is defined as: $\varepsilon(t) = -2\ln(R(t)/R_0)$, Where $R(t)$ and R_0 are the radii of the filament at times t and 0, respectively. The rheometer can be operated over the temperature range with an accuracy of ±0.5 K. PEHA0 and UPyPEHA2 are liquid-like at room temperature, and the resulting force is too small to be measured by the transducer at the relevant extensional rates. In contrast, the more highly cross-linked nature of UPyPEHA9 and UPyPEHA14 polymers meant that these could not be attached to the plate even at T =403 K; thus, only the UPyPEHA6 polymer was successfully measured using extensional rheology.

4.3 Results and Discussions

4.3.1 Linear viscoelasticity and validity of TTS

The SAOS results for our series of polymers were determined as outlined in the experimental section. To obtain the SAOS response over a wider frequency range than what is possible in a single measurement, we investigate in detail to what extent TTS can be used to extend the dynamic range. The master curves obtained using TTS at a reference temperature of 363 K are shown in Figure 4.2a. For each polymer, the

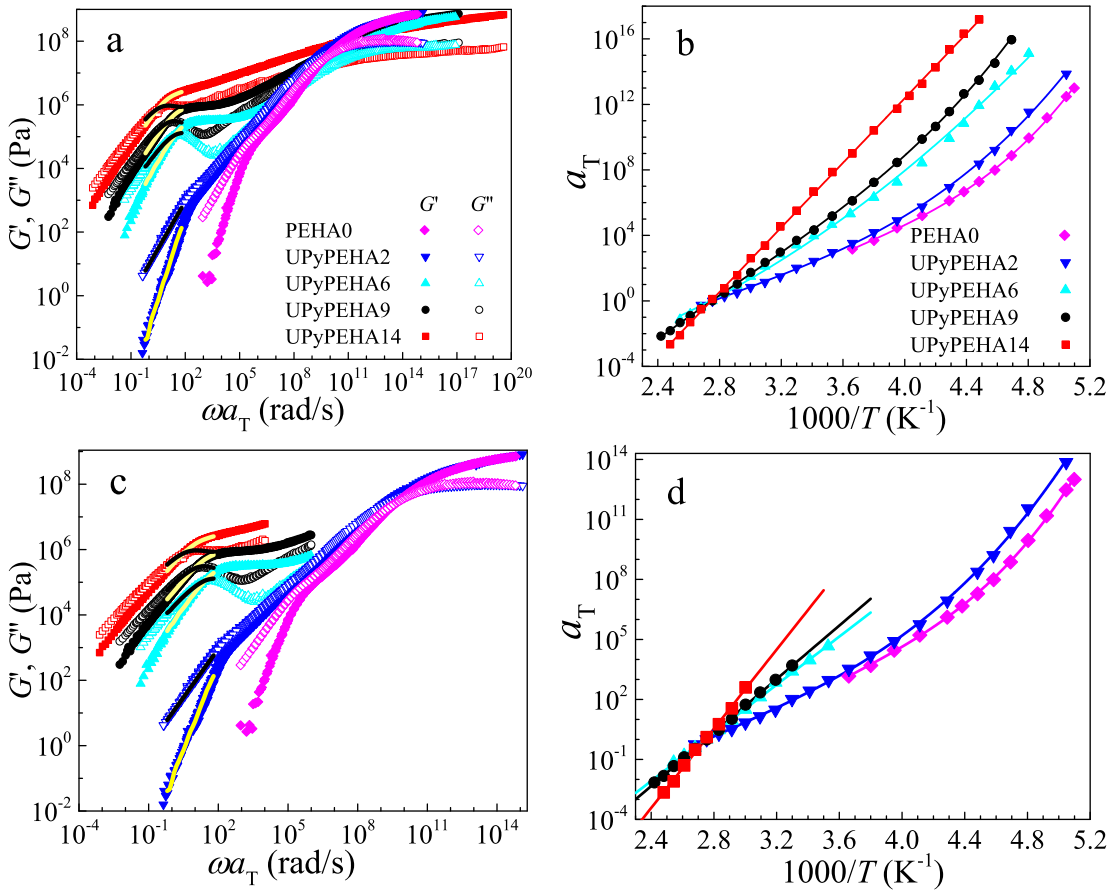

Figure 4.2: (a) Master curves for the samples with varying ϕ_{UPy} referring to 363 K. The black and yellow solid lines are the single small amplitude oscillatory rheological measurements at 363 K. (b) the shift factors used to build the corresponding master curves in panel (a). The solid lines are the VFT fits, except for the UPyPEHA14 which is fitted by the Arrhenius equation. (c) Part of master curves where TTS works and (d) corresponding shift factors. In (d), the shift factors for PEHA0 and UPyPEHA2 are fitted with VFT equation, whereas other samples are fitted with the Arrhenius equation. Note that the master curve for PEHA0 was referred to 263 K, because the torque at 363 K is too small for the oscillation shear measurement. Thus, shift factors referring to 263 K is extrapolated to 363 K and the extrapolated shift factor at 363 K is used to shifted the master curve for PEHA0 in (a) and (c).

data taken at the reference temperature are shown in black and yellow lines for G'' and G' respectively, to allow for easy comparisons between the different polymers. The

temperature-dependent horizontal frequency shift factors a_T used to create the master curves are shown in Figure 4.2b.

Before evaluating the accuracy of using TTS to describe these samples in detail, we focus on the immediate observations. Since the molecular weight for all samples are below the entanglement molecular weight, M_e, no plateau should be observed in the absence of supramolecular effects and this is indeed observed for the PEHA0 samples. Also the lowest UPy concentration sample UPyPEHA2 shows little evidence of a plateau. For the UPyPEHA samples containing more than 2 mol% UPy, however, we clearly observe rubber-like plateaus, and the plateau modulus increases systematically with increasing ϕ_{UPy}. This is expected since, as discussed above, the UPy dimers act as physical cross-links leading to the formation of an elastic network. Moreover, it is also clear that addition of associating UPy groups leads to a delay of the terminal relaxation for all supramolecular polymers compared to the non-supramolecular polymer PEHA0 and that the terminal relaxation times increase with increasing ϕ_{UPy}.

To evaluate the validity of TTS for our supramolecular polymers, we plot the loss tangent tan(δ) as a function of complex modulus G^* in a so-called Van-Gurp-Palmen (VGP) plot[137, 138] in Figure 4.3. This representation removes all explicit time-dependence from the data, and so indicates whether an accurate frequency-shift TTS is possible or not. In a tan(δ) vs G^* representation, the SAOS data for PEHA and UPyPEHA2 (blue rings in Figure 4.3a and b) are relatively smooth and continuous across the whole temperature range, indicating (but not guaranteeing) that the TTS has the potential to work well for these two samples. However, for higher ϕ_{UPy} and particularly for 9 and 14 mol%, the curves (blue rings) show discontinuities from one temperature to the next in the mid to high modulus range. This behaviour clearly indicates a failure of TTS at low temperatures. For each polymer, we estimate the temperature where the curves start to show clear discontinuities. Based on this information, we modify the master curve plots in Figure 4.2c so that the TTS master curves are terminated at low temperatures, where we have indications that TTS is not a good approximation, and the shift factor plots resulting from this procedure are shown in Fig 4.2d, respectively. To only include the data for which we find strong indications of TTS working well (as we do above) is probably the most defensible position to take when TTS is found to break over some parts of the dynamic range. Certainly, we would expect TTS errors to be cumulative, such that a small TTS error repeated over many increments in temperature

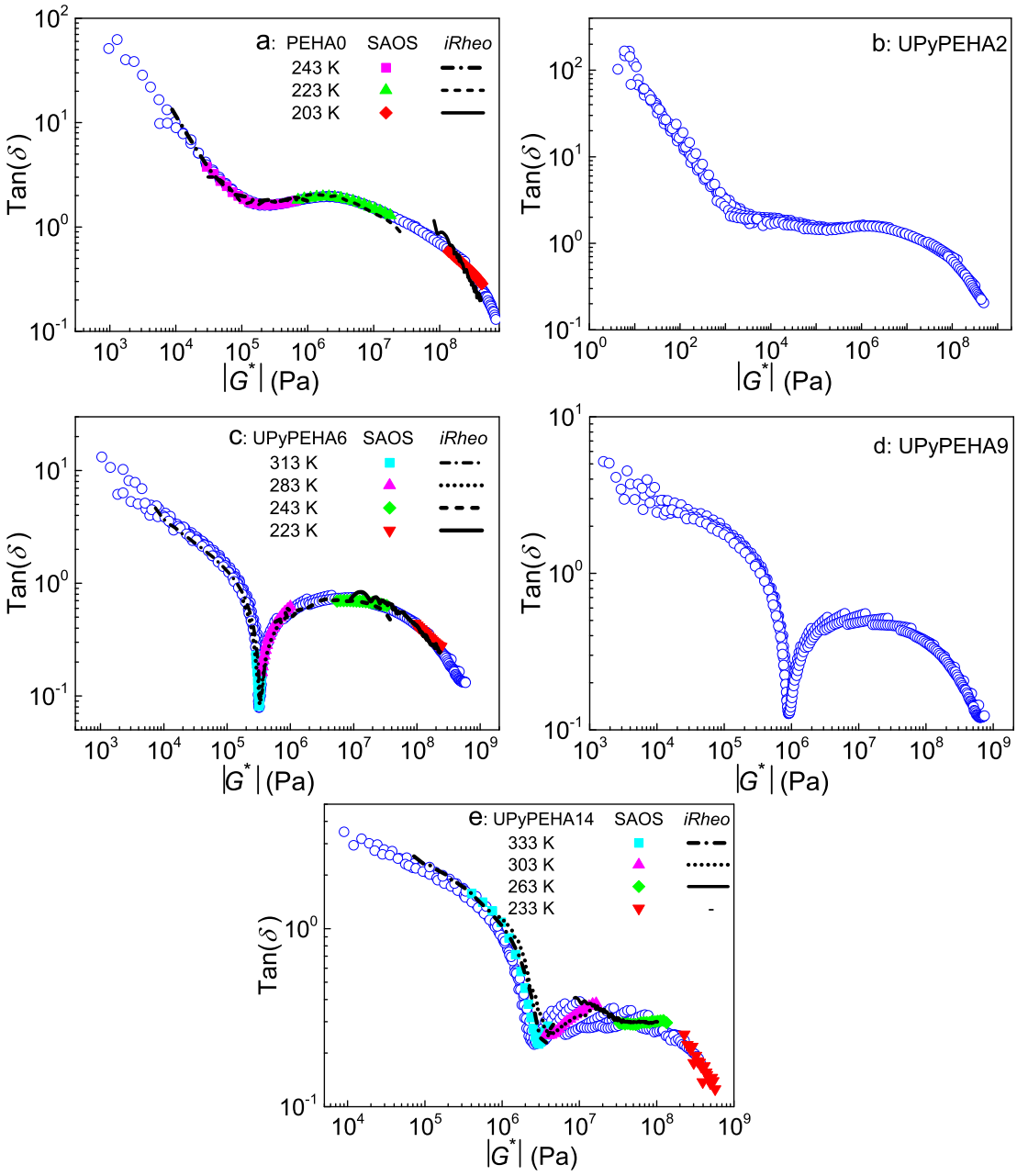

Figure 4.3: Plot of tan(δ) as a function of G^* for all samples. The blue symbols are the small amplitude oscillation shear (SAOS) measurements at all temperatures. The colour symbols on the figure for PEHA0, UPyPEHA6 and UPyPEHA14 are the SAOS measurements at the temperatures where the stress relaxation experiments are conducted. The black lines are calculated from the dynamic modulus from the stress relaxation measurements at the temperatures corresponding to the colour symbols.

will add together to give a largely incorrect placement (and shape) of the data at temperatures distant from the reference (and correspondingly at frequencies distant from the measured frequency). Nevertheless, the question remains: relatively close to the original measurement frequency, how well do the TTS-shifted data actually represent the real behaviour?

To further investigate the effect of the supramolecular interactions on TTS, and to test the accuracy of the TTS-shifted data, we compare these with the dynamic modulus obtained from stress relaxation after step strain measurements performed on the same polymers. The latter technique can in principle probe a much wider dynamic range within a given duration of an experiment and a comparison of data taken using this technique and the TTS method, respectively, provides direct information on the validity of TTS.

The analysis software, *iRheo*, was used to perform the transformation from the stress relaxation data to the dynamic modulus. An advantage of the analysis method used in this software is that it permits stress and strain data taken during the non-instantaneous initial step to be used, and improves the accuracy at high frequencies.[145] To test the reliability of the *iRheo* transformation, we take our stress relaxation result for UPyPEHA14 at T =263 K as an example, and compare it with our TTS results. The results of this comparison are plotted in Figure 4.4a (black lines from *iRheo* and green symbols from TTS). As expected, the moduli from the *iRheo* analysis and from the TTS analysis overlap well in the frequency range of a single SAOS measurement (between two vertical blue lines). However, since the stress for this sample does not fully relax in the time window of the $\sigma(t)$ step strain experiment, the *iRheo* transformation gives unphysical shapes in the low frequency range of its output. *iRheo* allows users to fit and extrapolate the $\sigma(t)$ curves at long times, which can improve the transformation at low frequencies. [145] To test to what degree we can trust the transformation result in the low frequency range, we altered the input $\sigma(t)$ data in two simple ways, and examined the transformed output. Firstly, we fit $\sigma(t)$ up to a time near the experimental end-time, and artificially extrapolate to longer time (equivalent to longer experiment time) to evaluate the effects of extending the dynamic range. Secondly, for further comparison, we investigate the effects of slightly decreasing the dynamic range by removing a few data points from the original $\sigma(t)$ curve near the experiment end-time. The transformation results obtained from the three $\sigma(t)$ curves are compared as the red,

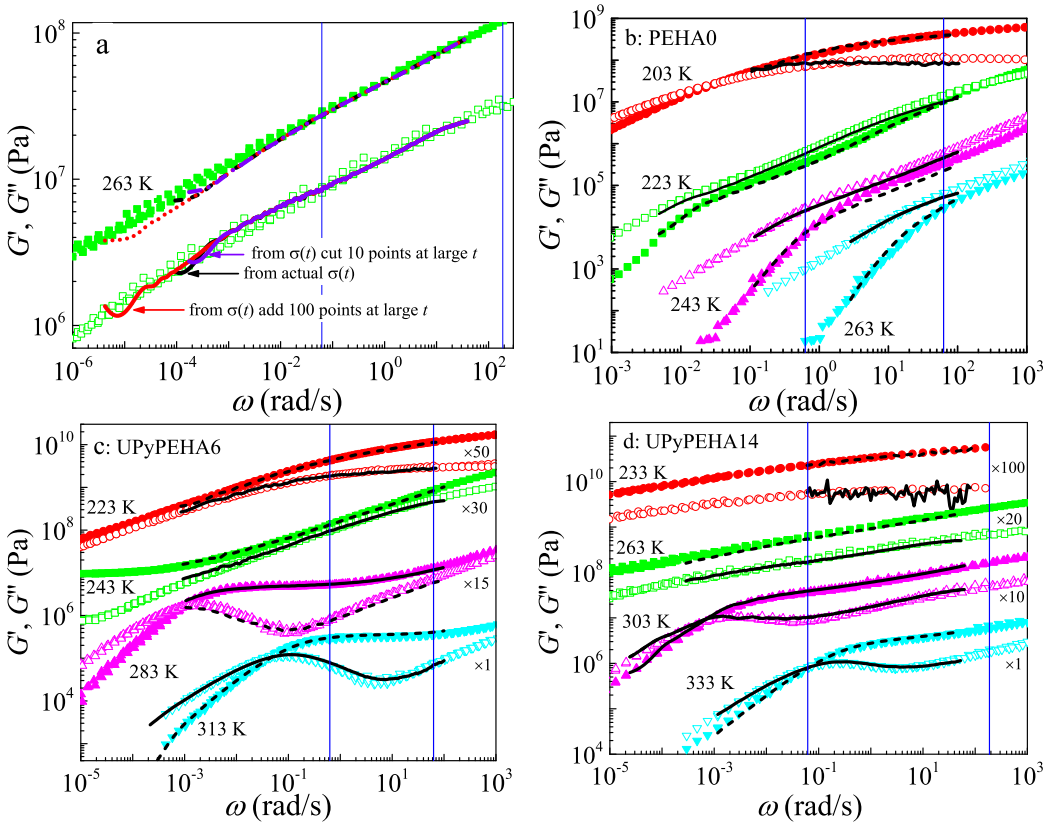

Figure 4.4: Comparison between the dynamic shear modulus obtained from TTS (symbols) and from the conversion (lines) of stress relaxation data using *iRheo*: (a) an example of UPyPEHA14 at 263 K to estimate the accuracy of *iRheo* at low frequencies, (b) PEHA0, (c) UPyPEHA6 and (d) UPyPEHA14 at various temperatures. The data for UPyPEHA6 and UPyPEHA14 in panels (c) and (d) are vertically shifted for clarity. The blue vertical lines indicate the frequency range of a single SAOS measurement.

black and purple lines in Figure 4.4a. It is clear from this comparison that the majority of the output is stable with respect to these changes in the input data, but the lowest frequency results (where the unphysical shapes are seen) are altered, as might be expected. We conclude that the transformation is uncertain in this low frequency regime, and thus cut the transformed output below the frequency where the three curves diverge. A similar procedure was followed for all other *iRheo* converted data reported in this paper.

We next compare the dynamic moduli obtained from TTS and stress relaxation

for the three samples PEHA0, UPyPEHA6 and UPyPEHA14 at a range of different temperatures, as shown in Figure 4.4b-d; the symbols show the TTS results and the lines show the modulus converted from the stress relaxation experiments. The data at different temperatures for UPyPEHA6 and UPyPEHA14 in panels (b) and (d) are vertically shifted for clarity, using shift factors shown in the figure. It is worth noting that the $\sigma(t)$ curves for PEHA0 at 203 K and UPyPEHA14 at 233 K are somewhat noisy; thus, more points on the transformed modulus curves are cut.

From the comparison in Figure 4.4b-d, it is clear that the TTS curves (symbols) and *iRheo* results overlap reasonably well with each other in the extended frequency range covered by the *iRheo* output. This is perhaps surprising since, in at least some cases such as the UPyPEHA14 sample at 263 K, the data span regions where TTS obviously breaks down (i.e. perfect overlap is not achieved in the TTS curves or in the VGP plots in Figure 4.3). Nevertheless, the TTS shifted data do (on average) closely follow the overall shape of the *iRheo* output. One reason for this becomes evident on examining Figure 4.3, where the stress relaxation results are also represented in the VGP plots for each sample (Figure 4.3a, c and e). Where TTS is found to work for the oscillatory shear data (e.g. PEHA0 and much of UPyPEHA6 data), the stress relaxation results follow the same curve as the oscillatory data, but span a wider range of moduli at each temperature. However, where TTS is breaking down (e.g. UPyPEHA14 sample at 263 K), the extended curve obtained by stress relaxation experiments at a given temperature still passes through the broad band swept out by the (non-overlapping) oscillatory rheology data taken at nearby temperatures, following the general shape of that band. The net result is that the cumulative error produced when TTS shifting oscillatory data obtained at temperatures close to the reference, is small. Consequently, the TTS curves match quite closely the *iRheo* output, over the frequency range obtainable by transforming stress relaxation data taken over a reasonable experimental time, as is clear in Figure 4.4.

The error in TTS shifting, however, accumulates when data from a much broader range of temperatures is shifted by larger extents in the frequency domain. This is apparent in Figure 4.5, where the stress relaxation data taken at different temperatures is shifted by the same factors as was used to create "master curves" from the oscillatory data in Figure 4.2a. Although the shifted stress relaxation data overlaps with the shifted oscillatory data taken at the same temperature, there is evidently a mismatch

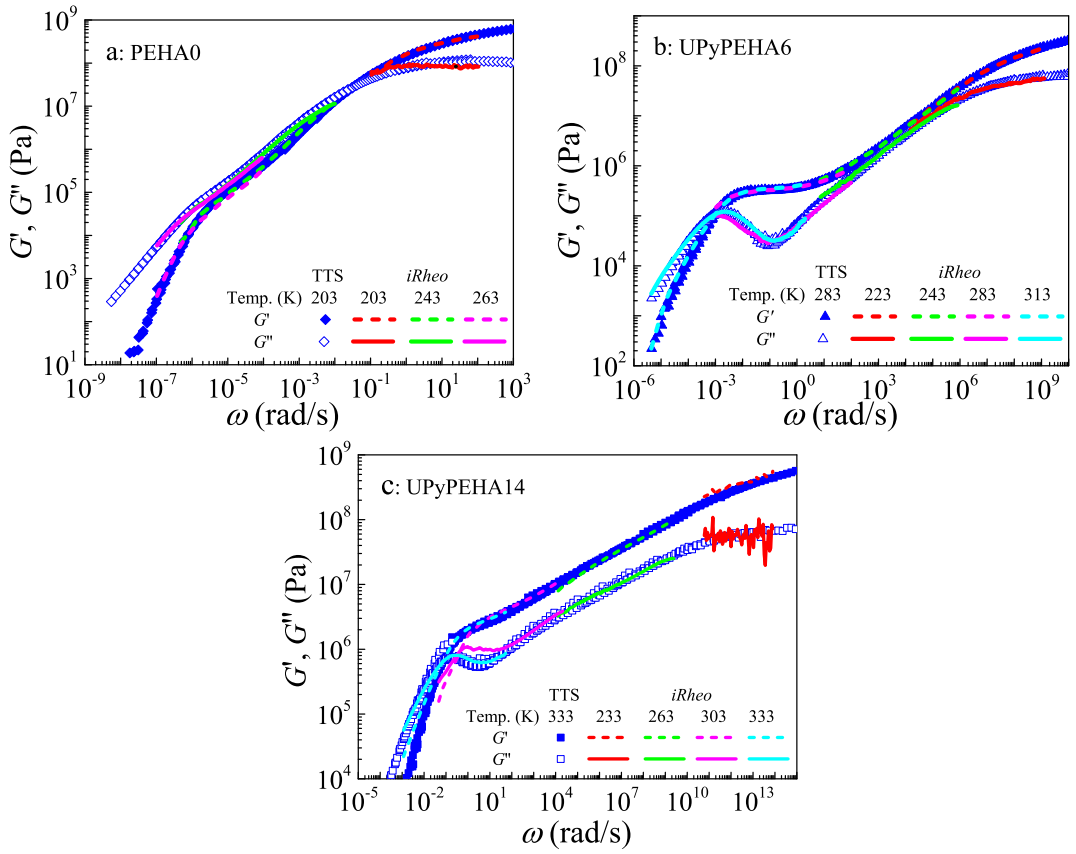

Figure 4.5: Comparison of the master curves from TTS (symbols) and from stress relaxation measurements (lines) for (a) PEHA0, (b) UPyPEHA6 and (c) UPyPEHA14. The colour lines are shifted horizontally using the TTS shift factors used to build the TTS master curves at the corresponding temperature. For example, the master curves for PEHA0 is built referring to 203 K. Thus the red lines are not shifted, but the green and pink lines are shifted using the TTS shift factors for 243 and 263 K.

between the shifted stress relaxation data obtained at different temperatures for the UPyPEHA14 sample (and weakly for the UPyPEHA6 sample). The PEHA0 data overlaps perfectly.

Hence, we conclude that construction of a reliable master curve across a broad frequency range is not possible for the samples with high ϕ_{UPy}; the cumulative shifting error means that sections of the spectrum are moved to the incorrect frequencies. In what follows, we thus use only the master curves depicted in Figure 4.2c and the shift factors in Figure 4.2d. From Figure 4.2c, the following general statements can be made:

as ϕ_{UPy} increases, (i) the plateau moduli increase, (ii) the terminal relaxation times increase, and (iii) the power law exponents at the lowest measured frequencies decrease. These results are consistent with results for several other reported supramolecular polymers. [186, 213, 300, 301] The temperature-dependent shift factors for PEHA0 and UPyPEHA2 can be well described using a WLF equation (C_1 = 9.9 and C_2 = 109.9 for PEHA0, C_1 = 11.3 and C_2 = 89.9 for UPyPEHA2). However, in the temperature range where we consider that TTS works (above 323 K) for UPyPEHA with $\phi_{UPy} \geq 2$ mol%, the shift factors can be fitted using the Arrhenius equation, which gives the activation energy for polymers to flow. As illustrated by the slope of the Arrhenius fitting in Figure 4.2d, the activation energies increases as ϕ_{UPy} increases, i.e. 78, 108, 116 and 191 kJ/mol for UPyPEHA2, UPyPEHA6, UPyPEHA9 and UPyPEHA14, respectively.

4.4 Modeling of linear shear rheology

4.4.1 "Classic" sticky Rouse model

The most commonly used model to describe the rheology of unentangled associating polymers, the sticky Rouse model, is based on the idea that stickers along the chain provide an additional effective drag, delaying the terminal relaxation time. [184, 253, 306, 307] The chemical dissociations and associations of the stickers occur on a time scale τ_{assos}, corresponding to the typical time a sticker will spend associated. However, following the idea of Rubinstein and Semenov [307], a dissociated sticker will often return to and re-associate with the same partner. Hence, stress relaxation only occurs when the stickers change partners, characterized by an average timescale τ_s, which may be significantly longer that the timescale τ_{assos}. Thus, τ_s is the relevant timescale for linear rheology. We assume that the sticker lifetime τ_s is significantly longer than the time-scale for the slowest Rouse-mode corresponding to chain segments between stickers, and thus $\tau_s \gg (N/N_s)^2\tau_0$. Here, τ_0 is the characteristic relaxation time of a Rouse monomer, and $N_s = M/M_{strand}$ is the average number of stickers per chain of molecular mass M, where M_{strand} is the average molar mass between stickers.

The slowest Rouse modes are uniformly retarded by the effective sticker friction, and so it is possible to decouple the stress relaxation function, $G(t)$, into two distinct summations over mode contributions, as proposed by Chen and co-workers. [184] The

first term in Equation (4.1) is the contribution to $G(t)$ from chain strands longer than M_{strand} that are unrelaxed, and thus elastically active at time t, and the second sum is the corresponding Rouse contribution from chain strands shorter than M_{strand}

$$G_s(t) = \sum_i \frac{\rho w_i RT}{M_i} \left[\sum_{p=1}^{N_{s,i}} \exp\left(-tp^2/\tau_s N_{s,i}^2\right) + \sum_{p=N_{s,i}+1}^{N_i} \exp\left(-tp^2/\tau_0 N_i^2\right) \right]. \tag{4.1}$$

Here, ρ is the mass density of the polymer, R the gas constant, T the temperature, w_i and M_i are the weight fraction and molecular weight of the i^{th} chain fraction, $N_i = M_i/M_0$ is the number of elementary Rouse monomers per chain, each with molar mass M_0, and $N_{s,i}$ is the average number of stickers on the i^{th} chain fraction. Note that have the relation

$$M_{\text{strand}} = \rho RT/G_N^0, \tag{4.2}$$

where G_N^0 is the (experimental) value of the plateau modulus. Given that ρ, T and M_i are known, G_N^0, τ_s and τ_0 are fitting parameters of this model, where the two timescale parameters shift the model predictions in time, or correspondingly frequency, in a frequency dependent representation.

4.4.2 The stochastic model

In this work, we demonstrate that the sticky Rouse model can capture the low frequency, long-time, linear rheological response for all four polymers. However, the model fails to predict the loss modulus at intermediate frequencies around the plateau region.[184, 186] Hence, we propose a number of modifications to the sticky Rouse model to make it better describe our particular supramolecular polymers.

The new model, we here call it the "stochastic model" addresses three particular assumptions made by the sticky Rouse model which are not relevant for our polymers: (i) the synthesis process, random co-polymerization, leads to a random placement of the stickers along the backbone and this is not accounted for in Equation Equation (4.1), which assumes that all stickers are equally spaced. Instead, we generate a number of chains with random distribution of sticky groups along the chain, rather than assuming

evenly spaced stickers, as is done in the Sticky Rouse model. (ii) in Equation Equation (4.1), the relaxation of chain-end segments (one free end and one associated) is treated in the same way as the relaxation of chain segments "trapped" between stickers (both associated). In the new model, instead we differentiate between these two "types" of chain segments. Accounting for these two factors leads to a modification of the "fast" relaxation modes of the sticky Rouse spectrum. At the time scale of τ_s, or longer, only the "trapped" chain segments contribute to the stress because the chain ends and internal modes of the trapped chains are fully relaxed. A model thus needs to be consistent with the random sticker placement and be able to describe the relaxation of the remaining chain modes. (iii) it would be possible to treat the long time motion of a chain by constructing a Rouse-like model with a friction proportional to τ_s concentrated at the randomly placed sticker positions. However, this would not properly represent the chain motion, since dissociation of a sticker and re-association with a new group involves a finite sized "hop" of the chain, with a hop amplitude dependent upon the lengths of chain to adjacent stickers, rather than a continuous motion with increased friction. Thus, instead a stochastic model with finite sized hops is constructed. The details of the stochastic model are presented in the Appendix.

4.4.3 Comparisons of two models with experimental data

Figures 4.6a and 4.6b show storage and loss moduli of experimental data, as reported above in Figure 4.2c, together with fits to the data using the stochastic model and the sticky Rouse model for the UPyPEHA6 and an indication of the contribution to the spectrum from fast internal Rouse modes and "sticky" modes. Figure 4.6c shows the fitting results of both models for the sample with different UPy contents. The parameters used for both models are shown in the Table 4.1. The parameter N_s, which describes the average number of stickers per chain between stickers, fixes the value of the plateau modulus (of G'_{sticky}) via Equation (4.2). The parameter τ_s effectively shifts G'_{sticky} and G''_{sticky} horizontally and is adjusted to fit the low frequency cross-over. The parameter τ_0 effectively shifts G'_{fast} and G''_{fast} horizontally, and is adjusted to fit the high frequency region near the plateau modulus.

The slopes at low frequency are well captured both by the stochastic model and the sticky Rouse model, which indicates that the "hop" picture described above for

Table 4.1: Parameters used in the stochastic and "classic" sticky Rouse models.

sample	M_n[a]	PDI[a]	N_s		τ_s (μs)		τ_0
codes	kg/mol		NMR[a]	Models[b]	Stochastic	Classic[c]	(ns)
UPyPEHA2	16.6	1.24	2	0.2	5	25	0.70
UPyPEHA6	22.0	1.38	7	3	29	65	1.0
UPyPEHA9	23.7	1.71	11	8	56	100	2.5
UPyPEHA14	24.6	2.38	17	21	83	200	500

[a] Identical to values of Table 3.1;

[b] Same parameters used in both models;

[c] Includes the factor π^2, Section A.3.6;

the large scale chain motion is meaningful, and that the polydispersity of the system is well captured in both models. However, the value of the relevant fitting parameter, the sticker time τ_s, is substantially different for the two models. The reason for this discrepancy is that the stochastic model considers finite distance hops of the discrete sticker groups, which are randomly placed along the chain, whereas the "sticky Rouse model" of Equation (4.1) considers continuous motion of a chain with distributed friction. We argue that the stochastic model is closer to the physical reality.

For frequencies in the rubbery plateau range, both models show a slight disagreement with the data, particularly in the loss modulus. For all materials, the fit is better for the stochastic model, because it includes: i) the distribution of length between stickers and stickers per chains, and ii) the separate contribution of the chain ends. Both of these factors give rise to a longer, smoother crossover between the high frequency Rouse spectrum (for sections of chain between stickers) and the plateau, because this crossover occurs at later times for longer chain sections between stickers, and for chains with one free end. Consequently, the storage and loss modulus are matched quite well at the high frequency end of the plateau region in the stochastic model, showing significant improvement over the sticky Rouse model.

Further improvement of the fit to data would require introducing yet more physical mechanisms with correspondingly more parameters. We consider the most likely cause of the remaining mismatch with data in the plateau region is that the model considers a single "sticker time". Introducing a spectrum of sticker times (which might be justified by supposing different local environments or configurations for paired stickers) would

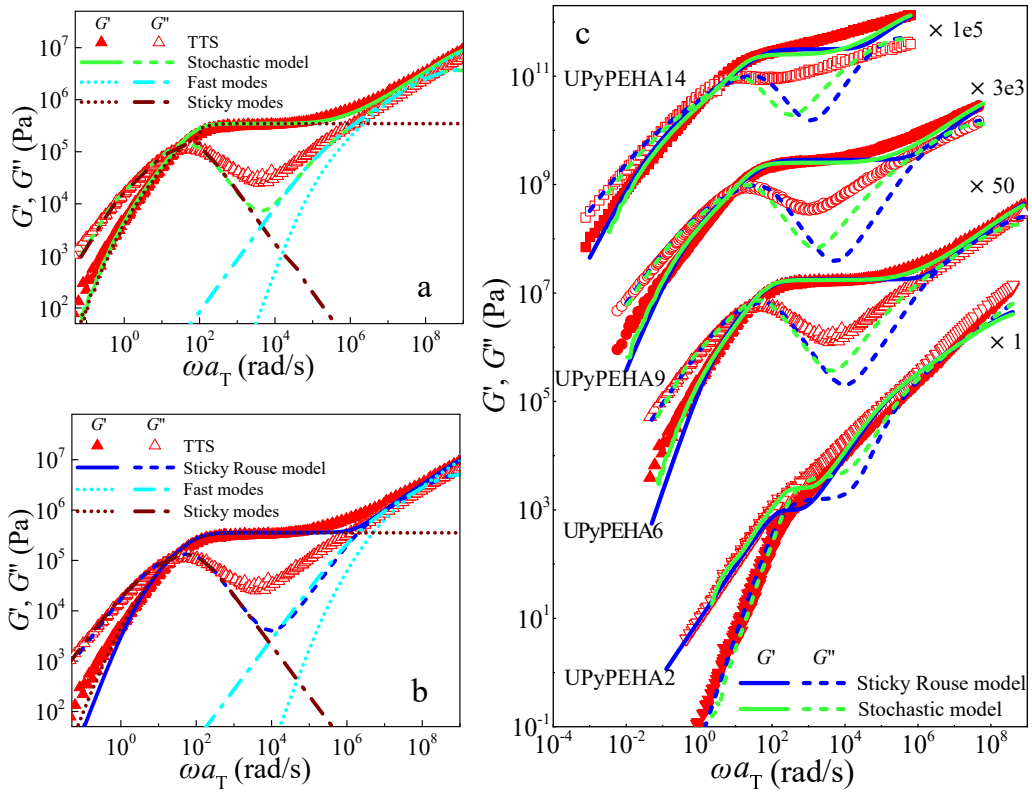

Figure 4.6: Master curves (symbols) for UPyPEHA6 referring to 343 K, and fitting (solid lines) by (a) the stochastic model and (b) the sticky Rouse model, and the contributions from the sticky modes and the fast modes. (c) master curves (symbols) for the samples with varying UPy contents, and the fitting by the sticky Rouse model and the stochastic model. The curves in (c) are vertically shifted for clarity. The parameters used in both models are given in Table 4.1.

certainly improve the model fits, at the expense of introducing and parameterizing a function for the distribution of sticker lifetimes.

One feature of the fitted value of the sticker time τ_s, that is true for both models, is that it increases with increasing concentration of stickers. It has been pointed out by Rubinstein and Semenov [307] that the effective sticker time in the model is not the fundamental time for sticker dissociation, since a dissociated sticker will return many times to the same partner, before finally finding another free partner with which to associate. Since returns to the same partner does not result in a significant chain rearrangement, to first approximation, these events do not relax the stress. Consequently,

the sticker time, τ_s, should be interpreted as the time to find a new partner. Whilst it may be that the fundamental sticker dissociation time changes with UPy content (and certainly the activation energy does seem to change), it is appealing to suggest that the differences in sticker time τ_s might be attributed to the relative difficulty of finding a new partner as UPy content is increased, i.e. stickers return more often to the same partner before swapping. This suggestion can be supported with a scaling argument showing that an increase of the number of UPy group per chain implies a decrease of the number of stickers present in a "search" volume of a detached sticker. Calling b^3 the volume of a sticker or monomer, and $N_m \equiv N/N_s$ the average number of monomers between stickers, then the number of stickers per unit volume, n_s, is defined as

$$n_s = \frac{\text{number of stickers per chain}}{\text{volume occupied by a chain}} \approx \frac{N_s}{N_s N_m b^3} = (N_m b^3)^{-1}. \tag{4.3}$$

When a sticker is free, it explores its neighbourhood in a volume limited by the typical dimensions of the chain between stickers, see Figure A.3, which obeys random walk statistics. Hence the explored volume, V_{search}, is of order

$$V_{search} \approx (N_m^{1/2} b)^3. \tag{4.4}$$

Therefore, the number of stickers, $N_{partner}$, in the exploration volume defined by Equation (4.4) scales as

$$\begin{aligned} N_{partner} &\approx n_s V_{search} \\ &\approx N_m^{1/2} \\ &\propto N_s^{-1/2}. \end{aligned} \tag{4.5}$$

$N_{partner}$ represents the number of potential partners available to a sticker, and it decreases as the number of stickers per chain, N_s, increases. Consequently, we expect the effective sticker time τ_s to increase with increasing number of stickers per chain. The above argument may be augmented by noting that for the largest concentration of stickers, the chain between stickers may in fact be not completely flexible. From Table 3.1, one can know that as ϕ_{UPy} increases, the N_m decreases from 16 for UPyPEHA6 to 6 for UPyPEHA14. Compared with the Kuhn length (~13 monomers) of a similar polymer (PHA),[231] the segments between two UPy groups are not flexible enough to search for a different partner in a surrounding volume, especially for high ϕ_{UPy} samples. To

relax stresses, cooperative dissociation of several stickers simultaneously is required for segments being flexible enough to search for a new partner. In other words, the activation energies for chain relaxations are determined by the event involving breaking of several stickers simultaneously. As ϕ_{UPy} increases (segments between two UPy groups becomes shorter), more stickers are required to be broken simultaneously for chain relaxations, leading to higher activation energies. This argument is consistent with the results from Figure 4.2d.

4.4.4 Extensional rheology and modelling

As noted above in Section II, we were only able to successfully measure the non-linear extensional rheology for the UPyPEHA6 sample. Figure 4.7a shows the extensional stress growth coefficient (i.e. stress divided by strain rate, $\sigma/\dot{\varepsilon}$) as a function of time for UPyPEHA6 with various stretching rates at T =343 K, whilst Figure 4.7b shows the stress as a function of Hencky strain for the same measurements.

We find that at short times before strain hardening occurs, the extensional stress growth coefficient (η_{E}^{+}) data follow the LVE envelope (Equation 4.8). However, for extension rates of 0.1 s^{-1} or below, at longer time (above a Hencky strain 200%), strain hardening is observed leading to stress growth coefficients with magnitudes up to 10 times higher than those of the LVE envelope. For these cases, the experiments were terminated when stresses were out of the limit of the rheometer transducer. For extension rates 0.1 s^{-1} or above, the extension is typically terminated for stresses in the region of 10^5 to 2×10^5 Pa (almost independent of strain rate) by brittle fracture. For the measurements performed at rates of 0.3 s^{-1} and above, the samples break before the strain hardening takes place.

The solid lines in Figure 4.7a and 4.7b correspond to the simplest possible non-linear rheological description of the data, in which each mode from multi-mode Maxwell fit of LVE data is assigned to an upper-convected Maxwell model (UCM)[317]. This model is one of the few non-linear models that can be exactly derived from a microscopic model without closure approximations. A collections of dumbbells (frictional beads separated by linear springs) embedded in a fluid give rise to a UCM model with single relaxation time. A "Rouse model" (many frictional beads with linear springs) in nonlinear flow gives rise to a superposition of mltiple UCM models with relaxation

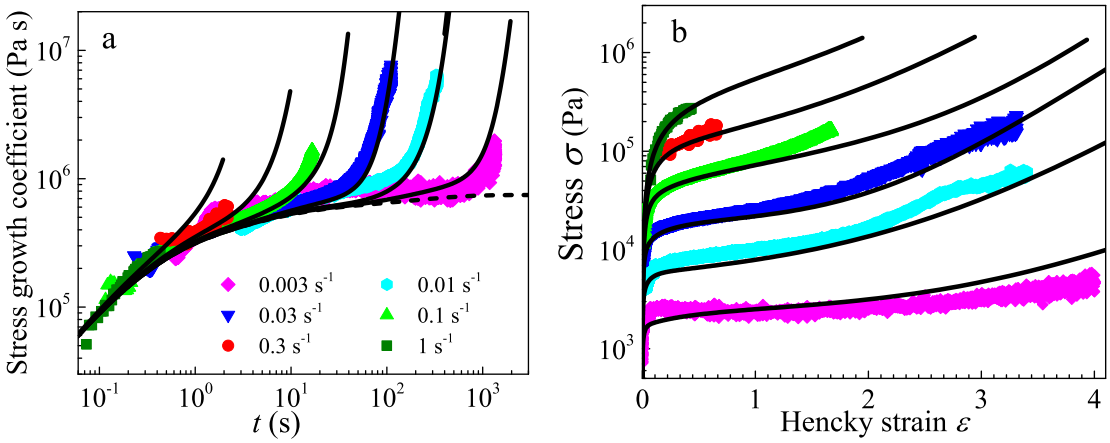

Figure 4.7: (a) Stress growth coefficient measured using the filament stretching rheometer for the UPyPEHA6 at 343 K with varying stretching rates. The dashed line represents the best fit of the multimode Maxwell model to the LVE data. (b) the stress as a function of Hencky strain corresponding to the same measurements in (a). The symbols represent the same stretching rates in both (a) and (b).

times of the models, corresponding to the Rouse relaxation spectrum.[317] Hence, if our polymer sample obeys Rouse-like dynamics, we may expect a multi-mode UCM model to successfully describe the data. We test this as follows. We fit the LVE data by assigning two Maxwell modes per decade (via a least square procedure) to obtain a set of relaxation times, τ_i , and weighting constants, g_i. The total stress is then given by

$$\boldsymbol{\sigma}(t) = \sum_i g_i \boldsymbol{\sigma}_i(t), \tag{4.6}$$

where $\boldsymbol{\sigma}_i$ is the conformation tensor associated with the i^{th} Maxwell mode, whose time evolution is given by the upper convected Maxwell model

$$\frac{\mathrm{d}\boldsymbol{\sigma_i}}{\mathrm{d}t} = \boldsymbol{\kappa} \cdot \boldsymbol{\sigma_i} + \boldsymbol{\sigma_i} \cdot \boldsymbol{\kappa}^T - \frac{1}{\tau_i}(\boldsymbol{\sigma_i} - \boldsymbol{I}), \tag{4.7}$$

where $\boldsymbol{\kappa}$ is the velocity gradient tensor and $\boldsymbol{I}$ is the isotropic tensor.

The dashed line in Figure 4.7a represents the stress growth coefficient corresponding LVE which, in extension, is given by

$$\eta_{\mathrm{E}}^{+}(t) = 3 \sum_i g_i \tau_i (1 - \exp\left(-t/\tau_i\right)), \quad \dot{\varepsilon}\tau_i \ll 1. \tag{4.8}$$

It is clear that this simple model can provide an excellent description of the extension hardening up to the point of either sample fracture or termination of the experiment. This supports the notion that Rouse-like chain motions are important given that the Rouse model is predicted to obey a multi-mode upper-convected Maxwell model in non-linear flow [317]. To understand the behaviour of supramolecular materials in the non-linear extensional regime as well as fracture at high deformation rates is important for the design and use of these types of materials. Although the linear viscoelasticity of supramolecular materials are increasingly being investigated, there has been much less focus on the the non-linear rheology and particularly extensional rheology and fracture behaviour and this is thus an area where a lot more work are needed in the future.

4.5 Conclusions

In this work, linear viscoelastic properties of a series of PEHA based supramolecular polymer with systematically increasing the concentration of UPy groups increasing the concentration of the supramolecular interactions and validity of TTS for these supramolecular polymers were investigated.The supramolecular interactions, i.e. hydrogen bonds between UPy groups, acting as a second friction for polymer chains, show a different temperature dependence to the segmental relaxations and thus makes this class of polymers not "thermorheologically simple". Thus, TTS is expected to break for supramolecular polymers. However, by comparing the modulus curves from stress relaxations and from the TTS, we found that TTS works reasonably well in a relatively narrow time or frequency window close to the reference temperature. Note that one should be cautious when constructing master curves in which data is shifted by many decades in frequency, because cumulative errors may lead to wrong shape of the master curve.

Modifications to the classical sticky Rouse model were performed to improve the predictions of LVE by taking into account of (i) random distribution of sticky groups along the chain, rather than assuming evenly spaced stickers when polymers, which is closer to reality when polymers are synthesised from randomly co-polymerization of two monomers; (ii) the contribution to relaxation from dangling chain ends, which is different from the relaxation modes of segments of chain "trapped" between stickers; (iii) the chain motion upon dissociation of a sticker and re-association, assumed to be

a finite sized "hop" of the chain, rather than a continuous motion with increased friction, as assumed in the standard sticky Rouse model. The modified model can describe data in the low frequencies range as good as the classical sticky Rouse model. The parameter τ_s which is the timescale for stickers to change partners is more physically meaningful than the corresponding parameter in the "classical" sticky Rouse expression, because it takes account of the "hop" process for a dissociated sticky group to search another sticky group. τ_s increases with increasing ϕ_{UPy} may be due to the increasing difficulty in finding different partners, and to the increased stiffness of the chain. The fits in intermediate zone are also improved because contributions from polydispersity of strands between stickers and dangling ends are included. However, it worth noting that the fits in the intermediate zone is still not perfect, indicating that extra physics needs to be considered, such as distribution of mean sticker lifetimes.

Extensional rheological measurements on one of our samples were conducted. At short times, the stress growth coefficient follows the LVE envelope. At long times, stress growth coefficients show the magnitudes ~10 times higher than the LVE envelope due to the strain hardening. The upper-convected Maxwell model, which is based on the LVE fit, works very well to model non-linear extensional data. At relatively low supramolecular interaction concentrations, the TTS works reasonably well to capture the LVE dynamics and properties of the materials.

Chapter 5

Supramolecular polymers based on UPy end-functionalised poly(propylene glycol): structure, dynamics, rheology and applications

In this chapter, the effects of chain-end functionalisation of poly(propylene glycol) (PPG) with hydrogen bond associating 2-ureido-4[1H]-pyrimidinone (UPy) groups to form a supramolecular polymer (UPyPPG) are investigated. Multiple hydrogen bonds can form between two UPy groups. i.e. forming dimers, which in turn can lead to chain extension and complex structures including fibre-like aggregates. Both chain extensions and aggregates lead to dramatic changes of material properties. Unfunctionalised PPG is a viscous liquid at room temperature whereas the supramolecular UPyPPG polymer is a rubbery material. The effects of supramolecular associations on structure, relaxation dynamics and rheological properties were investigated using various techniques. The end-functionalisation weakens and broadens the glass transition and increases the glass transition temperatures by ~ 20 K. Normal mode chain-relaxations, observed both in rheology and broadband dielectric spectroscopy, become slower upon end-functionalisation, reflecting the associating nature of the supramolecular interactions. The temperature dependence of the normal mode dynamics changes from VFT to Arrhenius behaviour, reflecting that a single energy-scale set by UPy-interactions is dominating chain relaxations of the supramolecular polymer. The secondary relax-

ation process observed in the glass state is not markedly affected by the end-group modification. In light of these findings, potential applications of this supramolecular material both as a solid electrolyte for lithium ion batteries and as a basic component in self-healing coatings are explored.

5.1 Introduction

Poly(ethylene glycol) (PEG), poly(propylene glycol) (PPG) and polytetrahydrofuran (PTHF) are three polyglycols with similar backbone structures, i.e. repeat units are composed of short alkyl units which are linked through ether groups. The backbones for these three polymers can be expressed as $-(CH_2CH_2O)_n-$, $-(CH_2CH(CH_3)O)_n-$ and $-(CH_2CH_2CH_2CH_2O)_n-$ respectively (Chapter 6 for more details on PTHF). These polymers have been of great interest for many years because of their wide applications in many fields including medicine, biology, lithium (Li) ion batteries and thermoplastic elastomers (TPE). [32, 216, 318–321] PEG and PPG have been significantly investigated as promising candidates for polymer electrolytes due to the strong Li ion coordination to the backbone ether oxygen atom. PEG is a semi-crystalline polymer which makes it difficult to investigate the ion transfer mechanisms in PEG-based polymer electrolytes over a wide temperature range.[318] On the other hand, the side group methyl groups (CH_3) in PPG prevent crystallization and makes it an appropriate alternative polymer to investigate ion transfer mechanisms.[322] To better understand the fundamental aspects of PPG based polymer electrolytes it is essential to understand relaxation dynamics of PPG both with and without lithium salts.

Relaxation dynamics of PPG have been investigated by various techniques, such as broad band dielectric spectroscopy (BDS),[272, 296, 323–341] calorimetry,[342] light or neutron scattering,[327, 343–346] mechanical experiments,[347] and nuclear magnetic resonance (NMR),[348] in varying conditions, such as under high pressures[322, 349] and in spatial confinements.[328, 344, 350] Using these techniques, it was shown that dynamics are affected both by molecular weights and end functionalisations.[324, 327, 341, 347] Oligomers, such as propylene glycol (PG), dipropylene glycol (DPG) and tripropylene glycol (TPG) are too short to show polymeric properties.[324, 336, 341] The dynamics of these oligomers are thus similar to those of classic small molecule glass forming liquids. For instance, a structural relaxation is observed by BDS near

the glass transition temperature.[351] Above a certain molecular weight threshold, typically around 7 monomers, a relaxation visible at the low frequency flank of the segmental relaxation relaxation in frequency dependent dielectric spectra becomes visible.[324, 341] This relaxation which is thus slower than the structural α relaxation is the so-called normal mode realaxation.[352–357] The normal mode relaxation can be attributed to motions of the end-to-end vector of a polymer backbone and can thus depending on the polymer chain-length be controlled by Rouse or reptation behaviour. A normal mode relaxation is observed in BDS for polymers that have a segmental dipole-moment component along the chain direction. The end-to-end dipole moment vector is the summation of the segmental dipole moment components along the backbone.[354] PPG is an example of a so-called type A polymer that has a dipole-moment component in the chain-direction and will thus show relaxations of the polymer end-to-end dipole-moment.

The normal mode spectrum for PPG below its entanglement molecular weight, M_e, can be described by the Rouse model.[324, 341] The relaxations of the normal modes thus strongly depend on the molecular weight. An increasing molecular weight or chain length leads to a slower normal mode relaxation. The hydroxyl end-groups of PPG have been demonstrated to lead to the formation of H-bond mediated clusters leading to only very small chain-length effects on the glass transition temperature for molecular weights above M_w ~400. [324, 327, 329, 337, 341, 347] Thus, as the chain length increases, a more well-separated normal mode can typically be observed in the dielectric spectra.[324, 337, 341]

To further illustrate the roles of end-functionalisation in determining the dynamics of PPG, several studies have been devoted to modifications of the OH end-groups of PPG, e.g. by amino groups, -NH_2[330] or methoxy groups, -OCH_3.[327, 334, 347] From density functional theory (DFT) calculations, the hydrogen bonding energy between two -OH groups is higher (15.7 kJ/mol) than that between two -NH_2 groups (6.4 kJ/mol).[330] On the other hand, no hydrogen bonds can be formed for PPG with terminal -OCH_3 groups[327, 334, 347] As a consequence of these end modifications, the relaxation dynamics differ in several ways between different types of PPG chain-series: i) glass transition temperatures of -NH_2 and -OCH_3 terminated PPGs are lower than those of -OH terminated PPG of the same molecular weight demonstrating that effective structures of larger molecular weight are formed due to H-bonding for

OH-terminated PPG.[330, 334] ii) PPGs with -NH_2 and -OCH_3 terminated groups are more fragile and thus typically have a larger m-value (for a description of fragility, see Chapter 1). and the fragilities show a less significant molecular weight dependence than those for -OH terminated PPGs.[330, 334] For example, as the molecular weights increase from $M_w \sim 200$ to 4000 g/mol, the fragility m-parameters for -NH_2 terminated PPGs remain around 105, whereas the m-parameters for -OH terminated PPGs increase from around 80 to 100.[330] iii) different end-functionalizations typically have little effect on the normal mode relaxation dynamics iv) the observed secondary relaxation speeds up for OCH_3 terminated PPGs for chain-lengths shorter than 5 monomer units and this is typically observed for oligomer systems which lack strong intermolecular interactions. However, for H-bonded OH terminated PPG, this effects disappears and it has been suggested ([334]) that this is due to molecular clustering leading to even the shortest PPG oligomers being part of clusters that are larger than the cut-off size needed for the speeding up of the dynamics. Instead, for the shortest PPG oligomers, a slowing down of the dynamics is observed and this has been suggested to be directly linked to the increasing degree of H-bonding for shorter PPG chains,[334]

The above mentioned studies were investigating the relaxation dynamics of PPGs with relatively weak H-bond interactions. For systems involving stronger hydrogen bonding groups, such as 2-ureido-4[1H]-pyrimidinone (UPy) that can form quadruple hydrogen bonds, the behaviour is still unclear. In the present work, a supramolecular polymer based on PPG with end-functionalised UPy groups was synthesised. Multiple hydrogen bonds can be formed between two UPy groups, leading to chain extension, the formation of more complex associations and dramatic changes in macroscopic properties.[33, 166, 225, 226, 242, 284, 285] The unfunctionalised PPG is a viscous liquid at room temperature whereas the supramolecular polymer UPyPPG is a rubbery material. The effects of chain-end UPy addition on the structure, dynamics and rheological properties have been investigated.

Solid polymeric electrolytes for lithium batteries have attracted a great amount of attention in the last few decades because of advantages, such as high safety and low cost, over traditional liquid lithium batteries.[321, 358–363] However, most solid polymeric lithium electrolytes show an ionic conductivity significantly below $\sim 10^{-3}$ S/cm at room temperature which is one factor limiting their utilization.[360, 363] It is therefore essential to understand the ion transfer mechanisms in polymer electrolytes to try

to improve the ionic conductivity. A significant amount of efforts have been put into investigations of polymeric electrolytes based on complexes based on various Li-based salts and the polymer polyethylene glycol (PEG)[320, 364–370] poly(propylene glycol) (PPG)[322, 364, 371–375] These polymers are typically chosen due to their ability to solvate salts well, the fact that the ether oxygen is a good coordination site for Li-ions and the relatively low glass transition temperatures that means leads to significant segmental mobility in the amorphous state within a typical operational temperature range.[320] Unfortunately, PEG is a semi-crystalline polymer and its ionic conductivity is mainly attributed to the amorphous phase of the PEG-salt complex[320, 370] This means that unless the crystallization can be quenched for a particular PEG-based system, PEG if often not useful unless the battery operation temperature is above the melting point of the relevant PEG-salt complex. The polymer choice of the present work, PPG, has the advantage that it is a fully amorphous polymer and we can thus investigate ion conductiviy effects without taking any effects due to crystallinity into account.[322, 364, 371–375] A further problem with the use of salt complexes made from either pure PEG or PPG as polymer electrolytes is that the electrolytes lack mechanical rigidity. One potential solution to this is to introduce supramolecular associations and this is the route we investigate in the present work.

Microphase separation has been observed in many PPG-lithium salt blends.[322, 371, 373, 374] For example, two glass transition temperatures due to microphase separation between ion-rich and ion-depleted regions have been observed for several PPG-salt complexes using differential scanning calorimetry (DSC) and broad band dielectric spectroscopy (BDS).[371, 373] Microphase separation is not unique to PPG-salt complexes and is also observed in other polymer-salt complexes, such as poly(vinyl methyl ether) (PVME)-$LiClO_4$.[376] Thus, it seems that microphase separation is commonly found in polymeric electrolytes and understanding the mechanisms of its origin and its effects on ion transfer is essential in designing polymeric electrolytes with better performance.

In this chapter, a PPG with a moderate molecular weight of 2000 g/mol and the corresponding UPy end-functionalised polymer UPyPPG are chosen for use as polymeric electrolytes. The salt LiTFSI is chosen to prepare electrolytes. Improvements in ion conductivity were demonstrated using LiTFSI salts due to the reduced crystallinity of PEG at room temperature, the enhanced dissociation and plasticizing effects of the

relatively large anionic group.[377] LiTFSI also has good solubility in polymers and low anionic group mobility in electrolytes.[377] The latter is advantageous since the goal is to achieve an efficient transport of only the Li cations, whereas it is ideal to have immobile anions.[378] PPG-LiTFSI complexes with varying salt concentrations from O:Li=5:1 to 1000:1 are investigated, and the relationship between ion concentrations and ion conductivities has been determined. Microphase separation is observed when the O:Li ratio is smaller than 40:1. We find evidence supporting that the ion conductivity is controlled not by the segmental relaxation as normally assumed, but by the slower normal mode relaxations. We also evaluated the self-healing property of UPyPPG using mechanical testing and some simple optical microscopy. Also, an initial exploration in how to prepare self-healing coatings by blending of UPyPPG with commonly used unsaturated reactants for UV curable coatings was performed; the self-healing property of these blended coatings were also investigated using optical microscopy.

5.2 Experimental section

5.2.1 Materials

All chemicals were purchased from Sigma Aldrich unless otherwise stated. 2-amino-4-hydroxy-6-methylpyrimidone (AHEP) and molecular sieves (4 Å) were used as received. Solvents, i.e. tetrahydrofuran (THF), dimethyl sulfoxide (DMSO), chloroform, dichloromethane (DCM) were dried for two days using molecular sieves before use. Tolylene 2,4-diisocyanate terminated poly(propylene glycol)(TDIPPG) was stored in a nitrogen-filled dry box to avoid moisture. Bis(trifluoromethane)sulfonimide lithium (LiTFSI) salt was dried at 393 K under vacuum for 2 days before use and THF was dried for a week using 4 Å pore size molecular sieves before use. 1-hydroxycyclohexyl-1-phenyl methanone (HPM), tripropylene glycol diacrylate (TPGDA) and diacrylate poly(propylene glycol) (DAPPG) of molecular weight M_n = 2000 g/mol, were provided by *allnex*, Belgium.

5.2.2 Synthesis of UPy end-functionalised poly(propylene glycol) (UPyPPG)

The procedure for synthesis of UPyPPG is shown in Figure 5.1. To conduct the reaction, AHEP (22 g, 0.176 mol) was dissolved in 200 ml of anhydrous DMSO in a 500 ml round bottom flask at 150°C. The solution was then cooled to room temperature and TDIPPG (20g, 8.69 mmol) was dissolved in 100 ml anhydrous chloroform. After this, TDIPPG solution was added dropwise into the AHEP solution over a one hour period under a nitrogen atmosphere. The mixture was stirred continuously for 6 hours. Most solvents were removed under a high vacuum using a rotary evaporator and a white solid was obtained. For purification a large amount of chloroform was added

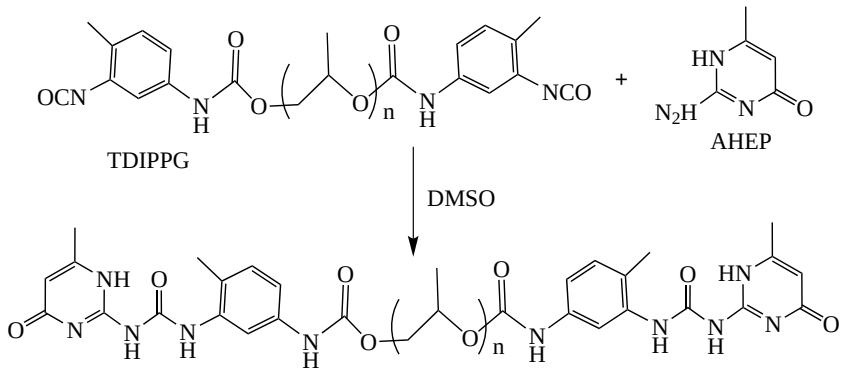

Figure 5.1: Synthesis of end-functionalised poly(propylene glycol)

to the white solid and after vigorous stirring for one hour, the white turbid suspension was filtered. To separate insoluble AHEP from soluble UPyPPG in chloroform, filtration was used to separate the excess AHEP from the product. The process was repeated twice to further extract UPyPPG. The filtered solutions containing UPyPPG were combined and concentrated resulting in a viscous liquid. To further remove unreacted AHEP, a 200 ml (10:1 volume ratio) mixture of chloroform and DMSO was added into the viscous liquid and washed with 100 ml of deionized water three times. The organic phase was collected and dried using magnesium sulfate ($MeSO_4$). After filtration, the final solution was collected and concentrated, resulting in a clear viscous liquid. The viscous liquid was further dried under vacuum at 90 °C for two days. After cooling to room temperature, a slightly yellow rubbery solid was obtained. This solid

was characterised using Size Exclusion Chromatography (SEC), Differential Scanning Calorimetry (DSC) and NMR. A summary of the result is: Yield: 21 g, 99%; M_n (g/mol): 3200 (SEC); PDI: 1.25 (SEC); T_g: 215 K (DSC); ^{1}H (500 MHz, $CDCl_3$) δ: 1.07-1.19 (-C$\underline{H}_3$ in polymer backbones), 2.08-2.21 (12H, benzene-C$\underline{H}_3$, pyrimidyl-C$\underline{H}_3$), 3.08-3.69 (-C$\underline{H}_2$-C$\underline{H}$- in polymer backbone), 4.95-5.09,(2H, -N$\underline{H}$-), 5.75 (2H, pyrimidyl-H) 6.47-7.12, (6H, benzene-H). ^{13}C (500 MHz, $CDCl_3$) δ: 17.3, 19.1, 66.8, 103, 117.1, 128.9, 130.9, 141.5, 152.4, 154.6, 169.5.

5.2.3 Preparation of polymeric electrolytes

Both pure PPG and UPyPPG were dried at 333 K under vacuum for 16 hours before use. Polymer electrolytes were prepared as follows: first PPG or UPyPPG and LiTFSI were separately dissolved in THF. Then two solutions were mixed by stirring overnight. The majority of solvents were slowly evaporated at room temperature in a fume hood for three days, which were further dried at T =333 K under vacuum; Weight losses during drying were carefully monitored to make sure that all solvents were removed. A range of samples with different ratios of ether oxygen to lithium ions O:Li (R) were prepared, ranging from 5:1 to 1000:1. For clarity, the samples were named by combining an acronym for the polymer matrix and the O:Li ratio. For example, PPG and UPyPPG with an O:Li ratio of 80:1 were named PPG80 and UPyPPG80, respectively.

5.2.4 Preparation of self-healing coatings

TPGDA and DAPPG are commonly used monomers or macromonomers for UV curable coatings. Since both TPGDA and DAPPG are bi-functional, a permanent network is formed after UV curing which hinders the flow of polymers and thus prohibits the self-healing properties. The idea here is to blend TPGDA and/or DAPPG with UPyPPG to combine the UV curable property with the temperature sensitivity of UPyPPG. At high temperatures, hydrogen bonds of UPyPPG are driven to the dissociative state and thus UPyPPG chains have sufficient mobility to heal a scratch. Several composite coatings were prepared as follows: solutions of TPGDA and/or DAPPG with UPyPPG were prepared in dichloromethane (DCM), followed by addition of small amounts of photo initiators (HPM). The solution was coated on clean glass slides and

subsequently polymer films were formed after the solvents were removed under vacuum at 313 K overnight. After drying, the films were cured under UV light for 3 min. The self-healing properties of the composite coatings could be tuned by changing the ratios between TPGDA, DAPPG and UPyPPG.

5.2.5 Characterisations

General characterizations to the chemical structures and general material properties using methods, such as nuclear magnetic resonance (NMR), size exclusion chromatography (SEC), differential scanning calorimetry (DSC), X-ray measurements and atomic force microscopy (AFM), are described in Section 3.2.3. Here, some specific details are provided below.

Broadband dielectric spectroscopy (BDS)

BDS measurements on PPG and UPyPPG are described in Section 3.2.3. The ion conductivities for PPG-salt complexes were measured using a gel cell with 18 mm in diameter and 6.8 mm in thickness (Figure 2.5), whereas the conductivities for UPyPPG-salt complexes were measured using two parallel plates separated by a *teflon* ring with 16 mm in diameter and 1 mm in thickness.

Rheology

Small amplitude oscillation shear measurements (SAOS) are described in Section 3.2.3. The experiments were conducted within a temperature range from T_g ($\approx$ 190 to 215 K) to T=373 K. Shear viscosities were measured using the same rheometer with plate-plate geometry of 10 mm diameter for PPG and 3 mm for UPyPPG. The viscosities were measured within a temperature range from 293 to 400 K in step of 10 K. The shear stress λ increasing linearly with shear rate $\dot{\gamma}$ is fitted and the slope of the fitted line is the viscosity (Chapter 2).

Optical microscopy

To evaluate self-healing properties of coatings, scratches were made on the surface using a sharp needle. Changes of scratches were observed using optical microscopy

equipped with a hot stage, temperature controller and camera. Pictures of the scratches were taken during heating of coatings (10 K/min from 303 to 423 K, ±0.5 K).

Universal mechanical testing system

Mechanical properties of UPyPPG strips were tested using the universal mechanical testing system (Zwick Z010) at room temperature. The sample strips were cut from UPyPPG films with thickness around 1.5 mm using a dumbbell cutter (ASTMD-638-v). After loading the sample strips into the testing machine, they were stretched at 60 mm/min and forces applied to the sample and strains were recorded.

5.3 Results and Discussions

5.3.1 Structure

Given the rather complex structures and supramolecular interactions of end UPy groups, an analysis of the structure is essential for the understanding of the polymer behaviour. Figure 5.2 shows AFM height and phase images for UPyPPG at room temperature. As shown in the height image (Figure 5.2a), the surface of spin cast film is very smooth, however, a weak contrast pattern of rod-like features can be observed. The AFM phase image (Figure 5.2b) clearly shows rod or fibre-like harder domains that are light in the image, on top of the darker continous amorphous phase corresponding to the PPG backbone. These structures are consistent with fibre-like structures previously observed for UPy-based supramolecular systems.[379–382] The average diameter and the spacing d between nanofibres are around 2 and 5 nm, respectively, as shown in the inset in Figure 5.2b.

The formation of nanofibre structures from hierarchical self-assembly of polymers containing urea units has been reported by many researchers[225, 226, 242, 383]. The formation typically involves three steps (Figure 5.3)[225]. The first step is the dimerisation of UPy groups, resulting in chain extension which can change the macroscopic properties dramatically from liquid to solid rubber at room temperature.[33, 166, 225, 226, 242, 284, 285] The second step involves stacking of the chain extended structures. Stacking of the formed UPy dimers can occur due to lateral hydrogen bonds

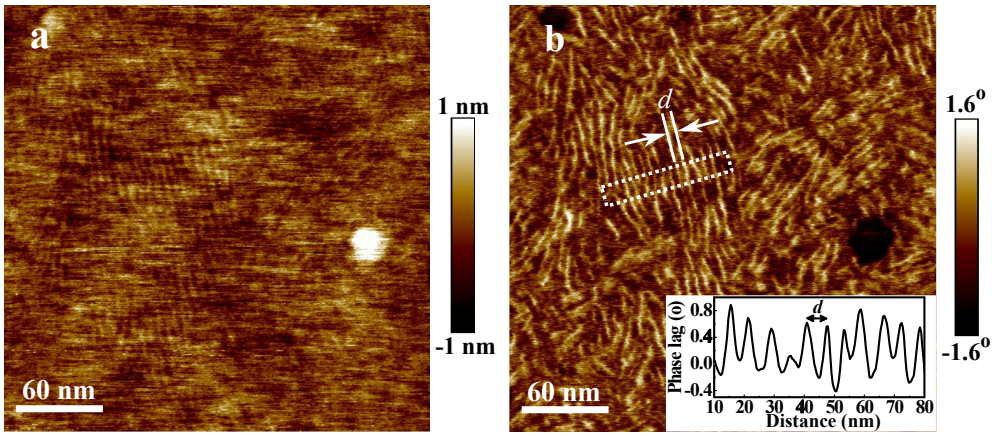

Figure 5.2: AFM height (a) and phase (b) images for UPyPPG after spin casting. The inset in (b) is the cross-sectional profile inside the dotted box, with the domain spacing *d* being the distance between the maxima of two neighbouring peaks.

between urea units.[172, 242, 283] It has been shown that the double lateral hydrogen bonds between urea units is the key driving force for the formation of nanofibres, and that several thermoplastic elastomers (TPE) can be formed from polymers only

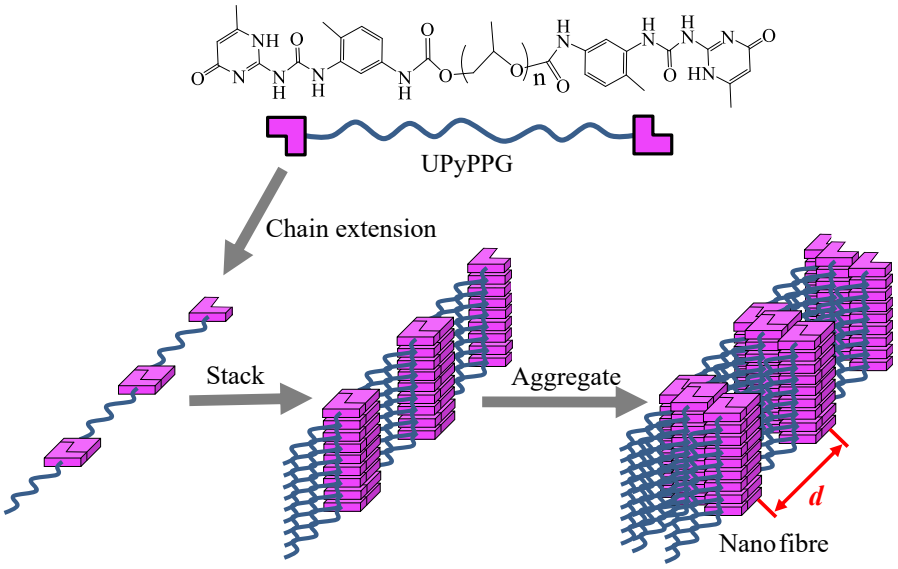

Figure 5.3: Schematic diagram showing the formation of nanofibres through hierarchical self-assembly involving three steps: i) chain extension through UPy dimerisation, ii) stack of UPy dimers and iii) aggregation induced phase separation of nanofibres.

containing urea units.[379–382] In our case, instead of urea units, the linking group between the UPy end-groups and the polymer chain is the amide unit which in principle can form a single lateral hydrogen bond. However, $\pi - \pi$ stack interaction between aromatic units (benzene rings) near chain ends in our case may also contribute to the formation of nanofibres.[23, 384] The third step consists of aggregation of the stacked structures.[225]

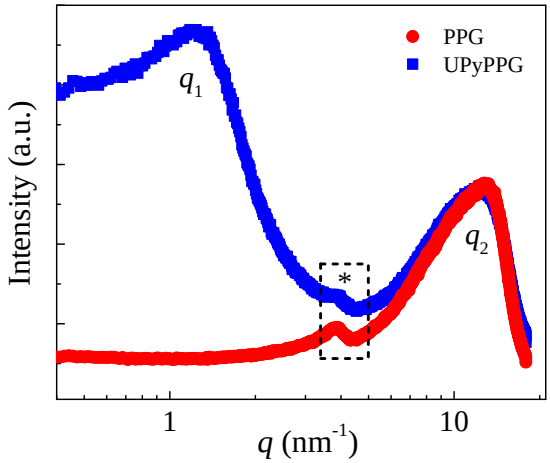

Figure 5.4: X-ray profiles for PPG and UPyPPG. Two peaks q_1 and q_2 are detected and the peak marked by $*$ is possibly due to antioxidants in PPG.[385, 386]

To investigate the structure further, both X-ray scattering measurements were performed on PPG and UPyPPG. As shown in Figure 5.4, a peak at $q_2 = 12.8$ nm^{-1} is observed for both PPG and UPyPPG. This corresponds to a characteristic distance of $2\pi/q_2 \sim 0.5$ nm and can be assigned to the typical interchain distance in amorphous polymers.[387] However, for $q < 3$ nm^{-1}, a significant difference between the PPG and the UPyPPG scattering results are observed. The profile for PPG does not show any significant features, whereas the profile for UPyPPG shows a clear peak at $q_1 = 1.22$ nm^{-1}, corresponding to an average domain spacing $d = 2\pi/q_1 \sim 5$ nm. The domain spacings determined from SAXS and AFM are thus consistent with each other (the inset in Figure 5.2b). The peaks marked with '*' appear at $q = 4$ nm^{-1} for both PPG and UPyPPG, indicating that this diffraction contribution is not due to the structure of UPy groups. Instead, we believe that the small peak is a Bragg peak from phenolic compounds which are usually used as antioxidants for PPG. Phenolic compounds are colorless crystalline solids which give the peak.[385, 386]

5.3.2 Dynamics and rheological response of PPG and UPyPPG

Figure 5.5 shows the specific heat capacity as a function of temperature near the glass transition for PPG and UPyPPG, respectively. The C_p curves reveal unambiguously that the characteristic step of the glass-to-melt transition for UPyPPG is at a higher temperature (Table 5.1), and is broader, compared with that for PPG. The differences can be quantified by extracting both onset and offset temperatures from which we deduce the broadness ΔT and the amplitude ΔC_p normalized by T_g of a glass transition, shown in Table 5.1. It is obvious that the glass transition becomes broader in UPyPPG, $\Delta T^{UPyPPG} > \Delta T^{PPG}$. The ΔC_p during a glass transition is related to the T_g and the change in rate of the entropy in liquid and solid states[155, 156]: $\Delta C_p = T_g(\partial S^{\text{melt}}/\partial T - \partial S^{\text{glass}}/\partial T)|_{T_g}$ (see Chapter 2). Thus, $\Delta C_p/T_g$ indicates the entropy released during a glass-to-melt transition. The $\Delta C_p/T_g$ for UPyPPG is smaller than that for PPG, which indicates that less entropy is released during the glass transition for UPyPPG than that for PPG. This is due to the fact that UPy dimers in the material act as rigid segments along backbones making PPG blocks less mobile.

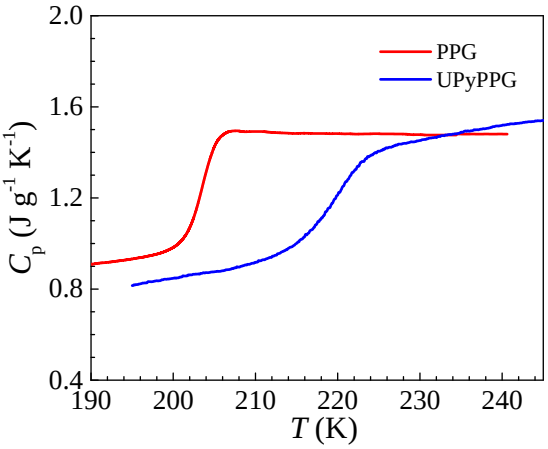

Figure 5.5: Specific heat capacity as a function of temperatures for PPG and UPyPPG

Figure 5.6 shows dielectric spectra for PPG at 216 K and 150 K, and for UPyPPG at 248 K and 150 K. At these temperatures, all relaxation modes are accessible in the frequency window of the dielectric analyser. The spectra are fitted by a sum of several

Table 5.1: Quantitative analysis of glass transitions for PPG and UPyPPG by DSC, BDS and rheological measurements.

	T_g^{DSC} (K)	$\Delta Cp/T_g$ (J K^{-2}g^{-1})	ΔT (K)	T_g^{α} (K)	T_g^{rheo} (K)
PPG	202±2	2.8±0.2e-3	3.7±0.8	201±2	198±3
UPyPPG	215±3	2.2±0.4e-3	7.1±1.3	219±4	218±5

Havriliak Negami (HN) equations as follows:[272]

$$\varepsilon^* = \varepsilon_\infty + \sum_j \frac{\Delta\varepsilon_j}{(1 + (i\omega\tau_j)^{a_j})^{b_j}} + \frac{\sigma}{i\varepsilon_0\omega} + A\omega^B \tag{5.1}$$

where ε_∞ is high-frequency limiting dielectric permittivity, $\Delta\varepsilon_j$ and τ_j are relaxation strength and relaxation timescale for the jth relaxation process, a and b are shape parameters, and σ is the ionic dc-conductivity. The last power law term accounts for a high frequency contribution from a relaxation process outside the experimental frequency window. It has been shown by many researchers that PPG can show a slower relaxation process than the segmental relaxation, α, when molecular weights are higher than a threshold (~400 g/mol). This is the so-called normal mode relaxation, α', due to the motion of the end-to-end dipole vector resulting from a summation of segmental dipole moments along the backbone[329, 352, 354, 356].

In our case, two relaxation modes, α and α' are visible for both polymers at temperatures slightly higher than glass transition temperatures. The normal mode relaxations α' for both polymers are fitted using a Cole-Cole equation[388] ($b = 1$ in equation 5.1). The α relaxations for PPG and UPyPPG are fitted using a HN equation and a Cole-Cole equation, respectively. From the fitting, we determine the temperature dependent characteristic time-scales corresponding to the peak frequencies of the different relaxation contributions. The characteristic time-scale corresponding to the peak frequency is determined as $\tau = 1/(2\pi\omega_{\text{peak}})$. Since a Cole-Cole contribution is symmetric around the loss peak on a logarithmic frequency axis, we can use the characteristic time determined directly from the Cole-Cole fit. However, since the HN response is asymmetric on a logarithmic frequency axis, we use Equation 21 in Chapter 1 to determine the correct time-scale corresponding to the loss peak. The γ relaxation is fitted

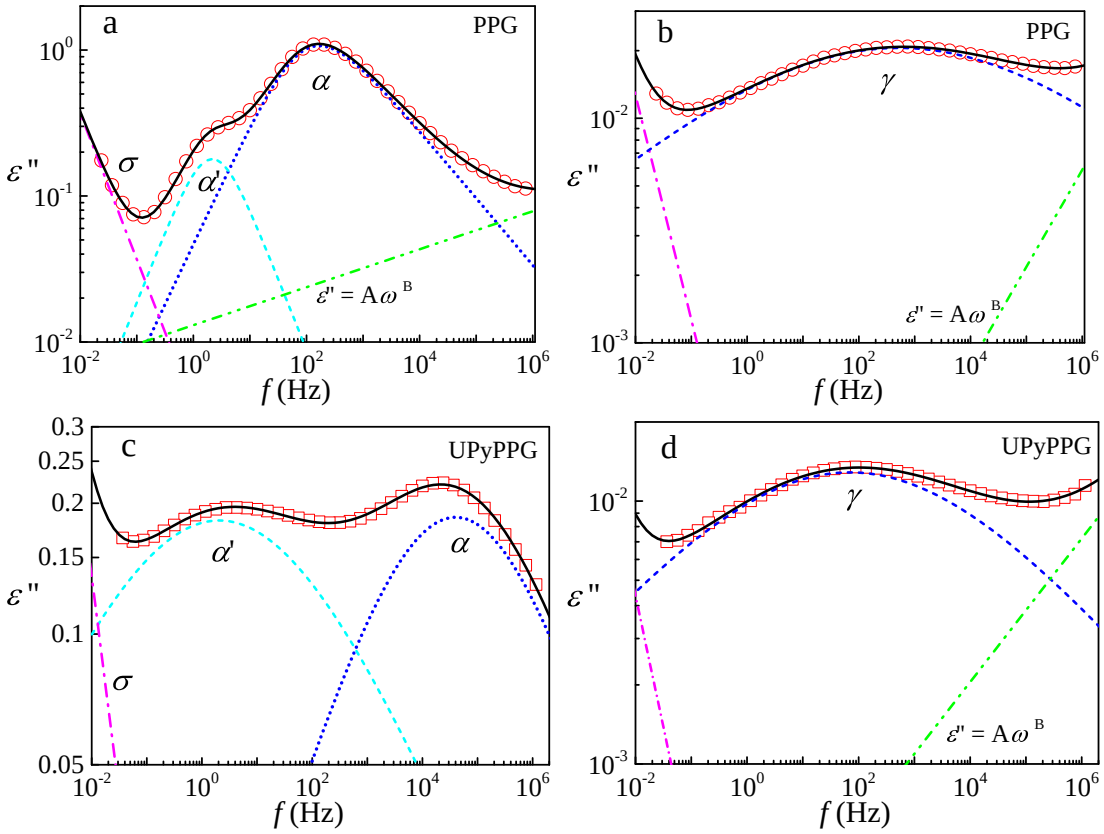

Figure 5.6: Imaginary part, ε'', of complex permittivity as function of frequencies for PPG at (a) $T = 216$ K and (b) $T = 150$ K, and for UPyPPG at (c) $T = 248$ K and (d) $T = 150$ K. The light blue dashed and blue dotted lines in (a) and (c) represent imaginary parts of α', α relaxation contributions, respectively. The blue dashed lines in (b) and (d) represent γ relaxation. At some temperatures, the spectra show a high frequency contribution which is described by a power law $\varepsilon'' = A\omega^B$ (green dot-dot-dashed lines) in (a), (b) and (d). The pink dot-dashed lines in (a) an (c) are the contributions from ion conductivity. The black lines in all figures are the total fitted results.

using a Cole-Cole expression together with two powerlaw expressions, where the latter account for the contributions at the lowest and highest frequencies.

Figure 5.7 shows dielectric spectra of PPG and UPyPPG at different temperatures. At these temperatures, relaxation modes α', α and γ, are in the accessible frequency range of the analyser. For clarity, contributions from conductivity at low frequencies

on some spectra are not shown in the figure. All relaxations for both samples become faster (move to higher frequencies) as temperature increases. For both samples the ε'' maxima for the α' and α relaxation modes decrease slightly as temperatures increases, whereas the maxima for the γ relaxation modes increases as the temperature increases.

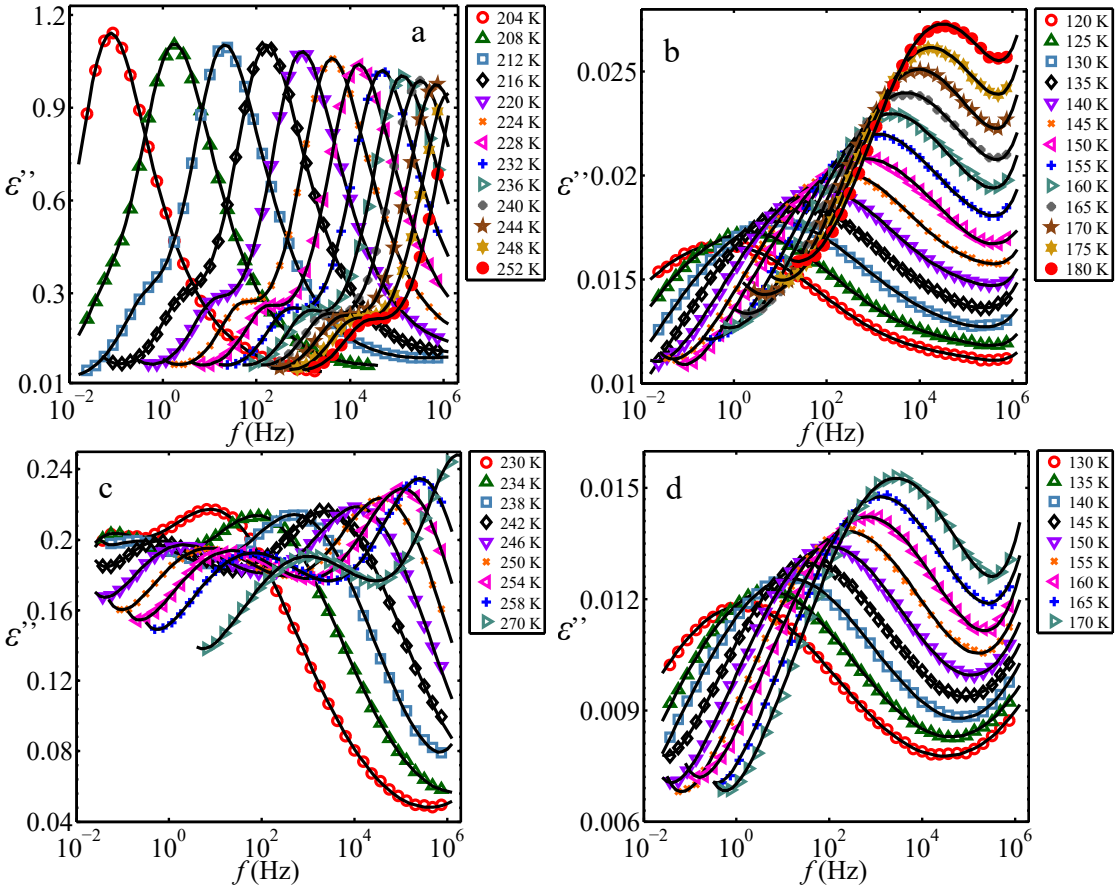

Figure 5.7: Dielectric spectra for PPG and UPyPPG at different temperatures showing normal modes α', segmental or structural modes α and subglass relaxation modes γ: (a) α', α, (b) γ relaxations for PPG, (c) α', α, (d) γ relaxations for UPyPPG. The black lines in all figures are the total fitted results as described in Figure 5.6.

Figure 5.8 shows the temperature dependences of the shape parameters used in equation 5.1. In the HN equation, the parameters a and $a \times b$ represent power law exponents of the low and high frequency flanks of the relaxation peak; thus, values of a and $a \times b$ indicate the broadness of a peak.[272, 388] All relaxation peaks are fitted using

the Cole-Cole equation (b = 1 in the HN equation), except for the α relaxation of PPG which is fitted using the HN equation. The α relaxation peaks of PPG and UPyPPG become slightly narrower with increasing temperatures (Figure 5.8A). The broadness of the α' relaxation peaks for PPG remain almost constant whereas that for UPyPPG becomes broader with increasing temperatures (Figure 5.8B). Modification of the end groups of PPG by UPy groups makes both the α and α' relaxation peaks broader, indicating a wide distribution of relaxation timescales. This is expected since relatively rigid UPy dimers added to the end of chains can introduce a gradient in mobility for segments along the backbones, which has been reported in other supramolecular materials and chemically cross-linked systems.[233, 275] The γ loss peaks for both PPG and UPyPPG become more narrow as the temperature increases as is typically observed for secondary glassy relaxations[296] and PPG shows the stronger temperature dependence (Figure 5.8C). Figure 5.8 D and E show relaxation strengths for different relaxation modes of PPG and UPyPPG. The α relaxation strengths for PPG and UPyPPG decrease as the temperature is increased, which is the typical behavior for α relaxations.[389] The strength of α' for PPG decreases while that for UPyPPG increases with increasing temperatures. The subglass relaxations are usually related to relatively local motions of a polymer. Thus, the relaxation strengths are usually quite low, which is true also in our case. Figure 5.8F shows the temperature dependence of the relative strength $\Delta\varepsilon^{\alpha'}/\Delta\varepsilon^{\alpha}$ of normal modes to segmental modes for PPG and UPyPPG. $\Delta\varepsilon^{\alpha'}/\Delta\varepsilon^{\alpha}$ for PPG remain around 0.1 which is close to the previously reported value.[324, 341]. $\Delta\varepsilon^{\alpha'}/\Delta\varepsilon^{\alpha}$ for UPyPPG is larger than that for PPG.

Figure 5.9a compares the linear viscoelastic response for UPyPPG and PPG determined using oscillatory rheology together with time-temperature superposition (T_{ref} =223 K). At high frequencies, the storage moduli G' for both samples tend to a plateau (~1 GPa) and the loss moduli G'' show peaks. These are characteristics of a glassy state. As the frequencies become lower, however, samples show significant differences. For UPyPPG, a clear plateau covering almost 5 decades is observed due to formation of effective cross-links mediated by the formation of end-to-end hydrogen bonds.[33, 166] For PPG, on the other hand, no clear plateau can be observed and G'' values are always larger than the corresponding G'. As frequencies are further reduced, a cross-over between G' and G'' is observed for UPyPPG at which the material enters the terminal flow

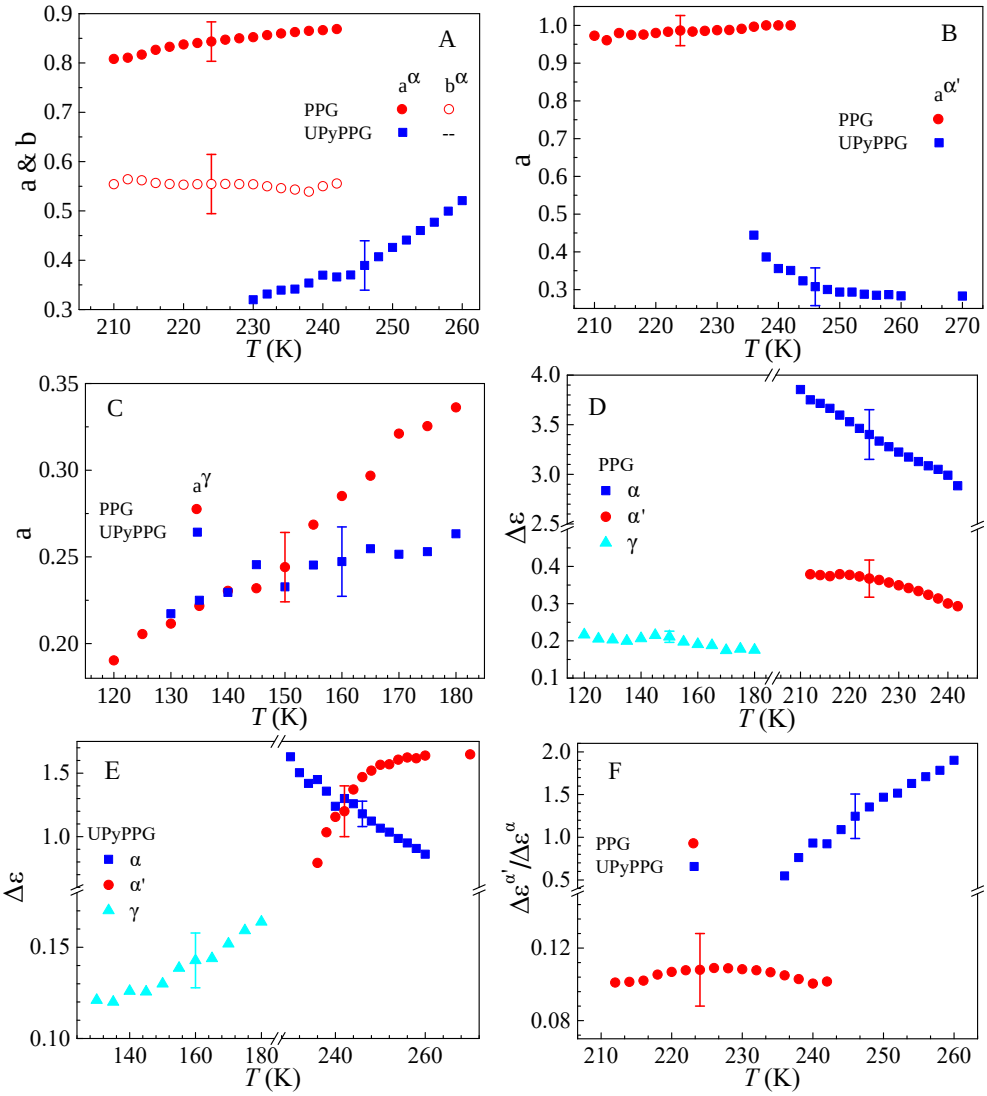

Figure 5.8: Temperature dependence of fitting parameters in equation 5.1. Shape parameters for (A) α, (B) α' and (C) γ relaxation modes for PPG and UPyPPG. Relaxation strengths $\Delta\varepsilon$ of different modes for (D) PPG and (E) UPyPPG. (F) Relative dielectric strengths $\Delta\varepsilon^{\alpha'}/\Delta\varepsilon^{\alpha}$ as a function of temperatures.

regime. In the terminal regime, G' and G'' show power law behaviour with exponents of about 1 and 2 for both samples, as indicated in Figure 5.9a.

Figure 5.9b shows the horizontal shift factors a_T for both samples as a function of reciprocal temperature. The shift factors for PPG can be well described using a VFT

equation as demonstrated by the red solid line. However, the temperature dependent behaviour appears to be more complex for UPyPPG. At high temperatures, where shift factors tracks chain dynamics, they can be described by an Arrhenius expression (blue dashed line), yielding an activation energy of 141 kJ/mol (Table 5.2). However, as temperatures get close to the glass transition temperature, they can be described well using a VFT equation (blue solid line). The temperature separating the two dynamical behaviours is ~283 K, as shown in Figure 5.9b. TTS is based on the concept of thermo-rheological simplicity[139], meaning that all underlying relaxation dynamics including the segmental (α) relaxation, chain relaxations (Rouse and/or reptation dynamics) and any supramolecular relaxation contribution follow the same temperature dependence.[143, 144] Thus, TTS is generally an approximation and for supramolecular systems which include supramolecular cross linking groups, we generally do not expect that TTS should work over a wide dynamic range[144, 230, 250] Thus, the observed change from a VFT to an Arrhenius behaviour should be due to different dynamics dominating the relaxation behaviour at low and high temperatures.

The shift factors below ~283 K track segmental dynamics and those above ~283 K track chain dynamics. In Chapter 5, we conclude that it is impossible to build master curves for supramolecular materials covering the whole frequency range from glass to melt. To present the LVE data in a reasonable way, we thus split the master curves for UPyPPG into two regions (Figure 5.9c), according to the temperature where dynamics change, i.e. ~283 K. Since two different regions in the dynamics are observed, two different reference temperatures, one in each dynamic region, are chosen to construct the master curves; they are 223 K and 331 K. Two absolute timescales corresponding to the temperatures 223 K and 331 K, respectively, are also defined. The characteristic timescale for the 223 K data was defined as the maximum of G'', shown in Figure 5.9, within the glass-transition related high frequency range, as $\tau_{223} = 1/\omega_{\text{peak}}$. The characteristic timescale for the 331 K data was defined from the cross-over frequency of G' and G'' within the terminal regime, as shown in Figure 5.9c, as $\tau_{331} = 1/\omega_{\text{cross}}$. The calculated timescales for the two regions show clear VFT (below 283 K) and Arrhenius (above 283 K) behaviours, respectively, which are fitted using the VFT and Arrhenius equation, and fitting parameters are shows in Table 5.2. The relaxation dynamics will be discussed in detail later, together with dielectric results.

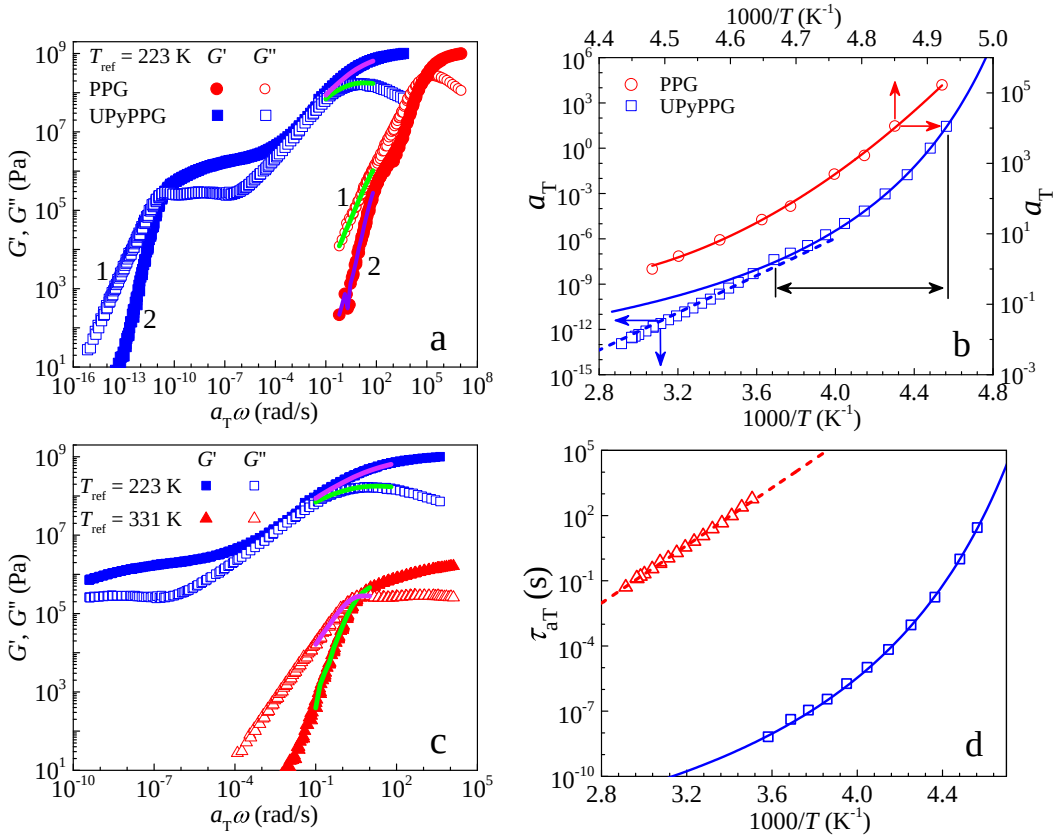

Figure 5.9: (a) Linear viscoelastic master curves referring to 223 K (T_{refer} = 223 K) for PPG and UPyPPG. The green and purple lines represent the SAOS data measured at 223 K. Power law exponents in terminal regions for both samples are 1 and 2 for G'' and G'. (b) The temperature dependence of the shift factors for PPG and UPyPPG. The solid lines are VFT fits whereas the dashed line is the Arrhenius fit. An obvious change from the VFT behaviour (between two vertical lines) to the Arrhenius behaviour is observed at T~283 K. (c) master curves for UPyPPG referring to 223 and 331 K. SAOS data measured below and above 283 K are referred to 223 and 331 K, respectively. The green and purple lines are the SAOS data measured at 223 and 331 K, respectively. (d) the temperature dependence of the relaxation timescales τ_{a_T} for UPyPPG from rheological measurements. τ_{a_T} is calculated: $\tau_{a_T} = \tau_{223} a_{T,223}$ (blue squares) or $\tau_{a_T} = \tau_{331} a_{T,331}$ (upper triangles). τ_{223} is the absolute timescale at 223 K obtained from the peak position by fitting glass region of G'' in (c); τ_{331} is the absolute timescale at 331 K obtained from the cross-over frequency of G' and G'' in (c); $a_{T,223}$ and $a_{T,331}$ are the shift factors used to build master curves in (c) referring to 223 and 331 K, respectively. The solid and dashed lines in (d) are the VFT and Arrhenius fits, and fitting parameters are shows in Table 5.2.

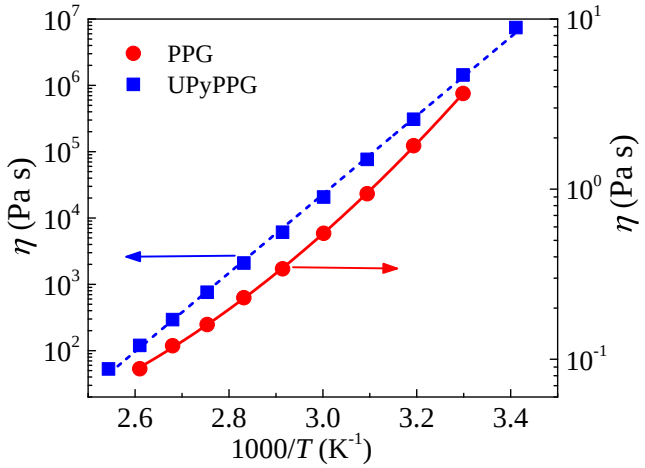

Figure 5.10: Shear viscosities for PPG and UPyPPG as a function of reciprocal temperature. The dashed and solid lines are the Arrhenius and VFT fits to the experimental data, and the fitting parameters are shows in Table 5.2.

Figure 5.10 shows shear viscosities as a function of temperature for PPG and UPyPPG. The temperature dependent viscosity for PPG can be described using the VFT equation (solid line). However, the viscosities determined for UPyPPG can be well described by using the Arrhenius equation (dashed line), yielding an activation energy of ~137 kJ/mol. The viscosity for UPyPPG are almost 10^4 times higher than that for PPG at the same temperature due to chain associations.

Figure 5.11a shows the time-scales determined from BDS and rheology in an Arrhenius plot. The end-functionalisation of PPG significantly delays the time-scales for the α and α' relaxations. The temperature dependences of the relaxation time-scales can be well described using the VFT equation (solid lines), except for the α' relaxation of UPyPPG, which shows an apparent Arrhenius behaviour (dashed line). The change from VFT behaviour to Arrhenius behaviour indicates a change from polymer segmental dynamics (friction) to supramolecular dynamics (reversible hydrogen bonds), which has been reported by many researchers.[33, 166, 186, 189, 213] Figure 5.11b compares $\tau_{\alpha'}$ and τ_{a_T} in the terminal region. It is found that the $\tau_{\alpha'}$ and τ_{a_T} against 1000/T are almost parallel to each other, i.e. follows the similar temperature dependence and gives the activation energy around ~140 kJ/mol, see Table 5.2. The relaxation of normal modes α' from BDS is due to the re-orientation of the end-to-end vector of a chain,

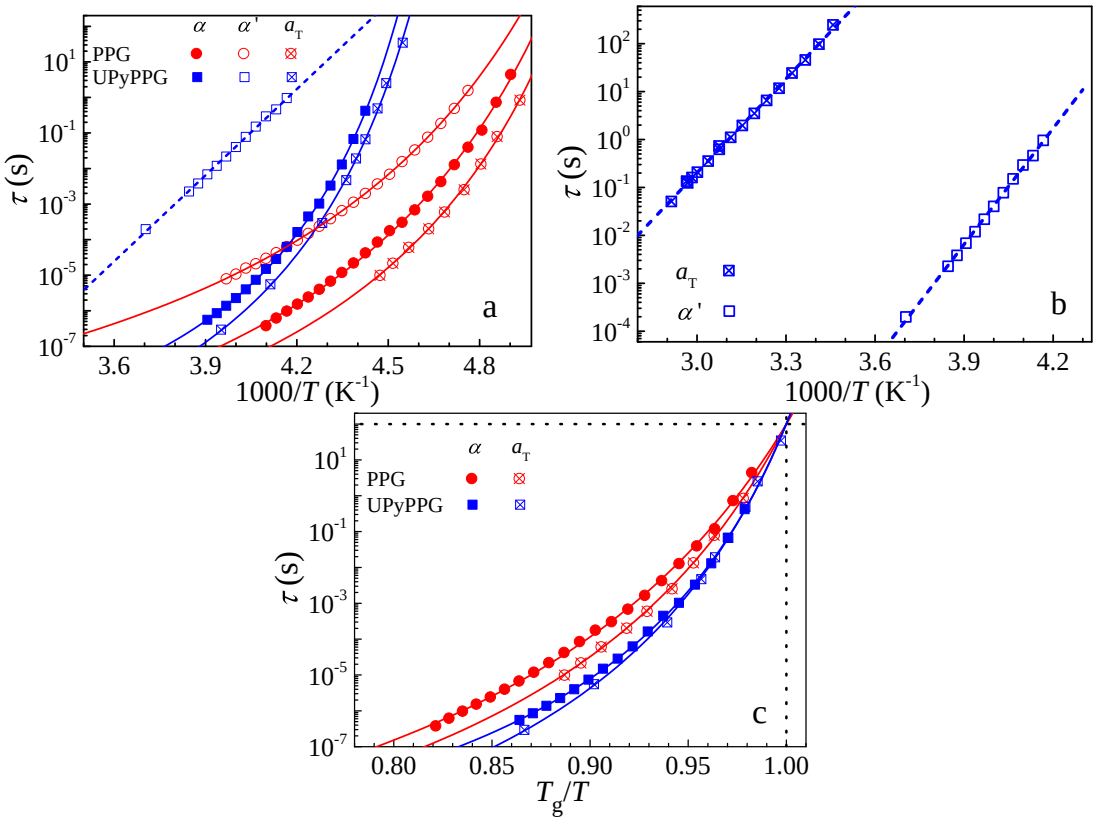

Figure 5.11: (a) The Arrhenius plot of relaxation timescales for segmental τ_α and normal modes $\tau_{\alpha'}$ relaxations from BDS, and the timescales calculated from the rheological measurements τ_{a_T} for PPG and UPyPPG; The solid lines are the VFT fits while the dashed line is the Arrhenius fit, with fitting parameters shown in Table 5.2. (b) comparison of $\tau_{\alpha'}$ and τ_{a_T} which track chain dynamics from BDS and rheological measurements. Calculations for τ_{a_T} are described in Figure 5.9 (c) Plots of relaxation timescales against the T_g/T.

which is the summation of dipoles of repeat units along the backbone.[324] Thus, the normal mode relaxation α'represents chain dynamics.[324, 341] The shift factors in the terminal region from rheology also track the chain dynamics. Thus, we compare the absolute relaxation times of chain dynamics from these two techniques for UPyPPG in Figure5.11b. Somewhat surprisingly, we find that the timescales for chain dynamics from rheology is over 6 decades in time slower than those from BDS. We speculate that this is related to the fact that the terminal relaxation time determined from rheology is

the longest characteristic timescale relevant for flow, whereas BDS also tracks chain-relaxations, but given the complexity arising from the additional dipolar component of UPy dimers, as well as the fact that UPy dimers self-assemble into fibre structures, it is not presently clear exactly which chain modes BDS are tracking, which needs further considerations.

Table 5.2: The Arrhenius and VFT fitting parameters of α, α' and γ relaxation timescales from BDS, shift factors a_T and shear viscosity η from rheological measurements for PPG and UPyPPG.

		-log(τ_0) (s)	D	T_0 (K)	m	T_g (K)	-log(τ_0) (s)	E_a (kJ/mol)
PPG	α	12.1±0.1	6.1±0.2	169±1	92±2	201±3	–	–
	α'	10.6±0.1	6.7±0.2	165±1	66 ±4	203±4	–	–
	γ	–	–	–	–	–	14.5±0.3	32.4±2
	a_T	10.7±0.7	3.1±0.8	181±3	98±4	198±5	–	–
	η	12.6±0.1	5±0.4	190±4	–	–	–	–
UPyPPG	α	11.5±0.2	3.5±0.2	199±1	133±6	221±3	–	–
	α'	–	–	–	–	–	33.4±0.5	144±4
	γ	–	–	–	–	–	14.6±0.1	35±3
	a_T	14.3±0.5	6.9±0.5	183±2	133±5	219±7	31.1±0.3	141±4
	η	–	–	–	–	–	13.5±0.2	137±4

The glass transition temperature is defined as the temperature at which τ_α reaches 100 s. Thus from VFT fits of τ_α, T_gs from different techniques can be calculated, which are shown in Table 5.2. T_gs from fits of τ_α of PPG and UPyPPG are close to the value from DSC measurements (Table 5.1). This is expected, because it has been widely shown that the glass transition is directly related to segmental dynamics. However, the T_gs from rheological measurements are slightly lower than those from τ_α, which is not uncommon. Typical scale factors between τ_α and τ_{aT} ranging from 2 to 10 has been reported for many glass forming systems.[282, 390–393] In our case, the scale factors are $\sim$ 3 and 11 for UPyPPG and PPG, respectively.

Figure 5.11c shows plots of τ_α for BDS and the timescales from rheology as a function of T_g/T which directly shows the variation in fragility. The fragility m is defined as[254, 394]: $m = \mathrm{d}(log_{10}\tau)/\mathrm{d}(T_g/T)|_{T=T_g}$. The fragility of a glass-former illustrates

how quickly the dynamics slow down when the temperature approaches the glass transition temperature. The m value for UPyPPG is larger than that for PPG (Table 5.2), indicating that the dynamics of UPyPPG slow down faster than those of PPG, or in other words, the dynamics of UPyPPG near T_g are more temperature sensitive. This is as expected, because at temperatures near T_g, dissocations of UPy dimers are much less active and thus the effective chain-length of UPyPPG is much longer than PPG. It has been reported that fragilities increase (larger m values) with increasing molecular weight for polymers[395–398] Moreover, the m values from BDS and rheological measurements are consistent with each other for PPG and UPyPPG, indicating that mechanical properties of PPG and UPyPPG are closely coupled to the segmental relaxations. This is similar to the supramolecular system reported by Lou etc.[282] In their work, a linear supramolecular polymer with weaker end-to-end hydrogen bonding groups and shorter spacers, compared to UPyPPG, was investigated. A slow Debye-like normal mode relaxation and a fast segmental relaxation were detected by BDS, and the mechanical relaxation was also coupled to the segmental relaxation process.[282]

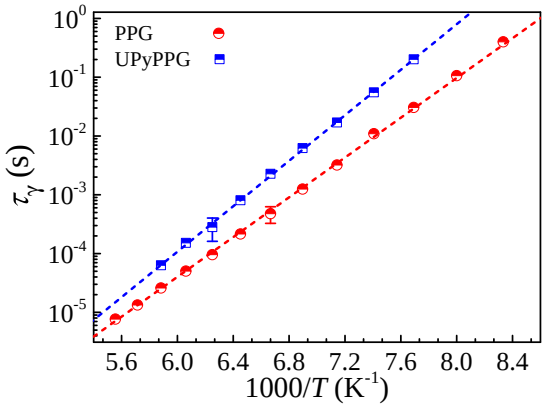

Figure 5.12: The Arrhenius plot of γ relaxation timescales, τ_γ, as a function of temperatures. The dashed lines are the Arrhenius fits to the data, and fitting parameters are shown in Table 5.2.

Figure 5.12 shows the Arrhenius plot for the γ relaxation time-scale, τ_γ, as a function of temperature. We find that that γ relaxations occur far below the glass transition temperatures for both PPG and UPyPPG. The temperature dependences of τ_γ, for both samples, can be described well by the Arrhenius equation. Activation energies for PPG

and UPyPPG are 32.4 and 35 kJ/mol, respectively, which are typical values for the secondary relaxation for PPG.[332, 399] Moreover, relaxation timescales for UPyPPG are slightly slower than those for PPG, indicating that end-functionalisation barely affects relaxation dynamics on the relatively local scale characteristic of the γ relaxation .

5.3.3 Ion transport in polymer electrolytes based on PPG and UPyPPG with added LiTFSI salts

Ion dc-conductivities (σ) for PPG and UPyPPG mixed with LiTFSI salts with ratios of ether oxygen atoms to Li-ions (O:Li, R) ranging from 5:1 to 1000:1 were measured using BDS in the temperature range from 353 K to 233 K. For clarity, samples are named by combining the polymer matrix and O:Li ratio; for example, PPG and UPyPPG with O:Li ratio of 80:1 are denoted PPG80 and UPyPPG80, respectively. Two methods were used to determine ion conductivities.

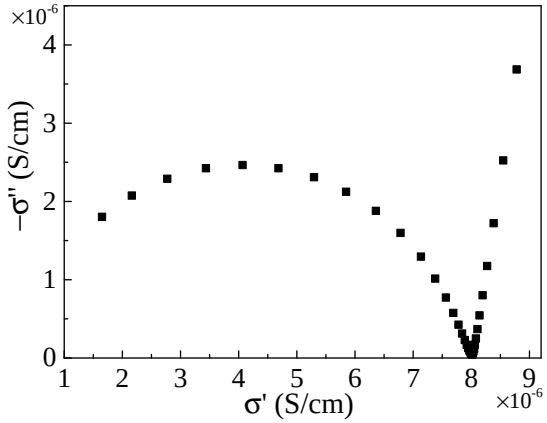

Figure 5.13: Plot of imaginary σ'' against real σ' part of the complex conductivity for PPG with ratio of O:Li (R) 80:1 (PPG80) at 308 K.

The first method is based on plotting $-\sigma''$ vs σ' (see Chapter 2), as shown in Figure 5.13. The ion conductivity is determined as the σ' value when σ'' approaches zero. The second method is based on fits of the imaginary part of the complex permittivity ε'' using equation 5.1. For samples with small R, i.e. containing a high concentrations of salts, a strong electrode polarisation (EP) (see Chapter 2) suppresses α and α'relaxations, which make it very difficult to fit the ε'' curves, Thus for those samples with high concentrations of salts, only the first method is used to determine ion

conductivities.[400, 401] The results using both methods are shown for the samples with $R = 1000$ in Figure 5.14 (red squares and plus (+) filled red squares) and it is clear that the results from both methods are almost identical.

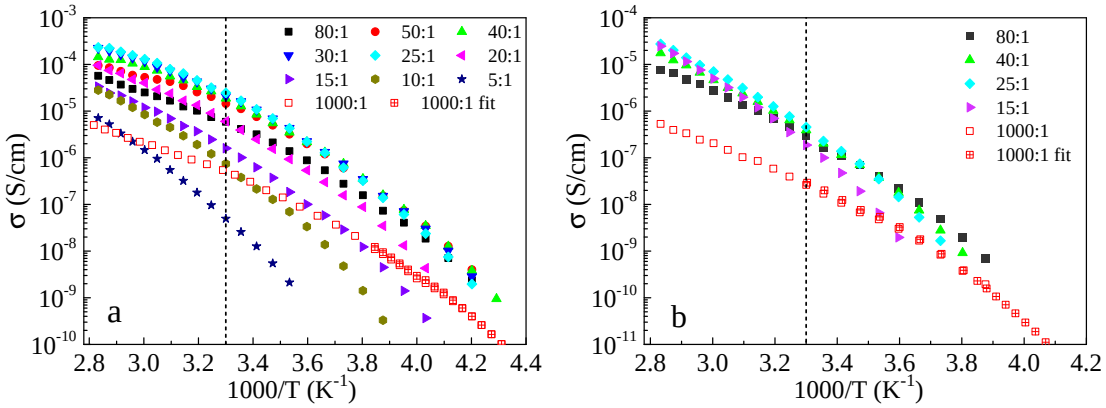

Figure 5.14: Plots of ion conductivities as a function of temperatures for PPG (a) and UPyPPG (b) with varying R. The vertical dashed lines indicate the temperature of 303 K.

Figure 5.14 shows ionic conductivities for (a) PPG and (b) UPyPPG as a function of temperatures and LiTFSI concentrations, quantified by R. As expected, ion conductivities σ for all samples increase with increasing temperatures, and σ reaches $\sim 3\times10^{-3}$ and 3×10^{-4} S/cm for PPG25 and UPyPPG25 at 353 K, respectively. To be successfully used as lithium polymer electrolytes, ion conductivities of polymer electrolytes should approach at least 10^{-4} S/cm at ambient temperature. Moreover, a successful polymer electrolyte should also show high ion conductivities in the typical working temperature range, i.e. ~230 to ~360 K. However, for most polymer electrolytes, ion conductivities decrease rapidly with decreasing temperatures. The R−dependences of σ for both systems are generally non-monotonic. This is illustrated in Figure5.15, where σ is plotted as a function of R at 303 K. It is clear that for both PPG and UPyPPG, σ first increases with increasing R. After reaching a maximum, it decreases as R increases further. For both systems, we find the maxima around $R \sim 25$. These results are consistent with previously reported results for polymer electrolytes based on PPG mixed with LiTFSI.[402, 403] LiTFSI is a salt with a typically high degree of ion dissociation.[321] Also, PPG has a relatively high dielectric constant which makes the attractive Coulomb interactions between the LiTFSI ion-pair relatively weak. For

large R (low concentrations of salt), ion conductivities increase with increasing R due to the fact that the free ion concentration increases. However, for small R (high Li-ion concentrations), ions are more likely to stay associated or form large aggregated clusters, leading to the decreases of ion conductivities.[322, 371–374]

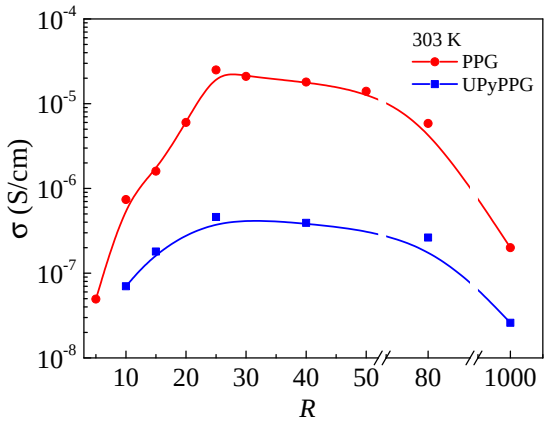

Figure 5.15: Plots of the ion conductivities as a function R for PPG and UPyPPG at 303 K. The lines are guide to eye.

Ion conductivities for PPG based electrolytes with various R in our studies are comparable to what has been reported for PPG with different molecular weights and with different lithium salts [321, 361, 404, 405]. A conductivity of 8×10^{-5} S/cm was reported for the mixture of PPG (4000 g/mol) and $LiCF_3SO_3$ (R = 23) at 303 K and a conductivity of 2×10^{-5} S/cm was reported for the mixture of PPG (426000 g/mol) and LiTFSI (R = 12) at T=295 K.[321, 322, 403] Ion conductivities of PPG based electrolytes are still too low, particularly at lower operational temperatures. However, there are several methods available to increase conductivities, e.g. addition of nanoparticles, e.g. Al_2O_3, TiO_2, SiO_2[362, 406, 407] or addition of materials with plastic crystalline phases.[408] However, one significant drawback remains, which is that pure PPGs are viscous liquids and thus lack the mechanical strength that is highly desirable for a real solid polymer electrolyte. However, the supramolecular end-functionalised UPyPPG meets this requirement, as previously discussed in Figure 5.9. It is thus very interesting to determine the ion conductivities of UPyPPG. Unfortunately, we find that the maximum conductivity of UPyPPG with LiTFSI, at 303 K is 4×10^{-7} S/cm, i.e. nearly 2 orders of magnitude lower than that for PPG. T_g for UPyPPG is almost 20

K higher than that for PPG (Table 5.1), which means that the segmental α relaxation slows down significantly in UPyPPG. Moreover, the normal mode α' relaxation also slows down significantly (Figure 5.11a). Slowing down of both segmental and normal mode relaxations leads to the significant decrease in ion conductivities for UPyPPG.

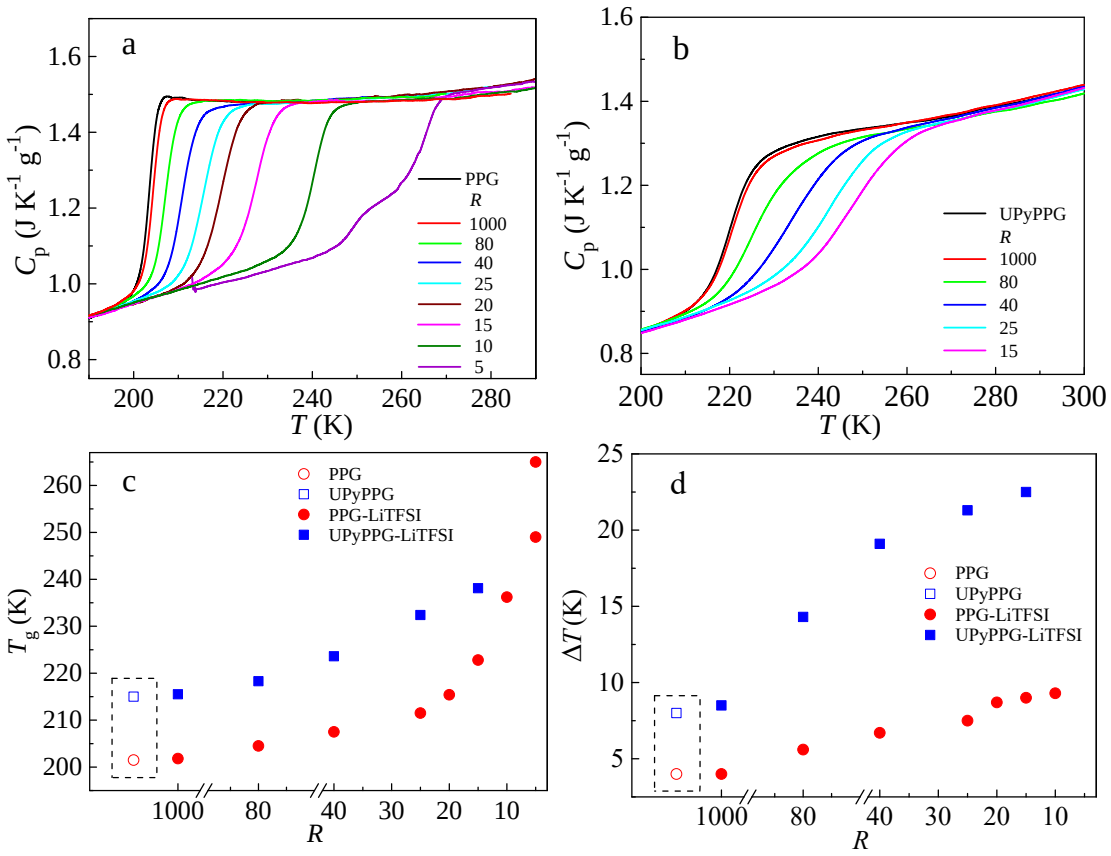

Figure 5.16: Heat capacity C_p as a function of temperatures for (a) PPG and (b) UPyPPG with varying ratio of O:Li, R. (c) Glass transition temperatures T_g and (d) broadness of glass transitions ΔT as a function of R for PPG and UPyPPG with varying R. Onset temperatures of glass transitions are used as T_g and $\Delta T = T_{\text{offset}} - T_{\text{onset}}$ is defined as broadness of a glass transition. The symbols in dashed frames are data points for pure PPG and UPyPPG. The error bars are smaller than symbol sizes.

To investigate the effects of different polymer relaxations on the ion conductivities, mixtures of polymers with LiTFSI with varying R were measured by DSC and BDS. Figure 5.16a and b shows heat capacity C_p as a function of temperatures for PPG

and UPyPPG with varying concentrations of LiTFSI. For all samples (except PPG5), a clear characteristic step in C_p is observed due to the glass transition and we find that the T_gs and the breadths of the glass transitions increase with decreasing R; Importantly, however, the C_ps for PPG and UPyPPG are almost identical to those of the pure polymers, as shown in Figure 5.16c and d. We use the onset temperatures to quantify T_g and the transition breadth is quantified by temperature differences between onset and offset temperatures, $\Delta T = T_{\text{offset}} - T_{\text{onset}}$. The increasing breadth of glass transitions is expected, since associations between Li-ions and ether oxygens in polymer backbones slow down the segmental relaxation[322], which results in a wider distribution of segmental relaxation time-scales. Thus, the more ions, the slower relaxation dynamics (higher T_g) and the broader glass transitions (larger ΔT). For PPG with the highest salt concentration, PPG5, a clear two-step behaviour in C_p is observed, indicating two distinguishable T_gs. This is consistent with previously reported results.[322, 371, 373] At high Li-salt concentrations, microphase separation between ion-rich and ion-depleted phases can occur, and each phase shows different glass transition temperatures.[322] Moreover, T_gs of PPG-LiTFSI mixtures are lower than those for UPyPPG-LiTFSI, because UPy end-groups of UPyPPG slow down relaxation dynamics further, see Table 5.1 and Figure 5.11.

To investigate the relationship between polymer dynamics and ion conductivities, BDS measurements were performed on PPG1000 and UPyPPG1000. For these investigations, low ion concentrations were chosen since it is necessary to determine both α and α' relaxations and ion conductivities. After adding LiTFSI into polymers, It is very difficult to see relaxation peaks on ε'' curves because of strong electrode polarizations (EP) and ion conductivities.[255]. As discussed in Chapter 2, ion conductivities can not be directly observed in the ε' data, thus to fit ε'' data precisely, an approximative procedure using the derivative analysis of ε' is applied:[184, 255, 409]

$$\varepsilon''_{\text{der}}(\omega) = -\frac{\pi}{2}\frac{\partial\varepsilon'(\omega)}{\partial \ln(\omega)} \tag{5.2}$$

This approximation gives information about ε'' from ε' avoiding effects from strong ion conductivities. Figure 5.17 show the real ε', imaginary ε'' and the derivative imaginary permittivity $\varepsilon''_{\text{der}}$, for PPG1000 at 228 K (Figure 5.17a) and UPyPPG1000 at 248 K (Figure 5.17b). We first fit $\varepsilon''_{\text{der}}$ curves using a combination of two Cole-Cole equations to account for the α' and α relaxations, and then the characteristic time-scales

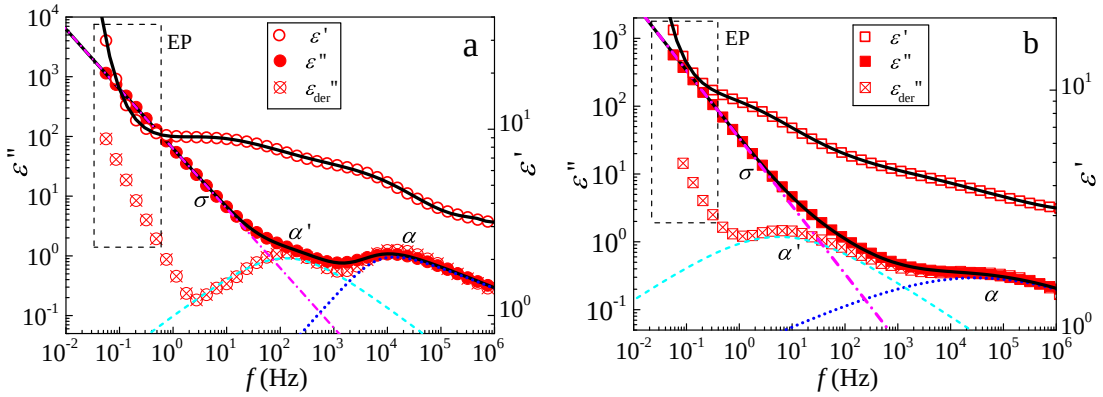

Figure 5.17: Real ε', imaginary ε'' and derivative imaginary permittivity ε''_{der} (equation 5.2) as a function of frequencies for (a) PPG1000 at 228 K and (b) UPyPPG1000 at 248 K. The pink dot-dashed, light blue dashed and blue dotted lines represent the different relaxation contributions (σ, α' and α), respectively. Electrode polarizations (EP) are indicated in the black dashed frames. The black solid lines in both figures are the total fitted results to ε' and ε'' curves.

from the fits were fixed in equation 5.1 to fit the ε'' data. Both ε' and ε'' are fitted simultaneously. At higher salt concentration (smaller R), EP becomes very strong and contributes to both ε' and ε'' curves (see Chapter 2) which precludes gaining relaxation dynamics from an analysis through derivative of real parts. The fitted results are shown in Figure 5.17a and b. The contributions from ion conductivities σ, normal modes α' and structural α relaxations are shown in Figure 5.17 by pink dot-dashed, light blue dashed and blue dotted lines. The fitted peak positions using this procedure are consistent with the step-like decrease characteristic of the ε' curves. The black solid lines represent the total fitting results to ε' and ε'' curves, which demonstrate that the permittivity data is well fitted using the chosen procedure.

Figure 5.18a and b show effects of adding a small amount of LiTFSI (R =1000) on the structural τ_α and normal modes $\tau_{\alpha'}$ relaxation time-scales. As shown, adding a small amount of LiTFSI does not markedly affect the structural relaxation time-scales for PPG and UPyPPG (filled circles and squares in Figure 5.18a, and filled upper and down triangles in Figure 5.18b). Since structural relaxations are related to glass transitions, the T_gs for PPG1000 and UPyPPG1000 should almost identical to those for PPG and UPyPPG, which is also evidenced by the DSC results in Figure

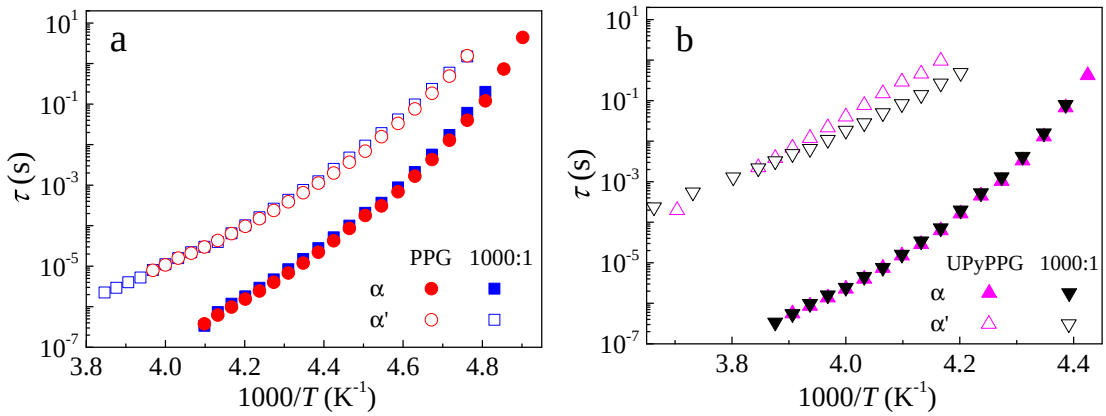

Figure 5.18: The Arrhenius plots of structural τ_α and normal modes $\tau_{\alpha'}$ relaxation timescales as a function of temperatures for (a) PPG and PPG1000, and (b) UPyPPG and UPyPPG1000.

5.16. As discussed above, the dielectric normal mode relaxations are due to motions of the end-to-end vector of a polymer backbone.[354] We find that the normal mode relaxation of PPG is not markedly affected by adding small amounts of LiTFSI (R = 1000 : 1), see Figure 5.18a. However, the slow dielectric relaxation of UPyPPG1000 does demonstrate some small changes from that of UPyPPG also for small addition of salt (Figure 5.18b). The reason for this is not clear, but we speculate that it may be attributed to interactions between the ions and the nitrogen and oxygen atoms in the UPy groups (see Figure 5.3), which could have a direct effect on the properties of the hydrogen bonding between UPy groups.

Ion conductivities in a material can be expressed as:

$$\sigma = \sum c_i \mu_i q_i \tag{5.3}$$

where c_i and μ_i are the concentration and mobility of all free ion species, respectively, q_i is the charge these ions carry. The equation above can be simplified as $\sigma = c\mu q$ in our case of LiTFSI where $q^+ = q^-$.[410] Based on the Einstein relation, the mobility of an ion in a medium is related to the diffusion coefficient D:

$$\mu = \frac{Dq}{k_B T} \tag{5.4}$$

Based on the Stokes-Einstein equation: $D = (k_B T)/(6\pi\eta r)$, where η is viscosity of the medium and r is radius of a ion. The diffusion coefficient D is related to the friction

felt by ions in the electrolytes,[411, 412] thus the relation between mobility of ions and the viscosity of a medium can be determined:

$$\mu \propto \eta^{-1} \tag{5.5}$$

According to the Maxwell equation, $\eta = G_\infty \tau_\alpha$, where G_∞ is the high frequency shear modulus and τ_α is structural relaxation timescale. Thus, the relation between mobility of an ion and structural relaxation timescale can be determined:

$$\mu \propto \tau_\alpha^{-1} \tag{5.6}$$

The physical meaning of the above equation is that the ion transport is controlled by the structural relaxation of the medium molecules. In the case of polymer electrolytes, the size of ions is much smaller than that of the medium molecules, i.e. the polymers. Thus, ion transport is controlled by segmental relaxations.[410] This is to say that ion conductivity in polymer electrolytes is controlled by the micro-viscosity felt by the ions. By assuming that the micro-viscosity is defined by segmental relaxations in the equation 5.3 and 5.6, the relation between the ion dc-conductivities σ and the segmental relaxation timescales τ_α can be written as:

$$\sigma \propto \tau_s^{-1} \tag{5.7}$$

σ drops significantly when the temperatures approach the glass transition (segmental relaxation slows down significantly). However, it has been reported that ion conductivities can be decoupled from segmental relaxations in some fragile materials.[410, 413–415] The fragility of a material is the steepness of the temperature dependence of the segmental relaxation when temperatures approach T_g (see Chapter 1). It was reported that the decoupling between ion motions and segmental relaxation is stronger in more fragile materials.[413] The segmental relaxation slows down more significantly than ion motions in fragile materials, which results in the decoupling. Moreover, some modified polymers, particularly with large side groups (e.g. benzene groups) along backbones, show even stronger decoupling.[414] However, ion conductivities of these systems are very low because these polymers have poor ion association abilities.[414, 415]

To test the decoupling idea, plots of ion conductivities σ as a function of segmental τ_α and normal mode $\tau_{\alpha'}$ relaxation timescales are shown in Figure 5.19. Generally,

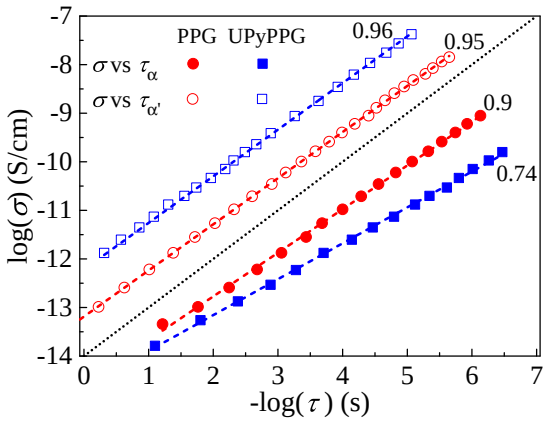

Figure 5.19: Plot of ion conductivity σ as a function of segmental τ_α and normal modes $\tau_{\alpha'}$ relaxation timescales. The dotted line indicates the slope of 1, and the dashed lines are the linear fits to the data.

the ion conductivities is proportional to the segmental relaxation timescales with a powerlaw exponent:

$$\sigma \propto \tau_\alpha^{\nu} \tag{5.8}$$

where ν is the powerlaw exponent, which equals 1 in the ideal case. In the log-log plot of σ against τ, a straight line with the slope of μ is expected. The dotted line in Figure 5.19 indicates a slope of 1, which means that σ and τ_α follow the same temperature dependence. In our case, plots of σ against τ_α and $\tau_{\alpha'}$ are approximately straight lines, and the slopes as indicated in the figure. The slopes of σ against τ_α for PPG and UPyPPG are 0.9 and 0.74, respectively, indicating a degree of decoupling of σ from segmental relaxation timescales. On the contrary, the slopes of σ against $\tau_{\alpha'}$ for PPG and UPyPPG are ~0.96, indicating that σ and normal mode relaxations nearly follow the same temperature dependence, i.e. ion conductivities are closely coupled to normal mode relaxations.

Polymer electrolytes composed of PPG with molecular weights of 425, 1000 and 4000 g/mol and $LiClO_4$ have been investigated by Fan.[322] They observed slow and fast segmental relaxation modes, originating from structural relaxations in ion-rich and ion-depleted phases, respectively. Reports on microphase separation in PPG-lithium complexes for a wide range of lithium species and concentrations [322, 371, 373, 374] seem to support their arguments. They also observed an additional ion relaxation mode

which they argued was due to polarization caused by a separation of ionic mobilities where the Li-ions are more strongly associated with the backbone ether oxygens whereas the counter ions are more free to move. As reported by Fan, the ion mode and fast segmental relaxations in the ion-depleted regions show the same temperature dependence. They also reported that ion conductivity is coupled to the slow segmental mode. However, our results show some differences to theirs. i) we also observe two relaxation modes: normal modes at relative low frequency and segmental modes at relative high frequency. The relaxation timescales of both segmental and normal modes for PPG and PPG1000 are identical (Figure 5.18a), and the DSC C_p curves for PPG and PPG1000 are also almost identical. Since there is no microphase separation in pure PPG, these results demonstrate that microphase separation is less likely to occur in PPG1000 in our case. ii) We do not find any evidence for an additional ion mode. However, it is worth noting that the type of lithium salts and the molecular weight in two studies are different. The salt used in the present study LiTFSI anionic ions are very easily dissociated in polyethers such as PPG which means that effects due to ion aggregation are less likely. Also, any effects resulting from the behaviour of anion could be different between the two salts since TFSI anionic ions are significantly larger than ClO_4^- ions. These differences may lead to the observed differences. However, this needs further confirmation.

5.3.4 UPyPPG as an effective component for self-healing coating

Coatings are everywhere in the world around us, defined as thin layers applied on the surfaces of a substrate. Coatings are usually used for decorative and/or functional purposes, such as corrosion resistance and wear resistance etc. Coatings are an important subject of material science. In this section, one class of coatings, i.e. ultraviolet (UV) curable coating, will be introduced briefly, which is related to investigations discussed in this section.

Some coatings are applied onto surfaces of a substrate in a liquid state, followed by a curing process which involves evaporation of solvents and/or cross-linking reactions between effective components. For a UV curable coating, cross-linking reaction is initiated by UV. A typical UV coating is usually composed of i) unsaturated reactants which have more than one double bond and can form cross-linked networks through

reactions between them under UV; ii) photo-initiators which can generate radicals to initiate polymerisations; iii) some other components, such as solvents, accelerators to make reactions faster and other additives and fillers to improve performances. In the last few years, continuous attention has been paid to improve performances of coatings, and one of these efforts is to prepare self-healing coatings which can heal defects or scratches automatically under certain conditions, such as at high temperatures.

In this section, we first evaluate self-healing properties of UPyPPG, and start a very initial exploration to prepare self-healing coatings by blending UPyPPG with commonly used unsaturated reactants for UV curable coatings, such as tripropylene glycol diacrylate (TPGDA), diacrylate poly(propylene glycol) (DAPPG). The procedure to prepare these self-healing coating samples are described in the experimental section.

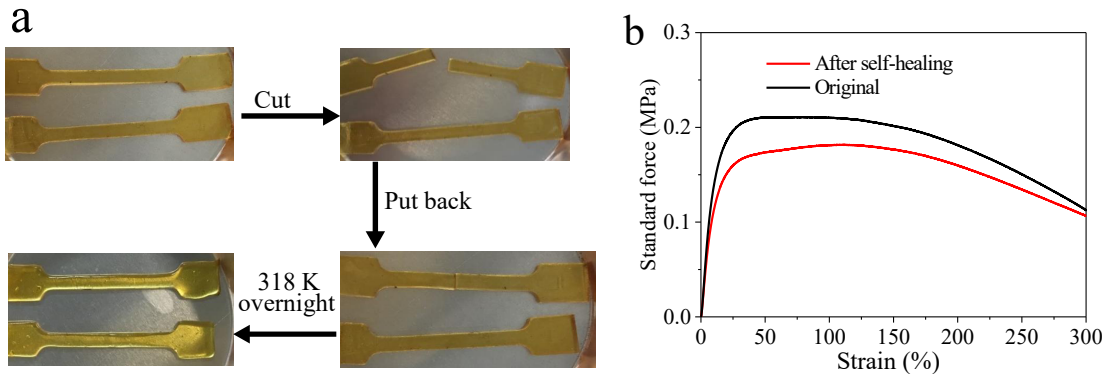

Figure 5.20: (a) Images show the self-healing property of pure UPyPPG after cutting the sample strip, (b) the force as a function of strain for the original strip and the strip after self-healing at 318 K overnight.

Self-healing of UPyPPG and supramolecular coatings

Self-healing properties of supramolecular materials rely on the use of non-covalent, reversible and transient bonds to generate networks, which can heal after breaking. [167, 220–224] The self-healing property of bulk UPyPPG is evaluated here. As shown in Figure 5.20a, a UPyPPG strip was cut into two parts using a knife, then the two parts were put back together. After staying at 318 K overnight, the interface between the two parts was not observable by eye. The disappearance of the interface indicates healing of the material. Figure 5.20b compares the force applied to the samples as a function

of strain at a stretching rate of 60 mm/min for the original strip (without cut) and the strip after self-healing (with cut and self-healing). At small strains (<20%), the force grows linearly with the increase of strain, and the tensile modulus (the slope) for both sample strips are almost the same. At large strains (>50%), the force for the self-healed strip is about 10% lower than that of the original one. Although this small difference is observed, the results still indicate that pure UPyPPG overall has good self-healing property.

The self-healing property of UPyPPG can also be evaluated using optical microscopy. Figure 5.21a-d shows evaluation of a scratch on a pure UPyPPG coating when the temperature is increased at 10 K/min. It is obvious that when the temperature reaches 413 K, the scratch is almost healed. However, it is worth noting that pure UPyPPG can not be used as a coating, since it is a thermoplastic material and flows at high temperatures.

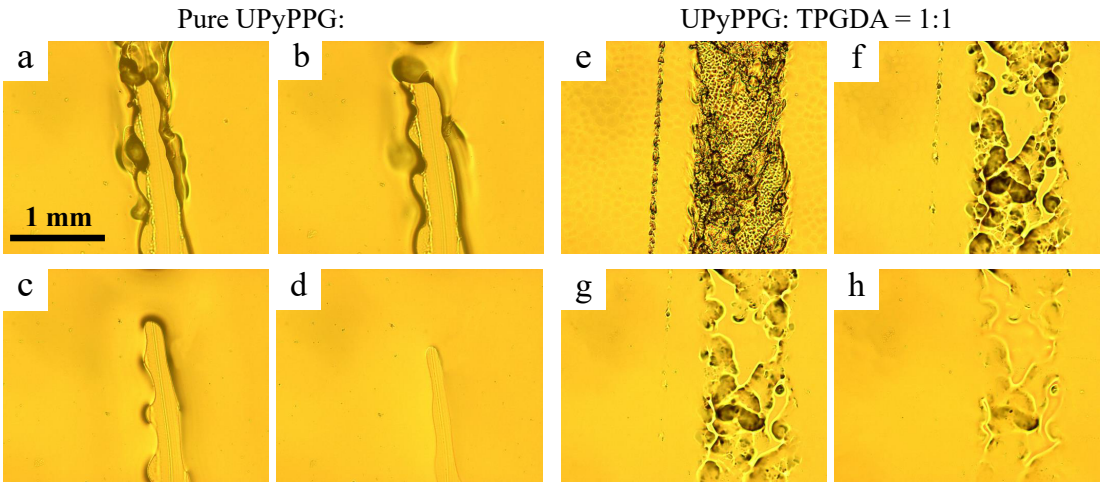

Figure 5.21: Images show the self-healing property of pure UPyPPG film (a - d) at different thermal stages heating from 303 K to 423 K at 10 K/min: (a) 303 K, (b) 333 K, (c) 373 K and (d) 413 K, and the mixture coating (e - h) of UPyPPG and TPGDA (1:1): (e) 303 K, (f) 343 K, (g) 393 K and (h) 423 K.

To be used as coatings, coating layers have to be thermosets (highly cross-linked) to provide strong mechanical properties, such as hardness and toughness. On the other hand, the self-healing property requires the mobility of chains, which means a sacrifice of mechanical properties. A good self-healing coating should balance the two

aspects.[416–418] To achieve these properties, we blend UPyPPG with TPGDA which is a commonly used monomer for UV curable coatings in ratio of 1:1 and 1:3. The chemical structure of TPGDA is shown in Figure 5.23a. Figure 5.21e-h show temperature dependences of scratches on the supramolecular coating composed of UPyPPG and TPGDA at a ratio of 1:1. A small scratch and a big scratch were made on the coating. As shown in the figures, both scratches tend to be healed when the temperatures increases. When the temperature reaches 393 K, the small scratch almost disappears. At higher temperature (423 K), the small scratch disappears completely, however, the big scratch heals to some extent but can not be completely healed. On other hand, for the case of UPyPPG and TPGDA in a ratio of 1:3, it is shown in Figure 5.22a-d that even at 423 K for 60 min, both the small and big scratches can not be healed. The sample with UPyPPG and TPGDA at a ratio of 1:1 feels too soft to be a practical coating, whilst a ratio of 1:3 yields a coating that is too brittle and has weak self-healing properties. The weak self-healing property may be due to the high cross-linking density of TPGDA, i.e. distances between two double bonds in TPGDA is too small, which hinders the motion of UPyPPG chains to heal scratches.

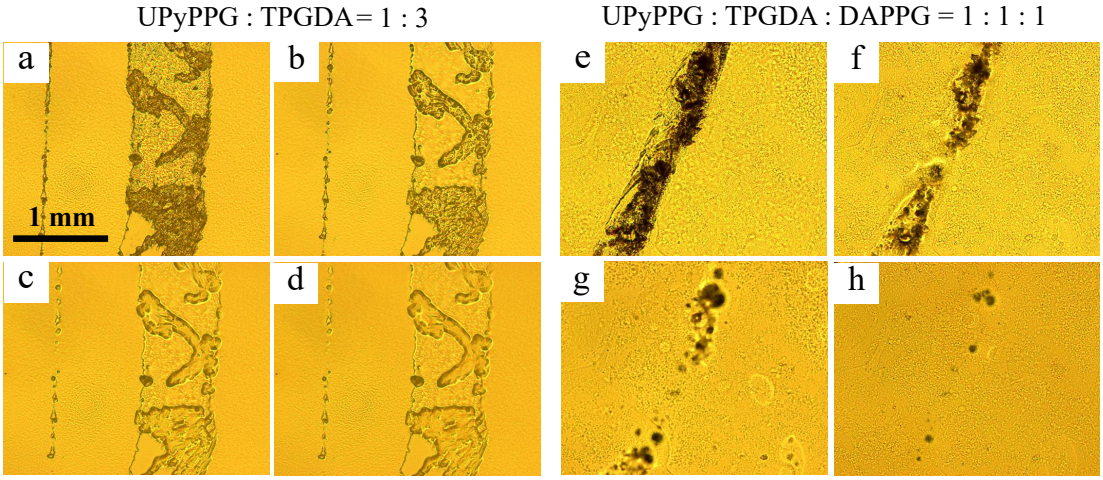

Figure 5.22: Pictures to show the self-healing property of the mixture coating (a - d) of UPyPPG and TPGDA (1:3) at different thermal stage heating from 303 K to 423 K at 10 K/min: (a) 303 K, (b) 343 K, (c) 373 K and (d) 423 K for 60 min, and the mixture coating (e - h) of UPyPPG, TPGDA and DAPPG (1:1:1): (e) 303 K, (f) 343 K, (g) 393 K and (h) 423 K for 10 min.

To increase the mobilities of UPyPPG chains in supramolecular coatings, DAPPG with molecular weight around 2000 g/mol (Figure 5.23b) is introduced into the mixture in a ratio of 1:1:1 as a first attempt to improve the self-healing properties. After introducing the third macro-monomer, DAPPG, the cross-linking density is reduced, see comparisons in Figure 5.23c and 5.23d. Figure 5.22e-h show temperature dependences of the scratch on the supramolecular coating of UPyPPG, TPGDA and DAPPG in a ratio of 1:1:1 when increasing temperatures from 303 to 423 K at a heating rate of 10 K/min. When the temperature reaches 393 K, some parts of the scratch are healed, but heating the coating also leads to formation of some holes, which may be due to evaporation of residual solvents in the coating. When the temperature increases further to 423 K for 10 min, the holes can be somewhat healed, but not completely. Compared to the Figure 5.22d, introduction of the macro-monomer DAPPG can improve the self-healing property.

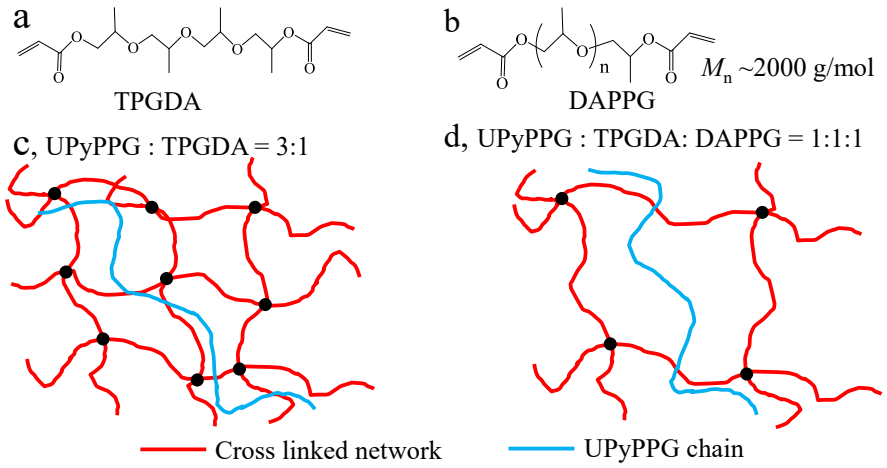

Figure 5.23: Chemical structures for (a) tripropylene glycol diacrylate (TPGDA), and (b) diacrylate poly(propylene glycol) (DAPPG). Schematic diagrams show networks with (c) high cross-linking density and (d) low cross linking density when introducing DAPPG into coatings.

In summary, UPyPPG shows good self-healing property at relative low temperatures. However, it can not be used as coating due to the fact that it flows at relative high temperatures. Blends of UPyPPG with commonly used monomers TPGDA and/or DAPPG were used to prepare UV curable coatings with self-healing properties. The idea is that TPGDA provides good mechanical properties to coatings through

formation of highly cross-linked networks, and UPyPPG provides self-healing features through diffusion of chains at high temperatures. The self-healing property is inversely correlated with cross-linking densities (the amount of TPGDA in coatings). The higher TPGDA ratio in coatings, the poorer the self-healing property is. Introduction of the macro-monomer DAPPG can decrease the cross-linking density, thus increase chain diffusion of UPyPPG and consequently increase self-healing properties. Finally, it is worth noting that at the present stage we have only performed these initial feasibility experiments to investigate the self-healing property of supramolecular coatings. More quantitative research should be conducted to determine the best compositions to optimize both self-healing and mechanical properties based on full rheological investigations of the synthesized materials, and a rheological model should be designed to describe the relationships between chain relaxations and self-healing properties. The work presented here is intended to demonstrate that supramolecular polymers can be potentially used to prepare self-healing coatings, and detailed work may be conducted in the future.

5.4 Conclusions

In this chapter, relaxation dynamics and rheological properties of PPG and UPyPPG are investigated. Exchange of the end OH groups of PPG for supramolecular UPy groups changes the macroscopic properties dramatically; the unfunctionalised PPG is a viscous liquid at room temperature whereas UPyPPG is a rubbery solid at room temperature. The difference in the macroscopic properties can be interpreted by two microscopic aspects. Firstly, the multiple end-to-end hydrogen bonds between UPy groups leads to chain extensions which leads to the entanglements of the extended chain. Secondly, the fibre-like structures through dimerisation, stacking and aggregation of UPy groups, act as physical cross-links. Both these two factors weaken and broaden glass transitions, and dramatically delay segmental and normal mode relaxations for UPyPPG. However, these two structural factors do not significantly affect the secondary relaxation of the supramolecular polymer.

Based on our understanding of the relaxation dynamics of the supramolecular polymer, we explored two potential applications of the material as solid polymeric electrolytes for lithium-ion batteries and for self-healing coatings. Ion conductivities of

PPG and UPyPPG blended with LiTFSI salts with different concentrations are measured. Ion conductivities show dependences on ion concentrations, first increasing as increasing ion concentrations; after reaching the maximum (4×10^{-4} and 5×10^{-7} S/cm for PPG and UPyPPG, respectively) when the ratio of O:Li is $\sim$ 25), ion conductivities decrease as further increasing ion concentrations . We find evidence that the Li-ion transport in PPG-based LiTFSI electrolytes are coupled to the normal modes relaxation. UPyPPG shows good self-healing property at relative low temperatures. Coatings from blends of UPyPPG with commonly used di-functional monomers or macro-monomers show self-healing property to some extent. Self-healing properties are inversely correlated to the cross-linking density. The higher cross-linking density, the poorer self-healing property. Introduction of the macro-monomer decreases the cross-linking density, thus increases chain diffusion of UPyPPG and consequently increases the self-healing property. Note that more quantitative work should be conducted to determine the best composition of coatings to optimize both self-healing and mechanical properties. The work presented here simply demonstrates a potential application of supramolecular materials for self-healing coatings.

Chapter 6

Chain-Length Dependent Relaxation Dynamics in Polytetrahydrofuran

6.1 Introduction

In the last three chapters, we demonstrated that strong hydrogen bonds (quadruple) can affect relaxation dynamics across multiple length-scales of polymers. Relatively weak hydrogen (H-) bonds such as the H-bonds between hydroxyl groups (OH) can also affect dynamics of small molecules, oligmers and polymers.[12, 419–426] Particularly, monohydroxy alcohols that contain only one OH-group within a molecule have been widely investigated by various techniques.[12, 419–426] Molecular clusters composed of several molecules linked through (H-) bonds have been reported.[427] In principle, each OH group can form hydrogen bonds with three other OH groups: the oxygen atom can act as acceptor for two hydrogen atoms from other OH groups and the hydrogen atom acts as a donor to an oxygen atom from another OH group.[3] Several structures such as chain-like[426], tree-like [425, 427–429] or ring-like[430–432] structures have been proposed. For example, liquid n-butanol has a rheological response similar to that of short-chain polymers at relative low temperatures near its glass transition.[426] The n-butanol molecules are held together by H-bonds between OH groups; thus, the dipole moments from each molecule add up and form a composite dipole moment. The reorientation of this composite dipole moment and thus the cluster structure can be directly detected using broadband dielectric spectroscopy. Free molecules in the surroundings can attach to either ends of the composite dipole or the molecule at the

end of the composite dipole can disattach from it. As the temperature approaches the glass transition temperature, T_g, the forming and breaking of H-bonds between OH groups become slow and the composite dipole is stable enough to show the Rouse-like relaxation dynamics of short polymers.[426]

To investigate the effects of OH groups on the relaxation dynamics of oligomers and/or polymers, significant effort has been made.[323, 327, 334, 347] A series of poly(propylene glycols) (PPG) with molecular weights ranging from oligomer to polymer and with different end-functionalization were studied. For example, the end OH groups of PPG can be changed to amino groups, -NH_2[323] or methoxy groups, -OCH_3[327, 334, 347]. The H-bonding strength between OH groups are stronger than between -NH_2 groups[323], whereas changing OH groups to -OCH_3 groups removes hydrogen bonds completely.[327, 334, 347]. As a consequence of these structural modifications, the dynamics for different PPG series differ. Compared to OH ended PPG, PPGs with -NH_2 and -OCH_3 end groups show different dynamics: i) glass transition temperatures are lower, and show stronger dependence on molecular weights;[323] ii) the distribution of the structural relaxations become broader; iii) fragilities are larger but show weaker dependence on molecular weights.[323, 334]. iv) normal mode relaxations are less affected by the chain-end functionalisation .[334, 347] The influence of the end modifications on the secondary relaxations is complex. For example, for OH end-capped PPG, the secondary relaxation becomes faster as the molecular weight is increased, but it becomes molecular weight independent for large enough molecular weights demonstrating that the secondary relaxation is related to the presence of the end-groups. On the contrary, for PPGs with one end or both ends capped with -OCH_3 groups, the secondary relaxation becomes faster as the molecular weights is decreased which is typically observed for non H-bonded liquids. The observations were interpreted as evidence of the formation of H-bond mediated clusters in shorter PPGs, where even short-chain PPG molecules are characterised by effective sizes large enough for the size-dependent effects on the secondary relaxation not to be observed. Thus, for short-chain PPG, only the effects due to the presence of H-bonds on the secondary relaxation are observed.[334] Still, the detailed mechanisms behind these effects are not well understood. To address these questions, we here investigate two different chain-systems that both have OH groups at the chain-ends. The first system

is linear polytetrahydrofuran (PTHF) with different molecular weights, and the second one is alkyl diols with varying alkyl lengths.

Polytetrahydrofuran (PTHF) was first obtained from polymerisation of tetrahydrofuran (THF) in the 1930s, and since then hundreds of applications have been developed that are based on PTHF.[32] In particular, PTHF can be used as a building block for thermoplastic elastomers (TPE), which have the advantages of low temperature flexibility, high abrasion resistance, and excellent resilience over a wide range of temperatures. Thus, products using PTHF as a building block, are found for instance in the fields of coatings, adhesives, sealants and automotives.[32] Despite this, some fundamental aspects of PTHF are still not fully understood. Relaxation dynamics of PTHF were investigated by dielectric spectroscopy,[433–435] mechanical spectroscopy [435, 436], nuclear magnetic resonance[434] and neutron scatting.[437] The results from these techniques demonstrate that both the structural α-relaxation and a secondary relaxation are observed. The relaxation observed by dielectric spectroscopy at temperatures around 220 K was assigned to the structural, α, relaxation, related to the glass transition.[433, 434] This relaxation can also be observed in mechanical relaxation spectroscopy (at an oscillation frequency of 10 Hz), thus confirming that this is the structural α relaxation directly linked to the glass transition. The second relaxation observed at lower temperatures ~155 K, was assigned to the secondary β relaxation[433, 434] and it was proposed that the β relaxation arises from a type of main-chain motion, different from the cooperative chain motions responsible for the structural relaxation, and proposed that it was a relatively 'local mode'.[438] More specifically, Willbourn investigated the secondary relaxation by dynamic mechanical analysis, and proposed that the secondary relaxation is due to motions of short $(CH_2)_n$ units with $n > 3$. This interpretation was supported by the fact that the relaxation occurred at 10 Hz and similar temperatures (~155 K) in nylons, polyethylene and poly(alkyl methacrylates) which all have alkyl units longer than three methylene units.[435]

With regards to the primary structural α relaxation for PTHF, a number of properties have been observed that set this polymer aside including: (i) a very broad structural relaxation response that has been interpreted as caused by a broad distribution of characteristic α relaxation times and (ii) a dynamically relatively 'strong'

behaviour where the structural relaxation times were relatively insensitive to temperature changes. Long-chain polymers are often fragile, which can be described by the fragility m, as discussed in Chapter 1. The fragility of PTHF is around $\sim$ 80 which is smaller than the typical value ($\sim$150) for many other polymers (see Chapter 1). It was argued that both these features were directly linked to the flexible chain structure of PTHF as due to the flexible $-C-O-$ (ether) groups along the backbone.[439] Also, the effects of chain entanglements in PTHF melts were investigated using neutron scattering[437, 440] and the tube diameter for PTHF (see Chapter 1) was determined to be around 0.3 nm, which was consistent with the value calculated from viscoelastic data using the Doi-Edwards theory.[83, 84]. The tube diameter of PTHF is thus close to that of polyethylene but is smaller than that of polystyrene (0.8 nm).[441] This was attributed to the structural difference, since PTHF has a very flexible main chain with ether linkages along the backbone without any large side groups. In contrast, the phenyl rings along the backbone of polystyrene hinder chain motions and polystyrene chains are thus less flexible.

With regards to the literature studies of PTHF, mentioned above, it is worth mentioning two facts: i) the molecular weights for all the investigated PTHF samples are above 10000 g/mol, i.e. larger than the estimated entanglement molecular weight M_e ($\sim$ 1500 g/mol) of PTHF;[32] ii) PTHF is a semi-crystalline polymer and for all the reported data, discussed above, the measured samples contain both amorphous and crystalline phases, which complicate the interpretations. For example, dynamics within the amorphous regions can be affected by the presence of the crystalline regions. Additionally, molecular relaxations can even take place in the crystalline phase, as reported for polymers such as polyoxymethylene and polyethylenglycol.[442, 443], which made it even more difficult to determine relaxation dynamics in the amorphous phase. To avoid or minimise these effects, measures have to be taken to avoid crystallisation or at least to minimise the degree of crystallinity in the samples. One way to achieve this is to perform a rapid temperature quench from a temperature above the melting point so that the polymers go from their melt to glassy states within a very short time and there is thus not enough time for crystallization to occur. As discussed in detail in the experimental section, we find that such temperature quenches are necessary for PTHF samples to reach a mainly amorphous state. It was previously demonstrated that the dynamics in quenched PTHF samples show the same relaxation time characteristics

as un-quenched samples in terms of their temperature dependent relaxation dynamics both for the the α-relaxation and secondary relaxations. However, the quenched PTHF samples show a stronger dielectric permittivity, thus demonstrating a higher amorphous fraction, because the α-relaxation of PTHF arises from relaxation within the amorphous regions.[433]

In this chapter, we investigate chain-length dependent dynamics of the linear polytetrahydrofuran (PTHF), spanning from the oligomeric to the polymeric range both near the glass transition temperature and in the melt using rheometry, NMR relaxometry, dielectric spectroscopy and calorimetry. We compare our results to those of other relevant polymer systems and to relevant theories of molecular relaxation and glass-formation. Our systematic studies of PTHF, both in the low and high temperature ranges, presented in this chapter can provide guidance for understanding the structure-property relationships of thermoplastic elastomers, where PTHF is used as soft building blocks. Moreover, we have initiated detailed investigations of the relaxation dynamics of alkyl diols. Short linear alkyl units with a number of carbons from 2 to 7, all with OH groups at both ends are chosen for the investigation. These molecules are chosen because of their similar structure but systematically increasing number of carbons, which allows to investigate effects of the length of alkyl units on the relaxation dynamics.

6.2 Experimental section

6.2.1 Materials

Polytetrahydrofuran (PTHF) samples with molecular weights M_n of 250, 650, 1000, 2000 and 2900 g/mol were purchased from Sigma Aldrich and one PTHF sample with molecular weight of 1400 g/mol was provided by BASF. All PTHFs are linear polymers with hydroxyl end-groups, as shown in Figure 6.1. Note that 1,4-butanediol is included in the investigation of the series of PTHF samples because this sample corresponds to a PTHF with a degree of polymerization of n =1. Six alkane diols: ethanediol, 1,3-propanediol, 1,4-butanediol, 1,5-pentanediol, 1,6-hexanediol and 1,7-heptanediol were purchased from Sigma Aldrich. For clarity, we use abbreviations to denote all samples in this chapter. These abbreviations are composed of a capital “P”

together with the molecular weights. For example, P250 and P90 are the abbreviations for the PTHF with molecular weight of 250 g/mol and 1,4-butanediol, respectively.

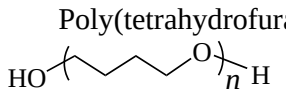

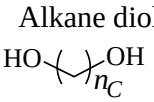

n	3	9	14	20	28	40
M_n (g/mol)	250	650	1000	1400	2000	2900
Abbreviations	P250	P650	P1000	P1400	P2000	P2900
n_C	2	3	4	5	6	7
M (g/mol)	62	76	90	104	118	132
Abbreviations	P62	P76	P90	P104	P118	P132

Figure 6.1: Chemical structures and abbreviations for PTHF and alkane diols.

6.2.2 Characterizations

The general introduction to the characterization methods used to determine dynamics is found in Chapter 2. Here, the experimental details relevant for the work in this Chapter is included.

Differential scanning calorimetry (DSC)

DSC measurements were performed using a TA Q2000 heat-flux instrument. To determine its glass-transition temperature without interference from crystallization, the polymer samples were quenched by quickly submerging the melt into liquid nitrogen, thus avoiding or significantly lowering the degree of crystallization. The adapted procedure is as follows: a PTHF sample with weight around 10 mg was placed in a T-zero DSC pan. The sample pan was first heated to $T = 353$ K on a hot stage and held for 5 min to melt the polymer completely. Then, the sample pan was submerged into liquid nitrogen as quickly as possible and was kept in the liquid nitrogen for 10 minutes to make sure that the temperature of the sample is far below T_g ~170 K. In parallel, the standby temperature (sample stage temperature) of the DSC machine was set to $T = 120$ K under a continuous dry nitrogen gas flow. When the temperatures for both the sample and the stage were far below the sample T_g, the sample pan was

transferred from the liquid nitrogen into the pre-cooled DSC sample stage. The reason for pre-cooling the sample stage of the DSC machine is that the quenched sample can start to cold-crystallize when the temperature is just slightly higher than T_g and this procedure avoids the increase of the sample pan temperature before the actual measurements start. Since PTHF crystallizes each time when temperature is higher than T_g, the quench procedure needs to be repeated for every measurement. The heating traces of the quenched samples at varying heating rates from 5 to 30 K/min were recorded to determine the calorimetric response of the samples. The same procedure was used to measure the glass transitions of the alkane diols.

Broadband dielectric spectroscopy (BDS)

Broadband dielectric spectroscopy (BDS) was performed on a Novocontrol spectrometer with an alpha-N frequency analyser (10^{-2} to 10^6 Hz) connected to a sample cell through a high impedance active test interface (Novocontrol 2-Wire Test Interface ZG2). The spectra were recorded in the temperature range from T=120 to 353 K using a Novocontrol Quatro cryo-system with a temperature control of ±0.1 K. The polymer samples were prepared by melting the polymer on a 20 mm gold coated metal electrode and a few 100 μm thick silica spacers were added to the sample to make sure that the capacitor geometry has a fixed thickness. Subsequently, a 10 mm electrode top plate was added to sandwich the configuration. To avoid or minimise crystallization in the PTHF samples, the samples used in the BDS measurements also have to be temperature quenched. To achieve this, the sample cell was pre-heated using a hot air gun (to approximately 150 °C) and then submerged into liquid nitrogen; it was kept in the liquid nitrogen for 10 min to ensure that the temperature was stable and far below T_g. In parallel, the sample compartment of the cryo-system was pre-cooled to T =120 K using cold nitrogen gas. When both the sample cell and the cryostat were cold enough, the sample was rapidly transferred into the cryostat. This procedure was applied to avoid crystallization of PTHF before the actual measurements. Spectra were recorded within a frequency range of $\sim 10^{-2}$ to 10^6 Hz over a temperature range from 120 to 353 K upon heating.

Viscosity measurements

Shear viscosities of all samples were measured using an Anton Paar MCR 302 stress-controlled rheometer with a 50 mm diameter plate-plate geometry. The viscosities were measured within a temperature range from 303 to 383 K in steps of 10 K. Figure 6.2 shows shear stress λ increases linearly as increasing shear rate $\dot{\gamma}$ in shear rate below 100 s^{-1}. The red line is the linear fit to the data, and the slope of the fitted line is the viscosity. The same procedure has been applied to all other viscosity measurements.

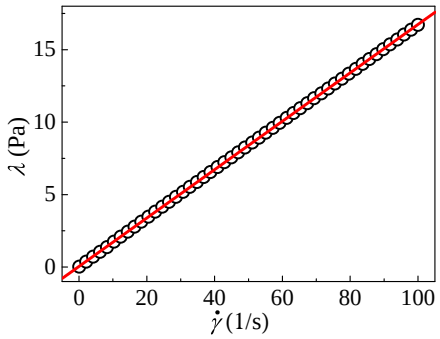

Figure 6.2: An example for the viscosity measurement on P650 at 313 K shows that shear stress λ increases linearly as increasing of shear rate $\dot{\gamma}$ in shear rate below 100 1/s. The red line is the linear fit to the date, and the slope of the fitted line is the viscosity.

Nuclear magnetic resonance spectroscopy (NMR)

A MARAN bench-top pulse NMR analyzer from Resonance Instruments Ltd, UK, operating at 20 MHz, was used to conduct T_1 and T_2 measurements. The pulse sequences for T_1 and T_2 measurements are introduced in Chapter 2. The NMR relaxometry measurements are conducted in the temperature range from 323 to 383 K in steps of 10 K.

6.3 Results and Discussions

The results from rheology, NMR, BDS and DSC measurements characterising dynamics and thermodynamics for the chain-series of PTHF and alkane diols, both in the

glass and melt states, are discussed in following sections.

6.3.1 Dynamics in the melt

Figure 6.3a shows the measured viscosity as a function of temperature and molecular weight for the PTHF samples. As expected, the viscosity increases upon increasing molecular weight, but decreases for increasing temperatures. The temperature dependence of the viscosity can be well described using a VFT equation, $\eta = \eta_0 \exp(DT_0/(T - T_0))$, (red lines in the figure), and we clearly observe that all samples follow very similar temperature dependences, as demonstrated by the VFT fitting parameters in Table 6.1). To directly compare the temperature dependence of the viscosities, the viscosities for each polymer are scaled onto the fit for the P2900 sample using a scale-factor A, as shown in Figure 6.3b. It is clear that the temperature dependences for the different molecular weight samples are very similar. The inset in Figure 6.3b shows the determined scale factor A as a function of molecular weight, demonstrating a clear change of the behaviour observed around a molecular weight of 1400 g/mol. To further investigate this, viscosities for chosen temperatures are plotted as a function of molecular weights in Figure 6.4a, and viscosities at various temperatures are scaled to the data taken at 303 K, as shown in Figure 6.4b.

The molecular weight dependence of viscosity can usually be described by $\eta \propto M^{\alpha}$, where α equals 1 for unentangled polymers and ~ 3.4 for entangled polymers. Based on the Maxwell theory $\eta = G(\tau)\tau$.[85] For Rouse behaviour, the modulus corresponding to the timescale of the longest Rouse mode is related to the product of the number density of chains and thermal energy kT, $G(\tau) = kT\phi/(Nb^3)$ (Chapter 1). The relaxation time of the longest Rouse mode is $\sim \tau_0 N^2$, thus, $\eta = G(\tau)\tau \propto N$, which means that for unentangled polymers, the viscosity is proportional to the molecular weight. For entangled polymers, the tube model discussed in Chapter 1, predicts that the viscosity is proportional to M^3. In reality, one typically observes a larger exponent which is due to constraint release and polymer contour length fluctuations, as described in Chapter 1. Thus, the viscosity scales as $\eta \propto M^{3.4}$.[52, 83]

Our viscosity data for different temperatures are scaled onto the T=303 K data using the scaling factor B in Figure 6.4b. It is clear that viscosity data measured at different temperatures overlap well. As shown in Fig. 4b, the scaling relation $\eta \propto M$

can describe the samples with molecular weights of 250, 650 and 1000 g/mol well even though the fact that we have only a few data points within this range makes it difficult to state anything about the exact scaling relation. It is clear though that if one assumes that that the 250, 650 and 1000 g/mol samples follow the expected Rouse behaviour, the lowest M sample P90 deviates from the behaviour. Two possible reasons can be considered for this. Firstly, the Rouse model will not be a reasonable description for short enough molecules. It has been reported that at least ~5 fundamental Rouse units are required in a chain for the Rouse model to work.[52] As discussed later, there are only around two Rouse units in P90. Secondly, the OH end-groups that can form hydrogen bonds play a more important role in determining the viscosity for P90 than for other polymers and these interactions are of course not accounted for within a Rouse model. It can thus be expected that the higher density of H-bonds for P90 leads to a higher viscosity than what is predicted by the $\eta \propto M$ scaling.

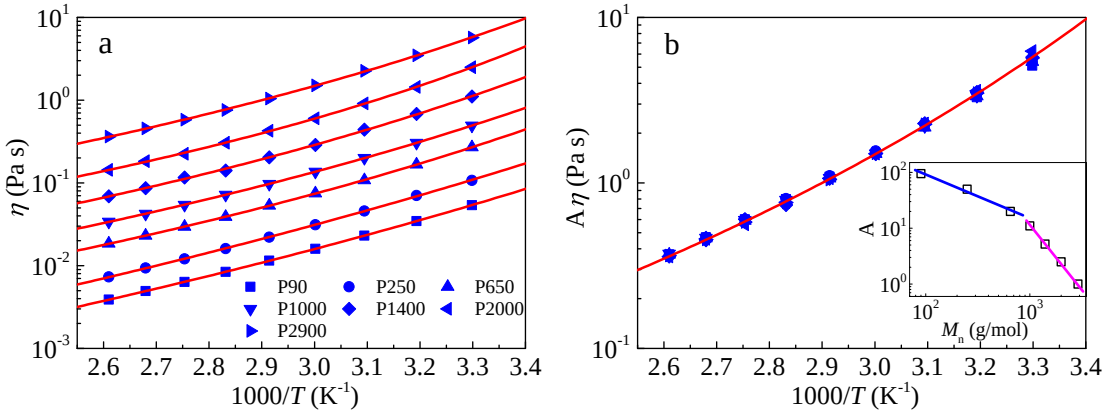

Figure 6.3: a) Viscosity and (b) scaled viscosity as a function of temperature for samples with varying molecular weights. The red lines are VFT fits to the data and fitting parameters are given in Table 6.1. The viscosities in (b) are scaled to the viscosity of P2900 with scaling factors A. The scaling demonstrates that the viscosities for all samples follow a very similar temperature dependence. The inset in (b) shows the scaling factor A as a function of molecular weight. A clear change in behaviour around 1400 g/mol is observed as indicated by the pink and blue lines.

For $M_n \geq 1400$ g/mol, we find an approximate scaling exponent of 2.4, which is smaller than the reported value ~3.4 for many other polymers.[52, 83] The reason for

Table 6.1: VFT fitting parameters for the viscosities as a function of temperature (red lines in Figure 6.3).

	P90	P250	P650	P1000	P1400	P2000	P2900
-log(η_0)	5.1±0.05	5.0±0.15	4.9±0.3	4.8±0.2	4.7±0.3	4.9±0.6	4.8 ±0.3
D	13.9±0.8	14.2±1.2	12.9±0.4	13.2±0.3	12.7±0.9	11.0±0.6	11.8±0.8
T_0	119±5	117±8	124±4	129±2	121±6	132±6	131±7

the deviation from the predication of the tube model is not clear. However, two possible reasons may be considered. Firstly, the deviation of from 3.4 may just indicate that we are situated within a transition regime between unentangled and entangled polymer behaviour. In other words. the exponent of 2.4 may be attributed to the onset of entanglements in PTHF. To verify this, more samples with higher molecular weights should be measured. Unfortunately, we have no access to samples with molecular weights higher than 2900 g/mol. Secondly, Jeong et al. reported for alkane melts that the self-diffusion coefficient scales as $D \sim M^{\beta(T)}$ for chains with lengths varying from 6 to 100 backbone carbons.[256] The exponent β is not a constant, but has a temperature dependence.[256] Based on the link between self-diffusion coefficient and viscosity, it is a reasonable speculation that the viscosity might also show a temperature dependence $\eta \propto M^{\alpha(T)}$. Indeed, for alkane melts they observed that diffusion coefficients vary with exponents varying within the range from -1.85 to -2.72. In contrast to the temperature dependent behaviour observed for the alkanes, however, the viscosity behaviour for the PTHF within the investigated temperature range is independent of temperature. It is thus clear that the reason for our observed behaviour needs further investigations either by experiment or simulations. However, irrespective of the detailed interpretation, it is clear that we do observe a change in the molecular weight dependence of the viscosity around $M_n \sim 1400$ g/mol and this does indicate an onset of a different physical mechanism and it is reasonable to speculate that this is due to the early onset of entanglements.[52]

To investigate relaxation dynamics further in the melts, NMR T_1 and T_2 measurements (Chapter 2) are conducted. Figure 6.5a and b show the T_2 relaxation as measured using NMR relaxometry, as a function of temperature and molecular weight,

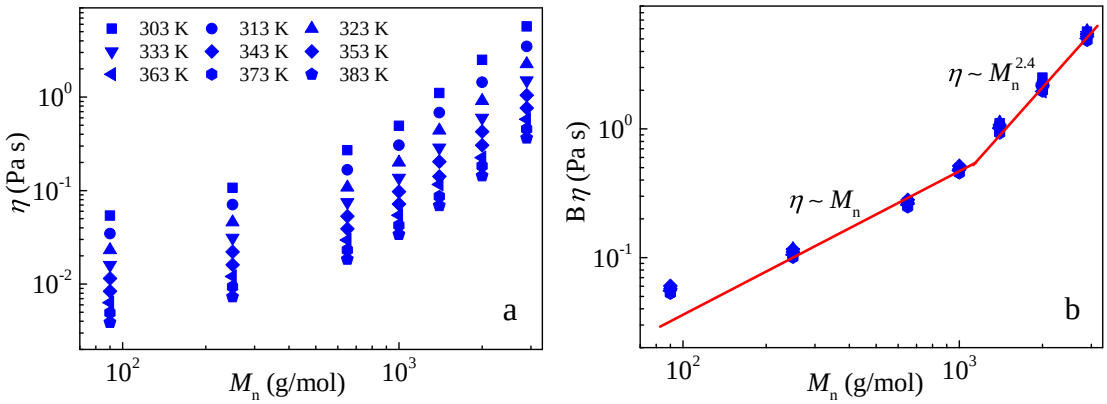

Figure 6.4: (a) Viscosity and (b) scaled viscosity as a function of molecular weights at varying temperatures. The viscosity in (b) are scaled to the viscosity at 303 K with scale factors B. The red line in (b) is the guide to eye.

respectively. We find that T_2 increases with increasing temperature, but decreases with increasing molecular weights at a given temperature.

Linear polymers in the melt with molecular weights below the entanglement molecular weight M_e can typically be described using the Rouse model (see Chapter 1).[52] The time scale for a particular Rouse mode, τ_p, can be described as:

$$\tau_p = \frac{\tau_0}{\sin^2(\pi p/2N)} \tag{6.1}$$

Here, N is the number of Rouse units in a polymer chain and τ_0 is the fundamental Rouse unit relaxation time. p enumerates the Rouse modes and thus varies from 1 to N. When p equals N, $\tau_p = \tau_0$. The number of Rouse units in a polymer chain equals:

$$N = \frac{M_n}{N_a M_{\text{mono}}} \tag{6.2}$$

where M_n is the molecular weight, N_a is the number of monomers in a Rouse unit, and M_{mono} is the monomer molecular weight.

The relaxation function, $\Phi(t)$, of transverse nuclear magnetization follows a single exponential law:

$$\Phi(t) = \exp(\frac{-t}{T_2}) \tag{6.3}$$

where T_2 equals

$$1/T_2 = \frac{6\Delta^2\tau_0}{\pi}\ln(N) \tag{6.4}$$

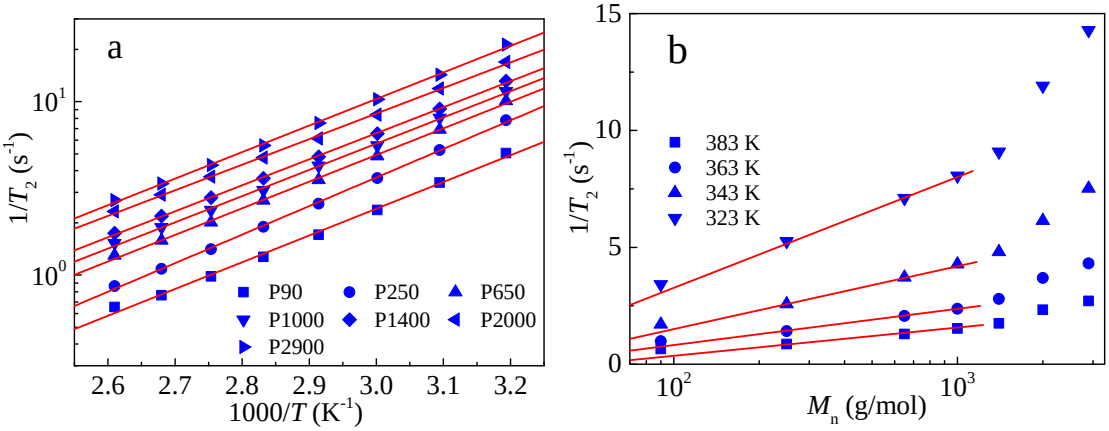

Figure 6.5: (a) T_2 as a function of temperatures for samples with varying molecular weights and (b) T_2 as a function of molecular weights at varying temperatures. The red lines in (a) are guides to eye and the lines in (b) are the fit using equation 6.6 in the range of $M_n \leq 1000$ g/mol (Rouse model region but excluding P90). Fitting parameters are shown in Table 6.2

.

Here, Δ is the dipole interaction strength which equals,

$$\Delta = \frac{\gamma^2 \hbar \mu_0}{8\pi N_a d^3} \tag{6.5}$$

and, γ and $\hbar$ are the gyromagnetic ratio of the proton and the reduced Plank constant, respectively. μ_0 is the permittivity of free space and d is the proton-proton distance. The d value (1.76×10^{-10} m) for polyethylene glycol (PEO) is used in this work since it is not known for PTHF and given the similarity in the molecular structures; PEO ($-(CH_2CH_2O)_n-$) has a similar chain structure to PTHF ($-(CH_2CH_2CH_2CH_2O)_n-$). Substituting equation 6.2 into equation 6.4 gives a relation between the reverse of the transverse nuclear magnetization, $1/T_2$, and the molecular weight, M_n:

$$1/T_2 = \frac{6\Delta^2\tau_0}{\pi}(\ln(M_n - \ln(N_a M_{\text{mono}})) \tag{6.6}$$

Thus, a straight line can be expected from a plot of $1/T_2$ against $\ln(M_n)$ based on equation 6.6. Thus, from linear fits in such plots, N_a and the fundamental Rouse relaxation time scale, τ_0, can be obtained.[444]

We have measured T_2 at temperatures from 303 to 383 K. In principle, both τ_0 and N_a should be temperature dependent. However, to first approximation we make

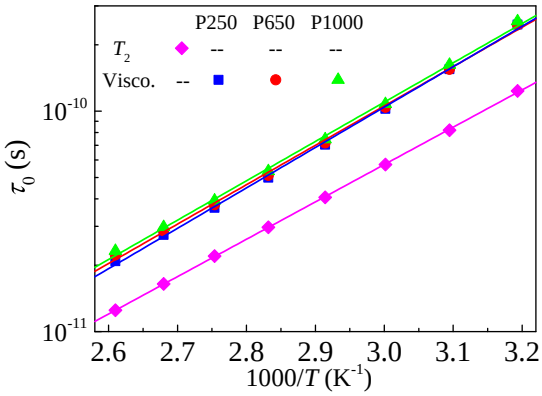

Figure 6.6: Fundamental Rouse relaxation time τ_0 as a function of temperatures obtained from viscosity and NMR T_2 measurements. The lines are the Arrhenius fits, which give activation energies of 33 and 35 kJ/mol from T_2 and viscosity measurements, respectively. Fitting parameters are shown in Table 6.2. Errors are smaller than the size of symbols.

the assumption that N_a does not change with temperature. Thus, a simultaneously fit for all T_2 data obtained at different temperatures with one fixed N_a value is conducted, as shown by the red lines in Figure 6.5b. Note that only the data points for samples with molecular weights of 250, 650 and 1000 g/mol which are in the range that can be described by a linear molecular weight behaviour and thus a Rouse description is included in the fit. From the fitted slopes and intercepts, N_a and τ_0 can be calculated.[444] The calculated time scales are shown in Figure 6.6. We find that N_a is ~0.5, which means that each monomer approximately contains two Rouse units. The N_a value for PEO investigated by the same technique is ~1, meaning that each monomer contain approximately one Rouse unit.[444] There are 3 chemical bonds in the monomer for PEO, thus, the length of the fundamental Rouse unit for PEO is around 3 chemical bonds. Whereas, there are 5 chemical bonds in the monomer for PTHF, which corresponds to a similar fundamental Rouse length to PEO.[444] From the value of N_a and M_n, the number of Rouse modes that are relevant to include for each polymer can be calculated. Thus based on equations 6.7 and 6.8, τ_0 can be calculated and is plotted as a function of temperature in Figure 6.6.

Based on the Rouse model discussed in Chapter 1, the viscosity is related to the

relaxation time of the fundamental Rouse mode τ_0 using the following equations:[52]

$$\tau_0 = \frac{2\eta}{k_B T c_p \Phi_N} \tag{6.7}$$

$$\Phi_N = \sum_{p=1}^{N} \frac{1}{\sin^2(\frac{p\pi}{2N})} \tag{6.8}$$

Here, c_p is number density of polymers, and k_B and T are the Boltzmann constant and temperature, respectively. p is an index which enumerates the Rouse modes and ranges from 1 to N. Φ_N is the summation over the p modes within the Rouse model. To calculate τ_0 from the viscosity of a particular sample with a certain chain-length, the number of Rouse modes p relevant for this polymer length is required and this can be estimated from knowledge of the Rouse molecular weight, which in turn can be determined from the NMR measurements, as discussed above.

Interestingly, τ_0 determined for P250, P650 and P1000 from the viscosity measurements are identical, indicating that τ_0 is independent of molecular weight. Moreover, we find that τ_0 determined from T_2 measurements is slightly smaller than that from the viscosity measurements but within a factor of 2. We note that the temperature dependence of the viscosity data and thus τ_0 are best described using a VFT behaviour even though the behaviour over the measured temperature range is close to Arrhenius. The temperature dependence of τ_0 determined from T_2 NMR measurements is well described using an Arrhenius expression. As shown in Figure 6, we find that if we approximately describe τ_0 from both techniques using Arrhenius expressions, the resulting activation energies are very similar (33 and 35 kJ/mol from T_2 and viscosity measurements, respectively). The inter-proton vector sits at a angle to the end-to-end vector of the chain. However, when determining Δ in equation 6.5, this is not considered.[445], which leads to a difference in Δ with a factor k. To quantitatively calculate the τ_0 for polyethylene (PE) in Ref([445], a Monte Carlo simulation was performed to calculate the dimensions of PE chains.[445, 446] The value of k is typically close to 1 and for PE it was found to be $\sim$ 0.8.[445] In our calculation above, k is set to 1. Thus, based on the results for PE, this approximation may lead to a difference in $\tau_0$of a factor of 2.

Figure 6.7a shows the plots of $1/T_1$ as a function of temperature. As shown, T_1 increases as the temperature is increased but decreases as the molecular weight is increased. The red lines in Figure 6.7a are the linear fits to the data, which shows the Arrenius behaviour. Based on the BPP theory (see Chapter 2),[447] T_1 and T_2 can be expressed as:

$$\frac{1}{T_1} = 2K\left(\frac{\tau_c}{1+\omega^2\tau_c^2} + \frac{4\tau_c}{1+4\omega^2\tau_c^2}\right) \tag{6.9}$$

$$\frac{1}{T_2} = K\left(3\tau_c + \frac{5\tau_c}{1+\omega^2\tau_c^2} + \frac{2\tau_c}{1+4\omega^2\tau_c^2}\right) \tag{6.10}$$

where τ_c is the correlation time, and K is a constant which equals:

$$K = \frac{3\mu_0^2}{320\pi^2}\frac{\hbar^2\gamma^4}{d^6} \tag{6.11}$$

Here, μ_0 is the magnetic permeability of free space, $\hbar$ is the reduced Planck constant, γ is the nuclear gyromagnetic ratio, d is the proton-proton distance, which is the same as in equation 6.5, and ω is the operating frequency of the NMR equipment.

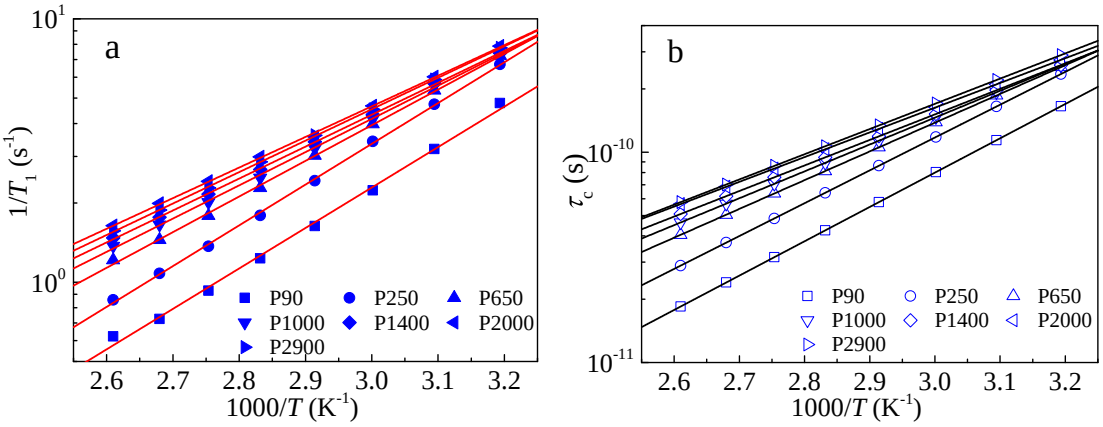

Figure 6.7: (a) $1/T_1$ as a function of temperatures for samples with varying molecular weights. The red lines are guides to eye. (b) correlation timescales τ_c by solving equation 6.12. The black lines in (b) are the Arrhenius fits. Fitting parameters are shown in Table 6.2. Errors are smaller than the size of symbol.

Figure 6.7b shows the Arrhenius plots of the correlation timescales τ_c determined from BPP theory as a function of temperatures for samples with different molecular weights. In BPP theory, one assumes that there is only one effective correlation

timescale for both T_1 and T_2 relaxations. This is generally true for small molecules. However, for polymers, this is not true. T_2 measurements can probe dynamics which are much slower than T_1 measurements. T_2 relaxations are sensitive to the motions of various pth Rouse modes, whereas T_1 relaxations are sensitive to local motions of a chain which is a function of its surroundings, i.e. viscosity or molecular weight. Thus the correlation timescales for T_1 and T_2 relaxations are different for polymers, and the correlation times τ_c for T_1 relaxations can be obtained by solving the equation 6.12.

$$\frac{1}{T_1} - 2K\left(\frac{\tau_c}{1+\omega^2\tau_c^2} + \frac{4\tau_c}{1+4\omega^2\tau_c^2}\right) = 0 \tag{6.12}$$

We find that τ_c becomes larger with increasing molecular weight, and can be well described using the Arrhenius equation. The fitting parameters are shown in Table 6.2. The activation energies decrease for increasing molecular weights (up to 1000 g/mol). When $M_n \geq 1400$ g/mol, the activation energies almost remain constant (see Table 6.2), which also indicates that the behaviour changes around a molecular weight of 1400 g/mol, which was also observed in the viscosity measurements in Figure 6.3 and 6.4.

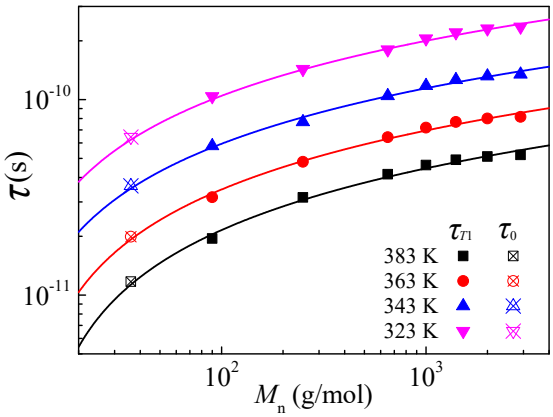

Figure 6.8: Plot of τ_c from T_1 relaxations as a function of molecular weights at various temperatures, and extrapolation to the timescales τ_0 for the fundamental Rouse units from the Rouse modelling of T_2 relaxations. The lines are guides to eyes.

Figure 6.8 shows τ_c as a function of molecular weight for varying temperatures. In BPP theory, one assumes that only one effective correction timescale τ_c is involved in the relaxation dynamics. In reality, this is only an approximation and τ_c thus represents

an effective time-scale, as observed for each molecular weight; as the molecular weight decreases, τ_c decreases. On the other hand, the timescale for the fundamental Rouse unit, τ_0, is estimated by application of the Rouse model on T_2 measurement data, as shown in Figure 6.6 and Equation 6.6 and given the applied model, τ_0 should be representative of the fundamental Rouse mode timescale without interference from the higher Rouse mode contributions. Interestingly, a simple approximate extrapolation of τ_c as a function of M_n (solid lines in Figure 6.8) is consistent with the data points for the fundamental Rouse unit timescales. We note, however, that there is a factor k in Δ (equation 6.5) which is set to 1 in our calculation and can lead to an uncertainty in τ_c. Simulations are required to determine the factor k precisely.[445] In the case of PE, the factor k was determined to be ~2.

Table 6.2: The Arrhenius fit parameters for τ_c from T_1 analysis.

	P90	P250	P650	P1000	P1400	P2000	P2900
-log(τ_0) (s)	13.5±0.2	13.9±0.1	13.7±0.2	14.2±0.2	14.0±0.1	13.6±0.2	13.9±0.2
E_a (kJ/mol)	31.2±0.1	29.9±0.3	26.2±0.2	24.5±0.4	23.2±0.3	22.4±0.1	22.2±0.2

6.3.2 Dynamics near the glass transition

The dynamics of a chain-series of PTHF samples with systematically increasing molecular weights are investigated near the glass transition using DSC and BDS. PTHF is a semi-crystalline polymer. To measure the glass transitions for PTHF polymers, the samples need to be quenched in liquid nitrogen (see Experimental section) and quenching PTHF melts into liquid nitrogen was a straightforward way to decrease the temperature under the current experimental conditions. As mentioned in Chapter 1, if the cooling rate is fast enough, in principle, any material can go into the glassy state without crystallization. Figure 6.9a shows a typical DSC C_p trace for quenched P2000. A step-like increase in the C_p trace around 180 K is a characteristic feature for a glass transition; this is shown as the inset of Figure 6.9a. Moreover, a cold crystallization peak around 198 K and a melting peak around 290 K are detected. The cold crystallization occurs only about 20 K above the glass transition temperature, indicating that PTHF chains tend to go to the crystalline state once they have enough mobility.

The integrated area of the cold crystallization peak is 30 J/g, whereas the value for the melt peak is 100 J/g. The difference in these two values indicates that there are both amorphous and crystalline fractions in the sample. Figure 6.9b shows the specific heat as a function of temperature for all quenched PTHF samples. Step features for all samples are observed, which means that glass transitions for these samples with different molecular weights can be detected after quenching. We observe that P650 has a larger value of ΔC_p than the other samples, indicating that the P650 sample has a larger amorphous fraction than the other samples. This conclusion is also strengthened by the fact that the cold crystallization peak for P650 is larger than for the other samples, as shown in Figure 6.14b.

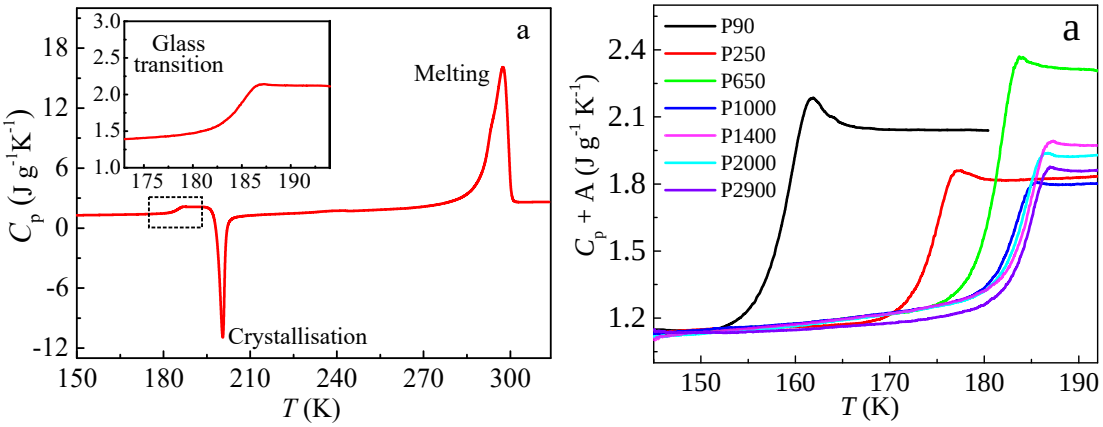

Figure 6.9: (a) A typical DSC C_p trace for the quenched P2000 shows a glass transition, a cold crystallization and a melting transition on the heating trace. The inset in (a) is the magnification of the dashed squares to show the step-like glass transition. (b) heat capacity C_p as a function of temperatures for samples with various molecular weights. The traces are shifted to the glass-side C_p of P90 by a constant A.

Figure 6.10a shows the dependence of T_g on M_n. T_g first increases for increasing M_n and then it remains almost constant when $M_n > 1000$ g/mol. The standard way of describing the molecular weight dependence on T_g is to use a so called Fox-Flory equation:[52] $T_g = T_\infty - C/M$, where T_∞ is the high M_n limit of T_g. The blue lines in Figure 6.10a and 6.10b is the fitted results using the Fox-Flory equation. The fitted results show a good agreement with experimental data except for P90 which sits above the fitted line. One explanation for this is that H-bonds play a more significant role in

P90 than the other samples (see interpretation to viscosity of P90 in Figure 6.4).

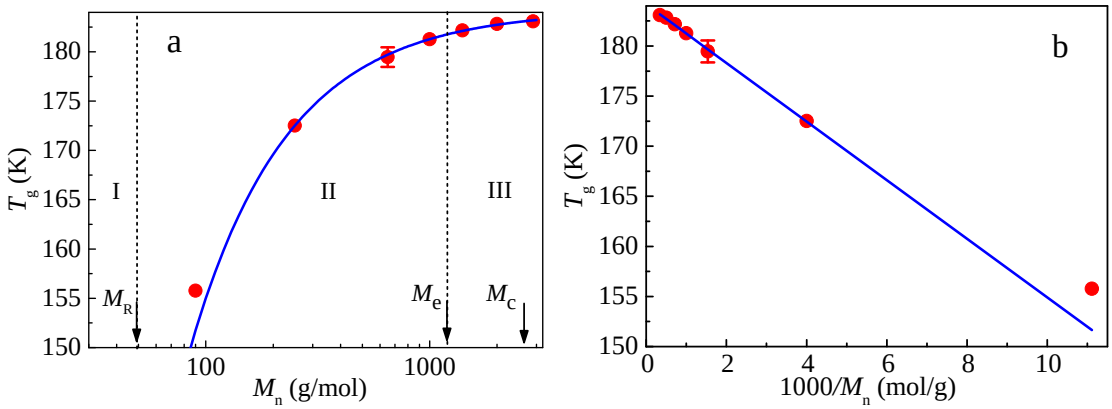

Figure 6.10: ((a) Glass transition temperatures T_g as a function of molecular weights M_n. The onset temperature during a glass transition process is used as T_g. (b) Plot of T_g as a function of the reciprocal of M_n. The blue lines are the fitted results using the Flory-Fox equation. The vertical dashed lines in (a) show the molecular weight dependence of T_g in three regions, of which transition molecular weights are M_R and M_e or M_c ($M_c \sim 2M_e$).

It has been reported that the Fox-Flory equation does not work for low molecular weight samples.[115, 448, 449] Although the Fox-Flory expression works quite well for our samples, excluding the P90 sample, experiments on different polymer chain-series show that the molecular weight dependence of T_g can not be easily be described by a single function over the whole molecular weight range. Instead, the molecular weight dependence of T_g typically shows three distinct regions. [115, 448, 449] Region I refers to low molecular weight oligomers where T_g shows an approximately logarithmic dependence of the molecular weight. Region II also shows a similar logarithmic dependence but with a weaker dependence on M_n. Region III refers to high molecular weight polymers with molecular weights of the order of the critical molecular weight and above, for which T_g does not show a molecular weight dependence.[115, 448, 449] The transition molecular weight between region I and II (M_I) is usually close to the molecular weight of the fundamental Rouse unit. The transition from region II to III (M_{II}) has been suggested to be situated near the entanglement molecular weight, M_e.[115, 448, 449] However, it has also been argued that M_{II} is closer to the criti-

cal molecular weight M_c by comparing with the behaviours for a range of different polymers.[450, 451]

In our case, the lack of data points makes it very difficult to be sure what scenario is true with any accuracy. However, as an illustration we add the determined fundamental Rouse molecular weight from our NMR studies as well as the entanglement molecular weight and estimate the critical molecular weight as $M_c \sim 2M_e$, as shown in Figure 6.10a. The fundamental Rouse molecular weight $M_R \sim 50$ g/mol. From the viscosity measurements in Figure 6.4, M_e is somewhere between 1000 and 1400 g/mol. Thus an estimate of region II would be someplace between M_R and M_e or $M_c \sim 2M_e$. Within this region, T_g increases with increasing molecular weights, however, it is hardly described using a logarithmic relationship. Note that the behaviour with three regions is true for polymers without hydrogen bonding ability. The PTHFs, however, are capped with hydrogen bonding OH groups, which might lead to this difference. For several polymer systems, such as polystyrene or PMMA, region III where T_g is molecular weight independent has been show to start close to M_c.

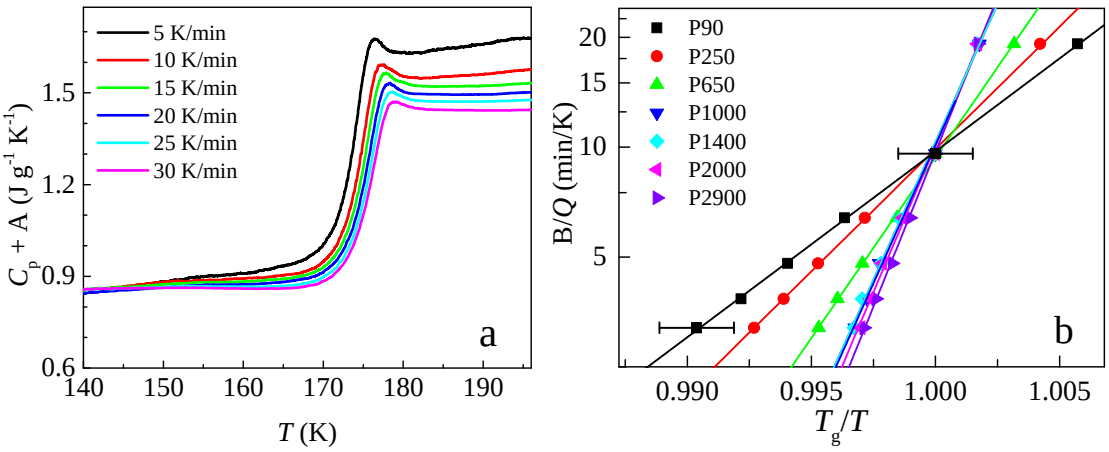

Figure 6.11: (a) Heat capacity C_p traces for P250 as a function of temperatures measured at varying heating rates from 5 to 30 K/min. The traces are shifted by a constant A to the glass-side C_p with the heating rate of 10 K/min. (b) Plots of the reciprocal of heating rates (equivalent to time) a function of T_g/T for samples with varying molecular weights. The onset temperature during a glass transition process with the heating rate of 10 K/min is used as T_g.

It is well known that glass transition temperatures measured by DSC depend on

the applied heating or cooling rates.[159] Heating or cooling rates set the probed timescales, and faster rates lead to shorter timescales. Thus, the step feature in C_p curves characterising the glass transition as a function of temperatures can be observed at higher temperatures for the measurement with higher heating or cooling rates. Note that T_g from DSC measurements are defined at a specific rate of 10 K/min, approximately corresponding to 100 s relaxation time. A series of measurements on samples with varying heating rates from 5 to 30 K/min have been conducted. Figure 6.11a shows an example of C_p traces at varying heating rates for the sample P250. For increasing heating rates, T_g increases, and ΔC_p decreases, which indicates that entropy difference in the glassy and liquid states becomes smaller (see Chapter 2). The entropy differences may be attributed to the chain contributions. More importantly, it is highly possible that the amorphous fractions after quenching of the sample in each measurement are different, which can also lead to the entropy difference.

Figure 6.11b shows the plot of the reciprocal of heating rates a function of T_g/T. The y-axis in this plot is equivalent to timescales which are proportional to the structural relaxation timescales with a factor B.[159] In general, the temperature dependence of the structural relaxation follows the VFT behaviour. However, in a narrow temperature range it can be treated as the Arrhenius behaviour. This is the case for the plot in Figure 6.11b where the linear relationships between equivalent timescales and scaled temperatures, T_g/T, are obtained. The slopes of solid lines indicate the fragility which increases with increasing molecular weights and remains almost constant when molecular weight is larger than 1400 g/mol.[100] This behaviour changes around 1400 g/mol was also observed in viscosity and NMR measurements in melt in Figure 6.4 and 6.5, indicating the onset of the entanglement.

Dielectric spectroscopy is also used to investigate the dynamics of the samples. Figure 6.12a shows an example of the ε'' curve for P250 at 182 K and fitted contributions from conductivity σ, structural α relaxation and the secondary β relaxation using a power law, a HN equation and a Cole-Cole equation, respectively (see Chapter 2). Figure 6.12b shows the ε'' curve for P250 at 150 K which are fitted using a power law and the Cole-Cole equation, accounting for the low frequency contribution and the β relaxation. The black lines are the total fits to the data. From the figures one can see that the experimental data can be described well using above mentioned contri-

butions. The same procedure is applied to fit data sets for other samples at different temperatures.

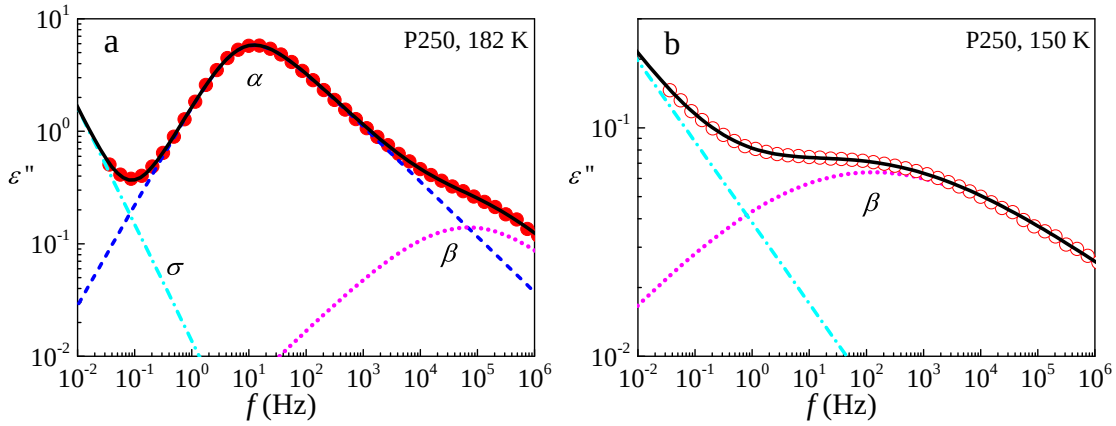

Figure 6.12: (a) dielectric loss permittivity ε'' curves for P250 at (a) 182 K and (b) 150 K. The dash-dotted, dashed and dotted lines in the figure are the contributions from conductivity σ, structural relaxation α and secondary relaxation β fitted using a power law, a HN equation and a Cole-Cole equation, respectively.

Figure 6.13 shows the ε''curves for P90 and P250 at different temperatures, and the best fits to the data (solid black lines) using the fitting procedure described in Figure 6.12. For clarity, contributions from ion conductivity at low frequencies are not shown for some temperatures. As described in Figure 6.12, both α and β relaxations are detected by BDS, which become faster with increasing temperatures. The maxima of ε'' for the α relaxation for both samples remain almost constant as the temperature increases. However, sudden drops in ε'' for both samples are observed when the temperature increases from 170 to 174 K for P90 and from 188 to 190 K for P250, respectively. These sudden drops are due to the cold-crystallization of the samples (see Experimental section and Figure 6.9a). For semi-crystalline samples, the dielectric signal comes from amorphous components. As cold-crystallization happens, the amorphous component in the samples decreases, which results in the sudden drops in ε''.

We also tried to measure the α relaxations for samples with $M_n > 250$ g/mol. However, it turns out that we are not able to do it under the current experiment condition. Figure 6.14a shows ε'' curves for samples with $M_n \geq 250$ g/mol at 188 K. For P250,

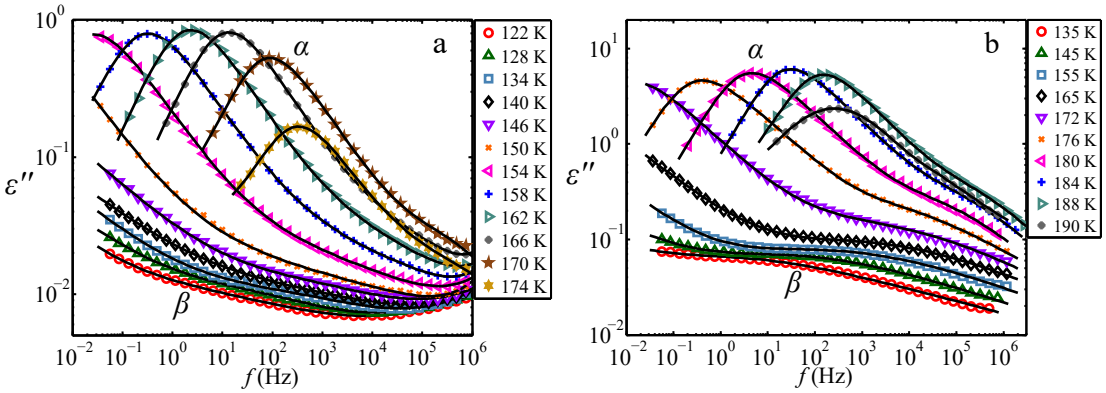

Figure 6.13: Dielectric loss permittivity ε'' curves for (a) P90 and (b) P250 at varying temperatures. The solid lines are the best fits to the data as discussed in Figure 6.12.

an apparent α loss peak is observed within the probed frequency window. For samples with $M_n > 250$ g/mol, we expect that for a fixed temperature the α loss peaks should appear on the low frequency side, compared with data for P250. This is, however, not the case in the experimental data, as shown in Figure 6.14a. No well-defined loss peaks corresponding to the structural relaxations can be observed. Moreover, the ε'' amplitude is almost two decades lower than that for P250. These observations indicate that when the temperature (188 K) is slightly higher than T_g, cold crystallization happens quickly and makes it impossible to measure the α relaxations for samples with $M_n > 250$ g/mol. Cold crystallization can be observed by DSC measurements. Figure 6.14b shows C_p curves of P250, P650 and P2000 as a function of temperatures. Clear and strong crystallization peaks on the C_p curves are observed at the temperature around 15 to 20 K higher than T_g. For clarity, C_p curves for P1000, P1400 and P2900 are not shown in Figure 6.14b. Although the detected cold crystallization temperatures are around 15 to 20 K higher than T_g detected by DSC, it is still possible that cold crystallization can happen at lower temperature during BDS measurements, because heating rates during BDS measurements are lower than that in DSC (10 K/min).

As discussed above, α relaxations for samples with $M_n > 250$ g/mol can not be measured using BDS, due to cold crystallizations. However, β relaxations were measured successfully. Figure 6.15 shows ε'' curves for samples with $M_n > 250$ g/mol at varying temperatures. The data above 174 K for these samples are not shown in the figure, which are affected by cold crystallization. The solid black lines are the best fits

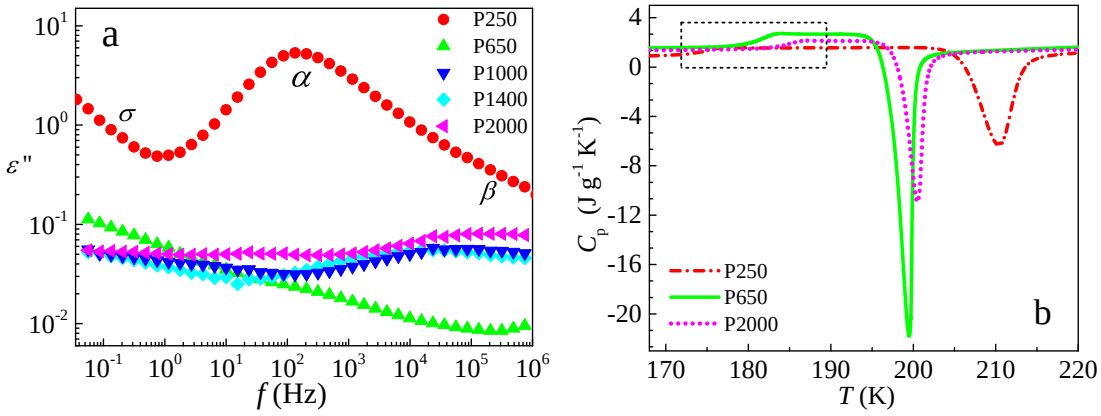

Figure 6.14: (a) Dielectric loss permittivity ε'' curves for samples with varying molecular weights at 188 K. (b) DSC C_p curves at 10 K/min for P250, P650 and P2000 show cold crystallization peaks around 15 to 20 K higher than T_g (indicated in the dashed frame).

to the data using the same fitting procedure described in Figure 6.12b, i.e. a Cole-Cole equation is used to fit the β relaxation loss peaks and a power law is used to account for the contribution at low frequencies. For clarity, the contributions at low frequencies are not shown in the figures. For these investigated samples, the β relaxation peak maxima in ε'' increases and the peak positions move to higher frequencies with increasing temperatures.

The temperature dependences of the determined timescales for different relaxations are shown in Figure 6.16. Figure 6.16a summarizes the α relaxation timescales from BDS and from rate-dependent DSC (RDSC) measurements, β relaxation timescales from BDS, and the relaxation timescales for fundamental Rouse units τ_0 from viscosity and NMR T_2 measurements. The α relaxation timescales become larger when the molecular weights increase from 90 to 250 g/mol. This is expected from the increase of T_g (Figure 6.10a). The temperature dependence of the α relaxation timescales for both P90 and P250 can be well described by the VFT equation (dashed lines in Figure 6.16a). It has been widely accepted that the glass transition temperature depends on the heating or cooling rate.[159] Thus, one can probe the dynamics of the glass transition using DSC measurements with systematically varying heating rates. The timescales are proportional to the reciprocal of heating rates Q, $\tau \sim B/Q$, where B is a constant. The RDSC results after shifted can overlap with the α relaxation timescales from BDS

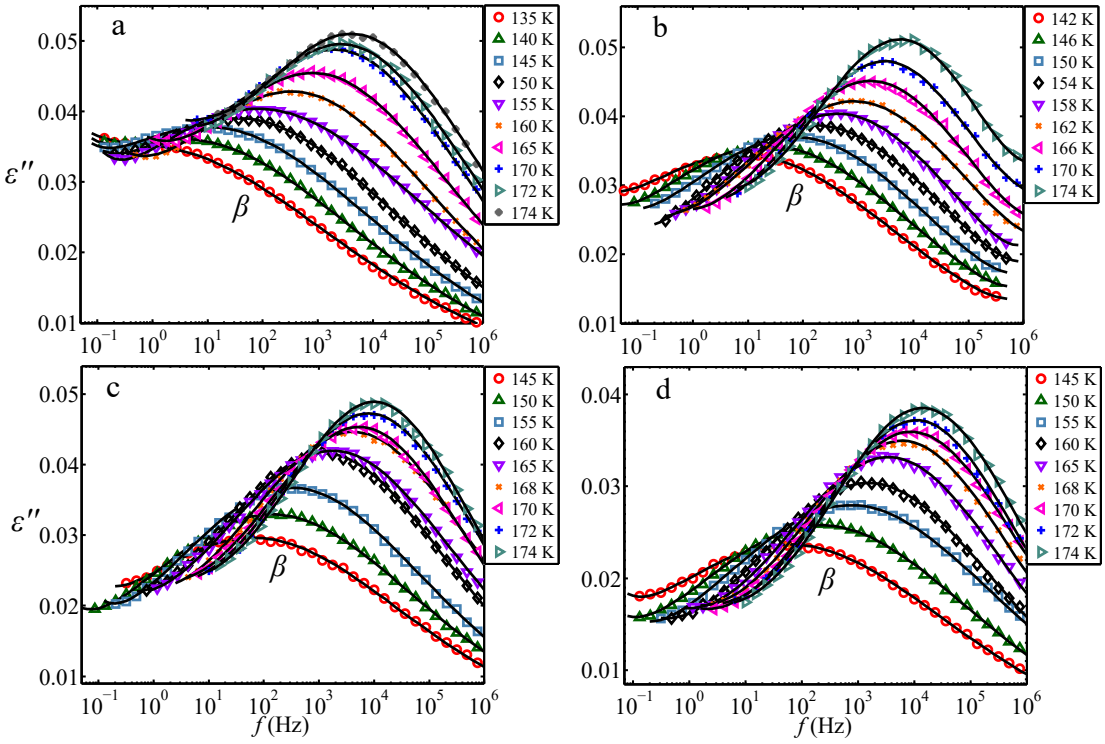

Figure 6.15: Dielectric loss permittivity ε'' curves show β relaxation peaks for (a) P650, (b) P1000, (c)P1400 and (d) P2000 at varying temperatures. The solid lines are the best fits to the data as described in Figure 6.12b.

measurements (Figure 6.16c) which confirms that both the α relaxation determined from BDS and RDSC measurements detect the structural relaxations. With the assumption that the constant B does not change with molecular weight, the α relaxation timescales for samples with $M_n > 250$ g/mol (can not be measured using BDS due to cold crystallizations, see Figure 6.14) and their temperature dependences maybe be estimated using RDSC measurements (Figure 6.16c).

Figure 6.16b highlights the β relaxation timescales for samples with varying molecular weight. As expected, the β relaxations for all samples become faster with increasing temperature. The temperature dependences of β relaxations follow the Arrhenius behaviour (solid lines), and the fitting parameters are shown in Table 6.3. Except for P90, β relaxations become slightly faster with increasing molecular weights, and activation energies are also similar, $\sim$ 40 kJ/mol (Table 6.3). β relaxation timescales for a series of OH-capped PPG with systematically increasing molecular weights have

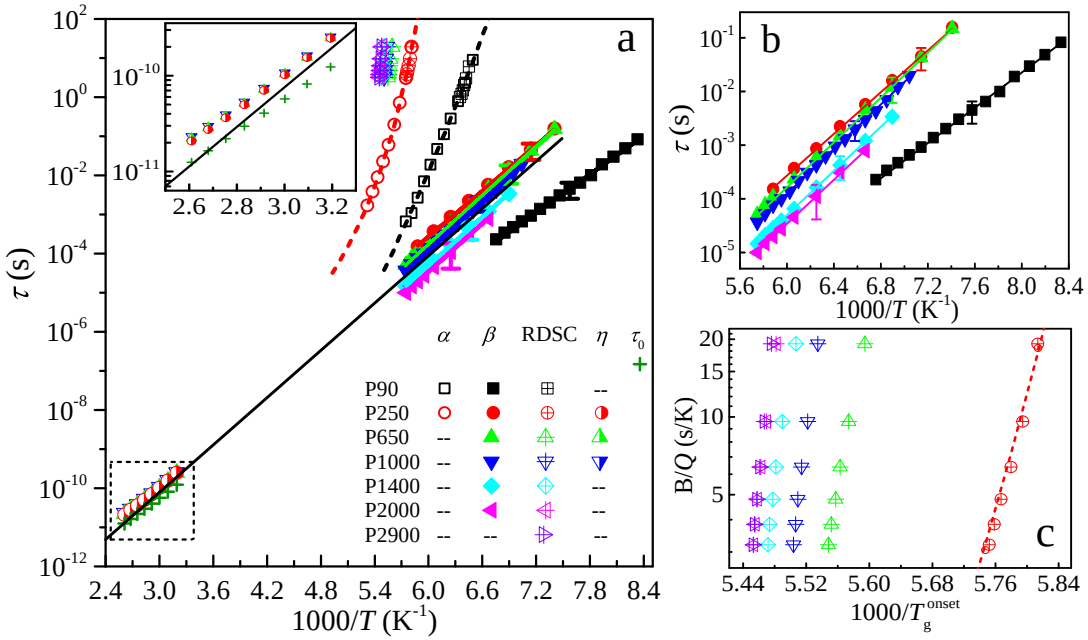

Figure 6.16: (a) The Arrhenius plots of timescales from various techniques as a function of temperatures: α and β relaxations from BDS, equivalent structural relaxation timescales from rate dependent DSC (RDSC), the relaxation timescales for fundamental Rouse units τ_0 calculated from viscosity and NMR T_2 measurements. The inset in (a) is the amplification of the timescales at high temperatures indicated in the dashed square. (b) and (c) are the highlights of β and α relaxations from BDS and RDSC measurements, respectively. Dashed and solid lines are the VFT and Arrhenius fits and fitting parameters are shown in Table 6.3.

been investigated using BDS.[334] It was shown that β relaxations become faster with increasing molecular weights up to ~1000 g/mol, which is consistent with our results here. For PPGs with $M_n > 1000$ g/mol, β relaxation timescales are independent of molecular weights. For both PTHFs and PPGs, with increasing molecular weights, the effects of hydrogen bonding on the β relaxations become less and less important, and after a certain threshold (for the case of PPGs), the effects of the OH end-groups are so weak that they do not affect the β relaxations any longer.[334]

We average the β relaxation timescales determined for all samples excluding those for P90 and fit the average timescale values using an Arrhenius expression. Interestingly, if we extrapolate the Arrhenius temperature dependence to high temperatures,

the behaviour is approximately consistent with the relaxation time-scales for the fundamental Rouse units τ_0 calculated from viscosity and NMR T_2 measurements, see the black solid line and the inset in Figure 6.16a. Interestingly, these results might indicate that the relaxation unit related to β relaxation is the same size to the fundamental Rouse unit, which is also consistent with results on different polymer systems showing that the behaviour of the β relaxation typically becomes approximately molecular weight independent above a molecular weight near M_R.

Table 6.3: The VFT and Arrhenius fitting parameters for α and β relaxations with varying molecular weights.

	VFT fits					Arrhenius fits	
	-log(τ_0) (s)	D	T_0 (K)	m	T_g (K)	-log(τ_0) (s)	E_a (kJ/mol)
P90	16.2±1.5	32.3±5.9	86±12	49±3	148±1.2	14.8±0.1	31.7±0.3
P250	9.5±0.3	4.6±0.3	145±1.1	80±4	170±2.2	15.2±0.2	37.4±0.1
P650	–	–	–	–	–	16.3±0.2	40.1±0.2
P1000	–	–	–	–	–	16.4±0.1	40.2±0.1
P1400	–	–	–	–	–	16.6±0.1	39.8±0.3
P2000	–	–	–	–	–	16.8±0.1	39.8±0.2

6.3.3 Dynamics of alkane diols

Inspired by the effect of molecular weights on the dynamics of PTHF, we also investigated another series of samples, i.e. alkane diols. The alkane diols used in this work has linear alkyl units with varying number of carbons (n_C) situated between two end-hydroxyl groups. The structures are shown in Figure 6.1. α and β relaxations of diols are investigated using BDS. To conduct BDS measurements, samples need to be quenched following the same procedure for PTHF as described in Experimental section. Because of the strong tendency to form crystals, the structural relaxations for the samples with more than 4 carbons can not be measured by BDS. Figure 6.17 shows α and β relaxation timescales as a function of temperatures. For α relaxations, the timescales do not change in a systematic way with increasing n_C. To be more specific, α relaxation timescales for P62 and P90 are close to each other, which are almost a

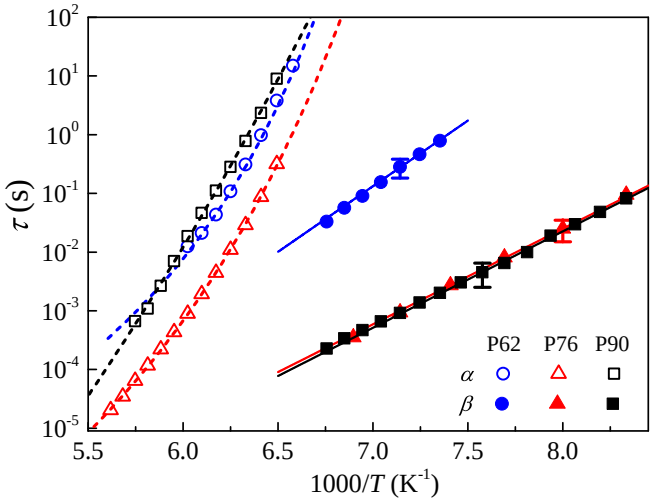

Figure 6.17: α and β relaxations timescales as a function of temperatures from BDS for the P62, P76 and P90. The dashed and solid lines are the VFT and the Arrhenius fits to the data, and fitting parameters are shown in Table 6.4.

decade faster than those for P76. The temperature dependences of α relaxations can be well described using the VFT equation (dashed lines in the figure), and fitting parameters are shown in Table 6.4. The fragility m decreases with increasing the number of carbons, which is 69 for P62 and 49 for P90. For polymers, fragility normally increases with increasing molecular weights, which is the opposite way to our results reported here.[255] However, since molecules measured here are quite small compared to polymers, it is not necessary to follow the rules for polymers.

For β relaxations, the timescales for P76 and P90 are almost identical. However, the β relaxation for P64 is far slower (almost 3 decades) than those for P76 and P90. The reason for this is not clear. However, we speculate that it may relate to cluster structures formed through hydrogen bonds between ended OH groups. For example, several cluster structures such as chain-like[426] or tree-like [425, 427–429] and ring-like[430–432] for monoalcohols have been proposed. With similarities to monoalcohols, alkane diols investigated here may also form different cluster structures which leads to different β relaxations. The temperature dependences of β relaxations can be fitted using the Arrhenius equation, and fitting parameters are shown in the Table 6.4. The activation energy for P62 ($\sim$ 43 kJ/mol) is also slightly higher than those for P76 and P90 ($\sim$ 32 kJ/mol).

Table 6.4: The VFT and Arrhenius fit parameters for α and β relaxations for P62, P76 and P90.

	VFT fits					Arrhenius fits	
	-log(τ_0) (s)	D	T_0 (K)	m	T_g (K)	-log(τ_0) (s)	E_a (kJ/mol)
P62	9.6±0.8	5.3±0.9	122±3	68±4	148±1.5	15.5±0.1	43.1±0.2
P76	12.1±0.3	10.1±0.7	112±2	59±2	146±2.2	14.6±0.1	31.8±0.1
P90	16.2±1.5	32.3±5.9	86±12	49±3	148±1.2	14.8±0.1	31.7±0.3

It has been shown that many physical properties are related to the size of a series of molecules with similar structures. For example, the boiling point which is the transition temperature from liquid to vapour for a series of alkanes, alcohols and alkane diols are shown in Figure 6.18. These series are chosen for comparison, because alcohols and diols can be considered as relatives of the alkanes with one and two ends capped with OH groups. The boiling point is related to the inter-molecular interactions and the molecular size. Stronger inter-molecular interaction and larger molecular size result in higher boiling points. For diols, OH groups at both ends can form hydrogen bonds, whereas for alcohols there is only one OH group in each molecule that can form hydrogen bonds. For alkanes, no hydrogen bonds can be formed. Thus, i) boiling points for the three series samples increase with increasing n_C ii) boiling points for diols are higher than those for alcohols and boiling point for alcohols are higher than those for alkanes at a given n_C.

Figure 6.19a shows T_g as a function of molecular weights M or n_C for alkanes,[454] alcohols[455] and diols. T_gs for diols were measured using DSC following the quenching procedure described in Experimental section. The T_gs for alkanes are obtained from the extrapolation of the viscosity to 10^{13} Pa·s using the empirical equation: $\log(\eta) = \log(A) + B/(T - T_0)$[454, 456] (also see Chapter 1). T_gs for alcohols were measured using the differential thermal analysis method.[455] T_gs for all series (when $n_C \geq 3$) increase with increasing molecular weights M or the number of carbons n_C. At a given M or n_C value, T_gs for diols, alcohols and alkanes show the same order as the boiling points, i.e. T_g for diols > T_g for alcohols > T_g for alkanes. Note that T_gs for the molecules have one or two carbons does not follow the general tendency as

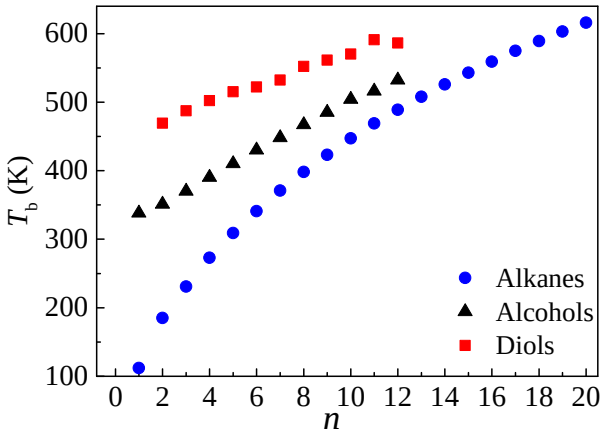

Figure 6.18: Boiling points for alkanes,[452] alcohols and diols as a function of the number of carbons n_C in linear alkyl units. The data for alcohols and diols are taken from an online chemical data base, ChemSpider.[453]

discussed above. For example, T_gs for P62 ($n_C = 2$) is larger than the T_g for P76 ($n_C = 3$). We speculate that structures formed through hydrogen bonds for these very short molecules are somehow different from others with $n_C \geq 3$ carbons. Interestingly, extrapolation of n_C to 0 for diols corresponds to the structure of hydrogen peroxide, H_2O_2, (top *x*axis in Figure 6.19a). The extrapolation line (dashed line in Figure 6.19a) goes through the reported T_g value for H_2O_2.[457]

Figure 6.19b shows scaled T_g values for diols and alcohols with a constant λ in the x-axis direction. To make the data for diols and alcohols follow the n_C dependence of T_g for alkanes (the dashed line in Figure 6.19b), λ is found to be 9 and 4 for diols and alcohols, respectively. Based on this, one can speculate that the effective chains or clusters formed through hydrogen bonds contain ~ 9 or 4 molecules for diols and alcohols, respectively. Similar studies on series of glycols ($HO(C_3H_6)_nOH$) and glycols with one ($HO(C_3H_6)_nOCH_3$) and two ends ($CH_3O(C_3H_6)_nOCH_3$) capped by OCH_3 groups has been reported, and λ equals 8 and 2 for $HO(C_3H_6)_nOH$ and $HO(C_3H_6)_nOCH_3$,[334] which are close to our reported values here. These results probably indicate a general physical mechanism governing glass transitions for these small molecular glass-formers with hydrogen bonds. It is worthy of further studies to investigate the phenomenon in detail.

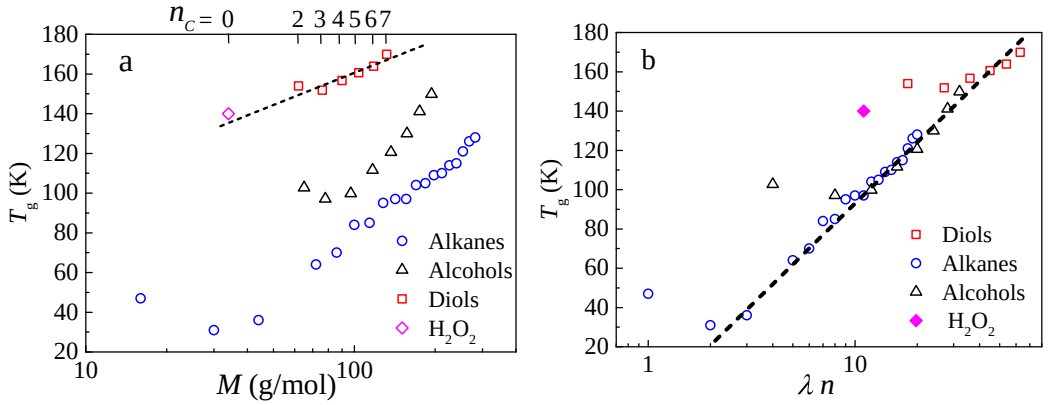

Figure 6.19: (a) Glass transition temperatures T_g for alkanes, alcohols and alkane diols as a function of molecular weights M. For diols, $M = 14n_C + 34$; for alcohols, $M = 14n_C + 18$; for alkanes, $M = 14n_C + 2$, where n_C is the number of carbons. Hydrogen peroxide (H_2O_2) corresponds to $n = 0$. n_C for diols are also shown on the top x-axis. (b) T_g values for alcohols and diols are scaled to the values for alkanes by a constant λ in the x-axis direction. The λ for alcohols and diols are 4 and 9, respectively. The dashed line is guide to eye.

6.4 Conclusions

Relaxation dynamics for PTHFs with systematically increasing molecular weights in melts are investigated by rheometry and NMR measurements. Viscosities decrease with increasing temperature and with decreasing molecular weight. The same temperature dependence of viscosities, regardless of molecular weight, has been observed, which can be well described by the VFT equation. The dependence of viscosities on molecular weights show three different regions. When $90 < M_n \leq 1000$ g/mol, the viscosity scales with M_n, as predicted by the Rouse model; when $M_n \geq 1400$ g/mol, the viscosity scales with $M_n^{2.4}$, showing deviation from the predication of tube model $\eta \sim M^{3.4}$. The reason for the deviation is not clear. However, it is likely due to the onset of entanglements. When $M_n = 90$ g/mol (the monomer), the viscosity does not follow the above two relations, which can be attributed to either the higher hydrogen bond density or that the Rouse model breaks down for very short molecules (less than ~5 fundamental Rouse units). By the use of a Rouse model analysis of NMR T_2 data, the length N_a and relaxation time τ_0 of the fundamental Rouse unit can be calculated.

The dependence of the glass transition temperatures on molecular weight follow the Fox-Flory equation, except for P90 which is too short to show polymer behaviour. An investigation of α relaxations for samples with $M_n > 250$ g/mol is difficult due to the cold crystallization. However, α relaxations and their temperature dependences for samples with different molecular weights may be estimated using the rate dependent DSC measurements. The β relaxations for samples with $M_n \geq 250$ g/mol become slightly faster with increasing molecular weight. The extrapolation of the average Arrhenius behaviour for the β relaxations timescales are consistent with the timescales for the fundamental Rouse unit τ_0, as determined from viscosities and T_2 measurements. This might indicate that the relaxation unit for the β relaxation is of the same size as the fundamental Rouse unit.

The glass transition temperatures for diols with a number of carbons n_C ranging from 2 to 7 in the alkyl unit have been measured using DSC. T_g increases with increasing n_C, except that for $n_C = 2$. This exception has been observed in many other series of molecules, such as in alcohols, alkanes and glycols. The presence of hydrogen bonding OH-groups can increase the boiling points T_b as well as the glass transition temperatures T_g through an increase of the inter-molecular interactions. T_g data for molecules with one or two OH groups can be approximately scaled onto data for molecules without OH groups by applying a factor λ in the x-direction, which might indicate a general physical mechanism governing the glassy dynamics for these hydrogen bonding glass-formers.

Chapter 7

Conclusions and outlook

7.1 Overall conclusions

This thesis aims at reaching a better understanding of the effects of supramolecular interactions on the structure, relaxation dynamics, thermodynamics and rheological properties of supramolecular polymers over a wide temperature range, i.e. from the glassy state to the melt states. A range of experimental techniques are used, including broadband dielectric relaxation spectroscopy (BDS), differential scanning calorimetry (DSC), temperature-modulated DSC (MDSC), shear and extensional rheology and nuclear magnetic resonance (NMR) relaxometry (T_1 and T_2 measurements). Four different supramolecular polymer systems with different structures (linear or network) and hydrogen bonding strength (quadruple hydrogen bonds or single hydrogen bond) were either synthesized in-house or purchased. The first system (system I) is based on a comb-like polymeric backbone of PEHA to which a random distribution of UPy side-groups are added. Quadruple hydrogen bonds can be formed between two UPy groups, forming UPy dimers. The UPy dimers act as physical cross linking points for the supramolecular polymers. The second system (system II) is based on PPG for which the chain-ends are modified using supramolecular UPy groups. Chain extension occurs due to the end-to-end hydrogen bonds between UPy groups and changes the macroscopical property dramatically from a viscous liquid (unfunctionalised PPG) to a rubbery solid (UPyPPG) at room temperature. The final systems are based on hydroxyl-capped PTHF (system III) and alkane diols (system IV) with varying molecular weights, respectively. Relatively weak hydrogen bonds can be formed between the

end OH-groups and the effects of such weak supramolecular hydrogen bonds will thus become more prominent for short chains. These supramolecular polymers are chosen because they are good examples of different types of supramolecular polymers with a variety of both polymer structures and interaction strengths.

The relaxation dynamics and rheological properties of the three supramolecular polymers of system I-III are determined over wide temperature ranges from the glass to the melt states. Generally, the glass transitions are affected by the supramolecular interactions. For system I, the glass transitions become weaker, broader and T_g increases, as the concentration of UPy side groups increases. The UPy dimers in system I act as physical cross links between the polymer chains and slow down the segmental relaxation and lead to a wider distribution of segmental relaxation times. For system II, the UPy dimers are located at the end of each UPyPPG chain, which in turn form longer extended chains through the UPy inter-molecular interactions. The UPy dimers thus, in a sense, act as the hard segments of many thermoplastic elastomers. Moreover, the chain-extended UPyPPG chains can aggregate into fibre-like structures. Both the effects of the addition of hard segments to PPG and the fibre-like structure lead to the observed slower and wider distribution of segmental relaxation times and thus the higher T_g for UPyPPG. For system III, the end hydrogen bonds seems play less important role in determining the T_g and effects are observed only for the lowest molecular weights and the behaviour can for most of the molecular weight range be described using a Fox-Flory behaviour. For system IV, the T_g increases with increasing the number of carbons n_C between two hydroxyl groups, with the except that for $n_C = 2$. Extrapolation of n_C dependence of T_g to $n_C = 0$ implies the T_g for hydrogen peroxide, which is consistent with the reported value in literature

The secondary transitions for the four supramolecular polymers, such as α^* for system I, γ for system II and β for system III and IV, are less affected by supramolecular interactions. For system I, the α^* relaxation is related to the relaxation of alkyl chains α_{PE} in the nano-phase separated alkyl rich region. For systems II and III, the secondary relaxations are related to the local motion of polymer chains. In principle the local motions of polymer chains is less affected the supramolecular interactions, which is in consistent with our experimental observations. For the system IV, the β relaxations for 1,3-propanediol and 1,4-butanediol are almost identical, which is nearly 2 decades faster than that for ethanediol.

Supramolecular interactions show different influence on rheological properties of the four systems. For system I, the interactions between chains dramatically delay the terminal relaxation time, and decrease the power law exponent in the terminal region from 1 for G'' and 2 for G' to around 0.7 for both G' and G'' when the concentration of UPy groups increases from 0 to 14 mol%. The supramolecular interactions act as extra friction between polymer chains which slows down the motion of polymer chains, and cooperative breaking of UPy dimers are required for chains to flow. The plateau for PEHA and UPyPEHA2 are not detected because of the low UPy concentration. For the samples with more than 2 mol% UPy groups, clear plateaus are observed although the molecular weights are smaller than M_e, and the plateau modulus increases as the UPy concentration increases. For system II, both the entanglements due to chain extension and the fibre-like structure (formed through the stacking of UPy groups at chain ends) act as physical cross linkages, thus the plateau covers almost 5 decades for UPyPPG. Whereas for PPG no plateau is observed and it is a viscous liquid at room temperature. The $G'(\omega), G''(\omega)$ in the terminal region for both UPyPPG and PPG can be well described by the Maxwell model (slope 1 and 2 for G'' and G'), indicating that the end-to-end interactions along the polymer backbone do not affect the chain flow or diffusion in the terminal region. For system III, the relaxation behaviour in the melt state can be described by the Rouse model. The fundamental Rouse unit can be estimated from NMR and viscosity measurements, together with Rouse model. Moreover, the relaxation time for the estimated fundamental Rouse unit is coincidently consistent with the extrapolation of the β relaxation time to the high temperature range. We speculate that the relaxation unit for the β relaxation is similar to the fundamental Rouse unit which is around the size of half of monomer.

Time-temperature superposition (TTS) is usually used to investigated the rheological properties over a wide frequency range, because of the limited frequency range of a rheometer. However, TTS is based on the assumption of "thermorheologically simple", i.e. all relaxation processes of a polymer including segmental relaxations and chain modes follow the same temperature dependence. Supramolecular interactions in our systems, acting as a second friction for polymer chains, show different temperature dependences to the segmental relaxations and thus makes the supramolecular polymers not "thermorheologically simple". Thus, the validity of TTS was tested, and we found that TTS works reasonably well in a relatively narrow time or frequency window close

to the reference temperature. However, one should be cautious when building master curves in which data is shifted by many decades in frequency.

The linear rheological response is investigated over a wide temperature range. For system I, the response is described using both a classic sticky Rouse model as well as a new modified model. The new model is proposed to better describe the linear viscoelastic response of unentangled supramolecular polymers. The modified model takes into account: (i) A random distribution of sticky groups which is closer to the reality when polymers are synthesised from random co-polymerization of two monomers. In the sticky Rouse model, it is assumed that stickers are distributed evenly. (ii) The contribution from dangling chain-ends, which are different from relaxation modes of segments of chains "trapped" between stickers; In the sticky Rouse model, this is not considered. (iii) The chain motion upon dissociation of a sticker and re-association with a new coordination involves a finite sized "hop" of the chain, rather than a continuous motion with increased friction, as assumed in the sticky Rouse model. We find that both models can describe the experimental data well in the low measured frequency range. However, the modified model improves the fits in the intermediate frequency region because contributions from polydispersity of strands between stickers and dangling ends are included.

Two potential applications based on UPyPPG are also explored. The first application is to use PPG and UPyPPG as polymeric electrolytes. Ion conductivities and relaxation dynamics of polymer chains in polymeric electrolytes are investigated. The ion conductivities show a dependence on the concentration of lithium ions (expressed in ratio of O:Li) in the mixture. As the concentrations increase, the ion conductivities for both polymers first increase. After reaching a maximum ion conductivity ($4e^{-4}$ and $5e^{-7}$ S/cm for PPG and UPyPPG at 298 K, respectively) when O:Li ~25, ion conductivities decrease as increasing lithium salt concentration. Glass transition temperatures increase for an increasing lithium salt concentration, and two glass transition temperatures can be observed for a sample with O:Li =5, as observed in DSC measurements. This is due to the microphase separation between the ion-rich and ion-depleted regions occuring for high concentrations of lithium. We also found evidence that the ion conductivity is coupled to the normal mode spectrum of polymer chain dynamic rather than the segmental relaxation. The second investigated application is to use UPyPPG as a component in self-healing polymer coatings. UV curable coatings based on

blends of UPyPPG with commonly used difunctional monomers or macro-monomers show varying degrees of self-healing properties. However, the results presented in this thesis is only a simply demonstration of the potential application of supramolecular materials for self-healing coatings, and we note that more quantitative work should be conducted to optimize both self-healing and mechanical properties of the coatings.

7.2 Outlook

The results presented in this thesis provide some examples how the supramolecular interactions affect the relaxation dynamics at different molecular levels, from sub-glass of local motion of molecules to segmental levels, and to the whole chain dynamics. In order to fully understand the relationships between structures, properties and applications, supramolecular materials with more complex structures such as star and dendritic structures are worth to be investigated in future.

The impact of the fundamental research in this thesis might provide guidelines to design and improve new applications of these supramolecular materials. For example, permeation of oxygen through polymeric film is important for the performance of packaging material. It has been shown that permeation of oxygen is closely related to the secondary relaxation of polymers.[458] Thus, plus the reversibility of supramolecular polymers, understanding of secondary relaxation mechanism of supramolecular polymers could provide new ideas to design sustainable package materials with improved performance to isolated oxygen and also the advantages of supramolecular materials, such as easy processing and re-cycling. Addtionally, sugar glass can be used to stabilise or preserve proteins, which has important applications in biotechnology and medical application, for instance the cryopreservation of biological matter.[459, 460] It has been shown that the ability of sugar glass to stabilise proteins is directly related to the secondary relaxations.[461] Finally, temperature responsivity of supramocecular polymers in the plateau and terminal regions is directly related to many applications, including printing,[243, 249] cosmetic,[245, 246] adhesive[299] and coating.[248] For example, several supramolecular inks have been patented. Low viscosity ink is required for ejection in small droplets. On the other hand, highly viscous or even solid is required for high printing quality once the ink droplets are ejected to a paper. The ink

mixture of UPy based supramolecular polymers with other components such as stabilizers, antioxidants and colorants is solid at room temperature because of the network through the hydrogen bonds between UPy groups. However, at evaluated temperatures, the dissociation of UPy leads to the disappearance of network, thus the dramatic decrease of viscosity of the ink which is favour of ink-jet printing. Thus, an understanding of the these behaviours of supramolecular polymers at different molecular levels is key to development of novel materials. The fundamental research work presented in this thesis might lead to a highly important avenue to more applications in future.

Appendix A

The stochastic model

The stochastic model containing several modifications to "Classic" sticky Rouse model was inspired by the discussions of linear viscoelastic (LVE) data with Mr. Victor Boudara and Dr. Daniel Read from School of Mathematics, University of Leeds. The detailed mathematical work was conducted by Victor and Daniel. I was responsible for collecting, analysing the LVE data and discussing to improve the fitting of the new model. The model includes more realistic assumptions with regards to (i) the random placement of the stickers along the backbone, (ii) the contributions from dangling chain ends and (iii) the chain motion upon dissociation of a sticker and re-association with a new coordination involves a finite sized "hop" of the chain. The detail of the model is shown as follows.

A.1 Random placement of stickers on a chain

We first generate a numerical ensemble of chains that accounts for the distribution of the distance between stickers and the length of the dangling ends. For a given molecular mass, M, we build N_c chains. Beginning from one chain end, we generate a series of molecular masses, M_i, which defines the distance to consecutive stickers, from the probability distribution: [462]

$$p(M_i) = \frac{1}{M_{\text{strand}}} \exp\left(-\frac{M_i}{M_{\text{strand}}}\right). \tag{A.1}$$

We add the first sticker at a distance M_1 from the chain end, and then generate a new M_i for the distance to the next sticker, and so on. Hence, the first sticker is placed

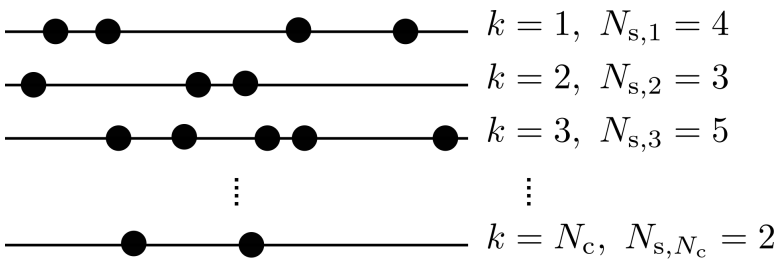

Figure A.1: Example of a set of N_{c} chains. On each chain k the stickers (black circles) are placed via Equation (A.1).

after after a chain length M_1, then another sticker is placed after a chain length M_2, etc., until we exceed the given molecular weight of the considered chain, i.e. we stop when $\sum_i M_i > M$. We generate N_{c} chains according to this process, see Figure A.1. Each chain, k, has $N_{\text{s},k}$ stickers distributed along the chain according to the set of strand molar masses connecting them: $\{M_{k,i}\},\ i = \{1, 2, \ldots, N_{\text{s},k}\}$. From this process, we obtain chains with a distribution of distances between stickers and a Poisson distribution for the number of stickers per chain. In the following Section, we detail how the stress relaxation function is computed for that set of chains.

A.2 "Fast" Rouse modes – G_{fast}

A.2.1 Trapped and dangling chain strands

Let us consider that the number of chains per unit volume is n_M/N, where N is the degree of polymerisation of the chain, and $n_M = \rho N_{\text{A}}/M_0$ is the number of Rouse monomers per unit volume, with ρ the polymer density, N_{A} the Avogadro constant and M_0 the Rouse monomer molar mass. Thus, the "unit of modulus" per chain is

$$\begin{aligned} G^0_{\text{chain}} &= \frac{n_M k_{\text{B}} T}{N} \\ &= \frac{\rho R T}{M}, \end{aligned} \tag{A.2}$$

where we used the relation between the gas constant R and the Boltzmann constant k_{B}, $R = N_{\text{A}} k_{\text{B}}$, T is the temperature, and $M = N M_0$ is the chain molar mass.

We have to consider the Rouse relaxation process of the segments "trapped" between two stickers, and that of the "dangling ends" (chain extremities). For each chain

k, of molar mass M, we write the stress relaxation function of the "fast" Rouse modes as

$$G_{\text{fast},k}(t) = \frac{\rho RT}{M}(G_{\text{trapped},k}(t) + G_{\text{ends},k}(t)). \tag{A.3}$$

Trapped chain segments – G_{trapped}. For each chain k, the strand of chain of molar mass $M_{k,i}$ "trapped" between two stickers, $(i-1)$ and i, behaves as a Rouse chain with both ends fixed, and so relaxes via Rouse modes with relaxation time $\tau_{k,i} = N_{k,i}^2\tau_0/p^2$, with $p = \{1, 2, 3, \dots\}$, and $N_{k,i} \equiv M_{k,i}/M_0$ the number of Rouse monomers in the i^{th} strand (of molar mass $M_{k,i}$) of the k^{th} chain. Hence,

$$G_{\text{trapped},k}(t) = \sum_{i=2}^{N_{\text{s},k}} \sum_{p=1}^{N_{k,i}} \exp\left(-\frac{tp^2}{N_{k,i}^2\tau_0}\right). \tag{A.4}$$

Note that the first sum excludes the chain ends. The second-sum cut-off, $N_{k,i}$, is chosen such that the fastest Rouse mode corresponds to relaxation time of a Rouse monomer, τ_0.

Chain ends – $G_{\text{ends}}(t)$. For each chain k, the two end segments of molecular weight $M_{k,1}$ and $M_{k,(N_{\text{s},k}+1)}$, see Figure A.2, behave as a Rouse chain with one end free and one end fixed, and so relax with the same Rouse spectrum corresponding to the "odd" modes of a chain twice as long. Thus, the Rouse relaxation times are $\tau_{k,i} = (2N_{k,i})^2\,\tau_0/p^2$, with $p = \{1, 3, 5, \dots\}$. The corresponding stress relaxation function is

$$G_{\text{ends},k}(t) = \sum_{i=\{1,N_{\text{s},k}+1\}} \sum_{p=1,\ p_{\text{odd}}}^{N_{k,i}} \exp\left(-\frac{tp^2}{4N_{k,i}^2\tau_0}\right). \tag{A.5}$$

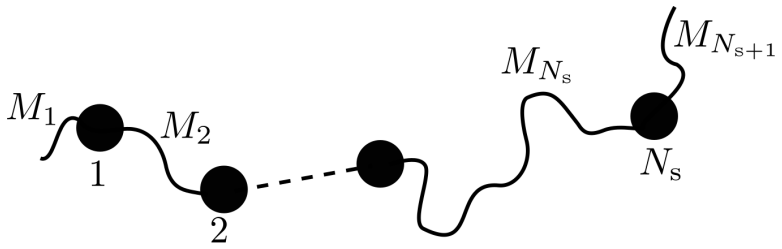

Figure A.2: Cartoon of the system. N_s stickers are randomly placed along the backbone, separated by chains strands of molar masses M_i. M_1 and M_{N_s+1} are the molar masses of the two chain-ends.

A.2.2 Storage and loss moduli – $G'(\omega), G''(\omega)$.

The expressions for the storage and loss moduli, for each chain k, from the stress relaxation function of the "trapped" and "end" strands are summarised below:

$$G'_{\text{fast},k}(\omega) = \sum_{i=2}^{N_{s,k}} \sum_{p=1}^{N_{k,i}} \frac{(\omega N_{k,i}^2 \tau_0 p^{-2})^2}{1+(\omega N_{k,i}^2 \tau_0 p^{-2})^2} + \sum_{i=\{1,N_{s,k}+1\}} \sum_{p_{\text{odd}}}^{N_{k,i}} \frac{(4\omega N_{k,i}^2 \tau_0 p^{-2})^2}{1+(4\omega N_{k,i}^2 \tau_0 p^{-2})^2}, \tag{A.6}$$

$$G''_{\text{fast},k}(\omega) = \sum_{i=2}^{N_{s,k}} \sum_{p=1}^{N_{k,i}} \frac{\omega N_{k,i}^2 \tau_0 p^{-2}}{1+(\omega N_{k,i}^2 \tau_0 p^{-2})^2} + \sum_{i=\{1,N_{s,k}+1\}} \sum_{p_{\text{odd}}}^{N_{k,i}} \frac{4\omega N_{k,i}^2 \tau_0 p^{-2}}{1+(4\omega N_{k,i}^2 \tau_0 p^{-2})^2}. \tag{A.7}$$

The expression of the total elastic and loss moduli from the contribution of the "fast Rouse" motion and summing over the N_c chains of identical molecular weight, but of different number of stickers placed randomly along the chain backbone, is

$$G'_{\text{fast}}(\omega) = \frac{\rho RT}{M} \frac{1}{N_c} \sum_{k=1}^{N_c} G'_{\text{fast},k}(\omega), \tag{A.8}$$

$$G''_{\text{fast}}(\omega) = \frac{\rho RT}{M} \frac{1}{N_c} \sum_{k=1}^{N_c} G''_{\text{fast},k}(\omega). \tag{A.9}$$

A.2.3 Polydispersity

The above Equations (A.8) and (A.9) assume a perfectly monodisperse system, i.e. all chains have the same molar mass M. We can generalise to the polydisperse case. If we assume that the molecular mass distribution is discretised into a set of q modes, $\{(w_\ell, M_\ell)\}$, $\ell = \{1, \ldots, q\}$, and that N_c chains are generated as described above for each molar mass, then the elastic and loss moduli are written

$$G'_{\text{fast}}(\omega) = \sum_{\ell=1}^{q} \frac{\rho w_\ell RT}{M_\ell} \frac{1}{N_c} \sum_{k=1}^{N_c} G'_{\text{fast},k,\ell}(\omega), \tag{A.10}$$

$$G''_{\text{fast}}(\omega) = \sum_{\ell=1}^{q} \frac{\rho w_\ell RT}{M_\ell} \frac{1}{N_c} \sum_{k=1}^{N_c} G''_{\text{fast},k,\ell}(\omega). \tag{A.11}$$

A.3 "Sticky" modes – $G_{\text{sticky}}(t)$

We now describe a stochastic algorithm, which we use to model the motion of chains on long time scales, and which we can use to obtain the relaxation spectrum for the slow chain modes.

A.3.1 Initial spatial configuration

Each of the N_c chains is initialized to have a Gaussian configuration. We start by positioning the first sticker at an arbitrary position, $\boldsymbol{R}_0$, (e.g. $\boldsymbol{R}_0 = \boldsymbol{0}$) and define the position of the following sticker, i, (relative to the previous sticker) by subsequently generating a random vector, $\Delta\boldsymbol{R}_i$, sampled from the Gaussian probability distribution

$$p(\Delta\boldsymbol{R}_i) = \left(\frac{3}{2\pi b^2 N_i}\right)^{3/2} \exp\left(-\frac{3(\Delta\boldsymbol{R}_i)^2}{2b^2 N_i}\right), \tag{A.12}$$

where $N_i \equiv M_i/M_0$ is the number of Rouse monomers on the strand connecting the stickers $(i-1)$ and i, and M_0 the molar mass of a Rouse monomer. Then, we place the sticker i at the position $\boldsymbol{R}_i$ such that

$$\boldsymbol{R}_i = \boldsymbol{R}_{i-1} + \Delta\boldsymbol{R}_i. \tag{A.13}$$

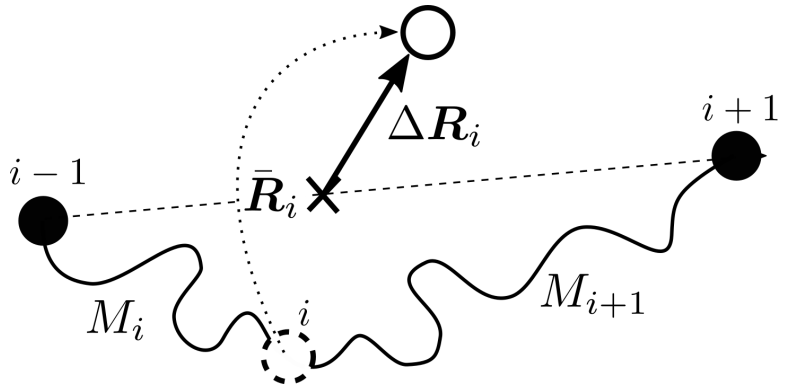

Figure A.3: Sticker i detaches (dashed circle), takes a local "hop", and reattaches to a new position: $\boldsymbol{R}_i^{\text{new}} = \bar{\boldsymbol{R}}_i + \Delta \boldsymbol{R}_i$, (circle).

A.3.2 Sticker "hop"

We made the assumption that the average time during which the stickers stay attached is much longer than any of the internal Rouse relaxation times of the segments of chain delimited by the stickers. We consider that once a sticker, i, detaches, it takes a "hop" to a new position which is a vector $\Delta \boldsymbol{R}$ from a mean position $\bar{\boldsymbol{R}}_i$, where it re-attaches, see Figure A.3. As described in the introduction of this chapter, this "hop" motion is the result of the change of partner that a sticker undergoes, on average, every τ_s. Here we assume that between detachment and reattachment, the sticker is able to explore the full configurational space available to it, given that it is constrained by the chain and its neighbouring stickers do not move, see Figure A.3. The mean position $\bar{\boldsymbol{R}}_i$, around which the sticker re-attaches, is defined by the molecular weight of the strands (M_i, M_{i+1}) that are connected to the sticker and by the position of the neighbouring stickers $(\boldsymbol{R}_{i-1}, \boldsymbol{R}_{i+1})$ as the weighted average position,

$$\bar{\boldsymbol{R}}_i = \frac{M_{i+1}\boldsymbol{R}_{i-1} + M_i \boldsymbol{R}_{i+1}}{M_i + M_{i+1}}. \tag{A.14}$$

Additionally, we obtain the probability distribution function of the "hop variance", $\Delta \boldsymbol{R}_i$, (i.e. how much far from the average position, $\bar{\boldsymbol{R}}_i$, the sticker will attach) as

$$p(\Delta \boldsymbol{R}_i) = \left(\frac{1}{2\pi\sigma_i^2}\right)^{3/2} \exp\left(-\frac{(\Delta \boldsymbol{R}_i)^2}{2\sigma_i^2}\right), \tag{A.15}$$

where the variance is $\sigma_i^2 = k_B T / k_{\text{eff},i}$, with $k_{\text{eff},i}$ the effective spring constant associated to the sticker i, which depends on the neighbouring chain segments

$$k_{\text{eff},i} = \frac{3k_B T}{b^2 N_i} + \frac{3k_B T}{b^2 N_{i+1}}, \tag{A.16}$$

with b the statistical length of a Rouse monomer, and $N_i = M_i/M_0$ is the number of Rouse monomers in M_i.

Assuming isotropy of the "hop", each coordinate $(\Delta x_i, \Delta y_i, \Delta z_i)$ of $\Delta \boldsymbol{R}_i$ follows the same probability distribution

$$p(\Delta x_i) = \left(\frac{1}{2\pi\sigma_i^2}\right)^{1/2} \exp\left(-\frac{(\Delta x_i)^2}{2\sigma_i^2}\right). \tag{A.17}$$

Therefore, when a sticker detaches and reattaches, its new position, $\boldsymbol{R}_i^{\text{new}}$ is given by

$$\boldsymbol{R}_i^{\text{new}} = \bar{\boldsymbol{R}}_i + \Delta \boldsymbol{R}_i. \tag{A.18}$$

For the first sticker ($i = 1$) and last sticker ($i = N_s$), we use

$$\bar{\boldsymbol{R}}_1 = \boldsymbol{R}_2, \quad \text{and} \quad \bar{\boldsymbol{R}}_{N_s} = \boldsymbol{R}_{N_s - 1}, \tag{A.19}$$

and for the effective spring constants Equation (A.16), we use

$$k_{\text{eff},1} = \frac{3k_B T}{b^2 N_2}, \quad \text{and} \quad k_{\text{eff},N_s} = \frac{3k_B T}{b^2 N_{N_s}}. \tag{A.20}$$

The above rules ensure that the chains continue to obey the correct equilibrium Gaussian chain distribution upon hopping. We assume the time between detachment and reattachment is negligible.

A.3.3 Sticker detachment dynamics

We have N_c chains with a certain amount of stickers – which were generated according to Equation (A.1). The total amount of stickers over the N_c chains is $N_{s,\text{tot}} = \sum_{k=1}^{N_c} N_{s,k}$.

For a given sticker, the cumulative distribution function for the detachment time t_d of that sticker (time after which an associated sticker detaches) is

$$p(t_d \leq t) = 1 - \exp\left(-\frac{t}{\tau_s}\right). \tag{A.21}$$

Therefore, the probability that a sticker did not detach after a time t is $p(t \leq t_{\text{d}}) = \exp(-t/\tau_{\text{s}})$. Hence, the probability that none of the $N_{\text{s,tot}}$ stickers have detached after a time t is

$$[p(t \leq t_{\text{d}})]^{N_{\text{s,tot}}} = \exp\left(-\frac{N_{\text{s,tot}}\, t}{\tau_{\text{s}}}\right). \tag{A.22}$$

We conclude that the probability density function of the detachment time of the first sticker to detach amongst the $N_{\text{s,tot}}$ stickers is

$$p(t_{\text{d,first}}) = \frac{N_{\text{s,tot}}}{\tau_{\text{s}}} \exp\left(-\frac{N_{\text{s,tot}}\, t_{\text{d,first}}}{\tau_{\text{s}}}\right). \tag{A.23}$$

Given a uniformly distributed (pseudo) random number $0 < \theta < 1$, we generate from Equation (A.23) a time, $t_{\text{d,first}}$, after which a first sticker detaches:

$$t_{\text{d,first}} = -\tau_{\text{s}} \ln(\theta)/N_{\text{s,tot}}. \tag{A.24}$$

Then, we choose a sticker randomly amongst the $N_{\text{s,tot}}$ stickers and allow it to make a "hop" as described by Equation (A.18). We then repeat this process many times to find the next detachment time amongst the stickers, selecting a random sticker to move each time.

A.3.4 Stress tensor and stress relaxation

A microscopic expression for the stress tensor is [317]

$$\sigma_{\alpha\beta} = \frac{1}{V} \sum_{\text{springs},m} F_{m\alpha} R_{m\beta}, \tag{A.25}$$

where the summation is made over all the springs in the system, the Greek letters are the Cartesian coordinates, $\boldsymbol{F_m} = 3k_{\text{B}}T\boldsymbol{R_m}/N_m b^2$ is the entropic spring force acting in the m^{th} strand, $\boldsymbol{R_m}$ is the vector connecting the two beads neighbouring the strand m, and $V = N_{\text{c}}N/n_M$ is the volume occupied by the N_{c} chains.

Equation (A.25) can be written in terms of a sum over the N_{c} chains and, for each chain, a sum over the number of chain segments between two stickers

$$\begin{aligned} \sigma_{\alpha\beta} &= \frac{1}{V} \sum_{k=1}^{N_{\text{c}}} \sum_{i=2}^{N_{\text{s},k}} \frac{3k_{\text{B}}T}{N_i b^2} R_{i,\alpha} R_{i,\beta} \\ &= \frac{\rho RT}{MN_{\text{c}}} \sum_{k=1}^{N_{\text{c}}} \sum_{i=2}^{N_{\text{s},k}} \frac{3}{N_i b^2} R_{i,\alpha} R_{i,\beta}, \end{aligned} \tag{A.26}$$

where M is the molar mass of the chain. Note that the two end segments (polymers ends) are excluded from this stress expression as we consider that they are relaxed and their contributions were already accounted for in G_{fast}, see Section A.2.1.

In computer simulations, the most convenient way of evaluating $G(t)$ is by using the fluctuation-dissipation theorem [463, 464]:

$$\begin{aligned} G_{\text{sticky}}(t) &= \frac{V}{k_{\text{B}}T}\frac{1}{t_{\text{sim}}-t}\int_0^{t_{\text{sim}}-t}\sigma_{xy}(t+\tau)\sigma_{xy}(\tau)\,\mathrm{d}\tau \\ &= \frac{V}{k_{\text{B}}T}\langle\sigma_{xy}(t+\tau)\sigma_{xy}(\tau)\rangle \\ &= \frac{MN_{\text{c}}}{\rho RT}\langle\sigma_{xy}(t+\tau)\sigma_{xy}(\tau)\rangle \end{aligned} \tag{A.27}$$

where xy is any two orthogonal directions, and t_{sim} the total simulation time.

Since our system is isotropic, one can average over different directions defining the pair of perpendicular axis (xy). In isotropic systems there are two arbitrary angles to select the direction of x axis and one more angle to select the direction of y-axes perpendicular to it. Averaging over these three angles gives the following result [463, 464]

$$\begin{aligned} G_{\text{sticky}}(t) &= \frac{MN_{\text{c}}}{5\rho RT}\Big(\langle\sigma_{xy}(t)\sigma_{xy}(\tau)\rangle + \langle\sigma_{yz}(t)\sigma_{yz}(\tau)\rangle + \langle\sigma_{zx}(t)\sigma_{zx}(\tau)\rangle\Big) \\ &\quad + \frac{MN_{\text{c}}}{30\rho RT}\Big(\langle N_{xy}(t)N_{xy}(\tau)\rangle + \langle N_{xz}(t)N_{xz}(\tau)\rangle + \langle N_{yz}(t)N_{yz}(\tau)\rangle\Big), \end{aligned} \tag{A.28}$$

where $N_{\alpha\beta} = \sigma_{\alpha\alpha} - \sigma_{\beta\beta}$. Using the latter expression instead of Equation (A.27) improves the statistical accuracy of the results.

In order to evaluate correlation functions in simulations, we use a multiple-tau correlator algorithm proposed by Ramirez.[464]

A.3.5 Polydispersity

If we assume that the molecular mass distribution is discretised into a set of q modes, $\{(w_\ell, M_\ell)\}$, $\ell = \{1, \ldots, q\}$, then we compute G_{sticky} as

$$G_{\text{sticky}} = \sum_{\ell=1}^{q} w_\ell G_{\text{sticky},M_\ell}, \tag{A.29}$$

where G_{sticky,M_ℓ} is computed using Equation (A.28) for a chain of molar mass $M = M_\ell$.

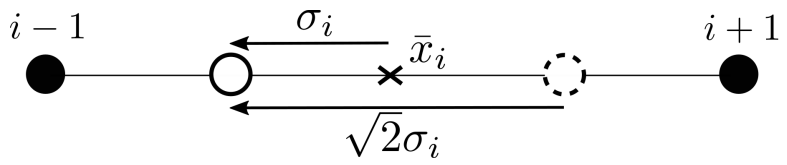

Figure A.4: Sticker "hop" projected on the x-axis. Upon detachment its new position (circle) is defined, on average, as $x^{\text{new}} = \bar{x}_i + \sigma_i$, which is, on average, $\sqrt{2}\sigma_i$ away from its current position (dashed circle).

A.3.6 Sticker times

In this section, we will show that, to compare the values of the sticker time τ_s in the "classic" sticky Rouse model with the stochastic sticky Rouse model in a fair way, we need to multiply the former by a factor π^2. To do so, we take the special where the stickers equally spaced along the chain. Therefore, the number of Rouse monomers between stickers is fixed to $N_m = N/N_s$, and so Equation (A.16) reduces to

$$k_{\text{eff}} = \frac{3k_BT}{b^2N_m} + \frac{3k_BT}{b^2N_m} = \frac{6k_BT}{b^2N_m}. \tag{A.30}$$

In Equation (A.17), σ_i represents the mean square displacement around the mean position defined by $\bar{\boldsymbol{R}}$. Figure A.4 illustrates this process, projected on the x-axis. Upon detachment, a sticker "hops" to its new position defined as

$$x^{\text{new}} = \bar{x}_i + \sigma_i. \tag{A.31}$$

This new position is, on average, at a distance $\sqrt{2}\sigma_i$ away from its current position (because σ_i is measured from the center position $\bar{x}_i$, and we add the variance). Therefore, the actual mean square displacement of the sticker $\langle \Delta x^2 \rangle$, is

$$\begin{aligned} \langle \Delta x^2 \rangle &= 2\sigma_i^2 \\ &= 2k_BT/k_{\text{eff}} \\ &= \frac{b^2N_m}{3}. \end{aligned} \tag{A.32}$$

In one dimension, the effective diffusion coefficient, D, is of form

$$\langle \Delta x^2 \rangle = 2Dt, \tag{A.33}$$

where here $t \equiv \tau_s$. Hence, we have

$$D = \frac{b^2 N_m}{6\tau_s}, \tag{A.34}$$

and we can define the effective sticker friction coefficient as

$$\begin{aligned} \zeta_{\text{sticker}} &\equiv k_B T / D \\ &= \frac{6\tau_s k_B T}{b^2 N_m}. \end{aligned} \tag{A.35}$$

Now, we can use the definition of the Rouse time for a chain of N beads, of friction coefficient ζ, connected by springs of length b: [317]

$$\tau_R = \frac{\zeta N^2 b^2}{3\pi^2 k_B T}. \tag{A.36}$$

To find the Rouse time of a chain composed of N_s "springs" of step length $(N_m b^2)^{1/2}$, we therefore make the following substitutions in Equation (A.36):

$$N \to N_s, \quad b^2 \to N_m b^2, \quad \zeta \to \zeta_{\text{sticker}},$$

to obtain the Rouse relaxation time of a Rouse chain composed of N_s springs

$$\begin{aligned} \tau_R &= \frac{\zeta_{\text{sticker}} N_s^2 N_m b^2}{3\pi^2 k_B T} \\ &= \frac{2 N_s^2 \tau_s}{\pi^2}. \end{aligned} \tag{A.37}$$

Finally, the relaxation modulus for such chain is

$$G(t) = \frac{\rho RT}{M} \sum_p \exp\left(\frac{-2p^2 t}{\tau_R}\right). \tag{A.38}$$

The reason for the factor of two appearing in the exponential is that there is a factor of two difference between the relaxation time for the stress contribution of the p^{th} mode and the relaxation time of molecular orientation from the p^{th} mode (τ_R) [465]. Using Equation (A.37), we obtain

$$G(t) = \frac{\rho RT}{M} \sum_p \exp\left(\frac{-\pi^2 p^2 t}{N_s^2 \tau_s}\right). \tag{A.39}$$

Comparing the latter expression for the relaxation modulus with the corresponding term in Equation 4.1, we see that there is a factor π^2 difference. Therefore, if we want to compare the sticker-time parameter of the stochastic sticky Rouse model with the sticker-time parameter of the "classic" sticky Rouse model, Equation (4.1), we need to multiply the latter by a factor π^2.

Appendix B

References

[1] David S. Lawrence, Tao. Jiang, and Michael. Levett. Self-assembling supramolecular complexes. *Chemical Reviews*, 95(6):2229–2260, 1995. 1

[2] Alberto Ciferri. *Supramolecular polymers*. CRC press, 2014. 1, 2, 6, 11

[3] Jonathan W Steed and Jerry L Atwood. *Supramolecular chemistry*. John Wiley & Sons, 2013. 1, 2, 3, 200

[4] Quan Chen, Gregory J Tudryn, and Ralph H Colby. Ionomer dynamics and the sticky rouse model a. *Journal of Rheology*, 57(5):1441–1462, 2013. 2, 34

[5] R Amadelli, R Argazzi, CA Bignozzi, and F Scandola. Design of antenna-sensitizer polynuclear complexes. sensitization of titanium dioxide with [ru (bpy) 2 (cn) 2] 2ru (bpy (coo) 2) 22. *Journal of the American Chemical Society*, 112(20):7099–7103, 1990. 2

[6] J Benjamin Beck, Jennifer M Ineman, and Stuart J Rowan. Metal/ligand-induced formation of metallo-supramolecular polymers. *Macromolecules*, 38(12):5060–5068, 2005. 3

[7] Alenka Luzar and David Chandler. Hydrogen-bond kinetics in liquid water. *Nature*, 379(6560):55, 1996. 3

[8] C Fonseca Guerra, F Matthias Bickelhaupt, Jaap G Snijders, and Evert Jan Baerends. The nature of the hydrogen bond in dna base pairs: the role of charge

transfer and resonance assistance. *Chemistry-A European Journal*, 5(12):3581–3594, 1999. 3

[9] Wolfgang H Binder and Ronald Zirbs. Supramolecular polymers and networkswith hydrogen bonds in the main-and side-chain. In *Hydrogen bonded polymers*, pages 1–78. Springer, 2006. 4, 9

[10] Liulin Yang, Xinxin Tan, Zhiqiang Wang, and Xi Zhang. Supramolecular polymers: Historical development, preparation, characterization, and functions. *Chemical Reviews*, 0(0):null, 0. PMID: 25768045. 4

[11] Roland Bohhmer, Catalin Gainaru, and Ranko Richert. Structure and dynamics of monohydroxy alcohols¢milestones towards their microscopic understanding, 100years after debye. *Physics Reports*, 545(4):125 – 195, 2014. Structure and dynamics of monohydroxy alcohols¢Milestones towards their microscopic understanding, 100years after Debye. 4

[12] Roland Bhmer, Catalin Gainaru, and Ranko Richert. Structure and dynamics of monohydroxy alcoholsmilestones towards their microscopic understanding, 100years after debye. *Physics Reports*, (0). 4, 200

[13] Ranko Richert, Alexander Agapov, and Alexei P Sokolov. Appearance of a debye process at the conductivity relaxation frequency of a viscous liquid. *The Journal of chemical physics*, 134(10):104508, 2011. 4

[14] Christoph Klieber, Tina Hecksher, Thomas Pezeril, Darius H Torchinsky, Jeppe C Dyre, and Keith A Nelson. Mechanical spectra of glass-forming liquids. ii. gigahertz-frequency longitudinal and shear acoustic dynamics in glycerol and dc704 studied by time-domain brillouin scattering. *The Journal of chemical physics*, 138(12):12A544, 2013. 4

[15] Cecile Dalle-Ferrier, Stefan Eibl, Catherine Pappas, and Christiane Alba-Simionesco. Temperature dependence of three-point correlation functions of viscous liquids: the case of glycerol. *Journal of Physics: Condensed Matter*, 20(49):494240, 2008. 4

[16] C. Gainaru, S. Kastner, F. Mayr, P. Lunkenheimer, S. Schildmann, H. J. Weber, W. Hiller, A. Loidl, and R. Böhmer. Hydrogen-bond equilibria and lifetimes in a monohydroxy alcohol. *Phys. Rev. Lett.*, 107:118304, Sep 2011. 4, 5, 6

[17] Yangyang Wang, Philip J. Griffin, Adam Holt, Fei Fan, and Alexei P. Sokolov. Observation of the slow, debye-like relaxation in hydrogen-bonded liquids by dynamic light scattering. *The Journal of Chemical Physics*, 140(10):–, 2014. 4

[18] Justin L. MacCallum and D. Peter Tieleman. Structures of neat and hydrated 1-octanol from computer simulations. *Journal of the American Chemical Society*, 124(50):15085–15093, 2002. PMID: 12475354. 4

[19] M. A. Floriano and C. A. Angell. On the relaxation between debye and nonexponential relaxation in supercooled monohydric alcohols and water: A solution study. *The Journal of Chemical Physics*, 91(4):2537–2543, 1989. 4

[20] C. Gainaru, R. Meier, S. Schildmann, C. Lederle, W. Hiller, E. A. Rössler, and R. Böhmer. Nuclear-magnetic-resonance measurements reveal the origin of the debye process in monohydroxy alcohols. *Phys. Rev. Lett.*, 105:258303, Dec 2010. 5

[21] D. Fragiadakis, C. M. Roland, and R. Casalini. Insights on the origin of the debye process in monoalcohols from dielectric spectroscopy under extreme pressure conditions. *The Journal of Chemical Physics*, 132(14):–, 2010. 5

[22] F. X. Hassion and R. H. Cole. Dielectric properties of liquid ethanol and 2-propanol. *The Journal of Chemical Physics*, 23(10):1756–1761, 1955. 5

[23] Chelsea R Martinez and Brent L Iverson. Rethinking the term pi-stacking. *Chemical Science*, 3(7):2191–2201, 2012. 6, 171

[24] L Brunsveld, JAJM Vekemans, JHKK Hirschberg, RP Sijbesma, and EW Meijer. Hierarchical formation of helical supramolecular polymers via stacking of hydrogen-bonded pairs in water. *Proceedings of the National Academy of Sciences*, 99(8):4977–4982, 2002. 6

[25] T. Aida, E. W. Meijer, and S. I. Stupp. Functional supramolecular polymers. *Science*, 335(6070):813–817, 2012. 6

[26] Ruijiao Dong, Yongfeng Zhou, Xiaohua Huang, Xinyuan Zhu, Yunfeng Lu, and Jian Shen. Functional supramolecular polymers for biomedical applications. *Advanced Materials*, 27(3):498–526, 2015. 7

[27] Masato Ikeda, Tatsuya Tanida, Tatsuyuki Yoshii, and Itaru Hamachi. Rational molecular design of stimulus-responsive supramolecular hydrogels based on dipeptides. *Advanced Materials*, 23(25):2819–2822, 2011. 7

[28] Brigitte JB Folmer, RP Sijbesma, RM Versteegen, JAJ Van der Rijt, and EW Meijer. Supramolecular polymer materials: Chain extension of telechelic polymers using a reactive hydrogen-bonding synthon. *Advanced Materials*, 12(12):874–878, 2000. 7

[29] Rint P Sijbesma, Felix H Beijer, Luc Brunsveld, Brigitte JB Folmer, JHK Ky Hirschberg, Ronald FM Lange, Jimmy KL Lowe, and EW Meijer. Reversible polymers formed from self-complementary monomers using quadruple hydrogen bonding. *Science*, 278(5343):1601–1604, 1997. 15, 7, 8

[30] H. Hofmeier, R. Hoogenboom, M. E. L. Wouters, and U. S. Schubert. High molecular weight supramolecular polymers containing both terpyridine metal complexes and ureidopyrimidinone quadruple hydrogen-bonding units in the main chain. *Journal of the American Chemical Society*, 127(9):2913–2921, 2005. 7, 137

[31] Parvin Shokrollahi. Supramolecular poly (tetrahydrofuran) based on a pyrimidinone associating motif. *Iran. Polym. J*, 19:65–74, 2010. 15, 7, 8

[32] P Dreyfuss and M Dreyfuss. Polytetrahydrofuran. *Fortschritte der Hochpolymeren-Forschung*, pages 528–590, 1967. 7, 161, 202, 203

[33] Rint P. Sijbesma, Felix H. Beijer, Luc Brunsveld, Brigitte J. B. Folmer, J. H. K. Ky Hirschberg, Ronald F. M. Lange, Jimmy K. L. Lowe, and E. W. Meijer.

Reversible polymers formed from self-complementary monomers using quadruple hydrogen bonding. *Science*, 278(5343):1601–1604, 1997. 7, 98, 99, 137, 163, 169, 176, 180

[34] Johan Mattsson, Rikard Bergman, Per Jacobsson, and Lars Börjesson. Effects of hydrogen bonding on supercooled liquid dynamics and the implications for supercooled water. *Physical Review B*, 79(17):174205, 2009. 8

[35] George Odian. *Principles of polymerization*. John Wiley & Sons, 2004. 9

[36] Jiahui Li, Kelley D Sullivan, Edward B Brown, and Mitchell Anthamatten. Thermally activated diffusion in reversibly associating polymers. *Soft Matter*, 6(2):235–238, 2010. 9

[37] Serge HM Söntjens, Rint P Sijbesma, Marcel HP van Genderen, and EW Meijer. Stability and lifetime of quadruply hydrogen bonded 2-ureido-4 [1 h]-pyrimidinone dimers. *Journal of the American Chemical Society*, 122(31):7487–7493, 2000. 9

[38] Takashi Kato, Masahisa Nakano, Tomonori Moteki, Toshiyuki Uryu, and Seiji Ujiie. Supramolecular liquid-crystalline side-chain polymers built through a molecular recognition process by double hydrogen bonds. *Macromolecules*, 28(26):8875–8876, 1995. 15, 9, 10

[39] Takashi Kato, Hideyuki Kihara, Uday Kumar, Toshiyuki Uryu, and Jean MJ Fréchet. A liquid-crystalline polymer network built by molecular self-assembly through intermolecular hydrogen bonding. *Angewandte Chemie International Edition*, 33(15-16):1644–1645, 1994. 9

[40] Baolei Zhu, Nils Jasinski, Alejandro Benitez, Manuel Noack, Daesung Park, Anja S Goldmann, Christopher Barner-Kowollik, and Andreas Walther. Hierarchical nacre mimetics with synergistic mechanical properties by control of molecular interactions in self-healing polymers. *Angewandte Chemie International Edition*, 54(30):8653–8657, 2015. 15, 9, 10

[41] Marcus Weck. Side-chain functionalized supramolecular polymers. *Polymer international*, 56(4):453–460, 2007. 9

[42] Kathleen E Feldman, Matthew J Kade, EW Meijer, Craig J Hawker, and Edward J Kramer. Model transient networks from strongly hydrogen-bonded polymers. *Macromolecules*, 42(22):9072–9081, 2009. 15, 9, 10

[43] Jiaxi Cui, Dapeng Wang, Kaloian Koynov, and Aránzazu del Campo. 2-ureido-4-pyrimidone-based hydrogels with multiple responses. *ChemPhysChem*, 14(13):2932–2938, 2013. 9

[44] Mary J Cloninger. Biological applications of dendrimers. *Current opinion in chemical biology*, 6(6):742–748, 2002. 11

[45] Woo-Dong Jang, KM Kamruzzaman Selim, Chi-Hwa Lee, and Inn-Kyu Kang. Bioinspired application of dendrimers: from bio-mimicry to biomedical applications. *Progress in Polymer Science*, 34(1):1–23, 2009. 11

[46] George Richard Newkome, Charles N Moorefield, Fritz Vögtle, Fritz Vögtle, Fritz Vögtle, and Germany Chemist. *Dendrimers and dendrons: concepts, syntheses, applications*, volume 623. Wiley Online Library, 2001. 11

[47] Owen A Matthews, Andrew N Shipway, and J Fraser Stoddart. Dendrimers-branching out from curiosities into new technologies. *Progress in polymer science*, 23(1):1–56, 1998. 16, 11, 12

[48] Manabu Kawa and Jean MJ Fréchet. Self-assembled lanthanide-cored dendrimer complexes: enhancement of the luminescence properties of lanthanide ions through site-isolation and antenna effects. *Chemistry of Materials*, 10(1):286–296, 1998. 16, 11, 12

[49] Chie Kojima. Design of stimuli-responsive dendrimers. *Expert opinion on drug delivery*, 7(3):307–319, 2010. 12

[50] Paul J Flory. *Principles of polymer chemistry*. Cornell University Press, 1953. 13, 14, 15, 16, 17, 102

[51] Abraham Ravve. *Principles of polymer chemistry*. Springer Science & Business Media, 2013. 13, 14, 15, 16

[52] Michael Rubinstein and Ralph H Colby. *Polymer physics*, volume 23. Oxford University Press New York, 2003. 13, 23, 24, 25, 26, 27, 30, 33, 67, 208, 209, 210, 211, 214, 218

[53] Marcel Van Beylen, Stanley Bywater, Georges Smets, Michael Szwarc, and Denis J Worsfold. Developments in anionic polymerizationa critical review. In *Polysiloxane Copolymers/Anionic Polymerization*, pages 87–143. Springer, 1988. 13, 14

[54] Sadahito Aoshima and Shokyoku Kanaoka. A renaissance in living cationic polymerization. *Chemical reviews*, 109(11):5245–5287, 2009. 13

[55] Andrew Gregory and Martina H Stenzel. Complex polymer architectures via raft polymerization: From fundamental process to extending the scope using click chemistry and nature's building blocks. *Progress in Polymer Science*, 37(1):38–105, 2012. 15

[56] Krzysztof Matyjaszewski and Jianhui Xia. Atom transfer radical polymerization. *Chemical reviews*, 101(9):2921–2990, 2001. 15, 17

[57] Eite Drent and Peter HM Budzelaar. Palladium-catalyzed alternating copolymerization of alkenes and carbon monoxide. *Chemical reviews*, 96(2):663–682, 1996. 16

[58] Kevin Letchford and Helen Burt. A review of the formation and classification of amphiphilic block copolymer nanoparticulate structures: micelles, nanospheres, nanocapsules and polymersomes. *European journal of pharmaceutics and biopharmaceutics*, 65(3):259–269, 2007. 16

[59] Alexander H Soeriyadi, Cyrille Boyer, Fredrik Nystrom, Per B Zetterlund, and Michael R Whittaker. High-order multiblock copolymers via iterative cu (0)-mediated radical polymerizations (set-lrp): toward biological precision. *Journal of the American Chemical Society*, 133(29):11128–11131, 2011. 16

[60] Faheem Amir, Zhongfan Jia, and Michael J Monteiro. Sequence control of macromers via iterative sequential and exponential growth. *Journal of the American Chemical Society*, 138(51):16600–16603, 2016. 16

[61] Cameron C Lee, John A MacKay, Jean MJ Fréchet, and Francis C Szoka. Designing dendrimers for biological applications. *Nature biotechnology*, 23(12):1517–1526, 2005. 16

[62] Ludwik Leibler. Theory of microphase separation in block copolymers. *Macromolecules*, 13(6):1602–1617, 1980. 16

[63] Charles Gebelein and F Koblitz. *Biomedical and dental applications of polymers*, volume 14. Springer Science & Business Media, 2013. 16

[64] Ahmed Akelah and Abdelsamie Moet. *Functionalized polymers and their applications*. Springer, 1990. 16

[65] Raymond B Seymour and Charles E Carraher. *Polymer chemistry*, volume 181. Marcel Dekker New York, 2000. 17, 18, 19

[66] Graeme Moad, Y. K. Chong, Almar Postma, Ezio Rizzardo, and San H. Thang. Advances in raft polymerization: the synthesis of polymers with defined end-groups. *Polymer*, 46(19):8458–8468, 2005. 17, 21

[67] G. Moad, E. Rizzardo, and S. H. Thang. Living radical polymerization by the raft process a second update. *Australian Journal of Chemistry*, 62(11):1402–1472, 2009. 17, 18, 20, 21, 22, 98, 141

[68] Graeme Moad, Ezio Rizzardo, and San H. Thang. Raft polymerization and some of its applications. *Chemistry An Asian Journal*, 8(8):1634–1644, 2013. 17, 18, 21, 22

[69] Ezio Rizzardo, Ming Chen, Bill Chong, Graeme Moad, Melissa Skidmore, and San H. Thang. Raft polymerization: Adding to the picture. *Macromolecular Symposia*, 248(1):104–116, 2007. 17, 21, 141

[70] Zhengbiao Zhang, Wenxiang Wang, Hongda Xia, Jian Zhu, Wei Zhang, and Xiulin Zhu. Single-electron transfer living radical polymerization (set- lrp) of methyl methacrylate (mma) with a typical raft agent as an initiator. *Macromolecules*, 42(19):7360–7366, 2009. 17

[71] Brad M Rosen and Virgil Percec. Single-electron transfer and single-electron transfer degenerative chain transfer living radical polymerization. *Chemical reviews*, 109(11):5069–5119, 2009. 17

[72] Damien Quémener, Thomas P Davis, Christopher Barner-Kowollik, and Martina H Stenzel. Raft and click chemistry: A versatile approach to well-defined block copolymers. *Chemical communications*, (48):5051–5053, 2006. 17

[73] John Chiefari, YK Chong, Frances Ercole, Julia Krstina, Justine Jeffery, Tam PT Le, Roshan TA Mayadunne, Gordon F Meijs, Catherine L Moad, Graeme Moad, et al. Living free-radical polymerization by reversible addition- fragmentation chain transfer: the raft process. *Macromolecules*, 31(16):5559–5562, 1998. 20, 21

[74] Jared Skey and Rachel K. O'Reilly. Facile one pot synthesis of a range of reversible addition-fragmentation chain transfer (raft) agents. *Chemical Communications*, (35):4183–4185, 2008. 20

[75] Frank H Allen, Olga Kennard, David G Watson, Lee Brammer, A Guy Orpen, and Robin Taylor. Tables of bond lengths determined by x-ray and neutron diffraction. part 1. bond lengths in organic compounds. *Journal of the Chemical Society, Perkin Transactions 2*, (12):S1–S19, 1987. 23

[76] W. R. Sorenson. Reaction of an isocyanate and a carboxylic acid in dimethyl sulfoxide. *The Journal of Organic Chemistry*, 24(7):978–980, 1959. 23

[77] ARLPJ Abe, RL Jernigan, and PJ Flory. Conformational energies of n-alkanes and the random configuration of higher homologs including polymethylene. *Journal of the American Chemical Society*, 88(4):631–639, 1966. 25

[78] DY Yoon, PR Sundararajan, and PJ Flory. Conformational characteristics of polystyrene. *Macromolecules*, 8(6):776–783, 1975. 25

[79] LJ Fetters, DJ Lohse, and RH Colby. Chain dimensions and entanglement spacings. *Physical properties of polymers handbook*, 2:445–452, 2007. 26

[80] Robert Byron Bird, Robert Calvin Armstrong, Ole Hassager, and Charles F Curtiss. *Dynamics of polymeric liquids*, volume 1. Wiley New York, 1977. 26, 27

[81] PG De Gennes. Dynamics of entangled polymer solutions. i. the rouse model. *Macromolecules*, 9(4):587–593, 1976. 27

[82] Prince E Rouse Jr. A theory of the linear viscoelastic properties of dilute solutions of coiling polymers. *The Journal of Chemical Physics*, 21(7):1272–1280, 1953. 26, 28

[83] Masao Doi. Explanation for the 3.4 power law of viscosity of polymeric liquids on the basis of the tube model. *Journal of Polymer Science Part C-Polymer Letters*, 19(5):265–273, 1981. 30, 33, 203, 208, 209

[84] Masao Doi and Samuel Frederick Edwards. *The theory of polymer dynamics*, volume 73. oxford university press, 1988. 30, 203

[85] J. Clerk Maxwell. On the dynamical theory of gases. *Philosophical Transactions of the Royal Society of London*, 157:pp. 49–88, 1867. 33, 208

[86] Ludwik Leibler, Michael Rubinstein, and Ralph H Colby. Dynamics of reversible networks. *Macromolecules*, 24(16):4701–4707, 1991. 34

[87] LG Baxandall. Dynamics of reversibly crosslinked chains. *Macromolecules*, 22(4):1982–1988, 1989.

[88] Michael Rubinstein and Alexander N Semenov. Dynamics of entangled solutions of associating polymers. *Macromolecules*, 34(4):1058–1068, 2001. 34

[89] Michael Rubinstein and Alexander N Semenov. Thermoreversible gelation in solutions of associating polymers. 2. linear dynamics. *Macromolecules*, 31(4):1386–1397, 1998. 34

[90] MS Green and AV Tobolsky. A new approach to the theory of relaxing polymeric media. *The Journal of Chemical Physics*, 14(2):80–92, 1946. 34

[91] M. D. Ediger, C. A. Angell, and Sidney R. Nagel. Supercooled liquids and glasses. *The Journal of Physical Chemistry*, 100(31):13200–13212, 1996. 35, 36, 37, 39

[92] Jeppe C. Dyre. Colloquium: The glass transition and elastic models of glass-forming liquids. *Rev. Mod. Phys.*, 78:953–972, Sep 2006. 35, 36, 37, 39, 40, 41

[93] So much more to know. *Science*, 309(5731):78–102, 2005. 35

[94] L Dagdug and L S Garca-Coln. Theoretical framework for the arrhenius equation in strong glasses. *J. Phys.: Condens. Matter*, 11:2193, 1999. 36, 38

[95] Walter. Kauzmann. The nature of the glassy state and the behavior of liquids at low temperatures. *Chemical Reviews*, 43(2):219–256, 1948. 17, 36, 37

[96] Frank H. Stillinger Pablo G. Debenedetti. Supercooled liquids and the glass transition. *Nature*, 410:,259–267, 2001. 17, 36, 37, 39

[97] K.L. Ngai. Dynamic and thermodynamic properties of glass-forming substances. *Journal of Non-Crystalline Solids*, 275(12):7 – 51, 2000. 37

[98] C. A. Angell, K. L. Ngai, G. B. McKenna, P. F. McMillan, and S. W. Martin. Relaxation in glassforming liquids and amorphous solids. *Journal of Applied Physics*, 88(6):3113–3157, 2000. 38

[99] Ludovic Berthier and Giulio Biroli. Theoretical perspective on the glass transition and amorphous materials. *Rev. Mod. Phys.*, 83:587–645, Jun 2011. 38

[100] C. A. Angell. Formation of glasses from liquids and biopolymers. *Science*, 267(5206):1924–1935, 1995. 38, 39, 221

[101] Axel DS, Gerald Hinze, Bernd Schiener, Joachim Hemberger, and Roland Bhmer. Dielectric relaxation in the fragile viscous liquid state of toluene. *The Journal of Chemical Physics*, 107(6):1740–1743, 1997. 39

[102] Roland Böhmer, KL Ngai, CA Angell, and DJ Plazek. Nonexponential relaxations in strong and fragile glass formers. *The Journal of chemical physics*, 99(5):4201–4209, 1993. 39

[103] KL Ngai. Dynamic and thermodynamic properties of glass-forming substances. *Journal of Non-Crystalline Solids*, 275(1):7–51, 2000.

[104] Hans Sillescu. Heterogeneity at the glass transition: a review. *Journal of Non-Crystalline Solids*, 243(2):81–108, 1999.

[105] Ernst-Joachim Donth. *The glass transition: relaxation dynamics in liquids and disordered materials*, volume 48. Springer Science & Business Media, 2013. 39, 40

[106] Morrel H Cohen and David Turnbull. Molecular transport in liquids and glasses. *The Journal of Chemical Physics*, 31(5):1164–1169, 1959. 39

[107] Gary S Grest and Morrel H Cohen. Liquids, glasses, and the glass transition: A free-volume approach. *Adv. Chem. Phys*, 48:455–525, 1981. 40

[108] Chuan Zhang and Rodney D Priestley. Fragility and glass transition temperature of polymer confined under isobaric and isochoric conditions. *Soft Matter*, 9(29):7076–7085, 2013. 40

[109] Gerold Adam and Julian H Gibbs. On the temperature dependence of cooperative relaxation properties in glass-forming liquids. *The journal of chemical physics*, 43(1):139–146, 1965. 40

[110] Osamu Yamamuro, Itaru Tsukushi, Anna Lindqvist, Shuichi Takahara, Mariko Ishikawa, and Takasuke Matsuo. Calorimetric study of glassy and liquid toluene and ethylbenzene: Thermodynamic approach to spatial heterogeneity in glass-forming molecular liquids. *The Journal of Physical Chemistry B*, 102(9):1605–1609, 1998. 41

[111] J Heijboer. Molecular origin of relaxations in polymers. *Annals of the New York Academy of Sciences*, 279(1):104–116, 1976. 41

[112] Gyan P Johari and Martin Goldstein. Viscous liquids and the glass transition. ii. secondary relaxations in glasses of rigid molecules. *The Journal of Chemical Physics*, 53(6):2372–2388, 1970. 41, 42

[113] Andreas Schnhals Friedrich Kremer. *Broadband Dielectric Spectroscopy*. Springer, 2002. 41

[114] U Buchenau. Energy landscape-a key concept in the dynamics of liquids and glasses. *Journal of Physics: Condensed Matter*, 15(11):S955, 2003. 42

[115] Daniel Lindley Baker. *Relaxation dynamics in molecular glass-formers with systematic structure modifications*. PhD thesis, University of Leeds, 2014. 42, 45, 49, 52, 219

[116] P Lunkenheimer, U Schneider, R Brand, and A Loid. Glassy dynamics. *Contemporary Physics*, 41(1):15–36, 2000. 44, 80, 86

[117] A Schönhals and F Kremer. Broadband dielectric spectroscopy. Springer, 2003. 45, 46, 47, 48, 49, 52, 55, 56, 69

[118] CJF Bötther and P Bordewijk. Theory of electric polarisation, 1973. 45, 46, 47, 49

[119] John J Fitzgerald and James P Runt. *Dielectric Spectroscopy of Polymeric Materials: Fundamentals and Applications*. American Chemical Society, 1997. 45

[120] Catalin P Gainaru. *Dielectric Properties of Molecular Glass Formers; from the Liquid State to the Tunneling Regime*. PhD thesis, 2008. 45, 47, 48

[121] Thomas Blochowicz. *Broadband Dielectric Spectroscopy in Neat and Binary Molecular Glass Formers: Frequency and Time Domain Spectroscopy, Nonresonant Spectral Hole Burning*. Logos Verlag Berlin, 2003. 45, 47

[122] John G Kirkwood. The dielectric polarization of polar liquids. *The Journal of Chemical Physics*, 7(10):911–919, 1939. 45, 46

[123] TW Dakin. Conduction and polarization mechanisms and trends in dielectric. *IEEE Electrical Insulation Magazine*, 22(5):11–28, 2006. 45, 48, 49, 56

[124] Lars Onsager. Electric moments of molecules in liquids. *Journal of the American Chemical Society*, 58(8):1486–1493, 1936. 45, 46

[125] R Bergman. General susceptibility functions for relaxations in disordered systems. *Journal of Applied Physics*, 88(3):1356–1365, 2000. 49

[126] Kenneth S Cole and Robert H Cole. Dispersion and absorption in dielectrics i. alternating current characteristics. *The Journal of chemical physics*, 9(4):341–351, 1941. 51

[127] Donald W Davidson and Robert H Cole. Dielectric relaxation in glycerol, propylene glycol, and n-propanol. *The Journal of Chemical Physics*, 19(12):1484–1490, 1951. 51

[128] S Havriliak and S Negami. A complex plane representation of dielectric and mechanical relaxation processes in some polymers. *Polymer*, 8:161–210, 1967. 51

[129] S Havriliak and SJ Havriliak. Results from an unbiased analysis of nearly 1000 sets of relaxation data. *Journal of non-crystalline solids*, 172:297–310, 1994. 51

[130] G Katana, F Kremer, Erhard W Fischer, and R Plaetschke. Broadband dielectric study on binary blends of bisphenol-a and tetramethylbisphenol-a polycarbonate. *Macromolecules*, 26(12):3075–3080, 1993. 52, 56

[131] Ingvar Albinsson. *Dielectric and conductivity studies of polymer electrolytes*. Chalmers University of Technology, 1994. 53, 54

[132] Andrew K Jonscher. Dielectric relaxation in solids. *Journal of Physics D: Applied Physics*, 32(14):R57, 1999. 54

[133] Ronald G Larson. *The structure and rheology of complex fluids*, volume 150. Oxford university press New York, 1999. 57, 61, 70

[134] John D Ferry. *Viscoelastic properties of polymers*. John Wiley & Sons, 1980. 57, 61, 62, 65, 66, 68, 69, 71, 72, 118, 122, 138

[135] Thomas Mezger. *Applied Rheology With Joe Flow on Rheology Road*. Anton Paar, 2015. 57, 58, 61, 63, 66, 69, 70, 71, 72, 73, 74, 75, 76

[136] William Walter Graessley. *Polymeric liquids and networks: dynamics and rheology*. Garland Science, 2008. 57, 60, 64, 65, 66, 75

[137] Marnix Van Gurp and Jo Palmen. Time-temperature superposition for polymeric blends. *Rheol. Bull*, 67(1):5–8, 1998. 68, 105, 144

[138] Stefan Trinkle and Christian Friedrich. Van gurp-palmen-plot: a way to characterize polydispersity of linear polymers. *Rheologica Acta*, 40(4):322–328, 2001. 68, 105, 144

[139] M Shinozuka. Thermorheologically simple viscoelastic materials. *AIAA Journal*, 3(2):375–377, 1965. 68, 116, 138, 178

[140] Florian J Stadler, Wim Pyckhout-Hintzen, Jean-Marc Schumers, Charles-Andre Fustin, Jean-François Gohy, and Christian Bailly. Linear viscoelastic rheology of moderately entangled telechelic polybutadiene temporary networks. *Macromolecules*, 42(16):6181–6192, 2009. 68, 97, 138, 139

[141] Donald J. Plazek. Temperature dependence of the viscoelastic behavior of polystyrene. *The Journal of Physical Chemistry*, 69(10):3480–3487, 1965.

[142] Donald J. Plazek. The temperature dependence of the viscoelastic behavior of poly(vinyl acetate). *Polym J*, 12(1):43–53, 1980.

[143] D. J. Plazek, I. C. Chay, K. L. Ngai, and C. M. Roland. Viscoelastic properties of polymers. 4. thermorheological complexity of the softening dispersion in polyisobutylene. *Macromolecules*, 28(19):6432–6436, 1995. 116, 178

[144] Yifu Ding and Alexei P. Sokolov. Breakdown of timetemperature superposition principle and universality of chain dynamics in polymers. *Macromolecules*, 39(9):3322–3326, 2006. 68, 116, 138, 178

[145] Manlio Tassieri, Marco Laurati, Dan J. Curtis, Dietmar W. Auhl, Salvatore Coppola, Andrea Scalfati, Karl Hawkins, Phylip Rhodri Williams, and Jonathan M. Cooper. i-rheo: Measuring the materials linear viscoelastic properties in a step! *Journal of Rheology*, 60(4):649–660, 2016. 22, 73, 106, 117, 146

[146] H Lentzakis, D Vlassopoulos, DJ Read, H Lee, T Chang, P Driva, and N Hadjichristidis. Uniaxial extensional rheology of well-characterized comb polymers. *Journal of Rheology*, 57(2):605–625, 2013. 75

[147] FN Cogswell. Measuring the extensional rheology of polymer melts. *Transactions of the Society of Rheology*, 16(3):383–403, 1972. 75

[148] Aamir Shabbir. *Rheology of Supramolecular Polymers*. PhD thesis, Technical University of Denmark, 2016. 76

[149] Günther Höhne, Wolfgang F Hemminger, and H-J Flammersheim. *Differential scanning calorimetry*. Springer Science & Business Media, 2013. 77, 78

[150] Ernesto Freire. Differential scanning calorimetry. *Protein Stability and Folding: Theory and Practice*, pages 191–218, 1995. 77, 80

[151] P Gill, S Sauerbrunn, and M Reading. Modulated differential scanning calorimetry. *Journal of thermal analysis and calorimetry*, 40(3):931–939, 1993. 77, 80

[152] Bernhard Wunderlich, Yimin Jin, and Andreas Boller. Mathematical description of differential scanning calorimetry based on periodic temperature modulation. *Thermochimica acta*, 238:277–293, 1994. 77, 83

[153] Sindee L Simon. Temperature-modulated differential scanning calorimetry: theory and application. *Thermochimica acta*, 374(1):55–71, 2001. 77, 80, 81, 82, 84, 85, 86

[154] TA Instruments. Thermal analysis & rheology. *Auto DSC System*, 1998. 79, 83, 84

[155] Johan Sjostrom, Johan Mattsson, Rikard Bergman, and Jan Swenson. Hydrogen bond induced nonmonotonic composition behavior of the glass transition in aqueous binary mixtures. *The Journal of Physical Chemistry B*, 115(33):10013–10017, 2011. 79, 124, 172

[156] Dilip Kondepudi. *Introduction to modern thermodynamics*. Wiley, 2008. 79, 172

[157] Tao Xie and Ingrid A Rousseau. Facile tailoring of thermal transition temperatures of epoxy shape memory polymers. *Polymer*, 50(8):1852–1856, 2009. 80

[158] Hideki Yamasaki and Shigeaki Morita. Temperature dependence of isothermal curing reaction of epoxy resin studied by modulated differential scanning calorimetry and infrared spectroscopy. *Journal of Molecular Structure*, 1124:249–255, 2016. 80, 85

[159] Arne Hensel and Christoph Schick. Relation between freezing-in due to linear cooling and the dynamic glass transition temperature by temperature-modulated dsc. *Journal of non-crystalline solids*, 235:510–516, 1998. 80, 86, 221, 224

[160] S Weyer, A Hensel, and Ch Schick. Phase angle correction for tmdsc in the glass-transition region. *Thermochimica acta*, 304:267–275, 1997. 20, 84, 85, 86

[161] Peter Hore. *Nuclear magnetic resonance*. Oxford University Press, USA, 2015. 87, 89, 90, 91, 92, 94

[162] Malcolm H Levitt. *Spin dynamics: basics of nuclear magnetic resonance*. John Wiley & Sons, 2001. 87, 88, 89, 90, 91, 92

[163] Asanah Radhi. *NMR studies of cellulose dissolution in ionic liquids*. PhD thesis, University of Leeds, 2014. 87, 94

[164] Nicolaas Bloembergen, Edward Mills Purcell, and Robert V Pound. Relaxation effects in nuclear magnetic resonance absorption. *Physical review*, 73(7):679, 1948. 93

[165] Senbin Chen and Wolfgang H. Binder. Dynamic ordering and phase segregation in hydrogen-bonded polymers. *Accounts of Chemical Research*, 49(7):1409–1420, 2016. 97, 137

[166] B. J. B. Folmer, R. P. Sijbesma, R. M. Versteegen, J. A. J. van der Rijt, and E. W. Meijer. Supramolecular polymer materials: Chain extension of telechelic polymers using a reactive hydrogen-bonding synthon. *Advanced Materials*, 12(12):874–878, 2000. 98, 99, 115, 137, 163, 169, 176, 180

[167] Traian V Chirila, Hui Hui Lee, Mathieu Oddon, Marko ML Nieuwenhuizen, Idriss Blakey, and Timothy M Nicholson. Hydrogen-bonded supramolecular polymers as self-healing hydrogels: Effect of a bulky adamantyl substituent in the ureido-pyrimidinone monomer. *Journal of Applied Polymer Science*, 131(4):39932, 2014. 98, 194

[168] Shiao-Wei Kuo and Hsin-Tung Tsai. Self-complementary multiple hydrogen bonding interactions increase the glass transition temperatures to supramolecular poly(methyl methacrylate) copolymers. *Journal of Applied Polymer Science*, 123(6):3275–3282, 2012. 98, 99

[169] Johan Sjostrom, Johan Mattsson, Rikard Bergman, and Jan Swenson. Hydrogen bond induced nonmonotonic composition behavior of the glass transition in aqueous binary mixtures. *Journal of Physical Chemistry B*, 115(33):10013–10017, 2011.

[170] Mingyu Guo, Louis M. Pitet, Hans M. Wyss, Matthijn Vos, Patricia Y. W. Dankers, and E. W. Meijer. Tough stimuli-responsive supramolecular hydrogels with hydrogen-bonding network junctions. *Journal of the American Chemical Society*, 136(19):6969–6977, 2014. 97, 98, 137

[171] Taylor Ware, Keith Hearon, Alexander Lonnecker, Karen L. Wooley, Duncan J. Maitland, and Walter Voit. Triple-shape memory polymers based on self-complementary hydrogen bonding. *Macromolecules*, 45(2):1062–1069, 2012.

[172] L Brunsveld, JAJM Vekemans, JHKK Hirschberg, RP Sijbesma, and EW Meijer. Hierarchical formation of helical supramolecular polymers via stacking of

hydrogen-bonded pairs in water. *Proceedings of the National Academy of Sciences*, 99(8):4977–4982, 2002. 97, 114, 137, 170

[173] Lucia Carlucci, Gianfranco Ciani, Davide M. Proserpio, and Silvia Rizzato. New polymeric networks from the self-assembly of silver(i) salts and the flexible ligand 1,3-bis(4-pyridyl)propane (bpp). a systematic investigation of the effects of the counterions and a survey of the coordination polymers based on bpp. *CrystEngComm*, 4(22):121, 2002. 97

[174] S. J. Rowan and J. B. Beck. Metal-ligand induced supramolecular polymerization: a route to responsive materials. *Faraday Discuss*, 128:43–53, 2005. 98, 137

[175] R. Shunmugam, G. J. Gabriel, K. A. Aamer, and G. N. Tew. Metal-ligand-containing polymers: terpyridine as the supramolecular unit. *Macromol Rapid Commun*, 31(9-10):784–93, 2010. 137

[176] Metal/ligand-induced formation of metallo-supramolecular polymers. *Macromolecules*, 38,:5060–5068, 2005.

[177] Atsushi Noro, Satoru Matsushima, Xudong He, Mikihiro Hayashi, and Yushu Matsushita. Thermoreversible supramolecular polymer gels via metalligand coordination in an ionic liquid. *Macromolecules*, 46(20):8304–8310, 2013.

[178] Richard Hoogenboom, Jurriaan Huskens, and Ulrich S. Schubert. Grid forming metal coordinating macroligands: Synthesis and complexation. 928:63–71, 2006. 97, 137

[179] Konstantinos N. Raftopoulos and Krzysztof Pielichowski. Segmental dynamics in hybrid polymer/poss nanomaterials. *Progress in Polymer Science*, 52:136–187, 2016. 97

[180] Weian Zhang and Axel H. E. Mller. Architecture, self-assembly and properties of well-defined hybrid polymers based on polyhedral oligomeric silsequioxane (poss). *Progress in Polymer Science*, 38(8):1121–1162, 2013. 97

[181] Quan Chen, Hanqing Masser, Huai-Suen Shiau, Siwei Liang, James Runt, Paul C. Painter, and Ralph H. Colby. Linear viscoelasticity and fourier transform infrared spectroscopy of polyetherestersulfonate copolymer ionomers. *Macromolecules*, 47(11):3635–3644, 2014. 97, 137

[182] Gerald H Ling, Yangyang Wang, and RA Weiss. Linear viscoelastic and uniaxial extensional rheology of alkali metal neutralized sulfonated oligostyrene ionomer melts. *Macromolecules*, 45(1):481–490, 2011. 140

[183] Gerald H. Ling, Yangyang Wang, and R. A. Weiss. Linear viscoelastic and uniaxial extensional rheology of alkali metal neutralized sulfonated oligostyrene ionomer melts. *Macromolecules*, 45(1):481–490, 2012. 137

[184] Quan Chen, Gregory J. Tudryn, and Ralph H. Colby. Ionomer dynamics and the sticky rouse model. *Journal of Rheology*, 57(5):1441–1462, 2013. 97, 105, 119, 120, 137, 139, 150, 151, 188

[185] Sebastian Hackelbusch, Torsten Rossow, Peter van Assenbergh, and Sebastian Seiffert. Chain dynamics in supramolecular polymer networks. *Macromolecules*, 46(15):6273–6286, 2013. 97, 119

[186] Aamir Shabbir, Irakli Javakhishvili, Silvina Cerveny, Sren Hvilsted, Anne L. Skov, Ole Hassager, and Nicolas J. Alvarez. Linear viscoelastic and dielectric relaxation response of unentangled upy-based supramolecular networks. *Macromolecules*, 49(10):3899–3910, 2016. 99, 118, 119, 138, 139, 150, 151, 180

[187] Florian J. Stadler, Wim Pyckhout-Hintzen, Jean-Marc Schumers, Charles-Andr Fustin, Jean-Franois Gohy, and Christian Bailly. Linear viscoelastic rheology of moderately entangled telechelic polybutadiene temporary networks. *Macromolecules*, 42(16):6181–6192, 2009. 137

[188] Hadi Goldansaz, Evelyne van Ruymbeke, Jean-Franois Gohy, Charles-Andr Fustin, Michael E. Ries, and Christian Bailly. Local molecular dynamics and heterogeneity in peonicl2 supramolecular networks. *Macromolecules*, 48(7):2290–2298, 2015.

[189] Torsten Rossow, Axel Habicht, and Sebastian Seiffert. Relaxation and dynamics in transient polymer model networks. *Macromolecules*, 2014. 119, 180

[190] Keisuke Chino and Makoto Ashiura. Themoreversible cross-linking rubber using supramolecular hydrogen-bonding networks. *Macromolecules*, 34(26):9201–9204, 2001. 97, 137

[191] Jiaxi Cui, Dapeng Wang, Kaloian Koynov, and Arnzazu del Campo. 2-ureido-4-pyrimidone-based hydrogels with multiple responses. *ChemPhysChem*, 14(13):2932–2938, 2013. 97, 98, 137

[192] A. Matic, J. Mattsson, and R. Bergman. *Dynamics around the sol-gel transition in thermoreversible atactic polystyrene gels*, volume 708 of *Aip Conference Proceedings*, pages 72–75. 2004. 98

[193] Sona Sivakova, David A Bohnsack, Michael E Mackay, Phiriyatorn Suwanmala, and Stuart J Rowan. Utilization of a combination of weak hydrogen-bonding interactions and phase segregation to yield highly thermosensitive supramolecular polymers. *Journal of the American Chemical Society*, 127(51):18202–18211, 2005. 97, 98, 137

[194] M. Muluneh, J. Sprakel, H. M. Wyss, J. Mattsson, and D. A. Weitz. Direct visualization of ph-dependent evolution of structure and dynamics in microgel suspensions. *Journal of Physics-Condensed Matter*, 23(50), 2011. 97

[195] A. Prabhakar, D. K. Chattopadhyay, B. Jagadeesh, and K. V. S. N. Raju. Structural investigations of polypropylene glycol (ppg) and isophorone diisocyanate (ipdi)-based polyurethane prepolymer by 1d and 2d nmr spectroscopy. *Journal of Polymer Science Part A: Polymer Chemistry*, 43(6):1196–1209, 2005.

[196] Bas G. G. Lohmeijer and Ulrich S. Schubert. Water-soluble building blocks for terpyridine-containing supramolecular polymers: Synthesis, complexation, and ph stability studies of poly(ethylene oxide) moieties. *Macromolecular Chemistry and Physics*, 204(8):1072–1078, 2003. 97

[197] A Arbe, A-C Genix, J Colmenero, D Richter, and P Fouquet. Anomalous relaxation of self-assembled alkyl nanodomains in high-order poly (n-alkyl methacrylates). *Soft Matter*, 4(9):1792–1795, 2008. 98, 108

[198] V Arrighi, A Triolo, IJ McEwen, P Holmes, R Triolo, and H Amenitsch. Observation of local order in poly (di-n-alkyl itaconate) s. *Macromolecules*, 33(14):4989–4991, 2000. 98, 108

[199] Mario Beiner. Relaxation in poly(alkyl methacrylate)s: crossover region and nanophase separation. *Macromolecular rapid communications*, 22(12):869–895, 2001. 108, 122

[200] Arantxa Arbe, A-C Genix, Silvia Arrese-Igor, J Colmenero, and Dieter Richter. Dynamics in poly (n-alkyl methacrylates): a neutron scattering, calorimetric, and dielectric study. *Macromolecules*, 43(6):3107–3119, 2010. 98, 108, 109, 110, 122

[201] Christine Gerstl, Martin Brodeck, GJ Schneider, Y Su, J Allgaier, A Arbe, J Colmenero, and D Richter. Short and intermediate range order in poly (alkylene oxide) s. a neutron diffraction and molecular dynamics simulation study. *Macromolecules*, 45(17):7293–7303, 2012. 108, 109, 110, 111

[202] Xiaojun He, Jinrong Wu, Guangsu Huang, and Xiaoan Wang. Effect of alkyl side chain length on relaxation behaviors in poly(n-alkyl acrylates) and poly(n-alkyl methacrylates). *Journal of Macromolecular Science, Part B*, 50(1):188–200, 2010. 108, 110, 112

[203] Mario Beiner and Heiko Huth. Nanophase separation and hindered glass transition in side-chain polymers. *Nat Mater*, 2(9):595–599, 2003. 98, 108, 110, 112, 122, 132

[204] S Hiller, O Pascui, H Budde, O Kabisch, D Reichert, and M Beiner. Nanophase separation in side chain polymers: new evidence from structure and dynamics. *New Journal of Physics*, 6(1):10, 2004. 98, 108, 110

[205] Reid J Chesterfield, John C McKeen, Christopher R Newman, Paul C Ewbank, Demétrio A da Silva Filho, Jean-Luc Brédas, Larry L Miller, Kent R Mann, and C Daniel Frisbie. Organic thin film transistors based on n-alkyl perylene diimides: charge transport kinetics as a function of gate voltage and temperature. *The Journal of Physical Chemistry B*, 108(50):19281–19292, 2004. 98

[206] J Penfold, E Staples, S Ugazio, I Tucker, L Soubiran, J Hubbard, M Noro, B O'Malley, A Ferrante, G Ford, et al. The microstructure of di-alkyl chain cationic/nonionic surfactant mixtures: observation of coexisting lamellar and micellar phases and depletion induced phase separation. *The Journal of Physical Chemistry B*, 109(38):18107–18116, 2005. 98

[207] Holger Spanggaard and Frederik C Krebs. A brief history of the development of organic and polymeric photovoltaics. *Solar Energy Materials and Solar Cells*, 83(2):125–146, 2004. 98

[208] Rui-Qi Png, Perq-Jon Chia, Jie-Cong Tang, Bo Liu, Sankaran Sivaramakrishnan, Mi Zhou, Siong-Hee Khong, Hardy SO Chan, Jeremy H Burroughes, Lay-Lay Chua, et al. High-performance polymer semiconducting heterostructure devices by nitrene-mediated photocrosslinking of alkyl side chains. *Nature materials*, 9(2):152, 2010. 98

[209] Alessandra Micoli, Marko Nieuwenhuizen, Marcel Koenigs, Mildred Quintana, Rint Sijbesma, and Maurizio Prato. Supramolecular macrostructures of upy-functionalized carbon nanotubes. *Chemistry A European Journal*, 21(40):14179–14185, 2015. 98

[210] Koji Yamauchi, Jeremy R. Lizotte, and Timothy E. Long. Thermoreversible poly(alkyl acrylates) consisting of self-complementary multiple hydrogen bonding. *Macromolecules*, 36(4):1083–1088, 2003. 98, 99, 100, 102, 119

[211] Raghunath P. Ingale, Ramanand N. Jagtap, and Ravindra V. Adivarekar. Effect of molecular weight on performance properties of pressure-sensitive adhesive of poly (2-ethylhexyl acrylate) synthesized by raft-mediated miniemulsion polymerization. *The Journal of Adhesion*, 92(3):236–256, 2016. 98, 100

[212] Sebastian Seiffert. Effect of supramolecular interchain sticking on the low-frequency relaxation of transient polymer networks. *Macromolecular Rapid Communications*, 37(3):257–264, 2016. 98, 139

[213] Kathleen E. Feldman, Matthew J. Kade, E. W. Meijer, Craig J. Hawker, and Edward J. Kramer. Model transient networks from strongly hydrogen-bonded polymers. *Macromolecules*, 42(22):9072–9081, 2009. 98, 99, 123, 138, 139, 150, 180

[214] Felix H. Beijer, Rint P. Sijbesma, Huub Kooijman, Anthony L. Spek, and E. W. Meijer. Strong dimerization of ureidopyrimidones via quadruple hydrogen bonding. *Journal of the American Chemical Society*, 120(27):6761–6769, 1998. 98, 112, 120, 137

[215] Serge H. M. Sntjens, Rint P. Sijbesma, Marcel H. P. van Genderen, and E. W. Meijer. Stability and lifetime of quadruply hydrogen bonded 2-ureido-4[1h]-pyrimidinone dimers. *Journal of the American Chemical Society*, 122(31):7487–7493, 2000. 98, 112, 120

[216] Leda Klouda and Antonios G Mikos. Thermoresponsive hydrogels in biomedical applications. *European Journal of Pharmaceutics and Biopharmaceutics*, 68(1):34–45, 2008. 98, 161

[217] Carina Osterwinter, Christian Schubert, Christoph Tonhauser, Daniel Wilms, Holger Frey, and Christian Friedrich. Rheological consequences of hydrogen bonding: Linear viscoelastic response of linear polyglycerol and its permethylated analogues as a general model for hydroxyl-functional polymers. *Macromolecules*, 2014.

[218] Y. Q. Zhao, J. B. Beck, S. J. Rowan, and A. M. Jamieson. Rheological behavior of shear-responsive metallo-supramolecular gels. *Macromolecules*, 37(10):3529–3531, 2004. 98

[219] Shentong Li, Fei Huo, Quanlong Li, Chengqiang Gao, Yang Su, and Wangqing Zhang. Synthesis of a doubly thermo-responsive schizophrenic diblock copolymer based on poly[n-(4-vinylbenzyl)-n,n-diethylamine] and its temperature-

sensitive flip-flop micellization. *Polymer Chemistry*, 5(12):3910–3918, 2014. 98, 137

[220] Min Wei, Miqin Zhan, Dongqin Yu, Hui Xie, Manjie He, Keke Yang, and Yuzhong Wang. Novel poly(tetramethylene ether)glycol and poly(-caprolactone) based dynamic network via quadruple hydrogen bonding with triple-shape effect and self-healing capacity. *ACS Applied Materials & Interfaces*, 7(4):2585–2596, 2015. 98, 137, 194

[221] Baolei Zhu, Nils Jasinski, Alejandro Benitez, Manuel Noack, Daesung Park, Anja S. Goldmann, Christopher Barner-Kowollik, and Andreas Walther. Hierarchical nacre mimetics with synergistic mechanical properties by control of molecular interactions in self-healing polymers. *Angewandte Chemie International Edition*, 54(30):8653–8657, 2015. 137

[222] Jiaxi Cui and Aranzazu del Campo. Multivalent h-bonds for self-healing hydrogels. *Chemical Communications*, 48(74):9302–9304, 2012.

[223] Florian Herbst, Diana Dhler, Philipp Michael, and Wolfgang H. Binder. Self-healing polymers via supramolecular forces. *Macromolecular Rapid Communications*, 34(3):203–220, 2013. 115

[224] Florian Herbst, Sebastian Seiffert, and Wolfgang H. Binder. Dynamic supramolecular poly(isobutylene)s for self-healing materials. *Polymer Chemistry*, 3(11):3084, 2012. 98, 137, 194

[225] Wilco P. J. Appel, Giuseppe Portale, Eva Wisse, Patricia Y. W. Dankers, and E. W. Meijer. Aggregation of ureido-pyrimidinone supramolecular thermoplastic elastomers into nanofibers: A kinetic analysis. *Macromolecules*, 44(17):6776–6784, 2011. 98, 114, 137, 163, 169, 171

[226] Holger Kautz, D. J. M. van Beek, Rint P. Sijbesma, and E. W. Meijer. Cooperative end-to-end and lateral hydrogen-bonding motifs in supramolecular thermoplastic elastomers. *Macromolecules*, 39(13):4265–4267, 2006. 114, 137, 163, 169

[227] Anton W. Bosman, Rint P. Sijbesma, and E. W. Meijer. Supramolecular polymers at work. *Materials Today*, 7(4):34–39, 2004. 137

[228] Tom F. A. de Greef and E. W. Meijer. Materials science: Supramolecular polymers. *Nature*, 453(7192):171–173, 2008. 98, 137

[229] Casey L. Elkins, Taigyoo Park, Matthew G. McKee, and Timothy E. Long. Synthesis and characterization of poly(2-ethylhexyl methacrylate) copolymers containing pendant, self-complementary multiple-hydrogen-bonding sites. *Journal of Polymer Science Part A: Polymer Chemistry*, 43(19):4618–4631, 2005. 99, 102, 137, 138, 139

[230] Matthew G. McKee, Casey L. Elkins, Taigyoo Park, and Timothy E. Long. Influence of random branching on multiple hydrogen bonding in poly(alkyl methacrylate)s. *Macromolecules*, 38(14):6015–6023, 2005. 99, 108, 116, 119, 178

[231] L. J. Fetters, D. J. Lohse, and R. H. Colby. *Chain Dimensions and Entanglement Spacings*, pages 447–454. Springer, New York, 2007. 99, 118, 120, 140, 155

[232] LS Garca-Coln, LF Del Castillo, and Patricia Goldstein. Theoretical basis for the vogel-fulcher-tammann equation. *Physical Review B*, 40(10):7040, 1989. 99

[233] G. P. Baeza, C. Dessi, S. Costanzo, D. Zhao, S. Gong, A. Alegria, R. H. Colby, M. Rubinstein, D. Vlassopoulos, and S. K. Kumar. Network dynamics in nanofilled polymers. *Nat Commun*, 7:11368, 2016. 99, 122, 124, 176

[234] James E Mark. *Sub-Tg Transitions*, volume 1076, pages 217–232. Springer, New York, 2007. 99, 132, 134

[235] Singa D. Tobing and Andrew Klein. Molecular parameters and their relation to the adhesive performance of acrylic pressure-sensitive adhesives. *Journal of Applied Polymer Science*, 79(12):2230–2244, 2001. 100

[236] Yogita Patil-Sen, Amin Sadeghpour, Michael Rappolt, and Chandrashekhar V Kulkarni. Facile preparation of internally self-assembled lipid particles stabilized by carbon nanotubes. *Journal of Visualized Experiments*, (108):e53489–e53489, 2016. 103, 104

[237] Julia S Higgins and Henri Benoît. *Polymers and neutron scattering*. Clarendon press Oxford, 1994. 108

[238] Angel J Moreno, Arantxa Arbe, and Juan Colmenero. Structure and dynamics of self-assembled comb copolymers: comparison between simulations of a generic model and neutron scattering experiments. *Macromolecules*, 44(6):1695–1706, 2011. 108, 109, 110, 111, 112

[239] Umesh Gaur and Bernhard Wunderlich. The glass transition temperature of polyethylene. *Macromolecules*, 13(2):445–446, 1980. 110

[240] Frank S Bates. Measurement of the correlation hole in homogeneous block copolymer melts. *Macromolecules*, 18(3):525–528, 1985. 113

[241] J Huh, O Ikkala, and G Ten Brinke. Correlation hole effect in comblike copolymer systems obtained by hydrogen bonding between homopolymers and end-functionalized oligomers. *Macromolecules*, 30(6):1828–1835, 1997. 113

[242] D. J. M. van Beek, A. J. H. Spiering, Gerrit W. M. Peters, Klaas te Nijenhuis, and Rint P. Sijbesma. Unidirectional dimerization and stacking of ureidopyrimidinone end groups in polycaprolactone supramolecular polymers. *Macromolecules*, 40(23):8464–8475, 2007. 114, 163, 169, 170

[243] Masaru Shimada, Toshiyuki Kawanishi, Kakuji Murakami, Tamotsu Aruga, Hiroyuki Uemura, and Kiyofumi Nagai. Aqueous ink composition, 8 1987. US Patent 4,711,668. 115, 138, 237

[244] C Wayne Jaeger and Clifford R King. Phase change ink composition, 12 2001. US Patent 6,245,135. 115, 138

[245] Jean MJ Frechet, Damian Hajduk, Ezat Khoshdel, Mingjun Liu, Ralph B Nielsen, Euan Stuart Reid, and Keith Leslie Rutherford. Cosmetic and personal care compositions, 16 2003. US Patent 6,663,855. 115, 138, 237

[246] Nathalie Mougin, Aude Livoreil, and Jean Mondet. Cosmetic composition forming after application a supramolecular polymer, 15 2013. US Patent 8,354,097. 115, 138, 237

[247] Bartholomeus Johannes Margaretha Plum Less Johan Franz Gradus Antonius Jansen, Jacobus Antonius Loontjes. Supramolecular compound, 16 2000. US Patent 6,663,855. 115, 138

[248] Yasuhiro Asawa, Yasuhiro Ishizuka, Eiji Hayakawa, and S Peter Pappas. Two-layer imageable element comprising thermally reversible polymers, 7 2005. US Patent 6,902,860. 138, 237

[249] Peter S Pappas, Alan Monk, Shashikant Saraiya, and Jianbing Huang. Imageable element and composition comprising thermally reversible polymers, 28 2005. US Patent 6,911,296. 115, 138, 237

[250] John D. Ferry and Robert F. Landel. Molecular friction coefficients in polymers and their temperature dependence. *Kolloid-Zeitschrift*, 148(1):1–6, 1956. 116, 178

[251] C. M. Roland, K. L. Ngai, P. G. Santangelo, X. H. Qiu, M. D. Ediger, and D. J. Plazek. Temperature dependence of segmental and terminal relaxation in atactic polypropylene melts. *Macromolecules*, 34(18):6159–6160, 2001. 118, 137

[252] M. S. Green and A. V. Tobolsky. A new approach to the theory of relaxing polymeric media. *The Journal of Chemical Physics*, 14(2):80–92, 1946. 119, 139

[253] L. G. Baxandall. Dynamics of reversibly crosslinked chains. *Macromolecules*, 22(4):1982–1988, 1989. 119, 139, 150

[254] Roland Bhmer, KL Ngai, CA Angell, and DJ Plazek. Nonexponential relaxations in strong and fragile glass formers. *The Journal of chemical physics*, 99(5):4201–4209, 1993. 119, 182

[255] Andreas Schnhals Friedrich Kremer. *Broadband Dielectric Spectroscopy*. Springer, 2002. 120, 188, 228

[256] Cheol Jeong and Jack F. Douglas. Mass dependence of the activation enthalpy and entropy of unentangled linear alkane chains. *The Journal of Chemical Physics*, 143(14):144905, 2015. 121, 210

[257] JC Wang and YF Chen. The meyer–neldel rule in fullerenes. *Applied physics letters*, 73(7):948–950, 1998. 121

[258] Hong Qian. Entropy-enthalpy compensation. 1998. 121

[259] Jozef Bicerano, Robert L Sammler, Craig J Carriere, and Jerry T Seitz. Correlation between glass transition temperature and chain structure for randomly crosslinked high polymers. *Journal of Polymer Science Part B: Polymer Physics*, 34(13):2247–2259, 1996. 124

[260] H Stutz, K-H Illers, and J Mertes. A generalized theory for the glass transition temperature of crosslinked and uncrosslinked polymers. *Journal of Polymer Science Part B: Polymer Physics*, 28(9):1483–1498, 1990. 125

[261] B Nabeth, I Corniglion, and JP Pascault. Influence of the composition on the glass transition temperature of polyurethane and polyurethane acrylate networks. *Journal of Polymer Science Part B: Polymer Physics*, 34(3):401–417, 1996. 124, 125

[262] EA DiMarzio and JH Gibbs. On the second-order transition of a rubber. *J. Res. Nat. Bur. Stand. A*, 68:611–617, 1964. 124

[263] G Wisanrakkit and JK Gillham. The glass transition temperature (tg) as an index of chemical conversion for a high-tg amine. *JCT, Journal of coatings technology*, 62(783):35–50, 1990. 124

[264] C Austen Angell et al. Formation of glasses from liquids and biopolymers. *Science*, 267(5206):1924–1935, 1995. 125, 131

[265] Kaori Ito, Cornelius T Moynihan, and C Austen Angell. Thermodynamic determination of fragility in liquids and a fragile-to-strong liquid transition in water. *Nature*, 398(6727):492, 1999. 125

[266] LM Martinez and CA Angell. A thermodynamic connection to the fragility of glass-forming liquids. *Nature*, 410(6829):663, 2001. 125

[267] Srikanth Sastry. The relationship between fragility, configurational entropy and the potential energy landscape of glass forming liquids. *arXiv preprint cond-mat/0011317*, 2000. 125

[268] Mike Reading and Douglas J Hourston. *Modulated temperature differential scanning calorimetry: theoretical and practical applications in polymer characterisation*, volume 6. Springer Science & Business Media, 2006. 22, 125, 126

[269] Arne Hensel and Christoph Schick. Relation between freezing-in due to linear cooling and the dynamic glass transition temperature by temperature-modulated dsc. *Journal of non-crystalline solids*, 235:510–516, 1998. 126

[270] E. Hempel, G. Hempel, A. Hensel, C. Schick, and E. Donth. Characteristic length of dynamic glass transition near tg for a wide assortment of glass-forming substances. *The Journal of Physical Chemistry B*, 104(11):2460–2466, 2000.

[271] S. Weyer, A. Hensel, and C. Schick. Phase angle correction for tmdsc in the glass-transition region. *Thermochimica Acta*, 304:267–275, 1997. 126

[272] S. Havriliak and S. Negami. A complex plane analysis of -dispersions in some polymer systems. *Journal of Polymer Science Part C: Polymer Symposia*, 14(1):99–117, 1966. 128, 161, 173, 175

[273] F. X. Hassion and R. H. Cole. Dielectric properties of liquid ethanol and 2propanol. *The Journal of Chemical Physics*, 23(10):1756–1761, 1955. 129

[274] Kailong Jin and John M. Torkelson. Enhanced tg-confinement effect in cross-linked polystyrene compared to its linear precursor: Roles of fragility and chain architecture. *Macromolecules*, 49(14):5092–5103, 2016. 131

[275] V. Yu Kramarenko, T. A. Ezquerra, I. Åics, F. J. Balt-Calleja, and V. P. Privalko. Influence of cross-linking on the segmental dynamics in model polymer networks. *The Journal of Chemical Physics*, 113(1):447–452, 2000. 176

[276] NM Alves, Gómez Ribelles, Gómez Tejedor, and JF Mano. Viscoelastic behavior of poly (methyl methacrylate) networks with different cross-linking degrees. *Macromolecules*, 37(10):3735–3744, 2004. 131

[277] K Schmidt-Rohr, AS Kulik, HW Beckham, A Ohlemacher, U Pawelzik, C Boeffel, and Hans Wolfgang Spiess. Molecular nature of the β relaxation in poly (methyl methacrylate) investigated by multidimensional nmr. *Macromolecules*, 27(17):4733–4745, 1994. 134

[278] E Muzeau, J Perez, and GP Johari. Mechanical spectrometry of the β relaxation in poly (methyl methacrylate). *Macromolecules*, 24(16):4713–4723, 1991. 134

[279] Marianne Gaborieau, Robert Graf, Stefan Kahle, Tadeusz Pakula, and Hans W Spiess. Chain dynamics in poly (n-alkyl acrylates) by solid-state nmr, dielectric, and mechanical spectroscopies. *Macromolecules*, 40(17):6249–6256, 2007. 134

[280] Koji Yamauchi, Jeremy R. Lizotte, David M. Hercules, Matthew J. Vergne, and Timothy E. Long. Combinations of microphase separation and terminal multiple hydrogen bonding in novel macromolecules. *Journal of the American Chemical Society*, 124(29):8599–8604, 2002. 137

[281] M. L. Pellizzaro, S. A. Barrett, J. Fisher, and A. J. Wilson. Design, synthesis and binding studies of a novel quadruple adda hydrogen-bond array. *Organic & Biomolecular Chemistry*, 10(25):4899–4906, 2012.

[282] Nan Lou, Yangyang Wang, Xiaopeng Li, Haixia Li, Ping Wang, Chrys Wesdemiotis, Alexei P. Sokolov, and Huiming Xiong. Dielectric relaxation and rheological behavior of supramolecular polymeric liquid. *Macromolecules*, 46(8):3160–3166, 2013. 182, 183

[283] JHK Ky Hirschberg, Luc Brunsveld, Aissa Ramzi, Jef AJM Vekemans, Rint P Sijbesma, and EW Meijer. Helical self-assembled polymers from cooperative stacking of hydrogen-bonded pairs. *Nature*, 407(6801):167–170, 2000. 170

[284] Kathleen E. Feldman, Matthew J. Kade, Tom F. A. de Greef, E. W. Meijer, Edward J. Kramer, and Craig J. Hawker. Polymers with multiple hydrogen-bonded end groups and their blends. *Macromolecules*, 41(13):4694–4700, 2008. 163, 169

[285] M. BrzeziÅski and T. Biela. Supramolecular polylactides by the cooperative interaction of the end groups and stereocomplexation. *Macromolecules*, 48(9):2994–3004, 2015. 163, 169

[286] Christian Heinzmann, Iris Lamparth, Kai Rist, Nobert Moszner, Gina L. Fiore, and Christoph Weder. Supramolecular polymer networks made by solvent-free copolymerization of a liquid 2-ureido-4[1h]-pyrimidinone methacrylamide. *Macromolecules*, 48(22):8128–8136, 2015. 137

[287] H. Hofmeier and U. S. Schubert. Recent developments in the supramolecular chemistry of terpyridine-metal complexes. *Chem Soc Rev*, 33(6):373–99, 2004. 137

[288] Philip R. Andres, Harald Hofmeier, and Ulrich S. Schubert. Complexation parameters of terpyridine-metal complexes. 928:141–156, 2006. 137

[289] F. Han, M. Higuchi, and D. G Kurth. Metallo-supramolecular polymers based on functionalized bis-terpyridines as novel electrochromic materials. *Advanced Materials*, 19(22):3928–3931, 2007.

[290] J. Benjamin Beck and Stuart J. Rowan. The preparation of metallosupramolecular polymers and gels by utilizing 2,6-bis-(1-methylbenzimidazolyl)pyridinemetal ion interactions. 928:97–112, 2006.

[291] Harald Hofmeier, Marielle Wouters, Daan Wouters, and Ulrich S. Schubert. Thermal stability, rheology, and morphology of metallosupramolecular polymers based onbis-terpyridine-ruthenium(ii) complexes. 928:113–125, 2006.

[292] Justin R. Kumpfer, Jeong J. Wie, John P. Swanson, Frederick L. Beyer, Michael E. Mackay, and Stuart J. Rowan. Influence of metal ion and polymer core on the melt rheology of metallosupramolecular films. *Macromolecules*, 45(1):473–480, 2012.

[293] Ulrich S. Schubert, Oliver Hien, and Christian Eschbaumer. Functionalized polymers with metal complexing segments: a simple and high-yield entry towards 2,2:6,2-terpyridine-based oligomers. *Macromolecular Rapid Communications*, 21(16):1156–1161, 2000.

[294] S. Schmatloch and U. S. Schubert. Engineering with metallo-supramolecular polymers: linear coordination polymers and networks. *Macromolecular Symposia*, 199(1):483–498, 2003.

[295] H. Goldansaz, Q. Voleppe, S. Pioge, C. A. Fustin, J. F. Gohy, J. Brassinne, D. Auhl, and E. van Ruymbeke. Controlling the melt rheology of linear entangled metallo-supramolecular polymers. *Soft Matter*, 11(4):762–74, 2015. 137

[296] G. A. Schwartz, R. Bergman, J. Mattsson, and J. Swenson. Dielectric relaxation studies of poly(propylene glycol) confined in vermiculite clay. *European Physical Journal E*, 12:S113–S116, 2003. 137, 161, 176

[297] Lidia Gonzlez, Anne Ladegaard Skov, and Sren Hvilsted. Ionic networks derived from the protonation of dendritic amines with carboxylic acid end-functionalized pegs. *Journal of Polymer Science Part A: Polymer Chemistry*, 51(6):1359–1371, 2013. 137

[298] Taiho Park and Steven C. Zimmerman. Interplay of fidelity, binding strength, and structure in supramolecular polymers. *Journal of the American Chemical Society*, 128(44):14236–14237, 2006. 137

[299] Berend Eling and Christopher Lindsay. Supramolecular polymer forming polymer, 23 2003. US Patent App. 10/444,612. 138, 237

[300] Christopher L. Lewis and Mitchell Anthamatten. Synthesis, swelling behavior, and viscoelastic properties of functional poly(hydroxyethyl methacrylate) with ureidopyrimidinone side-groups. *Soft Matter*, 9(15):4058–4066, 2013. 138, 139, 150

[301] Christopher L. Lewis, Kathleen Stewart, and Mitchell Anthamatten. The influence of hydrogen bonding side-groups on viscoelastic behavior of linear and network polymers. *Macromolecules*, 47(2):729–740, 2014. 138, 139, 150

[302] KL Ngai, A Schönhals, and E Schlosser. An explanation of anomalous dielectric relaxation properties of polypropylene glycol. *Macromolecules*, 25(19):4915–4919, 1992. 138

[303] Diethelm Boese and Friedrich Kremer. Molecular dynamics in bulk cis-polyisoprene as studied by dielectric spectroscopy. *Macromolecules*, 23(3):829–835, 1990. 138

[304] Takashi Uneyama, Shinya Suzuki, and Hiroshi Watanabe. Concentration dependence of rheological properties of telechelic associative polymer solutions. *Phys. Rev. E*, 86:031802, Sep 2012. 139

[305] Tom Annable, Richard Buscall, Rammile Ettelaie, and Diane Whittlestone. The rheology of solutions of associating polymers: Comparison of experimental behavior with transient network theory. *Journal of Rheology*, 37(4):695–726, 1993. 139

[306] Ludwik Leibler, Michael Rubinstein, and Ralph H. Colby. Dynamics of reversible networks. *Macromolecules*, 24(16):4701–4707, 1991. 139, 150

[307] Michael Rubinstein and Alexander N. Semenov. Thermoreversible gelation in solutions of associating polymers. 2. linear dynamics. *Macromolecules*, 31(4):1386–1397, 1998. 139, 150, 154

[308] Mostafa Ahmadi, Laurence GD Hawke, Hadi Goldansaz, and Evelyne van Ruymbeke. Dynamics of entangled linear supramolecular chains with sticky side groups: Influence of hindered fluctuations. *Macromolecules*, 48(19):7300–7310, 2015. 139

[309] Michael Rubinstein and Alexander N. Semenov. Dynamics of entangled solutions of associating polymers. *Macromolecules*, 34(4):1058–1068, 2001.

[310] E Van Ruymbeke, K Orfanou, M Kapnistos, H Iatrou, M Pitsikalis, N Hadjichristidis, DJ Lohse, and D Vlassopoulos. Entangled dendritic polymers and beyond: Rheology of symmetric cayley-tree polymers and macromolecular self-assemblies. *Macromolecules*, 40(16):5941–5952, 2007.

[311] E Van Ruymbeke, D Vlassopoulos, M Mierzwa, Tadeusz Pakula, D Charalabidis, M Pitsikalis, and N Hadjichristidis. Rheology and structure of entangled telechelic linear and star polyisoprene melts. *Macromolecules*, 43(9):4401–4411, 2010.

[312] Victor AH Boudara and Daniel J Read. Stochastic and preaveraged nonlinear rheology models for entangled telechelic star polymers. *Journal of Rheology*, 61(2):339–362, 2017. 139

[313] Shengchang Tang, Muzhou Wang, and Bradley D. Olsen. Anomalous self-diffusion and sticky rouse dynamics in associative protein hydrogels. *Journal of the American Chemical Society*, 137(11):3946–3957, 2015. 139

[314] Florian J Stadler, Tim Still, George Fytas, and Christian Bailly. Elongational rheology and brillouin light scattering of entangled telechelic polybutadiene based temporary networks. *Macromolecules*, 43(18):7771–7778, 2010. 140

[315] Aamir Shabbir, Hadi Goldansaz, Ole Hassager, Evelyne van Ruymbeke, and Nicolas J. Alvarez. Effect of hydrogen bonding on linear and nonlinear rheology of entangled polymer melts. *Macromolecules*, 48(16):5988–5996, 2015. 140

[316] José Manuel Román Marín, Jakob Kjøbsted Huusom, Nicolas Javier Alvarez, Qian Huang, Henrik Koblitz Rasmussen, Anders Bach, Anne Ladegaard Skov, and Ole Hassager. A control scheme for filament stretching rheometers with application to polymer melts. *Journal of Non-Newtonian Fluid Mechanics*, 194:14–22, 2013. 142

[317] Masao Doi and Samuel Frederick Edwards. *The theory of polymer dynamics*, volume 73. oxford university press, 1988. 156, 157, 158, 246, 249

[318] J Milton Harris. *Poly (ethylene glycol) chemistry: biotechnical and biomedical applications*. Springer Science & Business Media, 2013. 161

[319] Allan S Hoffman. Hydrogels for biomedical applications. *Advanced drug delivery reviews*, 64:18–23, 2012.

[320] Zhigang Xue, Dan He, and Xiaolin Xie. Poly (ethylene oxide)-based electrolytes for lithium-ion batteries. *Journal of Materials Chemistry A*, 3(38):19218–19253, 2015. 164

[321] Lizhen Long, Shuanjin Wang, Min Xiao, and Yuezhong Meng. Polymer electrolytes for lithium polymer batteries. *Journal of Materials Chemistry A*, 4(26):10038–10069, 2016. 161, 163, 185, 186

[322] Fei Fan, Yangyang Wang, and Alexei P. Sokolov. Ionic transport, microphase separation, and polymer relaxation in poly(propylene glycol) and lithium perchlorate mixtures. *Macromolecules*, 46(23):9380–9389, 2013. 161, 164, 186, 188, 192

[323] R. J. Sengwa. A comparative dielectric study of ethylene glycol and propylene glycol at different temperatures. *Journal of Molecular Liquids*, 108(13):47–60, 2003. 161, 201

[324] Catalin Gainaru, Wolf Hiller, and Roland Bhmer. A dielectric study of oligo- and poly(propylene glycol). *Macromolecules*, 43(4):1907–1914, 2010. 161, 162, 176, 181

[325] K. L. Ngai, A. Schoenhals, and E. Schlosser. An explanation of anomalous dielectric relaxation properties of polypropylene glycol. *Macromolecules*, 25(19):4915–4919, 1992.

[326] K Grzybowska, A Grzybowski, J Ziolo, SJ Rzoska, and M Paluch. Anomalous behavior of secondary dielectric relaxation in polypropylene glycols. *Journal of Physics: Condensed Matter*, 19(37):376105, 2007.

[327] D. Engberg, J. Schller, B. Strube, A. P. Sokolov, and L. M. Torell. Brillouin scattering and dielectric relaxation in ppg of different chain lengths and end groups. *Polymer*, 40(17):4755–4761, 1999. 161, 162, 201

[328] A Schönhals and R Stauga. Broadband dielectric study of anomalous diffusion in a poly (propylene glycol) melt confined to nanopores. *The Journal of chemical physics*, 108(12):5130–5136, 1998. 161

[329] J. Mattsson, R. Bergman, P. Jacobsson, and L. Borjesson. Chain-length-dependent relaxation scenarios in an oligomeric glass-forming system: From merged to well-separated alpha and beta loss peaks. *Physical Review Letters*, 90(7), 2003. 162, 173

[330] K. Kaminski, W. K. Kipnusu, K. Adrjanowicz, E. U. Mapesa, C. Iacob, M. Jasiurkowska, P. Wlodarczyk, K. Grzybowska, M. Paluch, and F. Kremer. Comparative study on the molecular dynamics of a series of polypropylene glycols. *Macromolecules*, 46(5):1973–1980, 2013. 162, 163

[331] R. Bergman, J. Mattsson, C. Svanberg, G. A. Schwartz, and J. Swenson. Confinement effects on the excess wing in the dielectric loss of glass-formers. *Europhysics Letters*, 64(5):675–681, 2003.

[332] K Grzybowska, A Grzybowski, J Zioło, M Paluch, and S Capaccioli. Dielectric secondary relaxations in polypropylene glycols. *The Journal of chemical physics*, 125(4):044904, 2006. 184

[333] Taco Nicolai and George Floudas. Dynamics of linear and star poly(oxypropylene) studied by dielectric spectroscopy and rheology. *Macromolecules*, 31(8):2578–2585, 1998.

[334] J. Mattsson, R. Bergman, P. Jacobsson, and L. Borjesson. Effects of hydrogen bonding on supercooled liquid dynamics and the implications for supercooled water. *Physical Review B*, 79(17):174205, 2009. 162, 163, 201, 226, 230

[335] Johan Sjostrom, Rikard Bergman, Carl Wadell, Tobias Moberg, Jan Swenson, and Johan Mattsson. Effects of water contamination on the supercooled dynamics of a hydrogen-bonded model glass former. *Journal of Physical Chemistry B*, 115(8):1842–1847, 2011.

[336] M Khler, P Lunkenheimer, Y Goncharov, R Wehn, and A Loidl. Glassy dynamics in mono-, di-and tri-propylene glycol: From the -to the fast -relaxation. *Journal of Non-Crystalline Solids*, 356(11):529–534, 2010. 161

[337] J. Mattsson, R. Bergman, P. Jacobsson, and L. Borjesson. Influence of chain length on the alpha-beta bifurcation in oligomeric glass formers. *Physical Review Letters*, 94(16), 2005. 162

[338] Jeppe C. Dyre and Niels Boye Olsen. Minimal model for beta relaxation in viscous liquids. *Phys. Rev. Lett.*, 91:155703, Oct 2003.

[339] Martin S Beevers, David A Elliott, and Graham Williams. Molecular motion in melt samples of poly (propylene glycol) studied using dielectric and kerr effect relaxation techniques. *Polymer*, 21(1):13–20, 1980.

[340] Jovan Mijovic, Mingyun Sun, and Yuefeng Han. Normal and segmental mode dynamics of end-functionalized poly(propylene oxide) by dielectric relaxation spectroscopy and dynamic mechanical spectroscopy. *Macromolecules*, 35(16):6417–6425, 2002.

[341] Catalin Gainaru and Roland Bhmer. Oligomer-to-polymer transition of poly(propylene glycol) revealed by dielectric normal modes. *Macromolecules*, 42(20):7616–7618, 2009. 161, 162, 176, 181

[342] IK Moon, YH Jeong, and T Furukawa. Enthalpy and dielectric relaxation in the glass transition region of polypropylene glycol. *Thermochimica acta*, 377(1):97–104, 2001. 161

[343] Jae-Hyeon Ko and Seiji Kojima. Brillouin scattering study on the polypropylene glycol by using a nonscanning fabry–perot interferometer. *Physics Letters A*, 321(2):141–146, 2004. 161

[344] Yu B Melnichenko, J Schüller, Ranko Richert, Bernd Ewen, and C-K Loong. Dynamics of hydrogen-bonded liquids confined to mesopores: A dielectric and neutron spectroscopy study. *The Journal of chemical physics*, 103(6):2016–2024, 1995. 161

[345] C-H_ Wang, G_ Fytas, D_ Lilge, and Th Dorfmüller. Laser light beating spectroscopic studies of dynamics in bulk polymers: poly (propylene glycol). *Macromolecules*, 14(5):1363–1370, 1981.

[346] S Kojima, H Sato, and A Yosihara. Light scattering of supercooled propylene glycol. *Journal of Physics: Condensed Matter*, 9(46):10079, 1997. 161

[347] K Grzybowska, S Pawlus, M Mierzwa, M Paluch, and KL Ngai. Changes of relaxation dynamics of a hydrogen-bonded glass former after removal of the hydrogen bonds. *The Journal of chemical physics*, 125(14):144507, 2006. 161, 162, 201

[348] M Vogel and T Torbrügge. Nonexponential polymer segmental motion in the presence and absence of ions: H 2 nmr multitime correlation functions for polymer electrolytes poly (propylene glycol)-li cl o 4. *The Journal of chemical physics*, 126(20):204902, 2007. 161

[349] CM Roland, T Psurek, S Pawlus, and M Paluch. Segmental-and normal-mode dielectric relaxation of poly (propylene glycol) under pressure. *Journal of Polymer Science Part B: Polymer Physics*, 41(23):3047–3052, 2003. 161

[350] Gustavo A Schwartz, Rikard Bergman, and Jan Swenson. Relaxation dynamics of a polymer in a 2d confinement. *The Journal of chemical physics*, 120(12):5736–5744, 2004. 161

[351] Ludovic Berthier and Giulio Biroli. Theoretical perspective on the glass transition and amorphous materials. *Reviews of Modern Physics*, 83(2):587, 2011. 162

[352] ME Baur and WH Stockmayer. Dielectric relaxation in liquid polypropylene oxides. *The Journal of chemical physics*, 43(12):4319–4325, 1965. 162, 173

[353] Chen C Ku and Raimond Liepins. *Electrical properties of polymers*. MacMillan Publishing Company., 1993.

[354] Keiichiro Adachi and Tadao Kotaka. Dielectric normal mode relaxation. *Progress in polymer science*, 18(3):585–622, 1993. 162, 173, 190

[355] Kazunori Se, Keiichiro Adachi, and Tadao Kotaka. Dielectric relaxations in poly (ethylene oxide): Dependence on molecular weight. *Polymer Journal*, 13(11):1009–1017, 1981.

[356] R Casalini and CM Roland. Temperature and density effects on the local segmental and global chain dynamics of poly (oxybutylene). *Macromolecules*, 38(5):1779–1788, 2005. 173

[357] M Mierzwa, G Floudas, J Dorgan, D Knauss, and J Wegner. Local and global dynamics of polylactides.: A dielectric spectroscopy study. *Journal of non-crystalline solids*, 307:296–303, 2002. 162

[358] Liping Yue, Jun Ma, Jianjun Zhang, Jingwen Zhao, Shanmu Dong, Zhihong Liu, Guanglei Cui, and Liquan Chen. All solid-state polymer electrolytes for high-performance lithium ion batteries. *Energy Storage Materials*, 5:139–164, 2016. 163

[359] Jonas Mindemark, Bing Sun, Erik Törmä, and Daniel Brandell. High-performance solid polymer electrolytes for lithium batteries operational at ambient temperature. *Journal of Power Sources*, 298:166–170, 2015.

[360] Wolfgang H Meyer. Polymer electrolytes for lithium-ion batteries. *Advanced materials*, 10(6):439–448, 1998. 163

[361] A Manuel Stephan. Review on gel polymer electrolytes for lithium batteries. *European polymer journal*, 42(1):21–42, 2006. 186

[362] F Croce, GB Appetecchi, L Persi, and B Scrosati. Nanocomposite polymer electrolytes for lithium batteries. *Nature*, 394(6692):456, 1998. 186

[363] J-M Tarascon and Michel Armand. Issues and challenges facing rechargeable lithium batteries. *Nature*, 414(6861):359–367, 2001. 163

[364] S Schantz, LM Torell, and JR Stevens. Ion pairing effects in poly (propylene glycol)–salt complexes as a function of molecular weight and temperature: A raman scattering study using nacf3so3 and liclo4. *The Journal of chemical physics*, 94(10):6862–6867, 1991. 164

[365] A Vallée, S Besner, and J Prud'Homme. Comparative study of poly (ethylene oxide) electrolytes made with lin (cf3so2) 2, licf3so3 and liclo4: Thermal properties and conductivity behaviour. *Electrochimica acta*, 37(9):1579–1583, 1992.

[366] Kensuke Yoshida, Hiroyuki Manabe, Yoshiyuki Takahashi, and Takeo Furukawa. Correlation between ionic and molecular dynamics in the liquid state of polyethylene oxide/lithium perchlorate complexes. *Electrochimica Acta*, 57:139–146, 2011.

[367] DE Fenton, JM Parker, and PV Wright. Complexes of alkali metal ions with poly (ethylene oxide). *polymer*, 14(11):589, 1973.

[368] Peter V Wright. Electrical conductivity in ionic complexes of poly (ethylene oxide). *Polymer International*, 7(5):319–327, 1975.

[369] Masayoshi Watanabe, Junko Ikeda, and Isao Shinohara. Effect of molecular weight of polymeric solvent on ion conductive behavior in poly (propylene oxide). *Polymer Journal*, 15(1):65–69, 1983.

[370] Zlatka Gadjourova, Yuri G Andreev, David P Tunstall, and Peter G Bruce. Ionic conductivity in crystalline polymer electrolytes. *Nature*, 412(6846):520–523, 2001. 164

[371] C Vachon, M Vasco, M Perrier, and J Prud'Homme. Microphase separation in amorphous polyethers complexed with lithium perchlorate, sodium perchlorate and sodium iodide. *Macromolecules*, 26(15):4023–4031, 1993. 164, 186, 188, 192

[372] R Bergman, L Börjesson, G Fytas, and LM Torell. Photon correlation study of structural relaxations in nacf3so3 containing polymer electrolytes. *Journal of non-crystalline solids*, 172:830–837, 1994.

[373] C Vachon, C Labreche, A Vallee, S Besner, M Dumont, and J Prud'Homme. Microphase separation and conductivity behavior of poly (propylene oxide)-lithium salt electrolytes. *Macromolecules*, 28(16):5585–5594, 1995. 164, 188, 192

[374] Takeo Furukawa, Yasuhiko Mukasa, Toshikazu Suzuki, and Kenji Kano. Microphase separation and ion-conduction mechanisms in polypropylene oxide/lithium perchlorate (liclo4) complexes. *Journal of Polymer Science Part B: Polymer Physics*, 40(7):613–622, 2002. 164, 186, 192

[375] Kenji Kano, Yoshiyuki Takahashi, and Takeo Furukawa. Molecular weight dependence of ion-mode relaxation and dc conduction in polypropylene oxide complexed with liclo4. *Japanese Journal of Applied Physics*, 40(5R):3246, 2001. 164

[376] Shihai Zhang and James Runt. Segmental dynamics and ionic conduction in poly (vinyl methyl ether)- lithium perchlorate complexes. *The Journal of Physical Chemistry B*, 108(20):6295–6302, 2004. 164

[377] W Gorecki, M Jeannin, E Belorizky, C Roux, and M Armand. Physical properties of solid polymer electrolyte peo (litfsi) complexes. *Journal of Physics: Condensed Matter*, 7(34):6823, 1995. 165

[378] Bruno Scrosati. Recent advances in lithium ion battery materials. *Electrochimica Acta*, 45(15):2461–2466, 2000. 165

[379] Eva Wisse, L. E. Govaert, H. E. H. Meijer, and E. W. Meijer. Unusual tuning of mechanical properties of thermoplastic elastomers using supramolecular fillers. *Macromolecules*, 39(21):7425–7432, 2006. 169, 171

[380] Nicole E. Botterhuis, S. Karthikeyan, A. J. H. Spiering, and Rint P. Sijbesma. Self-sorting of guests and hard blocks in bisurea-based thermoplastic elastomers. *Macromolecules*, 43(2):745–751, 2010.

[381] Ron M. Versteegen, Rint P. Sijbesma, and E. W. Meijer. Synthesis and characterization of segmented copoly(ether urea)s with uniform hard segments. *Macromolecules*, 38(8):3176–3184, 2005.

[382] Rolf A. Koevoets, Ron M. Versteegen, Huub Kooijman, Anthony L. Spek, Rint P. Sijbesma, and E. W. Meijer. Molecular recognition in a thermoplastic elastomer. *Journal of the American Chemical Society*, 127(9):2999–3003, 2005. 169, 171

[383] Nicole E. Botterhuis, D. J. M. van Beek, Gaby M. L. van Gemert, Anton W. Bosman, and Rint P. Sijbesma. Self-assembly and morphology of polydimethylsiloxane supramolecular thermoplastic elastomers. *Journal of Polymer Science Part A: Polymer Chemistry*, 46(12):3877–3885, 2008. 169

[384] Christopher A Hunter and Jeremy KM Sanders. The nature of. pi.-. pi. interactions. *Journal of the American Chemical Society*, 112(14):5525–5534, 1990. 171

[385] D-N Horng, J-P Chyn, K-J Shieh, J-L Chou, and Y-S Wen. 3, 5-di-tert-butyl-1, 2-benzoquinone. *Acta Crystallographica Section C: Crystal Structure Communications*, 55(4):652–653, 1999. 25, 171

[386] Sigma Aldrich. Material safety data sheet of poly(propylrene glycol). Technical report. 25, 171

[387] James E Mark. *Physical properties of polymers handbook*, volume 1076. Springer, 2007. 171

[388] Graham Williams and David C Watts. Non-symmetrical dielectric relaxation behaviour arising from a simple empirical decay function. *Transactions of the Faraday society*, 66:80–85, 1970. 173, 175

[389] C Austin Angell, Kia L Ngai, Greg B McKenna, Paul F McMillan, and Steve W Martin. Relaxation in glassforming liquids and amorphous solids. *Journal of Applied Physics*, 88(6):3113–3157, 2000. 176

[390] Bo Jakobsen, Kristine Niss, Claudio Maggi, Niels Boye Olsen, Tage Christensen, and Jeppe C Dyre. Beta relaxation in the shear mechanics of viscous liquids: Phenomenology and network modeling of the alpha-beta merging region. *Journal of Non-Crystalline Solids*, 357(2):267–273, 2011. 182

[391] K. Adrjanowicz, B. Jakobsen, T. Hecksher, K. Kaminski, M. Dulski, M. Paluch, and K. Niss. Slow supramolecular mode in amine and thiol derivatives of 2-ethyl-1-hexanol revealed by combined dielectric and shear-mechanical studies. *The Journal of Chemical Physics*, 143(18):181102, 2015.

[392] Bo Jakobsen, Tina Hecksher, Tage Christensen, Niels Boye Olsen, Jeppe C. Dyre, and Kristine Niss. Identical temperature dependence of the time scales of several linear-response functions of two glass-forming liquids. *The Journal of Chemical Physics*, 136(8):081102, 2012.

[393] Henriette W. Hansen, Bernhard Frick, Tina Hecksher, Jeppe C. Dyre, and Kristine Niss. Connection between fragility, mean-squared displacement, and shear modulus in two van der waals bonded glass-forming liquids. *Phys. Rev. B*, 95:104202, Mar 2017. 182

[394] C Austen Angell. Formation of glasses from liquids and biopolymers. *Science*, 267(5206):1924, 1995. 182

[395] A Abou Elfadl, A Herrmann, J Hintermeyer, N Petzold, VN Novikov, and EA Rossler. Molecular weight dependence of fragility in polymers. *Macromolecules*, 42(17):6816–6817, 2009. 183

[396] PG Santangelo and CM Roland. Molecular weight dependence of fragility in polystyrene. *Macromolecules*, 31(14):4581–4585, 1998.

[397] R Casalini, CM Roland, and S Capaccioli. Effect of chain length on fragility and thermodynamic scaling of the local segmental dynamics in poly (methylmethacrylate). *The Journal of chemical physics*, 126(18):184903, 2007.

[398] Yifu Ding, VN Novikov, AP Sokolov, A Cailliaux, C Dalle-Ferrier, C Alba-Simionesco, and B Frick. Influence of molecular weight on fast dynamics and fragility of polymers. *Macromolecules*, 37(24):9264–9272, 2004. 183

[399] Johan Mattsson, Rikard Bergman, Per Jacobson, and Lars Borjesson. The alpha-beta relaxation scenario in glass forming oligomer systems of varying chain-end functionality. In *APS Meeting Abstracts*, 2004. 184

[400] HP Schwan. Electrode polarization impedance and measurements in biological materials. *Annals of the New York Academy of Sciences*, 148(1):191–209, 1968. 185

[401] HP Schwan. Alternating current electrode polarization. *Radiation and Environmental Biophysics*, 3(2):181–201, 1966. 185

[402] S. Lascaud, M. Perrier, A. Vallee, S. Besner, J. Prud'homme, and M. Armand. Phase diagrams and conductivity behavior of poly(ethylene oxide)-molten salt rubbery electrolytes. *Macromolecules*, 27(25):7469–7477, 1994. 185

[403] C. Roux and J. Y. Sanchez. Ionic conductivities of ppo-litfsi complexes. *Solid State Ionics*, 72:160–164, 1994. 185, 186

[404] Ian M Ward and Hugh V St A Hubbard. Polymer gel electrolytes: Conduction mechanism and battery applications. *Ionic Interactions in Natural and Synthetic Macromolecules*, pages 817–840, 2012. 186

[405] RC Agrawal and GP Pandey. Solid polymer electrolytes: materials designing and all-solid-state battery applications: an overview. *Journal of Physics D: Applied Physics*, 41(22):223001, 2008. 186

[406] F Croce, R Curini, A Martinelli, L Persi, F Ronci, B Scrosati, and R Caminiti. Physical and chemical properties of nanocomposite polymer electrolytes. *The Journal of Physical Chemistry B*, 103(48):10632–10638, 1999. 186

[407] N Kaskhedikar, J Paulsdorf, M Burjanadze, Y Karatas, B Roling, and H-D Wiemhöfer. Polyphosphazene based composite polymer electrolytes. *Solid State Ionics*, 177(26):2699–2704, 2006. 186

[408] Pierre-Jean Alarco, Yaser Abu-Lebdeh, Ali Abouimrane, and Armand Michel. The plastic-crystalline phase of succinonitrile as a universal matrix for solid-state ionic conductors. *Nature Materials*, 3(7):476, 2004. 186

[409] Michael Wübbenhorst and Jan van Turnhout. Analysis of complex dielectric spectra. i. one-dimensional derivative techniques and three-dimensional modelling. *Journal of Non-Crystalline Solids*, 305(1):40–49, 2002. 188

[410] Yangyang Wang, Fei Fan, Alexander L Agapov, Tomonori Saito, Jun Yang, Xiang Yu, Kunlun Hong, Jimmy Mays, and Alexei P Sokolov. Examination of the fundamental relation between ionic transport and segmental relaxation in polymer electrolytes. *Polymer*, 55(16):4067–4076, 2014. 190, 191

[411] William Sutherland. Lxxv. a dynamical theory of diffusion for non-electrolytes and the molecular mass of albumin. *The London, Edinburgh, and Dublin Philosophical Magazine and Journal of Science*, 9(54):781–785, 1905. 191

[412] Gabor L Hornyak, Joydeep Dutta, Harry F Tibbals, and Anil Rao. *Introduction to nanoscience*. CRC press, 2008. 191

[413] Alexei P Sokolov and Kenneth S Schweizer. Resolving the mystery of the chain friction mechanism in polymer liquids. *Physical review letters*, 102(24):248301, 2009. 191

[414] Alexander L Agapov and Alexei P Sokolov. Decoupling ionic conductivity from structural relaxation: a way to solid polymer electrolytes? *Macromolecules*, 44(11):4410–4414, 2011. 191

[415] Yangyang Wang, Alexander L Agapov, Fei Fan, Kunlun Hong, Xiang Yu, Jimmy Mays, and Alexei P Sokolov. Decoupling of ionic transport from segmental relaxation in polymer electrolytes. *Physical review letters*, 108(8):088303, 2012. 191

[416] E Uhde and T Salthammer. Impact of reaction products from building materials and furnishings on indoor air qualitya review of recent advances in indoor chemistry. *Atmospheric Environment*, 41(15):3111–3128, 2007. 196

[417] JL Garnett. Radiation curing-twenty five years on. *Radiation Physics and Chemistry*, 46(4-6):925–930, 1995.

[418] Marco Sangermano, Nicolò Razza, and James Vincent Crivello. Cationic uv-curing: Technology and applications. *Macromolecular Materials and Engineering*, 299(7):775–793, 2014. 196

[419] Li-Min Wang, Yongjun Tian, Riping Liu, and Ranko Richert. Calorimetric versus kinetic glass transitions in viscous monohydroxy alcohols. *The Journal of Chemical Physics*, 128(8):–, 2008. 200

[420] Li-Min Wang, Shervin Shahriari, and Ranko Richert. Diluent effects on the debye-type dielectric relaxation in viscous monohydroxy alcohols. *The Journal of Physical Chemistry B*, 109(49):23255–23262, 2005.

[421] Li-Min Wang and Ranko Richert. Dynamics of glass-forming liquids. ix. structural versus dielectric relaxation in monohydroxy alcohols. *The Journal of Chemical Physics*, 121(22):11170–11176, 2004.

[422] S. S. N. Murthy and Madhusudan Tyagi. Experimental study of the high frequency relaxation process in monohydroxy alcohols. *The Journal of Chemical Physics*, 117(8):3837–3847, 2002.

[423] C. Gainaru, S. Kastner, F. Mayr, P. Lunkenheimer, S. Schildmann, H. J. Weber, W. Hiller, A. Loidl, and R. Bhmer. Hydrogen-bond equilibria and lifetimes in a monohydroxy alcohol. *Physical Review Letters*, 107(11):118304, 2011.

[424] D. Fragiadakis, C. M. Roland, and R. Casalini. Insights on the origin of the debye process in monoalcohols from dielectric spectroscopy under extreme pressure conditions. *The Journal of Chemical Physics*, 132(14):–, 2010.

[425] C. Gainaru, R. Meier, S. Schildmann, C. Lederle, W. Hiller, E. A. Rssler, and R. Bhmer. Nuclear-magnetic-resonance measurements reveal the origin of the debye process in monohydroxy alcohols. *Physical Review Letters*, 105(25):258303, 2010. 200, 228

[426] C. Gainaru, R. Figuli, T. Hecksher, B. Jakobsen, J. C Dyre, M. Wilhelm, and R. Bhmer. Shear-modulus investigations of monohydroxy alcohols: Evidence for a short-chain-polymer rheological response. *Physical Review Letters*, 112(9), 2014. 200, 201, 228

[427] P. Sillren, A. Matic, M. Karlsson, M. Koza, M. Maccarini, P. Fouquet, M. Goetz, Th Bauer, R. Gulich, P. Lunkenheimer, A. Loidl, J. Mattsson, C. Gainaru, E. Vynokur, S. Schildmann, S. Bauer, and R. Boehmer. Liquid 1-propanol studied by neutron scattering, near-infrared, and dielectric spectroscopy. *Journal of Chemical Physics*, 140(12), 2014. 200, 228

[428] Per Sillren, Johan Bielecki, Johan Mattsson, Lars Borjesson, and Aleksandar Matic. A statistical model of hydrogen bond networks in liquid alcohols. *Journal of Chemical Physics*, 136(9), 2012.

[429] H Graener, TQ Ye, and A Laubereau. Ultrafast dynamics of hydrogen bonds directly observed by time-resolved infrared spectroscopy. *The Journal of Chemical Physics*, 90(7):3413–3416, 1989. 200, 228

[430] Sidney W Benson. Some observations on the structures of liquid alcohols and their heats of vaporization. *Journal of the American Chemical Society*, 118(43):10645–10649, 1996. 200, 228

[431] A Sahoo, S Sarkar, V Bhagat, and RN Joarder. The probable molecular association in liquid d-1-propanol through neutron diffraction. *The Journal of Physical Chemistry A*, 113(17):5160–5162, 2009.

[432] Ralf Ludwig. The structure of liquid methanol. *ChemPhysChem*, 6(7):1369–1375, 2005. 200, 228

[433] RE Wetton and G Williams. Dielectric relaxation in polytetramethylene oxide. *Transactions of the Faraday Society*, 61:2132–2139, 1965. 202, 204

[434] Akihiro Tsutsumi, Kunio Hikichi, and Motozo Kaneko. Nuclear magnetic resonance and dielectric dispersion of polytetrahydrofuran and poly-1, 3-dioxolane. *Japanese Journal of Applied Physics*, 7(6):577, 1968. 202

[435] AH Willbourn. The glass transition in polymers with the (ch2)n group. *Transactions of the Faraday Society*, 54:717–729, 1958. 202

[436] RE Wetton and G Allen. The dynamic mechanical properties of some polyethers. *Polymer*, 7(7):331–365, 1966. 202

[437] J. S. Higgins, L. K. Nicholson, and J. B. Hayter. Observation of single chain motion in a polymer melt. *Polymer*, 22(2):163–167, 1981. 202, 203

[438] Ychi Ishida, Masato Matsuo, and Kaoru Yamafuji. Dielectric behaviors of some polyvinyl esters. *Colloid & Polymer Science*, 180(2):108–114, 1962. 202

[439] P. G. Santangelo, K. L. Ngai, and C. M. Roland. Distinctive manifestations of segmental motion in amorphous poly(tetrahydrofuran) and polyisobutylene. *Macromolecules*, 26(11):2682–2687, 1993. 203

[440] Julia S. Higgins and Jaan E. Roots. Effects of entanglements on the single-chain motion of polymer molecules in melt samples observed by neutron scattering. *Journal of the Chemical Society, Faraday Transactions 2: Molecular and Chemical Physics*, 81(5):757–767, 1985. 203

[441] William W Graessley. Some phenomenological consequences of the doi–edwards theory of viscoelasticity. *Journal of Polymer Science Part B: Polymer Physics*, 18(1):27–34, 1980. 203

[442] Kunio Hikichi and Jiro Furuichi. Molecular motions of polymers having helical conformation. i. poly (ethylene glycol) and polyoxymethylene. *Journal of Polymer Science Part A: Polymer Chemistry*, 3(8):3003–3013, 1965. 203

[443] Akio Chiba, Akira Hasegawa, Kunio Hikichi, and Jiro Furuichi. Thermal motion of polyoxymethylene in crystalline region. i. *Journal of the Physical Society of Japan*, 21(9):1777–1781, 1966. 203

[444] M. E. Ries, P. G. Klein, M. G. Brereton, and I. M. Ward. Proton nmr study of rouse dynamics and ideal glass transition temperature of poly(ethylene oxide) licf3so3 complexes. *Macromolecules*, 31(15):4950–4956, 1998. 212, 213

[445] ME Ries, MG Brereton, IM Ward, JI Cail, and RFT Stepto. Rescaling approach to molecular orientation for nmr and optical properties of polymer networks. *Macromolecules*, 35(14):5665–5669, 2002. 214, 217

[446] DJR Taylor, RFT Stepto, RA Jones, and IM Ward. Computer simulation studies of molecular orientation and the stress- optical properties of polyethylene networks. *Macromolecules*, 32(6):1978–1989, 1999. 214

[447] N. Bloembergen, E. M. Purcell, and R. V. Pound. Relaxation effects in nuclear magnetic resonance absorption. *Physical Review*, 73(7):679–712, 1948. 215

[448] JMG Cown. Some general features of tg-m relations for oligomers and amorphous polymers. *European Polymer Journal*, 11(4):297–300, 1975. 219

[449] JULIA Hintermeyer, A Herrmann, R Kahlau, C Goiceanu, and EA Rossler. Molecular weight dependence of glassy dynamics in linear polymers revisited. *Macromolecules*, 41(23):9335–9344, 2008. 219

[450] AL Agapov and AP Sokolov. Does the molecular weight dependence of t_g correlate to m_e. *Macromolecules*, 42(7):2877–2878, 2009. 220

[451] Baker Daniel, Reynolds Matthew, Masurel Robin, Olmsted Peter, and Mattsson Johan. To be published. 220

[452] Eric W Lemmon and ARH Goodwin. Critical properties and vapor pressure equation for alkanes cnh2n+ 2: Normal alkanes with n=36 and isomers for n=4 through n= 9. *Journal of Physical and Chemical Reference Data*, 29(1):1–39, 2000. 32, 230

[453] Chemspider. http://www.chemspider.com/. Accessed June 4, 2017. 32, 230

[454] AA Miller. Kinetic interpretation of the glass transition: Glass temperatures of n-alkane liquids and polyethylene. *Journal of Polymer Science Part B: Polymer Physics*, 6(1):249–257, 1968. 229

[455] Arnold V Lesikar. On the self-association of the normal alcohols and the glass transition in alcohol-alcohol solutions. *Journal of Solution Chemistry*, 6(2):81–93, 1977. 229

[456] O Griffin Lewis. Relationships between polymer structure and glass temperature. i. the n-alkanes. *The Journal of Chemical Physics*, 43(8):2693–2696, 1965. 229

[457] Ayumi Minoguchi, Ranko Richert, and C Austen Angell. Dielectric studies deny existence of ultraviscous fragile water. *Physical review letters*, 93(21):215703, 2004. 230

[458] Kasi Visalakshi Sundaresan and Richard D Ludescher. Molecular mobility and oxygen permeability in amorphous β-lactoglobulin films. *Food hydrocolloids*, 22(3):403–413, 2008. 237

[459] Wendell Q Sun and Paul Davidson. Protein inactivation in amorphous sucrose and trehalose matrices: effects of phase separation and crystallization. *Biochimica et Biophysica Acta (BBA)-General Subjects*, 1425(1):235–244, 1998. 237

[460] Prakash Sundaramurthi and Raj Suryanarayanan. Trehalose crystallization during freeze-drying: Implications on lyoprotection. *The Journal of Physical Chemistry Letters*, 1(2):510–514, 2009. 237

[461] Marcus T Cicerone and Jack F Douglas. β-relaxation governs protein stability in sugar-glass matrices. *Soft Matter*, 8(10):2983–2991, 2012. 237

[462] Paul J Flory. Molecular size distribution in three dimensional polymers. i. gelation1. *Journal of the American Chemical Society*, 63(11):3083–3090, 1941. 239

[463] Alexei E Likhtman. Viscoelasticity and molecular rheology. *Polymer Science: A Comprehensive Reference*, 1:133–179, 2012. 247

[464] Jorge Ramirez, Sathish K Sukumaran, Bart Vorselaars, and Alexei E Likhtman. Efficient on the fly calculation of time correlation functions in computer simulations. *The Journal of chemical physics*, 133(15):154103, 2010. 247

[465] John M. Dealy and Ronald G Larson. *Structure and Rheology of Molten Polymers*. Carl Hanser Verlag GmbH & Co. KG, München, 2 edition, mar 2006. 249